Time-resolved X-ray and Optical Studies of Metalloproteins and Iridium Complexes

THÈSE N^{O} 6797 (2015)

PRÉSENTÉE LE 11 NOVEMBRE 2015

À LA FACULTÉ DES SCIENCES DE BASE
LABORATOIRE DE SPECTROSCOPIE ULTRARAPIDE
PROGRAMME DOCTORAL EN PHYSIQUE

ÉCOLE POLYTECHNIQUE FÉDÉRALE DE LAUSANNE

POUR L'OBTENTION DU GRADE DE DOCTEUR ÈS SCIENCES

PAR

Mahsa SILATANI

acceptée sur proposition du jury:

Prof. M. Q. Tran, président du jury
Prof. M. Chergui, directeur de thèse
Prof. A. Cannizzo, rapporteur
Dr E. Baranoff, rapporteur
Prof. J.-E. Moser, rapporteur

ÉCOLE POLYTECHNIQUE
FÉDÉRALE DE LAUSANNE

Suisse
2015

تقدیم به پدر و مادر عزیزم

Abstract

A wide variety of physical and chemical processes at the molecular level, in particular charge or energy transfer, electronic as well as vibrational relaxation, is at the origin of the biological functionality of proteins and organometalic compounds. The work reported in this thesis is devoted to the study of these molecular dynamics in different organometalic systems. More specifically, this study is focused on the role of these dynamics in the ultrafast photophysics and photochemistry of ferrous Myoglobin and tris-cyclometalated iridium complexes having a transition metal active center of $3d^6$ (Fe^{+2}) and $5d^6$ (Ir^{+3}).

The nature of ligand recombination to the active centre has a strong impact on the reactivity and activation of heme proteins. Using picosecond Fe K-edge X-ray absorption spectroscopy (XAS) we probed the NO-heme recombination kinetics with direct sensitivity to the Fe-NO binding in physiological solution. The transient XAS at 70 ps and 300 ps are identical, but they deviate from the difference between the static spectra of deoxyMb and nitrosyl myoglobin demonstrating the formation of an intermediate species that we propose to be a 6-coordinated domed species that is populated on a time scale of ~200 ps and relaxes in ~30 ps.

A broadband femtosecond luminescence study of the ultrafast photo-physics of $Ir(ppy)_3$ (**Ir1**), the heteroleptic compounds $Ir(ppy)_2(pic)$ (**Ir2**) and $[Ir(ppy)_2(bpy)]^+$ (**Ir3**) and of $Ir(ppz)_3$ (**Ir4**) provides the first extensive picture of the ligand dependence of their photo-cycle. Upon 266 nm excitation of the ligand-centered (LC) absorption band of **Ir1**, we directly clock the relaxation cascade leading to the lowest triplet metal-to-ligand charge transfer (^{3}MLCT) state. We find that the relaxation cascade proceeds within ≤ 10 fs, which is faster than some of the highest frequency

modes of the system. In **Ir4** an ultrafast bi-exponential (140 fs rise 530 fs decay) relaxation to the lowest ^{3}MLCT state which is strongly quenched by a thermally activated non-radiative channel. For **Ir1, 2, 3**, the emission upon 400 nm excitation, is dominated by intermediate ^{3}MLCT states at early times (<1ps), which are related to the ppy moiety. At later times (>100s ps), the emission evolves to the steady-state showing evidence of dual emission for **Ir1, 2** due to a double-well minimum of the lowest emitting ^{3}MLCT state involving the ppy moiety. For **Ir3**, the final emission involves the bpy moiety, pointing to the occurrence of a ppy to bpy inter-ligand energy transfer. The photoluminescence lifetime of **Ir1** in DMSO amounts to 170 ± 30 ns while **Ir4** decays with 1.6 ± 0.1 ns.

The studies of the electronic and geometric structure of **Ir1-4** by Ir L_3 XAS in DCM solution reveals overall identical above-edge multiple scattering (MS) resonances indicating similar bond lengths and angles in the first coordination sphere of the Ir. Simulation of the XAS for both pre-edge region using TDDFT and edge/above-edge region using FEFF9 shows overall good agreement with the experiment. The EXAFS region for all compounds is alike with no distinct feature up to 220 eV above the edge. The near-edge region of the spectra shows distinct differences among the complexes studied. Between homoleptic compounds, the WL intensity of **Ir4** is largest, indicating higher Ir 5d character in the region (weaker π-back donation). The XAS spectra of heteroleptic compounds indicate larger electron density with 5d character on the iridium. In the XAS spectra of **Ir1** and **Ir4** we observed weak pre-edge resonance being predominately metal ($2p_{3/2}$)-to-ligand charge transfer excitations. The absence of this shoulder in **Ir2** and **Ir3** is due to the reduced covalency of the bonds. However, the existence of such transitions remains open for debate since Ir^{+3} has only occupied t_{2g} orbitals ($5d^6$) in the low spin configuration.

By means of picosecond XAS we have successfully captured the transient spectrum at the Ir L_3-edge of both **Ir1** and **Ir4** probed 150 ps after laser excitation in solution. Upon optical excitation of a MLCT band, we observed a change of the oxidation state of Ir from +3 to +4. In DCM, the transient spectra are almost identical for both **Ir1** and **Ir4** within the error bars. For both samples the only significant changes are those observed around the white line. The photo-induced vacancy in dπ orbitals opens up a new channel for absorption at 11.215 keV. The calculations reproduce the blue shift of the absorption spectrum, indicating a transfer of electron density away from the

Ir, consistent with the MLCT excitation. The calculations also reproduce the feature, arising from the valence hole.

Keywords: Ultrafast spectroscopy, X-ray absorption spectroscopy, photoluminescence up-conversion, synchrotron radiation, Myoglobin, ligand recombination, Tryptophan, tris-cyclometalated iridium complexes, IVR, dual emission

Résumé

Une grande variété de processus physiques et chimiques au niveau moléculaire, tels que les transferts de charge ou d'énergie, la relaxation électronique ou vibrationnelle, est à l'origine de la fonctionnalité biologique des protéines ou des composés organométalliques. Le travail rapporté dans cette thèse est dédié à l'étude des processus moléculaires dynamiques de différents systèmes organométalliques. Plus spécifiquement, cette étude est focalisée sur le rôle de ces processus dynamiques dans la photophysique et la photochimie ultrarapide de la myoglobine ferreuse et de complexes d'iridium tricyclocoordinés ayant un centre métallique actif respectivement de $3d^6$ (Fe^{2+}) et $5d^6$ (Ir^{3+}), respectivement.

La nature de la recombinaison du ligand sur le centre actif a une conséquence importante sur la reactivité et l'activation des protéines hémiques. En utilisant la spectroscopie d'absorption X (XAS) au seuil K du fer, nous avons sondé la cinétique de recombinaison nitroxide-centre hémique avec une sensibilité directe de la liaison Fe-NO en solution physiologique. Les signaux XAS transitoires à 70 ps et 300 ps sont identiques mais ils dévient de la différence entre les spectres statiques de la déoxymyoglobine et de la nitrosy lmyoglobine démontrant la formation d'espèces intermédiaires que nous proposons comme étant des espèces hexacoordinées en forme de dôme, cette espèce étant formée sur une échelle de temps d'environ 200 ps et relaxant en environ 30 ps.

Une étude en luminescence femtoseconde en bande large de la photophysique ultrarapide des complexes homoleptiques $Ir(ppy)_3$ (**Ir1**), $Ir(ppz)_3$ (**Ir4**) et hétéroleptiques $Ir(ppy)_2(plc)$ (**Ir2**), $Ir(ppy)_2(bpy)+$ (**Ir3**) fournissent la première evidence d'une dépendance du ligand sur leur photophysique respective. Sous excitation à 266 nm centrée sur la bande d'absorption du ligand (LC) d'**Ir1**, nous chronométrons la durée de l'enchaînement de relaxations

conduisant à l'état triplet du transfert de charge métal vers ligand le plus bas. Nous déterminons que la cascade de relaxation se produit en moins de 10 fs, ce qui est plus rapide que les périodes des modes de plus haute fréquence du système. Pour **Ir4**, une relaxation ultrarapide biexponentielle (140 fs d'accroissement, 530 fs de relaxation) vers l'état le plus bas ^{3}MLCT est mesurée qui est fortement atténuée par une chaîne de relaxation non radiative, thermiquement activée. Pour **Ir1**, 2 et 3, l'émission sous excitation à 400 nm est dominée par des états ^{3}MLCT intermédiaires à délais courts (<1 ps), qui sont reliés aux ligands ppy. A des retards plus longs (>100 ps), l'émission évolue vers un état stationnaire montrant l'existence d'une double émission pour **Ir1, 2** à cause d'un puits à double minimum de l'état émetteur le plus bas ^{3}MLCT impliquant les ligands ppy. Pour **Ir3**, l'émission finale implique le ligand bpy, montrant l'apparition d'un transfert d'énergie entre les ligands ppy vers bpy. La durée de photoluminescence de **Ir1** dans le DMSO est mesurée à 170 ± 30 ns tandis que **Ir4** décroît en 1.6 ± 0.1 ns.

Les études de la structure électronique et géométrique de **Ir1-4** par Ir L_3 XAS en solution dans le DCM révèlent des résonances de multiples diffusions (MS) similaires au-dessus du seuil d'absorption montrant des angles et des longueurs de liaisons similaires dans la première sphère de coordination de l'Ir. Des simulations des spectres d'absorption X pour les deux régions avant le seuil utilisant la TDDFT et des simulations du seuil et au-delà en utilisant FEFF9 montrent un bon accord d'ensemble avec l'expérience. L'EXAFS pour tous les composés est similaire avec aucune forme distincte jusqu'à 220 eV au dessus du seuil. Dans les spectres, la région proche du seuil montre des différences distinctes parmi les complexes étudiés. Entre les complexes homoleptiques, l'intensité de la "raie blanche" de **Ir4** est la plus importante, montrant une contribution plus importante de Ir 5d dans cette region (plus faible π-rétrodonnation). Les spectres XAS des complexes hétéroleptiques indiquent une plus grande densité électronique avec une contribution 5d de l'iridium. Dans les spectres XAS de **Ir1** et **Ir4**, nous avons observé une faible résonance en dessous du seuil qui se trouve être majoritairement une excitation d'un transfert métal ($2p_{3/2}$) vers ligand. L'absence de cet épaulement dans **Ir2** et **Ir3** est due à la covalence plus faible des liaisons. Cependant, l'existence de telles transitions est toujours débattue puisque Ir3+ a uniquement des orbitales t2g (5d6) occupées dans la configuration bas spin.

En utilisant la Spectroscopie d'absorption X picoseconde nous avons mesuré avec succès le spectre transitoire au seuil Ir L_3 des deux complexes **Ir1** et **Ir4** sondés 150 ps après leur excitation laser en solution. Sous excitation optique d'une bande MLCT, nous observons un

changement de l'état d'oxydation de Ir 3+ à 4+. Dans le DCM, les spectres transitoires sont presque identiques (dans les barres d'erreurs) pour les deux complexes **Ir1** et **Ir4**. Pour les deux échantillons, les seuls changements significatifs sont observés autour de la "ligne blanche". Le trou photoinduit dans les orbitales dπ ouvre une nouvelle transition pour l'absorption à 11.215 keV. Les calculs reproduisent le décalage vers le bleu du spectre d'absorption, indiquant un transfert de densité électronique s'éloignant de l'Ir, en accord avec l'excitation MLCT. Les calculs reproduisent aussi la forme du spectre, émanant du trou de valence.

Mots-clés: spectroscopie ultrarapide, spectroscopie d'absorption X, conversion de photoluminescence, rayonnement synchrotron, myoglobine, recombinaison de ligand, tryptophane, complexes d'iridium tricyclométallés, IVR, émission duale.

Contents

List of Figures

List of Tables

List of Equations

Chapter 1 Introduction

Transition metals (TMs) are the active centre of the heme in many metalloproteins and play a crucial role in their reactivity and biochemistry. In particular iron, the active centre of heme trapped in the cage of amino acids forms the simplest metalloprotein Myoglobin (Mb). On the other hand, TMs can build up important organometallic compounds hosting simple or complex organic chelating ligands to form famous bis and tris cyclometalated compounds in the field artificial light harvesting complexes[3], dye-sensitized solar cell[4], photocatalysis, organic light emitting diodes (OLEDs)[5], and phosphorescent organic light emitting diodes (PHOLEDs). A common feature in the molecular and atomic regime in all these biological and chemical complexes is energy and electron transfer happening in a fraction of a picosecond. The valence shell (d orbitals) of the transition metals, sitting at the heart of the periodic table specially those at the 3rd (Fe), 4th(Ru, Rh), and the 5th (Os, Ir) row, usually dictates the photophysics of the compounds, *e.g.* intersystem crossing (ISC), internal conversion (IC), intramolecular vibrational redistribution (IVR), charge transfer and energy transfer.

Through the type of the ligands coordinating with the transition metal and the geometry of the molecule, one can manipulate its characteristics such as phosphorescence or fluorescence energy, decay time, photoluminescence quantum yield and external efficiency of a device applying them. Thanks to the techniques that have been developed in last two decades either in x-ray regime or UV-VIS ultrafast spectroscopy, we were able to follow in real time and under physiological conditions the dynamics upon photo-dissociation of the ligand in Nitrosy lmyoglobin (MbNO) and four types of tris-cyclometalated iridium complexes with static X-ray absorption spectroscopy (XAS) and time-resolved X-ray absorption spectroscopy (TR-XAS). Moreover, using optical ultrafast techniques, namely photoluminescence up-conversion (PLUC) and time correlated

single photon counting (TCSPC) we could investigate the radiative and non-radiative dynamics occurring after photoexcitation of the iridium tris –and bis-cyclometalated complexes.

Despite more than a century of extensive investigations on the functionality of Myoglobin, a complete understanding of the interplay between its structure and the ligand dynamics has not been achieved. In particular, the activation of the heme proteins upon binding of diatomic molecules, such as NO, O_2, CO, and CN is of importance: binding of the former two molecules is vital for human life and binding of the latter two are fatal causing carbon monoxide[*6] or cyanide poisoning. Among them, NO has been highlighted as a key biological messenger[7] whose level controls various physiological responses such as NO-synthases, message transduction (soluble guanylyl cyclases),[8,9] NO transport and oxidation (hemoglobin, myoglobin, nitrophorin)[10-12] and regulation of the NO/O_2 balance (neuroglobin).[13,14] In all these cases, the heme group that binds the NO ligand is chemically identical and therefore variations in the reactivity and function are thought to be closely related to the spin, electronic configuration and geometric structure upon binding[15] and/or are suggestive of different steric and electronic interactions of the bound NO with neighbouring protein residues.[16] Consequently, there is great interest in understanding the nature of NO binding to heme proteins and its biochemical role.

The binding kinetics of NO in Mb has been studied by a variety of time-resolved spectroscopic techniques. In such studies, ligand dissociation from the heme iron was triggered by excitation into either the Soret or the Q-bands, while the ensuing dynamics were probed using transient absorption (TA) in the UV-Visible,[17-26] the near infrared (IR),[27-29] the mid-IR[16,29,30] or by resonance Raman spectroscopy.[26] For UV-Vis and near-IR TA spectroscopy, the signals are dominated by the π-orbitals of the porphyrin, while mid-IR TA of the NO stretch mode is sensitive to the orientation of the NO dipole. Resonance Raman spectroscopy maps several vibrational modes of the porphyrin, but most studies have focused on the important Fe-N stretch vibration (at 220 cm^{-1}) with the proximal histidine,[26,31-33] which is sensitive to the out-of-plane position of the iron with respect to the heme plane and to the strain the protein exerts on the heme, through movements of the helices.[34,35] All of the TA studies report multi-exponential recombination kinetics with time

[*] Carbon monoxide mainly causes adverse effects in humans by combining with hemoglobin to form carboxyhemoglobin (HbCO) in the blood. This prevents hemoglobin from carrying oxygen to the tissue, effectively reducing the oxygen-carrying capacity of the blood, leading to hypoxia. Additionally, myoglobin and mitochondrial cytochrome oxidase are thought to be adversely affected. Carboxyhemoglobin can revert to hemoglobin, but the recovery takes time because the HbCO complex is fairly stable.

constants spanning from sub-ps to several hundreds of ps or even longer. Because the measured time constants somewhat vary with the observable and since the iron atom is the active site of the reaction, one would ideally like to probe it specifically. Time-resolved X-ray techniques seem to be most appropriate since they allow visualise the structure of the environment around the Fe atom. X-ray protein crystallography has been implemented on carboxy-myoglobin (MbCO) showing docking of the CO ligand at the Xe1 and Xe4 positions (see chapter 3 for details)[36-38]. However, solid samples are far from the physiological conditions under which proteins operate and it is desirable to investigate the ligand dynamics of heme proteins in physiological solutions. In addition, these can be flowed continuously to ensure the renewal of the sample and decrease the X-ray dose on it. Adapting such an approach, X-ray scattering studies of MbCO in solution with 100 ps resolution were recently reported,[39-41] but the spatial resolution is such that tertiary and global structural changes can be probed but not atomic-scale changes. In addition, this approach does not deliver information about the electronic structure of the active site, which plays a central role in the biochemistry and reactivity of heme proteins[42,43]. The valence 3d electrons of the iron atom are significantly delocalised over the porphyrin ligand $\pi*$ orbitals and the ability of the heme to redistribute charge and spin density plays an important role in the formation and stabilisation of a variety of intermediates important for biological function[43-45]. TR-XAS[46] offers the advantage of interrogating the electronic and geometric structure of the biochemically active centre of the system with elemental selectivity, *e.g.* solely the Fe atom. The high repetition rate scheme for ps XAS studies[47] was originally developed to investigate photo-induced processes in highly dilute media[48], such as proteins in physiological solutions, whose concentrations (1-4 mM) are one to two orders of magnitude lower than those of the metal complexes we investigated[49]. Using the high repetition rate scheme for picosecond (ps) XAS [47] we addressed the nature of the NO-heme recombination kinetics with direct sensitivity to the Fe-NO binding and 70 ps temporal resolution. The present work demonstrates the feasibility of ultrafast pump-probe X-ray absorption spectroscopic studies of proteins in physiological media, delivering insight into the electronic and geometric structure of the active center under physiological conditions. This way, the presented results should provide a more realistic picture of the local structure, because of the use of liquid solutions in an environment close to the natural one.

The photophysics of transition metal complexes has received significant attention due to their potential applications in photocatalysis and solar energy conversion or as emitters in organic light

emitting diodes or devices (OLEDs). Especially for the case of the latter purpose, the focus of research has been upon the heavier (4th or 5th row) transition metals with partially filled d-shells, such as iridium and platinum. The reason for this arises from the spin statistics of excited state formation after electrical excitation. Indeed, because only 25% form singlet states (S_1), in order to achieve high efficiency, one must ensure that the T_1 state (75% of the excited state) is effectively coupled to the molecular ground state (S_0). This is achieved through a strong spin-orbit coupling (SOC) between the two states. Second-generation phosphorescence-based OLEDs (PHOLEDs) overcame this limitation by doping the host layer with metal-organic emitters[5]. Through exploiting the large spin-orbit coupling (SOC) of the metal centre, it becomes possible to also harvest the triplet excitons and consequently achieve unity quantum efficiency. However, to date the only phosphorescent materials found practically useful are iridium and platinum complexes. This is because alternative complexes, based upon more abundant metal ions, tend to have smaller SOC and therefore exhibit much lower $T_1 \rightarrow S_0$ radiative rates. In such cases the emission decay times are too long and non-radiative processes, saturation and/or triplet-triplet annihilation effects lead to quenching of the triplet excited states, reducing the device efficiency[50].

Among the most popular candidates for PHOLEDs, iridium-based complexes have lately attracted strong interest, due to the flexibility they offer to engineer the ligand architecture and thus influence the relaxation pathways with improved performances. Indeed, tuning the luminescence properties is possible by engineering the ligand architecture of heteroleptic complexes of the kind Ir(III)(C^N)$_2$(A), where A is an ancillary ligand[51,52]. For instance, several heteroleptic Ir complexes emit in the red with moderate luminescence efficiencies[53]. Inter-ligand energy transfer has been proposed to explain the colour tuning in these systems, allowing phosphorescence to be emitted by triplet states lower in energy, localized on different ligands[54,55]. However, the temporal evolution of this process has never been revealed. To tune the phosphorescence to the blue, non-phenylpyridine cyclometalated ligands, like phenylpyrazole (ppz), have to be introduced in the metal-organic molecular structure.[56,57] However, compounds like Ir(ppz)$_3$ generally suffer from a strong temperature-dependence of the luminescence efficiency, with low quantum yields at RT,[51,58-60] that in some cases can be increased if the complexes are doped in host materials.[61]

Apart from interesting applications of TM complexes, the photophysics of these large compounds is still a fruitful topic to investigate the validity of commonly accepted principles in the

photophysics and photochemistry field. Most polyatomic molecules obey the Kasha rule[62] according to which the luminescence yield is appreciable only for the lowest excited state of a given multiplicity. The mechanisms involved along the relaxation pathways leading to this luminescence consist of intramolecular vibrational energy redistribution (IVR), internal conversion (IC) and intersystem crossing (ISC). IVR was specifically investigated in gas phase molecules such as anthracene.[63,64] It was found to strongly vary with excess excitation energy, in other words, with increasing density of states (DOS). One may ask how fast energy redistribution can be in this extreme regime of high DOS and strong intramolecular couplings. Because cascading among electronic states implies structural changes in the molecule, one anticipates the vibrational motions of the molecule to be the limiting factor.

Time-resolved fluorescence on the fs time scale is an appropriate approach to address relaxation dynamics in molecular systems. The strength of time-gated emission is that it measures only the luminescence of the sample; interpretation is thus less ambiguous compared to transient absorption. Monitoring time-resolved fluorescence leads to information on the evolution of the system in the excited state, on the time scale of its relaxation, and on eventual quenching phenomena. In recent years, ultrafast photoluminescence up-conversion (PLUC) with broadband detection has emerged as a powerful tool to map out the various steps in the electronic and vibrational relaxation processes of molecular systems[65]. In particular, in the case of TM complexes, the ability to capture "on the fly" very short-lived emission bands has allowed the observation of the fluorescence of the ^{1}MLCT state of $[Ru(bpy)_3]^{2+}$ [66], and $[Fe(bpy)_3]^{2+}$ [67], with a lifetime of < 40 fs, and even the ^{3}MLCT phosphorescence of the latter, delivering much insight into the ISC processes in these complexes.

Despite extensive optical studies on the cyclometalated iridium compounds aiming to unravel their remarkable "triplet harvesting" character for PHOLED and OLED applications, there is a lack of studies to directly probe the iridium as the active site of these complexes. Almost all X-ray studies on the iridium complexes focused on defining the geometric study of the cyclometalated iridium complexes via X-ray crystallography or diffraction. However, Kim *et. al* conducted XAS study on iridates (iridium oxides) powder samples at the L_2 and L_3 edges of Ir investigating the strength of spin-orbit coupling (SOC)[68]. Another XAS survey was done on relatively complicated system of a NDI-PMI-Ir catalyst triad to investigate the oxidation state change during the catalytic mechanism upon photoexcitation of PMI, which provided direct evidence of $Ir^{+3} \rightarrow Ir^{+4}$ oxidation state change[69].

The lack of element specific XAS and TR-XAS studies on this important class of organometallic compounds prompted us first to study the ground state of four different iridium cyclometalated complexes with XAS at the Ir L_3-edge. To the best of our knowledge, this is the first systematic study of these cyclometalated iridium complexes in solution via x-ray absorption spectroscopy providing more insight into the electronic and geometrical structure of the ground state and the triplet-d state.

Chapter 2 Theoretical Concept, Experimental Methods, and Data Analysis

The first section of this chapter (§ 2.1) is adapted from ref [70] in which it provides the theoretical background behind X-ray absorption spectroscopy (XAS) including the absorption and relaxation process in this regime and introduces the main parts of a typical X-ray absorption spectrum (XANES and EXAFS regions). Section (§ 2.2.1 and § 2.2.2) which are adapted from ref [71] provide a description of the experimental setup of static XAS and time-resolved XAS, as well as their data treatment in section § 2.2.4.

In parallel, in §2.3, I present some basic concepts behind photophysical processes (§2.3.1 is adapted from [72]. This chapter finishes with §2.3 introducing the experimental setup implemented for time-resolved optical spectroscopy in this thesis namely Photoluminescence up-conversion (PLUC) and time-correlated single photon counting (TCSPC) and their data treatment (in particular, § 2.4.3 is adapted from [72]).

2.1 Theoretical Concepts behind X-ray Absorption Spectroscopy

2.1.1 X-ray interaction with matter

X-rays, electromagnetic radiation with energies in the range 120 eV to 120 keV, have been discovered by Röntgen in 1895 [203]. Since then, they have become an invaluable tool to study the structure of matter. Progress in both the theoretical understanding of the interaction of X-rays with matter, and in our knowledge of how to exploit them experimentally, have contributed to the

structural elucidation of a vast amount of systems, ranging from simple systems such as small molecules, through to more complex and celebrated examples, such as DNA and proteins.

X-rays, like any other electromagnetic radiation, can be treated as either a wave or a particle. This wave-particle duality is described by the Planck relation

$$E = h\nu = \frac{hc}{\lambda_{ph}}$$

Equation 2-1

where E is the energy of the photon with h being Planck's constant and ν and λ_{ph} are frequency and the wavelength of the wave. Likewise, electrons possess the wave-particle duality. The wavelength λ_{el} and the momentum p_{el} of an electron are related by the de Broglie equation

$$\lambda_{el} = \frac{h}{p_{el}} = 2\pi/k_{el}$$

Equation 2-2

and its kinetic energy is given by

$$E_{el} = h^2/2m_e\lambda_{el}^2$$

Equation 2-3

with the electron mass m_e.

In general, an X-ray photon can interact with an atom in one of two ways: it can be scattered or it can be absorbed [204]. In scattering, X-ray photons are deflected from their original direction of propagation, either with (Compton scattering) or without (Rayleigh scattering) loss of energy, by collision with an atom. In the X-ray absorption process, the energy of the X-ray photon is used to expel an electron from the atom, leaving the atom ionized. The excess photon energy is transferred as kinetic energy to the electron. The process is called photoelectric absorption which was first rigorously described by Einstein in 1905 [205] for which he received the Nobel prize in physics in 1921. The remaining of this Chapter describes how this absorption process can be used as a probe of the structure of matter.

2.1.2 **Absorption coefficients and cross-sections**

Quantitatively, X-ray absorption can be described in terms of the linear absorption coefficient [68, 206]. By definition, the attenuation of a beam of intensity I_T through an infinitesimal sheet of thickness dz at depth z from the sample surface is given by

$$-dI_T = I_T(z)\mu dz$$

Equation 2-4

which, by integration, leads to the well-known Lambert-Beer law [207]:

$$I_T(z) = I_0 e^{-\mu z}$$

Equation 2-5

where I_0 is the incoming intensity (intensity without the sample). If the total sample thickness z is known, the absorption coefficient can thus be derived from the measured intensities, using $\mu = \ln(I_0/I_T)/\, z$, as described in **[§ 2.2.1].** The number of absorption events, W, in the thin sheet is proportional to I_T, and to the number of atoms per unit area, $\rho_a dz$ where ρ_a is the atomic number density. The proportionality factor is by definition the atomic absorption cross-section, σ_a, so that [204]

$$W = I_T(z)\rho_a dz\sigma_a = I_T(z)\mu dz$$

Equation 2-6

where in the last step **[Equation 2-4]** is used. The linear absorption coefficient and the absorption cross-section are therefore related by

$$\mu = \rho_a\sigma_a = \left(\frac{\rho_a\, N_A}{A}\right)\sigma_a$$

$$= c_{mol}N_A\sigma_a$$

Equation 2-7

where N_A, ρ_m, $and\ c_{mol}$ are the Avogadro's number, the mass density, the atomic mass number and the molar concentration, respectively. The absorption cross-section has a distinct dependence on the photon energy. An example is shown in **[Figure 2-1]** for the **[element Iridium]**, together with the elastic (Rayleigh) and inelastic (Compton) scattering contributions. The double-logarithmic plot illustrates that the absorption cross-section is approximately proportional to $1/E^3$ below and above the discontinuities. The latter occur at characteristic energies for which the X-ray photon has enough energy to expel an electron from an atomic core-level giving rise to a sudden increase of the absorption cross-section. These absorption edges lie at the basis of X-ray absorption spectroscopy (XAS), which will be discussed in detail in the following.

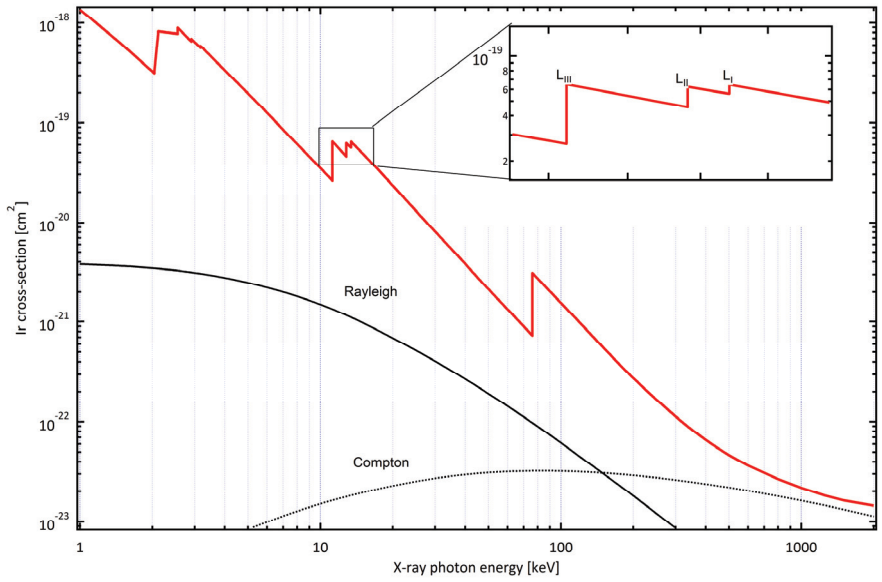

Figure 2-1: X-ray absorption (red) and scattering (black) cross-sections for the element Iridium as a function of photon energy (obtained using the XOP program [73, 74]). The inset zooms into the energy region around 11 keV where the L-edges occur. Note that both axes are in logarithmic scales.

2.1.3 **Absorption edges**

According to the Bohr model and the Aufbau principle, electrons within an atom occupy successive electronic shells with discrete element-specific energies. The shells are classified as K, L, M, etc, according to the values of their principal quantum number n=1, 2, 3; … respectively. In a pure Coulomb field, each shell has a degeneracy of n^2 and is capable of housing $2n^2$ electrons. Due to inter electron repulsion and coupling between spin and angular momenta, however, the degeneracy is lifted into subshells labelled as $\left(nl_j\right)^{2j+1}$ where, n, l and j are the principal, orbital angular momentum, and total angular momentum quantum numbers, respectively, of the single-electron states ($2j+1$ is the multiplicity). In the presence of an external electric or magnetic field, the levels are split further depending on the magnetic, $m = -l, \dots, 0, \dots, l-1, l$, and spin quantum numbers, $s = \pm 1/2$.

An X-ray absorption edge occurs if the photon energy matches the energy necessary to excite an atomic core-level electron in one of the subshells into an unoccupied level above the Fermi energy E_F. The latter can be either a valence orbital (in this case a bound-bound transition occurs) or a (quasi-) continuum level above the IP. In general, the intensity of the quantum-mechanical transition is governed by the transition matrix element $\langle f|\hat{\mathcal{E}}.r|i\rangle$ [209], where $|i\rangle$ is the initial core-level state, $\langle f|$ is the final state and $\hat{\mathcal{E}}.r$ is the electric dipole operator (see § 2.1.6). For the bound-

bound transitions the optical dipole selection rules ($\Delta j = 0, \pm 1/2\,, \Delta m = 0, \pm 1$; ignoring spin) can be applied.

The nomenclature (Sommerfeld notation) used to label the X-ray absorption edges is given in Figure 2-2 For example, the L_I, L_{II} and L_{III} edges arise for absorption from the $(2s)^2$, $(2p_{1/2})^2$ and $(2p_{3/2})^4$ subshells, respectively. The energies of the edges (or ionization energies) are unique to the type of atom that absorbs the X-ray, and hence themselves are signatures of the atomic species present in a material.

The energy-dependent absorption cross-section for a specific element (*e.g.* Pt shown in **[Figure 2-1]**) exhibits the following qualitative trends [204, 206]: (1) The energy difference between the subshells within each shell are always much smaller than that between the different shells; (2) The difference in energy between the successive absorption edges, K, L, M, *etc.*, decreases with increasing principal quantum number n; (3) The edge jump magnitudes (the ratio between the two

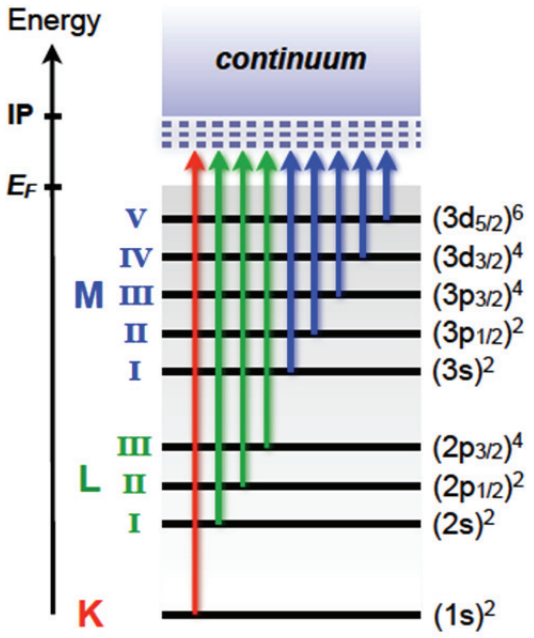

Figure 2-2: Schematics of the atomic energy levels and the nomenclature used to label the X-ray absorption edges of the elements. The electronic shells are labelled as $(nl_j)^{2j+1}$ (see text). The horizontal dashed lines just below the IP represent empty valence states. Transitions occur to all empty states above the Fermi level that exhibit appropriate symmetry governed by the dipole selection rules. (Redrawn and adapted from reference [204])

cross-section values just below and above the edge) generally decrease in going from low to high-energy edges, *e.g.* $L_{III} > L_{II} > L_I > K$; (4) With increasing atomic number Z, the absorption edges shift

to higher energies and the edge jumps show a decrease (although the overall cross-section scales with Z^4).

2.1.4 **X-ray absorption fine structure**

The X-ray absorption spectra of atoms in molecules or embedded in the condensed phase display a modulation of the absorption coefficient, typically by a few percent, around and above the absorption edge, which is absent for isolated atoms such as gas-phase rare gas atoms. This fine structure turns out to be a unique signature of a given material: it depends on the detailed atomic structure and electronic and vibrational properties of the material. For this reason XAS is a very important probe of materials, as knowledge about local atomic structure is essential in many scientific fields, such as chemistry, biology and material science.

In general, the XAS spectrum is divided into two regions differing in the energy of the photoelectron and the information content of the fine structure: the XANES region up 50 eV above the IP, and the EXAFS region ~50 eV above the IP, as the spectrum has been normalized as described in **[§ 6.I]**. This is illustrated in **[Figure 2-3]** for **[tris(2-phenylpyridine)Iridium, Ir(ppy)$_3$)]**.

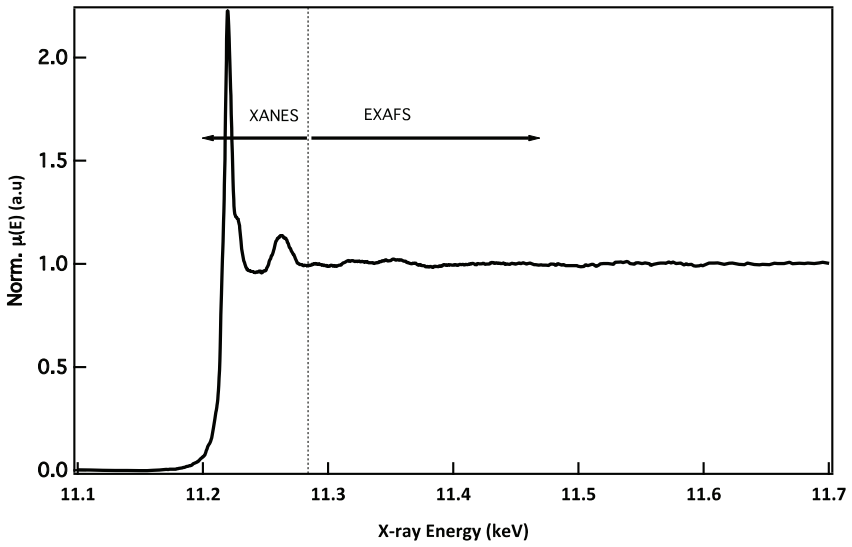

Figure 2-3: XAS spectrum of a molecule [Ir(ppy)$_3$] in solution illustrating the two regions: the low-energy XANES region up to ~50 eV above the IP and the high-energy EXAFS region ≥ 50 eV.

The XANES region (including the pre-edge region) contains valuable electronic information such as the energetics of hybridization orbitals, the electronic configuration, and the site symmetry. The edge position also contains information about the charge on the absorber. Due to predominance

of multiple scattering effects, the approximations necessary for the theoretical description, of the XANES spectra, are often only qualitative, as discussed in **[§ 6.I]**. The EXAFS spectrum is more directly related to the (geometric) structure around the absorbing atom. Electronic effects play a reduced role making the interpretation of the EXAFS spectrum straightforward**. [How accurate quantitative structural information is obtained from this part of the spectrum is described in § 2.1.6 and § 2.2.4.1.]**

2.1.5 X-ray relaxation processes

After excitation of the core-level electron in the X-ray absorption process, the excited atom can relax through several mechanisms, giving rise to fluorescence X-rays, Auger electrons, or secondary electrons as shown schematically in **[Figure 2-4]** [76, 204].

2.1.5.1 Radiative decay

The filling of an inner shell vacancy (core hole) by an outer shell electron produces X-ray fluorescence with an energy equal to the energy difference between the two shells **[(Figure 2-4b)]**. In the case of K-shell absorption, transitions from higher-lying L, M, and N shells to the K-shell core hole are designated as K_α, K_β and K_γ fluorescence, respectively, where transitions from within one shell are numbered $K_{\alpha1}$, $K_{\alpha2}$, $K_{\alpha3}$, etc. in sequence of decreasing energy. Similarly, L_α and L_β lines correspond to electronic transitions from the M and N shells to the L-shell, respectively. The fluorescent yield, or the radiative probability, ε_f is defined as the ratio of emitted X-rays to the number of primary vacancies created. It is a monotonically increasing function of atomic number Z, and it is larger for K-line emissions than L- or subsequent line emissions. The measured fluorescence intensity I_f is proportional to the incoming intensity I_0, the fluorescence yield I_f, the absorption coefficient μ(E) and the fractional solid angle of detection $\Omega/4\pi$, but care should be taken in the case of thick samples for which the different energies of absorption and emission should be taken into account **[(see § 2.2.1)]**.

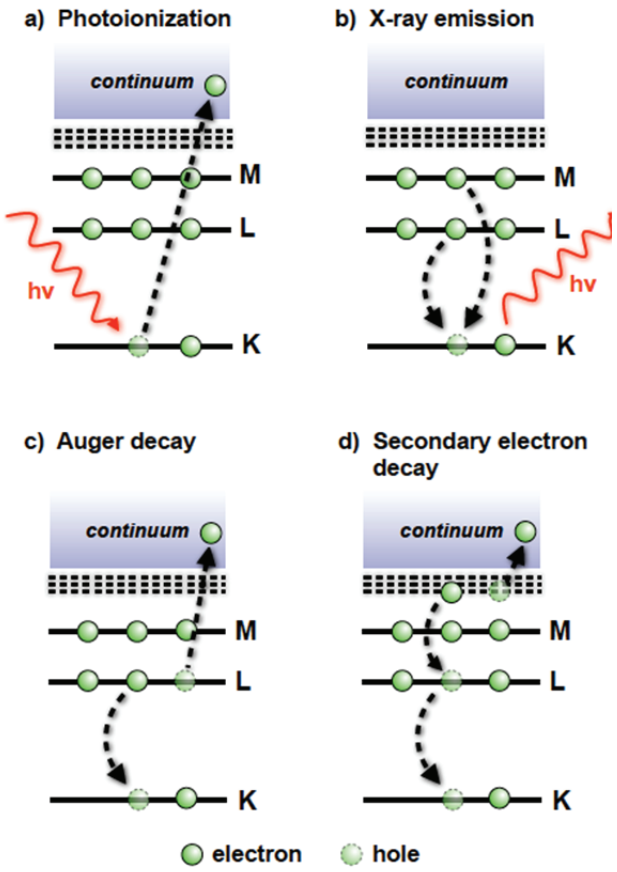

Figure 2-4: Schematic energy level diagrams of atomic excitation and relaxation processes. For clarity only the lowest three levels are indicated. Redrawn and adapted from reference [204].

2.1.5.2 Non-radiative decay

The other major phenomenon following photoelectric absorption is the Auger effect **[(**Figure 2-4**c)]**. In this process, the core hole is filled by an electron dropping from a higher shell while the atom simultaneously ejects another electron, usually from the same higher shell [76]. Auger decay is a radiationless process that can be seen as a "one-step two electron" Columbic readjustment to the initial core hole. On the other hand, secondary electron decay is a two- or multistep many-body radiationless process in which outer-shell electrons are ejected by Auger electrons or X-ray fluorescence photons, *e.g*. shake-up and shake-off processes **[(Figure 2-4d)]**. The total yield of radiationless processes εn is simply the complement of the fluorescence yield via $\varepsilon_n = 1-\varepsilon_f$. The relative yields depend on Z: the heavier the element (the higher Z), the larger the fluorescence yield [210]. Therefore, while Auger decay dominates the relaxation for light elements (Z= 1 - 10), heavy elements with Z> 40 mainly relax radiatively [206, 210, 211].

2.1.5.3 Broadening of the spectrum

The above described decay processes lead to a finite lifetime of the core-hole state. Through the Heisenberg uncertainty principle, any state with a finite life time does not have a sharp (or delta-function-like) energy level, but is better thought of as having a finite width, *e.g.* a Lorentzian line shape. This life time broadening, or natural width, of the XAS spectrum increases with Z, *e.g.* from 1 eV (V, Z= 23) up to 40 eV (W, Z= 74) for K-shell absorption, and for the LIII-shell from 3.7 eV (Nd, Z= 60) up to 7.4 eV (U, Z= 92) [211]. Due to this broadening, the energy resolution of the incident beam needs not be much smaller than the natural line width. These limitations can be overcome by dispersing the X-ray emission and detecting it with a better resolution than the natural line width [212].

The photoelectron loses energy due to inelastic interactions such as plasmon excitations, electron-hole pairs and scattering which destroy the coherence of the photoelectron wave. These losses give the final photoelectron state a finite lifetime and hence leads to an additional broadening of the absorption spectrum [213]. They can be accounted for phenomenologically by an energy-dependent electron mean-free path $\lambda(k_{el})$ (not to be confused with the de-Broglie wavelength λ_{el} of **[Equation 2-2)]**, typically in the range 5-20 Å, i.e. a lifetime broadening of a few eV. However, a more precise description of inelastic losses is obtained by using a complex, energy-dependent self-energy, which is particularly important for the XANES region. The net effect is that XAS can only measure the local (short-range) atomic structure over a range limited by the net lifetime (or effective mean free path) of the excited photoelectron.

2.1.6 Theory of EXAFS spectroscopy

X-ray absorption fine structure (EXAFS) refers to the oscillatory variation of the absorption coefficient as a function of photon energy just above (~ 50 eV) an absorption edge. Although the extended fine structure in XAS spectra has been known for a long time [215-216], its structural content was not fully recognized until the work of Stern, Lytle and Sayers in 1971 [217-219]. EXAFS is a final-state quantum-interference effect, involving scattering of the outgoing photoelectron from the neighboring atoms. In a qualitative golden-rule picture, the probability that a X-ray photon will be

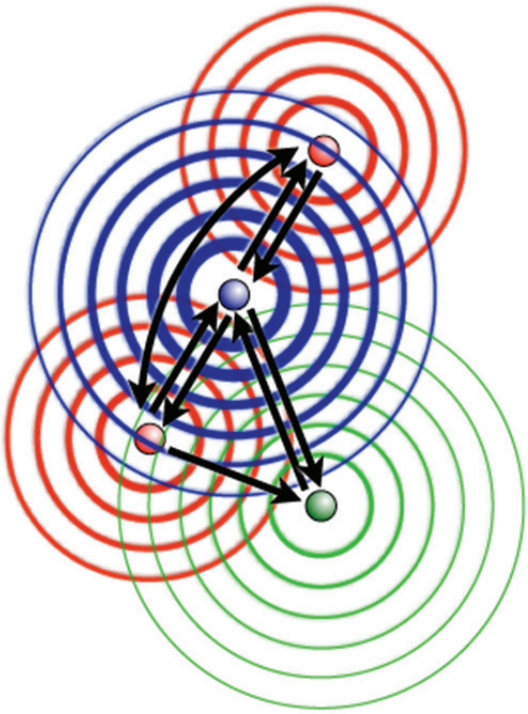

Figure 2-5: Pictorial view of the single- and multiple-scattering pathways of an outgoing photoelectron wave (blue) off 1st-shell (red) and 2nd-shell (green) neighboring atoms. The strength of the scattered wave is reflected in the line thickness (redrawn and adapted from reference[75]).

absorbed by a core electron depends on both the initial $|i\rangle$ and the final states $|f\rangle$ of the electron via the transition matrix element $\langle f|\hat{\mathcal{E}}.\boldsymbol{r}|i\rangle$ where $\hat{\mathcal{E}}.\boldsymbol{r}$ is the electric dipole operator. The initial state is the localized core level, while the final state is that of the ejected photoelectron represented as an outgoing spherical wave originating from the absorbing atom. This outgoing wave is backscattered by nearby atoms thereby producing an incoming wave at the absorption site. The amplitude of all the reflected waves at the absorbing atom interferes with the outgoing photoelectron wave and hence modulate the matrix element $\langle f|\varepsilon.\boldsymbol{r}|i\rangle$that controls the strength of the transition (and thus the magnitude of $\mu(E)$). The phase difference between the two components (outgoing and incoming) is approximately$2k_{el}R$, where R is the distance to the neighbouring atoms and $k_{el} = 2\pi/\lambda_{el}$ **[**Equation 2-2**]**. Since λ_{el} decreases with increasing energy, and the modulation in μ arises from interference, a modulation of alternating constructive and destructive interference leads to the modulation pattern observed as the photon energy is varied. The amplitude and frequency of the modulation depends on the type, bonding and number of neighboring atoms and their distances from the absorbing atom, respectively. Inelastic interactions of the photoelectron with the electrons and phonons of the surroundings destroy the coherence of the waves making them unsuitable for interference. This limits the maximum

interatomic distance that can contribute to the interference pattern, *i.e.* the EXAFS spectrum. Figure 2-5 pictorially illustrates the process of backscattering from 1st-shell (nearest) and 2nd-shell (next-nearest) neighboring atoms (with respect to the absorbing atom). If the photoelectron scatters of a neighboring atom only once (to and fro), this is referred to as single scattering (SS), in contrast to multiple scattering (MS) if the wave scatters of twice or multiple times before returning to the absorbing atom.

2.1.6.1 EXAFS equation

The initial development and application of EXAFS have been impeded by a great deal of confusion about its correct theoretical description. The question arose as to whether a long-range order theory formulated in terms of Bloch waves [215] or a short-range order theory in terms of scattering from nearby atoms [216, 220] was more appropriate. With the advent of synchrotron X-ray sources in the 1970s, a quantitative comparison between theory and experiment became possible for the first time. Since then it is generally established that the single-electron short-range-order description is adequate in most cases to explain the theory of EXAFS, although both approaches can be reconciled when appropriate broadening is introduced [213].

Within this picture, EXAFS can be phenomenologically described by the so-called EXAFS equation. Its derivation can be abundantly found in the literature [68, 204, 206]. Here we prefer to focus on the physical meaning of its various components and how the equation is used to extract structural information from the XAS spectrum. The EXAFS spectrum is defined phenomenologically as the normalized, oscillatory part of the absorption coefficient above a given absorption edge, *i.e*.

$$\chi(E) = \frac{\mu(E) - \mu_0(E)}{\mu_0(E)}$$

Equation 2-8

where $\mu_0(E)$ is the smoothly varying atomic-like background absorption of an "embedded atom" (in the absence of neighboring scatterers but incorporated in the lattice of neighboring potentials). In order to relate $\chi(E)$ to structural parameters, we need to make the transformation from (absolute) E-space into (relative) k-space. The kinetic energy of the photoelectron is given by the difference in energy E of the X-ray photon and the energy E0 necessary to expel the electron from its core level (the IP). By using **[**Equation 2-2**]** and **[**Equation 2-3**]** the electron wave vector is expressed as

$$k_{el} = \sqrt{\frac{2m_e}{\hbar^2}(E - E_0)}$$

Equation 2-9

which can be used to transform $\chi(E)$ into $\chi(k)$ (from now on, the wave vector subscript referring to the photoelectron is omitted). The latter is given by the EXAFS equation, expressed as a scattering path expansion generalized to include MS pathways [213]:

$$\chi(k) = \sum \frac{N_\gamma S_0^2 |f(k)|}{kR_\gamma^2} e^{-2\sigma^2 k^2} e^{-2R_\gamma / \lambda_{tot}(k)} \sin\left[2kR_\gamma + 2\delta_c + \phi(k)\right]$$

Equation 2-10

with the scattering path index, the number of equivalent scattering paths N_γ , the halfpath distance R_γ and the squared Debye-Waller (DW) factor σ^2. In the case of SS, R_γ represents the direct interatomic distance between absorber and scatterer. In addition, $f(k) = |f(k)|e^{i\phi(k)}$ is the complex backscattering amplitude for path γ, δ_c is the central atom phase shift of the final state, $\lambda_{tot}(k)$ is the energy-dependent mean free path and S_0^2 is the overall amplitude reduction factor, which was added later to account for many-body (shake-up, shake-off) effects **[(§2.1.5)]**.

In principle, Equation (2-10) contains all of the key elements that a correct theory must entail and it provides a convenient parameterization that allows fitting the local atomic structure around the absorbing atom to the experimental EXAFS data **[(see §2.2.4.1)]**. The relation between the oscillatory fine structure and the interatomic distances is clearly reflected by the $\sin(2kR_\gamma)$ term. The finite lifetime of the excited state consisting of the photoelectron together with the core hole where it came from is captured by the exponential damping term exp($-2R_\gamma / \lambda_{tot}(k)$). The strength of the reflected waves depends on the type and number of the neighboring atoms via the backscattered amplitude $|f(k)|$. The phase factors $\phi(K)$ and δ_C reflect the quantum-mechanical nature of the scattering process (the factor of 2 is due to the fact that the photoelectron encounters the potential of the central atom twice). These phases account for the difference between the measured and geometric interatomic distances, which are typically a few tenths of an Å and must be corrected for by using an experimental or theoretical reference [68]. Finally, the damping factor $e^{-2\sigma^2 k^2}$ is partially due to thermal effects causing the atoms to jiggle around their equilibrium

atomic positions with a root-mean-square deviation of σ. Thus the contributions of these atoms to the interference will not all be exactly in phase. Effects of static disorder are similar and they give rise to an additional contribution to σ^2. The Debye-Waller damping term is most pronounced for high energies making it essential for EXAFS, but its energy dependence is often negligible in XANES. In the case of a simple diatomic vibration and scattering along the interatomic axis, the squared DW factor can be expressed as [221]

$$\sigma^2 = \frac{h}{8\pi^2 \mu_{vib} \upsilon_{vib}} \coth\left(\frac{h\upsilon_{vib}}{2kT}\right)$$

Equation 2-11

where μ_{vib} is the reduced mass of the vibration, T is the temperature, and υ_{vib} is the frequency of the vibration. As σ^2 increases with T, the fine structure tends to "melt" at high temperatures, confining the spectrum to lower regions of energy.

2.2 Experimental Methods: Synchrotron radiation experiments

2.2.1 Steady-state XAS setup

Both methods of detection (transmission and fluorescence) are implemented in the time resolved data acquisition used in our experiments. The detectors used for each mode are described in **[(§ 2.2.1.1) and (§2.2.1.2)]**.

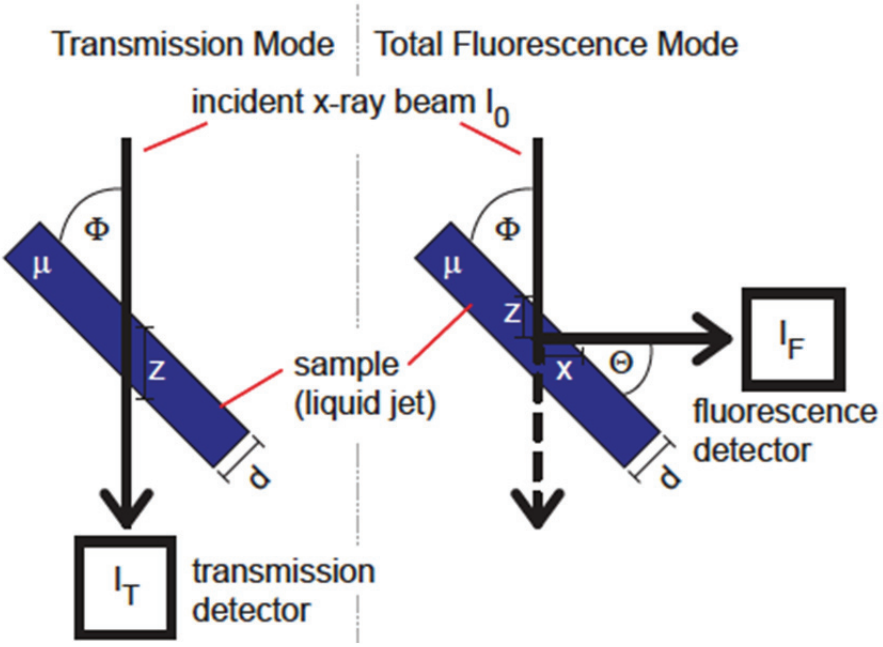

Figure 2-6: Schematic setup for fluorescence (right) and transmission (left) measurement modes in a X-ray absorption experiment. The incident beam I_0 is partially absorbed by the sample of the thickness d. The sample is set at an angle 45° with respect to the incident beam to increase the fluorescence yield I_F, while this geometry has no influence on the transmission I_T but the increase in path length z through the sample.

The difference between the fluorescence and transmission detection mode is visible at first glance in the positioning of the detectors (Figure 2-6). While the transmission detector is located in the direct X-ray beam, the total fluorescence is usually collected by a detector at the side of the sample, usually at about 90° to the incident beam.

2.2.1.1 Detection of the Transmission Signal

The transmitted intensity I_T is a function of the absorption cross-section of a medium $\mu(E)$ and is given by the Lambert–Beer law **[(see Equation 2-5)]**. Therefore, the absorption cross-section can be calculated directly using **[Equation 2-7]**, if the intensity of the incident beam I_0 and the transmitted beam I_T are measured simultaneously. In case of our liquid jet however, μ is the absorption cross-section of all components of the sample […] not only the designated absorber will absorb the X-rays, but so will all the other components. However, this is not an issue as long as none of the other components has an absorption edge or resonances in the energy region the X-ray absorption spectrum of the absorber is measured. The influence of the other absorbers is then only a static background, which can easily be accounted for.

In the experiments preformed, the liquid jet was set at an angle with respect to the incident X-ray beam. This does not affect the absorption measurements and results only in an increased path length $z = d.\sin\phi - 1$, which has to be used for the sample thickness in **[**Equation 2-1**]**.

2.2.1.2 Detection of the Fluorescence Signal

Sometimes it gives an experimental advantage to measure not only the transmission signal but also the total X-ray fluorescence. For example, if the absorption of a sample is too low, a small absorption signal has to be measured on a large background signal, which usually limits the detection sensitivity. […] In cases like these, the total fluorescence yield is usually preferred. The core hole decays by electron transfer from a higher lying shell, upon which the difference energy between two states involved is released as a X-ray photon, as is described in **[(§2.1.5)]**. Thus, measuring the total fluorescence yield as a function of incident energy will yield a similar spectrum as the X-ray absorption spectrum. It should be noted that the detection efficiency of our detector is not identical for all fluoresence from the sample. […]. In contrast to the straightforward approach of measuring the transmission of a sample to get the X-ray absorption signal, the total fluorescence yield I_F is only proportional to the X-ray absorption coefficient μ and has to be corrected for geometrical factors and quantum efficiency. Geometrical factors play a role, as the fluorescence light has to go through the sample to reach the detector, where the path length is given by the position of the detector and sample geometry as seen in **[Figure 2-6]**. Along this path, the fluorescence photons can be re-absorbed by the sample, giving rise to the so-called self-absorption effect. In the worst case of a thick sample of a pure element, a strong damping of the X-ray intensity occurs, making EXAFS analysis and comparison of line intensities challenging. An overall description of the X-ray fluorescence signal is given with

$$I_F(E) = I_0(E)\frac{\omega_f \Omega}{4\pi}\frac{\mu_{absorber}(E)\left(1 - e^{-\left(\frac{\mu(E)}{\sin\phi}+\frac{\mu(E_F)}{\sin\theta}\right)d}\right)}{\frac{\mu(E)}{\sin\phi}+\frac{\mu(E_F)}{\sin\theta}}$$

Equation 2-12

In **[Equation 2-12]** the angles θ and ϕ are defining the incident beam with respect to the sample surface, while the angle of detection of fluorescence photons is given by Ω. E and E_F are the incident and fluorescence energy respectively. The absorption coefficients μ and $\mu_{absorber}$ describe the absorption of the absorbing atom and the whole sample respectively, and ω_f is the fluorescence yield of the absorber[76]. In our geometry with $\sin\phi = \sin\theta = \sin 45^\circ$, the equation can be simplified to

$$I_F(E) = I_0(E)\frac{\omega_f \Omega}{4\pi}\frac{\mu_{absorber}(E)\left(1 - e^{-(\mu(E)+\mu(E_F)x)}\right)}{\mu(E)+\mu(E_F)}$$

Equation 2-13

with $x = d.\sin(45^{\circ})$ **[(see** Figure 2-6**]**. We now want to look at two extreme cases of samples and the influence on equation 5.14: The thick sample $(\mu(E) + \mu(E_F))x >> 1$ and the thin sample $(\mu(E) + \mu(E_F))x << 1$ limit.

In the thick sample limit, the exponential term goes against zero, resulting in

$$I_F(E) \approx I_0(E)\frac{\omega_f \Omega}{4\pi}\frac{\mu_{absorber}(E)x}{\mu(E) + \mu(E_F)}$$

Equation 2-14

whereas the thin sample limit the argument of the exponential term becomes small, so that IF can be approximated by a first order Taylor expansion to

$$I_F(E) \approx I_0(E)\frac{\omega_f \Omega}{4\pi}\frac{\mu_{absorber}(E)\big(\mu(E) + \mu(E_F)\big)x}{\mu(E) + \mu(E_F)} = I_0(E)\frac{\omega_f \Omega}{4\pi}\mu_{absorber}(E)x$$

Equation 2-15

As can be seen in [**Equations (2.14)] and (2.15)]**, the fluorescence is linearly proportional to the absorption coefficient of the absorbing atom $\mu_{absorber}$. Nonetheless, the fluorescence yield is directly proportional to the absorption coefficient $\mu_{absorber}$ of the absorbing atom. In addition, we overlapped the measured transmission spectrum and fluorescence spectrum, but no distortion of the spectral progression was visible.

2.2.2 Time-resolved X-ray absorption setup

Time-resolved X-ray absorption spectroscopy is the technique of choice in this work to elucidate the electronic and geometric structure of excited nitrosy lmyoglobin (MbNO) and tris-cyclometalated iridium complexes in solution. The absorption measurements were carried out at MicroXAS, of the Swiss Light Source (SLS) at the Paul Scherrer Institute in Switzerland. Here the experimental setup needed for time-resolved XAS measurements are presented, such as the Laser, the Data acquisition (DAQ) system as well as the detectors.

In this work, X-ray absorption spectroscopy is combined with time resolved measurement techniques. Time resolved measurements are used to follow the dynamics of a photo-induced process. With the introduction of pulsed laser sources, time resolved techniques became an even

more powerful tool in physical science and chemistry. By using ultrashort laser pulses of picosecond or even femtosecond duration to trigger a dynamic process inside a sample, atomic and electronic motions have become observable. The time resolved laser experiments usually involve using the same laser oscillator for the pump and the probe alike, while time resolved X-ray experiments involve two very different radiation sources which have to be synchronized: The synchrotron X-ray source and the laser **[([Figure** 2-7**)]**. In this work, the probe method is X-ray absorption spectroscopy. The technical implementation of triggering a process with a pulsed picosecond laser source and probing it with X-ray absorption pulse, based on the simple pump/ probe spectroscopy, the experimental setup has been published several times [42,146-152] and is shortly introduced in this section. The measurements presented in this work were obtained by our recently implemented high-repetition (MHz) laser system used for picosecond X-ray absorption spectroscopy. Details are published in reference [39].

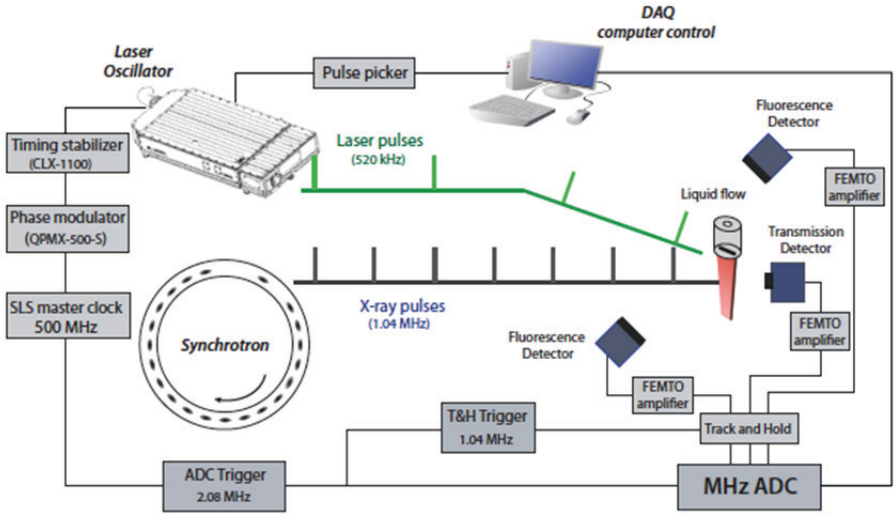

[Figure 2-7: The experimental set up: The DUETTO Laser system synchronized to the X-ray pulses from the hybrid bunch of the synchrotron are delivered to the same position on a liquid jet sample. The resulting pump-probe signal is measured by various detectors and processed in the data acquisition system (DAQ). A more detailed description is given in the text. From [39]

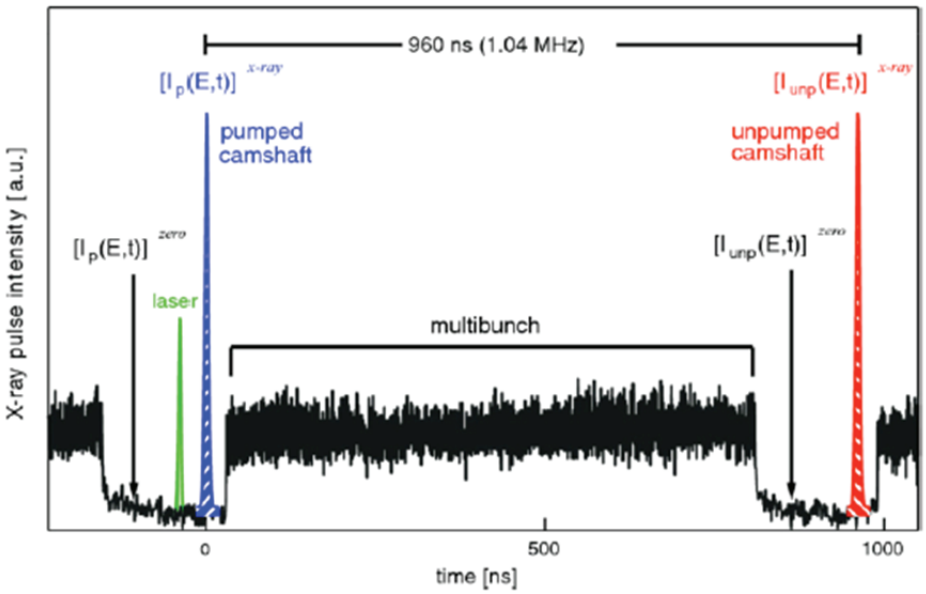

Figure 2-8 Electron filling pattern of the SLS in hybrid mode. The electrons are packed in bunches located in one of the evenly spaced buckets. The delay between two buckets is 2 ns. The multibunch is a train of filled buckets, whereas the hybrid bunch is located in an isolated position surrounded by not filled buckets. For pump-probe measurements, only X-rays originating from the hybrid bunch are used as probe on a shot to shot basis (see text).

Time-resolved XAS experiments exploit the tens of picoseconds X-ray pulses provided by the SLS. The SLS runs with a multibunch-filling pattern (see Figure 2-8), where in between the bunch train a hybrid bunch is placed within a gap of 170 ns. Only the hybrid bunch is used for the high-repetition XAS measurements, which has a duration of 70 ps, a repetition rate of 1.04 MHz and a

current of 4 mA, which is 1% of the total ring current. The time-resolution of any time-resolved measurement is limited by the source with the least time-resolution; in this case the X-rays coming from the hybrid bunch electron bunch with 70 ps length define the resolution. **[[Figure** 2-7**]** sketches different components involved in the experimental setup for time-resolved XAS. Performing time-resolved XAS experiments comes with technical challenges, such as the the synchronization of the laser system and the X-ray pulse and finding suited detectors, but also with difficult experimental execution, for example finding the spatial overlap and temporal overlap (time-zero). The following section introduces the main experimental devices, the optical setup and the most important experimental steps, while performing the experiment.

2.2.2.1 Instrumentation

The laser System used for the time-resolved X-ray absorption measurements is a compact and mobile picosecond laser system produced by Time Bandwidth Products, Switzerland with the trade description DUETTO. The portability enables the installation of the Laser at different beamlines at the Swiss Light Source, which offer different energy ranges and experimental conditions. The DUETTO laser has a time-resolution of 10 ps and a variable repetition-rate in the range between 200 kHz to 8.33 MHz). The laser consists of three main components: The oscillator and amplifier, a pulse on demand unit (PoD), and a unit housing non-linear optics (NLO). The synchronization to the X-ray pulse is done in an electronic synchronization unit (CLX).

Oscillator and Amplifier

The DUETTO laser system is a solid-state neodymium-doped yttrium-orthovanadat-based amplified system, which operates at a fundamental wavelength of 1064 nm. The oscillator and amplifier run at a repetition rate of 83.3 MHz. A Pockels cell releases the pulses from the resonator at any fraction of the internal frequency between 10 and 416, corresponding to outgoing pulse rate of 8.33MHz or 200 kHz respectively with an average output power greater 12W.

CLX

The CLX-1100 timing stabilizer stabilizes the relative phase between the reference frequency and the intrinsic frequency, by locking the phase of the laser oscillator to an input trigger with a jitter < 400 fs. Thus the laser can be synchronized with the RF reference signal of the synchrotron,

which is a 500MHz radio frequency signal at the SLS.

Pulse on Demand (PoD)

The PoD unit is located between the amplifier and the NLO unit. It allows sending the amplified laser beam either to its output or to an internal beam dump, by applying a control TTL signal. In addition, a Pockels cell can use an analogue voltage to adjust the output power seamlessly between zero and full power. This feature is mainly used for power dependence measurements and adjusting the incident pump power.

Non-linear Optics (NLO)

The NLO unit accepts the 1064nm beam from the PoD. The output wavelength can be chosen by adding to a doubling crystal, resulting in a 532nm output wavelength, to a mixing crystal, which sum frequency mixes 1064nm and 532nm photons to yield a 355nm output. The maximum output pulse energy depends on the laser repetition rate.

Data Acquisition System

The laser pump/ X-ray probe data is collected on a shot to shot basis, thus probing an excited state sample and a ground state sample in 4 μs with the laser running at a frequency of laser = 260 kHz. The synchronization is given by a 1.04 MHz optical signal provided by the synchrotron **[(see [Figure** 2-7**)]**. The signal is recorded by an analog-to-digital converter (ADC). To correct for a possible detector offset, a baseline of the detector is taken for each shot. Hence, the complete pump-probe signal is the pulse-to-pulse fast difference between the baseline corrected X-ray signal of the laser-excited sample and the baseline corrected X-ray signal of the ground state. The delay between the laser pump and the X-ray probe pulse can be adjusted via a computer based timing system. For delays larger than 6 ns it will change the laser oscillator round trip with the pulse picker resulting in a time change of 83.33 MHz^{-1} = 12 ns of the laser pulse with respect to the X-ray pulse of the hybrid bunch. The delay will be subsequently fine-adjusted by changing the oscillator phase the same way small delays are achieved. This way of use of the pulse picker helps to reduce the waiting time between measurements with different time delays. In addition to the signals fed into the ADC, two digital markers are created: One for laser and one for the X-rays, marking whether the signal is an excited state signal, a ground state signal or the corresponding base line signal. The averaged excited state and ground state signal are obtained by sorting the

single shot data accordingly. The error of the measurement is the standard deviation of the single shots from the average signal.

2.2.2.2 X-ray Detectors and Amplifiers

The detectors used for this kind of fast experiments at high repetition rates have to have a fast rise time in order to resolve the signal of the hybrid bunch before the multibunch starts. The detectors have to behave linearly in the X-ray energy ranges of interest. And the sensitivity of the detector needs to be high for X-rays but close to zero for photons from the laser. This can be achieved by an avalanche photo diode (APD) with an area of one square centimeter shielded with a 25 µm thin Be foil blocking the visible light. A bias voltage of about -350 V increases the sensitivity and time resolution. These sensitive detectors are ideal for detection of the total X-ray fluorescence. For transmission measurements a fast silicon based drift diode biased at 150 V is used, also shielded with Beryllium foil. The APD detectors signal is amplified by a fixed gain HCA series FEMTO current amplifier, whereas the silicon drift diode is amplified with a DHCPA-100 variable gain FEMTO current amplifier. The amplified signals are fed into a track-and-hold device, which holds the incoming signal level long enough for the slower digitalization by the analog-to-digital converter.

2.2.2.2.1 Optical and X-ray Setup

The optical setup is used to deliver the laser beam to the interaction zone of the liquid jet sample with the X-ray probe beam, as shown in **[Figure 2-9]**. Two mirrors after the laser provide full control over the beam position, while the subsequent telescope widens the beam for better focusing capabilities later on. The beam is lead over multiple mirrors towards the sample. In both beamlines, Phoenix and MicroXAS, the X-ray beam is higher than the laser beam, which makes the use of a periscope necessary to overcome the difference in height. A convex lens focuses the beam to a full width half maximum (FWHM) size of 1.5 times the FWHM of the X-ray spot to ensure a good overlap and a laser excitation of the whole probe region. One of the last mirrors is set in a computer controlled movable mount (Zaber T-MM-Series), which adjusts the laser spot position on the sample while X-rays are present and access to the laser setup located inside the X-ray safety hutch is prohibited.

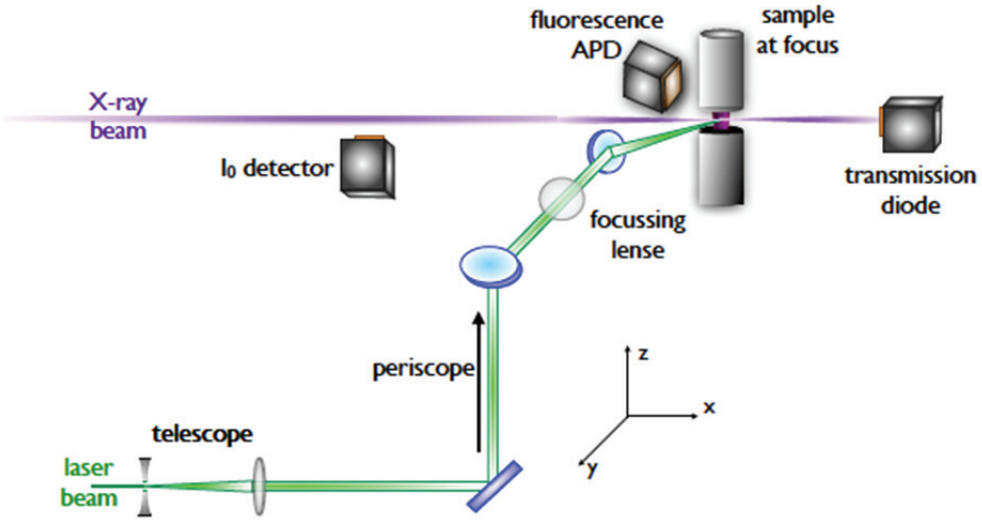

Figure 2-9: Generic experimental setup for laser pump-X-ray probe measurements. The laser beam is widened with a telescope to a centimeter diameter to allow smaller focusing later on. The widened beam is let via multiple mirrors to a lens focusing the beam on the X-ray position on the liquid jet sample. The signals are measured via total fluorescence yield with an avalanche photo diode (APD) or in transmission mode with a silicon diode. Adapted from [71]

2.2.2.3 Experimental execution

Spatial overlap

A good spatial overlap between the laser and the X-ray beam is mandatory for the success of time-resolved XAS experiments. Ideally, the laser beam is 1.5 times bigger than the X-ray spot at sample position, which facilitates to overlap both beams and allows some clearance in the case that the X-ray spot moves slightly without losing the spatial overlap. The overlap of the X-rays and the laser is achieved by centering a pinhole to the X-ray beam at the position of the sample and then adjusting the laser beam to go through the pinhole.

Temporal overlap, setting Time-zero

When starting an experiment, the time for which the laser and the X-ray signal of the hybrid bunch have zero time delay has to be set. This is achieved by monitoring the arrival time of the laser and of the X-ray pulse by a fast photo diode (Opto-Diode Corp., AXUVHS5) with a rise time of 700 ps, sensitive in the optical and X-ray regime, on an oscilloscope. The laser is then shifted towards the X-ray pulse by means of the pulse picker and phase shifter as explained above.

2.2.3 **Sample Handling**

2.2.3.1 Myoglobin Complexes

The simple protein of Myoglobin (Mb) is available as lyophilized powder from commercial companies, *e.g.*, Sigma-Aldrich. For the measurements in this work I used a lyophilized powder of equine skeletal muscle (Sigma-Aldrich, 95-100%). This commercial powder is predominantly on the oxidized (ferric) form with the oxygen present in air[77]. Hence, it is necessary to first reduce the iron atom to reach the ferrous state of deoxyMb that can bind to NO ligand and produce the ligated ferrous form of MbNO. In our experiments I followed the preparation method in ref.[30 78] For all the time-resolved XAS experiments I used physiological solutions of Nitrosy lmyoglobin (MbNO) of 4 mM concentration. In order to make solutions of unligated ferric Mb (metMb), the powder of Mb was dissolved in Sodium Phosphate buffer (100 mM, pH 7), and degassed by bubbling it with nitrogen gas (purity >99%) for at least 10 hours. By reducing the solution of metMb using a two-fold molar excess of Sodium dithionite ($Na_2S_2O_4$) dissolved in degassed buffer we obtain the MbNO. Right after, a degassed solution of the two-fold molar excess of Sodium nitrite ($NaNO_2$) was added to the ferrous Mb. All the preparation steps were done under nitrogen atmosphere. The sealed glass bottle of sample kept under nitrogen overpressure during the experiments.

2.2.3.2 Cyclometalated Iridium Complexes

The Ir complexes $Ir(ppy)_3$ (**Ir1**) and $Ir(ppz)_3$ (**Ir4**) were synthesized as follow: the $Ir(C^N)_2(acac)$ complexes (C^N = ppy or ppz; acac = acetylacetonate) were reacted with $BF_3 \bullet Et_2O$ to yield the bis-acetonitrile complexes as described in ref[79]. The bis-acetonitrile complexes were then directly reacted with an excess of C^N ligand in refluxing 2-ethoxyethanol for 4 hours to yield the target complexes with yields >90% after purification by column chromatography on silica gel. $Ir(ppy)_2(pic)$ (**Ir2**) is prepared as reported in ref.[80] and $Ir(ppy)_2(bpy)(PF_6)$ (**Ir3**) as in ref.[81] All samples are dissolved in $CHCl_3$ and/or DMSO at a concentration of approximately 1 mM providing an optical density (OD) typically between 0.1 and 0.3 OD (through the 0.2 mm thick flow cell) at the excitation wavelength. All measurements were performed at RT under aerated conditions.

For steady-state absorption and luminescence measurements, solute concentrations corresponding to 0.3 OD through a 1 mm quartz cell were used. Whereas, for ultrafast

fluorescence experiments (chapter 6), the concentration of **Ir1** was chosen (0.3-0.5 mM) to provide ≈0.1 OD (through a 0.2 mm thick flow cell) at the excitation wavelength we used (266 or 400 nm). Finally, for X-ray measurements (chapter 5) I used solutions of dimethylsulfoxide (DMSO) and dichloromethane (DCM). Details on concentration and optical path length as well as OD are tabulated in Table 2-1.

Table 2-1: samples and their concentration as well as optical path length used for X-ray measurements in Chapter 6.

Sample	Molecular mass (g/mol)	Concentration (mM)	Optical path length (micron)
Ir1	621.725	1.65	250
Ir2	662.7582	1.65	250
Ir3	529.3982	1.65	250
Ir4	654.78	3.11	250

2.2.4 **Data analysis**

The EXAFS **[Equation 2-10]** is a powerful tool to obtain the structural information from the experimental data. However, the EXAFS oscillatory pattern $\chi(E)$ needs to be first isolated from the X-ray absorption spectrum by data reduction procedure. Then Fourier transform of the EXAFS spectrum $\chi(E)$ (with respect to k) will deliver a corresponding frequency spectrum of the oscillatory part, where the characteristic frequencies will correspond to the interatomic bond distances between the absorber and the surrounding atomic shells [137]. This section presents the procedure applied for the EXAFS analysis using the program ATHENA [138]. The fitting procedure of the data is done by using the program ARTEMIS [139, 140].

2.2.4.1 EXAFS Extraction

The general procedure applied in the EXAFS analysis with Athena package is described in a stepwise way in order to give a better understanding of the underlying data processing.

1. **Energy calibration** to obtain the energetic position of the photoionization edge E_0 of the X-ray absorption data. In order to extract chemical information of the experimental data, the absolute edge position is necessary. For this purpose the X-ray absorption of a sample with a known edge position (*e.g.* calibration foil) is recorded during the measurement and compared to tabulated energies and shifted if necessary accordingly. The position E0 of the edge is usually fixed at the point of inflection of the photoionization edge.

2. **The Pre-edge background removal** of the part of the spectrum before the edge removes unnecessary absorption contributions from lower energy absorption edges or intensities from elastically scattered X-rays. In order to eliminate the pre-edge background, this spectral region is fitted by a linear combination of quadratic polynomial function, which is extrapolated throughout the entire spectrum and subtracted from μ(E).

3. **The Edge-jump normalization** of the data is necessary for comparison of μ and χ. In addition, the normalization enables the comparison between data from samples with different concentration, sample thickness or different detection settings. The normalization is usually achieved by dividing the X-ray absorption spectrum by the value of the edge-jump $\Delta\mu(E_0)$. For this, the post-edge polynomial fit is extrapolated to E_0. The difference between the pre-edge fit and the post-edge fit at E_0 gives $\Delta\mu(E_0)$.

4. **The Background subtraction** isolates the oscillatory pattern from the EXAFS $\chi(E)$. The background function describes ideally the absorption background of a hypothetic isolated atom $\mu_0(E)$ embedded in the Coulomb potential of the surrounding atoms. Since this background is not known, ATHENA uses an iterative background removal scheme (AUTOBK), which consists of a fit of a spline to the data. This spline is subtracted from c data and the Fourier transformed into fine structure. The AUTOBK makes use of the fact that $\mu_0(E)$ mainly contains low frequency components. In the final step, AUTOBK makes sure that low frequencies in the fine structure are minimized.

2.2.4.2 Time-resolved X-ray absorption spectroscopy

A time-resolved X-ray absorption transient signal $\Delta A(E,t)$ at given delay between the laser and the X-ray pulse is recorded by taking the difference between X-ray absorption spectra of the laser pumped sample $A^*(E,t)$ and the unpumped sample $A(E,t)$. This transient signal is time dependent due to the excited-state decay. The general transient signal is described by the difference of the excited and the ground state:

$$\Delta A(E,t) = A^*(E,t) - A(E,t)$$

Equation 2-16

The transient spectrum, also referred to as difference spectrum, can be obtained by measuring the X-ray transmission as well as the total fluorescence yield. For the transmission

measurement, the transient absorbance signal is described due to the Lambert Beer law **[(Equation 2.5)]** by

$$\Delta A^T(E,t) = \ln\left(\frac{I_T(E)/I_0}{I_T^*(E,t)/I_0}\right)$$

Equation 2-17

where $I^*(E,t)$ and $I(E)$ describe the transmitted intensity through the excited (pumped) and the ground state (unpumped) sample respectively. The difference signal obtained via total fluorescence yield is described by:

$$\Delta A^F(E,t) = \frac{I_F^*(E,t) - I_F(E)}{I_0(E)}$$

Equation 2-18

where $I_F^*(E,t)$ and $I_F(E)$ describe the fluorescence from the laser pumped and and unpumped sample respectively, with the incoming flux $I_0(E)$. In order to compare the transient fluorescence signal $\Delta A^F(E,t)$ with the transient signal of absorbance $\Delta A^T(E,t)$ measured in transmission, the transient signals are normalized to the incoming intensity $I_0(E)$ and the edge-jump of the X-ray absorption spectrum in transmission ΔA_{edge}^T and in fluorescence ΔA_{edge}^F .

$$\Delta A_{norm}(E,t) = \frac{\Delta A}{\Delta A_{edge}}$$

Equation 2-19

Usually, the laser excitation does not result in a 100% excitation of the sample. Hence, the pumped X-ray absorption spectrum contains a linear combination of the excited species and species in the ground state. In order to extract the X-ray absorption spectrum related to the pure excited state from the measured transient spectrum one needs to know the fraction of excited species in relation between the transient spectrum $\Delta A(E,t)$ and the normalized X-ray absorption spectrum of the sample in the ground-state $\mu(E)$ and excited state $\mu^*(E)$ is

$$\Delta A_{norm}(E,t) = f(t).(\mu_{norm}^*(E) - \mu_{norm}(E))$$

Equation 2-20

2.2.4.3 Estimation of the excitation yield

The magnitude of the measured transient $\Delta A_{norm}(E,t)$ is directly proportional to the excitation yield f(t) **[through Equation 2-21]**, which depends on many parameters, including the number of laser photons N_{ph}, the sample concentration c , the Avogadro constant NA , the molar extinction coefficient ε , and the sample thickness d , which is given by the tilted jet. The irradiated sample volume v results from $= d.\pi.r^2$, were r describes the radius of the laser spot size on the sample. If all of these variables are known the excitation yield can be calculated.

$$f = \frac{N_{ph}}{v.c.N_A}.(1 - 10^{(-\varepsilon.c.d)})$$

Equation 2-21

2.3 Photophysical Processes: some basic concept

2.3.1 Jablonski Diagram

When a molecule is electronically excited, the interactions it experiences with the environment and with the vacuum radiation field lead to its relaxation towards thermal equilibrium. This relaxation can occur through a large variety of phenomena and often through multiple paths. The Jablonski diagram, sketched in Figure 2-10, is commonly used to visualize the main deactivation mechanisms for a molecule in solution. Transitions between different electronic states can be achieved through a radiative process, where the energy is released through emission of a photon, or via isoenergetic non-radiative channels like internal conversion (IC) and inter-system crossing (ISC). On the contrary to fluorescence and IC, phosphorescence and ISC involve a spin change; they always occur on longer time scales. All these intrRaa-molecular transitions occur together with vibrational relaxation processes, which redistribute the vibrational energy through the normal modes of the molecule (intramolecular vibrational redistribution or IVR) or dissipate it towards the environment (vibrational cooling).

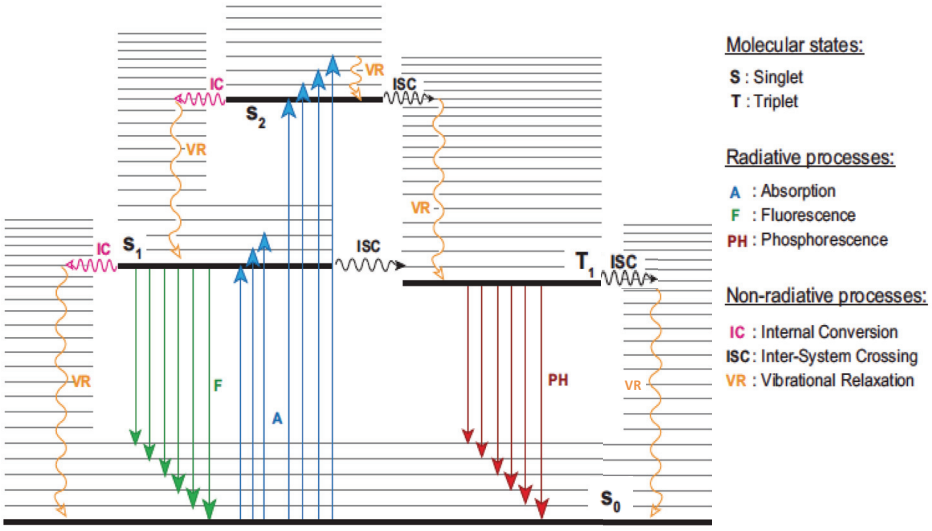

Figure 2-10: Jablonski diagram, pictorially showing the main intra-molecular deactivation mechanisms following light absorption. Processes are distinguished into radiative (solid arrows) and non-radiative (curved arrows). Horizontal lines indicate iso-energetic processes, while vertical lines imply the release of energy towards the environment.

2.3.2 Funnels from Excited Surface to Ground–state Surface: Conical intersection

The photophysical processes of non-radiative transitions and emission from an excited state occur from the minimum of the potential energy surface that correspond to geometries from which vertical adiabatic photophysical processes take place without any change in nuclear geometry. Figure 2-11 shows 3D potential energy (PE) surfaces descriptions of five limiting cases of funnel (F) leading from an electronically excited surface to a ground-state surface. Item d represents the case of surface crossing. Photochemical reactions involve the motion of the representative point on the excited surface from *R (excited reactant) from the FC minimum to other geometries, serving as "funnels" that take an excited –to a ground-state reactive intermediate, I, or conical intersection, F (*R→I or *R→F). The double cone in Figure 2-11d is termed a conical intersection (CI), resulting from the touching of two electronic PE surfaces when plotted against energy and reaction coordinate.[82] **"An important feature of a CI is that if it is accessible from *R, it serves as a very efficient funnel, F, that takes the representative point "rapidly" from an excited to ground state surface toward product P (photochemistry) or back to the ground state (photophysics). Movement of the representative point along the "wall" of a** [CI] **is essentially a vibrational relaxation.** […] [A CI] **will not generally be a rate-determining electronic bottleneck in a radiationless pathway between surfaces of the same spin multiplicity**, […] [instead] **the rate at which the representative point passes from *R to the CI. […] If there is**

no spin prohibition on the motion of the representative point, the rate of transition from the excited to the ground surface

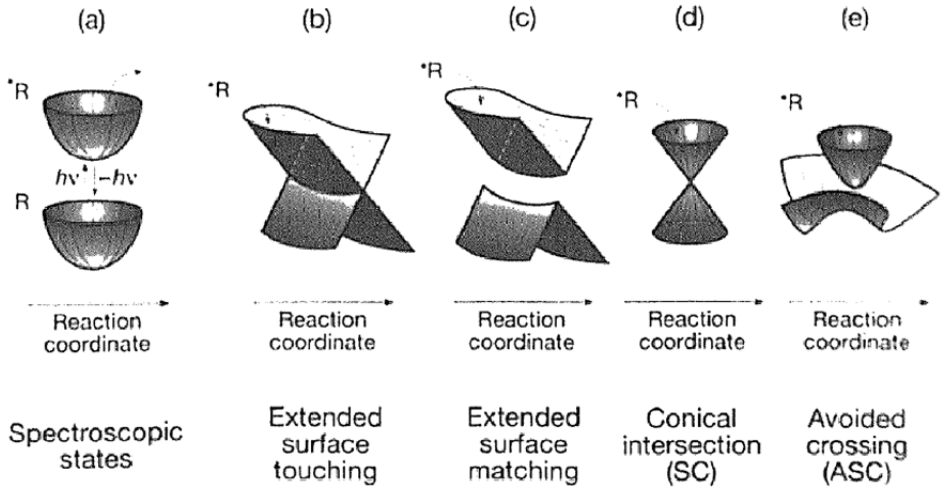

Figure 2-11: Three-dimensional PE surface descriptions of five limiting cases of funnels leading from an electronically excited surface to a ground-state surface. (a) A ground-state and Frank-Condon, or spectroscopic, excited surface with minima. (b) An excited surface touching. (c) An extended surface matching. (d) A surface crossing. (e) An excited-state minimum over a ground-state maximum due to a strongly avoided crossing. The picture is adapted from ref.[83]

will be limited only by the time scale of intramolecular vibrational relaxation *e.g.* ~ 100 fs -10 ps for a typical organic molecule."[83] Note that in the topology of an avoided crossing (Figure 2-11e), the geometry, r_c, of the avoided surface crossing (ASC) corresponds to the geometry of the ground-state maximum[83]. Thus the *ASC funnel is not a FC minimum corresponding to a geometry that is thermally equilibrated and do not obey the Born-Oppenheimer approximation (BO).

2.3.3 Intramolecular Vibrational Energy Redistribution (IVR)

Intramolecular vibrational redistribution (IVR) determines energy flow between vibrational modes within a molecule[84]. After excitation of a vibronic transition of a chromophore, the vibrational energy stored in the Franck-Condon active modes is redistributed through anharmonic coupling among the bath of other vibrational modes. In a simpler picture, when a selected vibrational state of a polyatomic molecule is excited, the population may be transferred from the initially populated state to other isoenergetic states even in the absence of collisions or any other

interaction of the molecule with its surrounding. Comprehensive reviews of IVR present some historical background and outline the current work in this large field.[85-89]

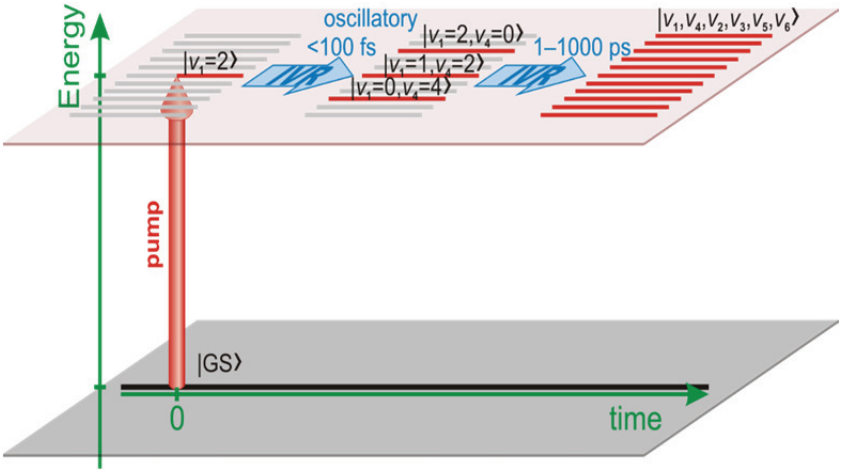

Figure 2-12: IVR in CF_3H (adapted from [90])

2.4 Experimental Methods: Optical Spectroscopy

2.4.1 Photoluminescence Up-Conversion Set-up

Steady-state absorption and emission measurements were carried out with a Shimadzu UV-3600 spectro-photometer and a Shimadzu RF-5301PC spectro-fluorimeter, respectively. Figure 2-13 shows the PLUC setup. The samples are excited with 150 kHz repetition rate at 400 nm or at 266 nm by frequency doubling or tripling 80 fs pulses at 800 nm provided by a Coherent-Rega Ti: Sapphire regenerative amplifier. The photoluminescence emitted by the investigated sample is collected by a parabolic mirror in forward-scattering geometry and directed to a second mirror that focuses it onto a □-barium borate (BBO) crystal. The luminescence is then up-converted by mixing with the 800 nm gate pulse in a slightly non-collinear geometry. The up-converted signal is spatially filtered and detected with a spectrograph and a liquid nitrogen-cooled CCD (charge-coupled device) camera.

The kinetics of the emitted signal can be measured by delaying the gate beam with respect to the onset of the fluorescence, while keeping the BBO crystal at a given angle. Polychromatic detection is obtained by rotating the BBO crystal by a computer-controlled motor during the accumulation time of the CCD camera, so as to phase-match a wide spectral region at each time delay. By measuring the Raman signal scattered from water, we estimate an IRF of the set-up of

approximately 150 fs at 266 nm excitation. The experiments we reported were carried out by exciting the samples with 400 nm or 266 nm pulses, having energies per pulse in the 10-50 nJ range. A typical measurement is obtained by averaging 10 to 50 scans.[91]

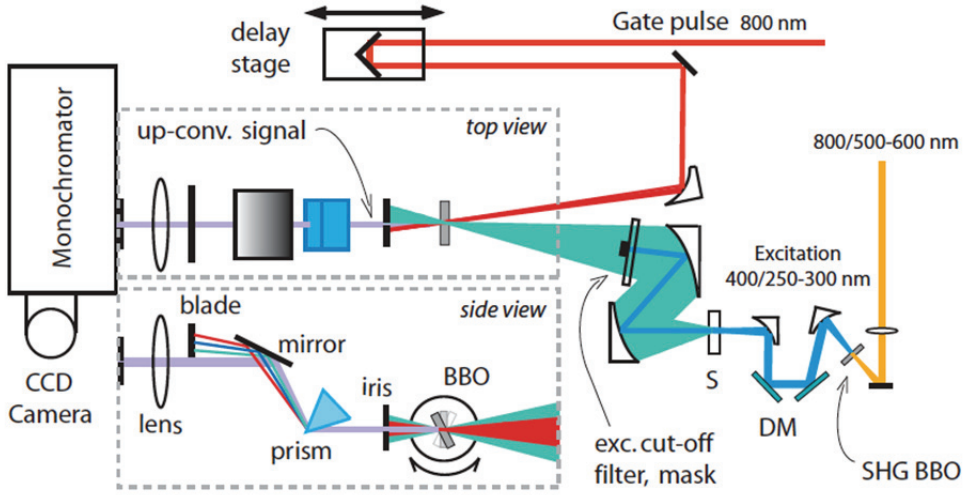

Figure 2-13: Scheme of the broadband time-gated up-conversion experimental set-up. The SFG process and the signal filtering parts are shown both from top and side view. The picture is adapted from[91]

2.4.2 **Time-Correlated Single Photon Counting**

Nanosecond-resolved luminescence was measured via a Time Correlated Single Photon Counting (TCSPC) set-up providing an experimental time resolution of 200 ps. Samples were excited with 150 kHz repetition rate at 400 nm or at 266 nm by frequency doubling or tripling 80 fs pulses at 800 nm provided by a Coherent-Rega Ti: Sapphire regenerative amplifier.

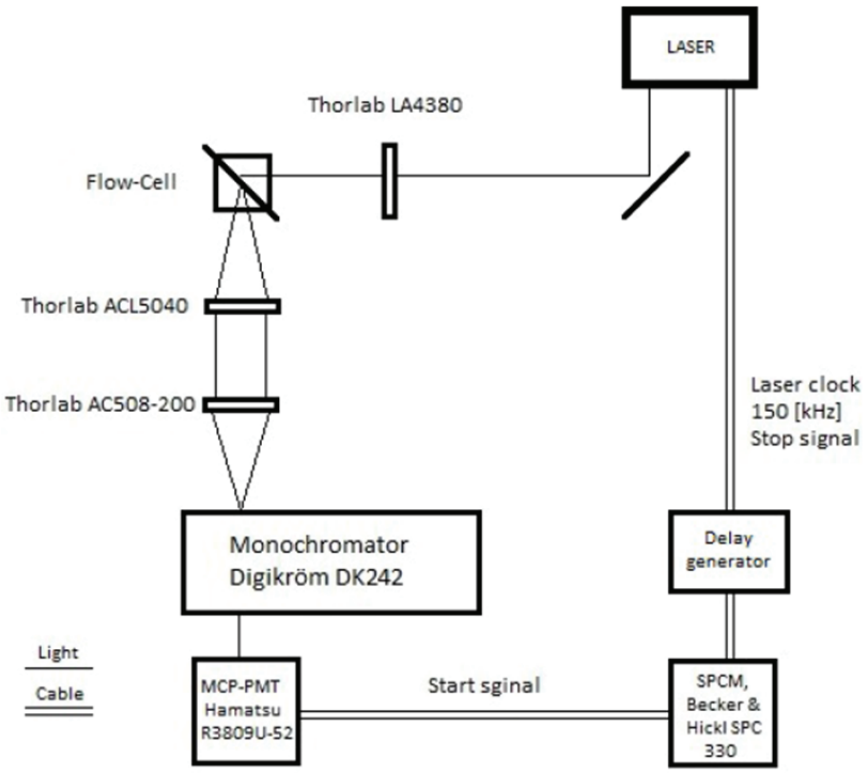

Figure 2-14: Schematic of the TCSPC set-up. From ref.[92]

2.4.3 **Data Analysis**

By writing the data in matrix form, a conceptually analogous global analysis can be performed by taking advantages from matrix calculus and decomposition algorithms. In particular the matrix Singular Value Decomposition (SVD) technique is known to efficiently act both as an instrument capable to reduce the fit dimensionality, and as a noise filter [180-182]. The m x n matrices of experimental data M(λ ,t) can be re-written as the product of three matrices

$$M(\lambda,t)_{m\times n} = S(\lambda)_{m\times n} \times W_{m\times n} \times T(t)^{T}_{n\times n}$$

Equation 2-22

where W is a matrix which is zero except for its diagonal entries w_{ii}, called singular values. This decomposition can always be performed, but under specific conditions the columns of the matrices S and T have a physical meaning. The original matrix of experimental data can be described as the sum of two contributions M' and ∈ the former representing the evolution of the system and the latter the experimental noise, which is assumed to be stochastic with zero average. [It] is possible to describe M' as

$$M'(\lambda, t) = \sum_{i=1}^{N} C_i(t)\varepsilon_i$$

[Equation 2-23

where C_i and ε_i denote the temporal evolution and the spectral shape of the i-th component, then the columns of S and T obtained from SVD of M can be interpreted as the singular spectral and kinetic vectors (often called “eigenspectra” and “eigentraces”). The j-th singular values w_{jj} thus represents the weight with which each singular eigenspectrum and its corresponding eigentrace contribute to the total signal. Note the implicit meaning of the sum in **[**[Equation 2-23**]** the N kinetic components that describe the signal have an overall amplitude evolution but their spectral shapes do not evolve in time.

For noise-free data, there are exactly N non-vanishing singular values, which are conventionally arranged in non-increasing order: $w_{11} \geq w_{22} \geq w_{33} \geq ... \geq w_{NN} > 0$. The presence of noise acts as a perturbation of the singular values and the respective singular vectors. It was demonstrated that the amount of perturbation can be directly related to the “isolation” of the singular values [181-182]. For any practical application, the only relevant singular values satisfy the condition $w_{ii} - w_{i+1,1+1} \gg w_{NN}$, the latter being entirely associated to experimental noise. Since the fit occurs on the eigenspectra and not on the raw data, the a_{jl} do not directly represent the DAS of the kinetics involved. The latter can be calculated from the eigenspectra U as

$$DAS_l(\lambda) = \sum_j a_{jl}\, w_{jj}\; U_j(\lambda)$$

Equation 2-24

When the same fit function is used, global fitting (GF) and singular value decomposition (SVD) analysis are equivalent and they must give the same results in terms of characteristic times and DAS. The obtained DAS express the weight of the specific kinetics as a function of wavelength and they should not be confused with the spectra of the different species that get populated during the system relaxation (Species Associated Spectra, SAS). The two concepts are however linked: the SAS are linear combinations of the DAS and, given a specific kinetic model, can be reconstructed from them. An example about this topic is given in chapter 5.

Since SVD and GF are capable of retrieving the same information, they offer two strategies of data analysis, having some advantages and disadvantages. SVD is able to suppress the stochastic

noise and is computationally less expensive. On the other hand, bands that narrow or shift in time can sometimes appear as different species, and a single process can be identified by several characteristic times. Since changes in band shapes are relatively frequent in fs spectroscopy, some attention should be paid when applying this algorithm. Finally, application of SVD to data presenting oscillations whose phase is not constant over all the observed spectral range is not straightforward.

A least square Global Fit becomes rapidly computationally expensive and when several parameters are experimentally determined on a large number of traces, it gets easily trapped in local minima. With respect to the SVD, however, it describes well spectral features whose shape changes in time, and it is more flexible, easily allowing to control the weights of different spectral regions on the total fit.

Chapter 3 Transition Metals in Biosystems and Organometallic Compounds

This chapter starts with a brief review of some important aspects of transition metal complexes and is dedicated to introduce all the molecular systems that have been investigated in this thesis. In particular, iron (Fe) as the active center of heme in Myoglobin (Mb) and iridium (Ir) in the general class of cyclometalated organometallic compounds. A short description of the structure of Mb is given in section 3.2, mentioning its biological functionality binding different ligands. The section follows with more details on the geometrical structure and electronic configuration of the ground state for ferrous hemes, deoxyMb and MbNO and ferric heme, metMb. Steady state spectra of these complexes are discussed in the separate section 0. The chapter continues with an introduction of cyclometalated iridium complexes giving a description of the geometrical and electronic structure of four different complexes named **Ir1-4** (3.3). In (§3.3.2) the steady state spectra of the **Ir1-4** complexes are shown introducing important features for each complex.

3.1 Transition Metals and Electronic Spectroscopy- Some Basic Concepts

Transition metal complexes represent are the basis of coordination chemistry[93] compounds and have been extensively studied as molecular model systems for complex interactions involving electronic, spin and structural degrees of freedom in catalysis, material synthesis, photochemistry and biology[93,94]. These molecules consist of a central transition metal bound to organic molecules

called ligands. Complexes formed by transition metal ions usually contain a well-defined number of ligands. The number of ligand atoms forming bonds with the metal is often referred to as the coordination number. The chemical reactivity of a given complex depends on the electronic properties of the system.[95] One of the main features of transition metal complexes is the presence of unpaired d electrons in the transition metal atom. These electrons are involved in molecular bonding and are the ones determining the complex chemistry of transition metal complexes[96,97]. An illustration of the 5 atomic d orbitals is shown in Figure 3-1-b[98].

The geometrical structure of a transition metal complex strongly depends on the electronic configuration. The bond length between the metal and the ligands, as well as its relative strength is reflected by the occupation of bonding and anti-bonding orbitals. For the following, it is supposed that the metal ion is placed in an octahedral array (Oh) of six ligands that are treated as point negative charges*, as shown in Figure 3-1. It is easy to see that qualitatively, an electron in an orbital whose lobes point toward the negatively charged ligands will have a higher electrostatic potential energy than an electron in an orbital whose lobes point elsewhere. More generally, the relative stabilities of a series of inherently similar orbitals will vary inversely according to the extent to which they bring the electron into proximity with the negative ligands. The presence of ligands lowers the spherical symmetry around the transition metal and breaks the energy degeneracy of the atomic d levels[93]. This is called Ligand Field Splitting. In this thesis we deal with the 3d orbitals for ions of Fe, and 5d orbitals of Ir. The splitting of d orbitals, in several important geometrical situations, are as follows: in both octahedral (Oh) and tetrahedral surroundings (D_{4h}), the d_{xy}, d_{yz} and d_{xz} orbitals remain equivalent (called t_{2g} because of three-fold degeneracy), as do the d_{x2-y2} and d_{z^2} orbitals (classified as eg with two-fold degeneracy). In square surroundings, the dxz and dyz orbitals remain equivalent, but the d_{xy}, d_{x2-y2} and d_{z^2} orbitals are not equivalent to any others. The actual magnitude of the splitting, Δ or 10Dq (in Oh), can be left as a parameter to be determined experimentally.

3.1.1 **Molecular Orbitals and optical transitions**

At this point, we only present a brief illustration of excitations (in particular of HOMO–LUMO excitations), the resulting states and their relevance for triplet emitters in OLEDs and metalloproteins like myoglobin. This section only addresses the compounds that have a central

* While the point charge model is not physically realistic, it does give results that are in general qualitatively correct.

metal ion with a d^6 configuration, such as Ir^{3+} [$5d^6$], and Fe^{+2} [$3d^6$]. The aim is to focus on organometalic complexes, such as tris [2-phenylpyridinato C^2, N] iridium (III) called $Ir(ppy)_3$, and metalloproteins like Myoglobin. For such compounds, different excitations involving various MOs have to be taken into account.

In general, the optical transitions like absorption and photoluminescence properties are largely determined by the nature of molecular orbitals (MOs), "frontier orbitals". These frontier orbitals are classified as highest occupied molecular orbital (HOMO) and lowest unoccupied molecular orbital (LUMO). HOMO and LUMO orbitals are mainly responsible for the electronic ground state and the lowest excited state. However, it is not sufficient to restrict the discussion to HOMO↔LUMO transitions. Energetically nearby lying orbitals can also dominate the emission properties. Thus, HOMO-1, HOMO-2, LUMO+1, LUMO+2, etc. also have to be included. In the organic molecules ligands that coordinate to the transition metal, the lowest excited states are dominantly determined by MOs which can be well described by the π-HOMO and the π*-LUMO, since MOs other than π and π* (asterisk means excited) character lie at significantly lower and higher energies, respectively. Adding a transition metal will involve its d orbitals in the LUMO and HOMO.

Figure 3-2 represents the types of frontier orbitals and electronic transitions typically encountered in transition metal complexes. Transitions A-D originate from ligand orbitals but terminate in metal orbitals and thus involve a charge transfer (CT) from the ligand to the metal. Depending on the direction of the CT, the nomenclature "ligand to metal" charge transfer (LMCT) or "metal to ligand" charge transfer (MLCT) is used *e.g.* transitions E and F in Figure 3-2. CT bands are quite intense e.g. with molar absorbtivities of around ~$1.5x10^3$ M^{-1} cm^{-1} in iridium complexes.

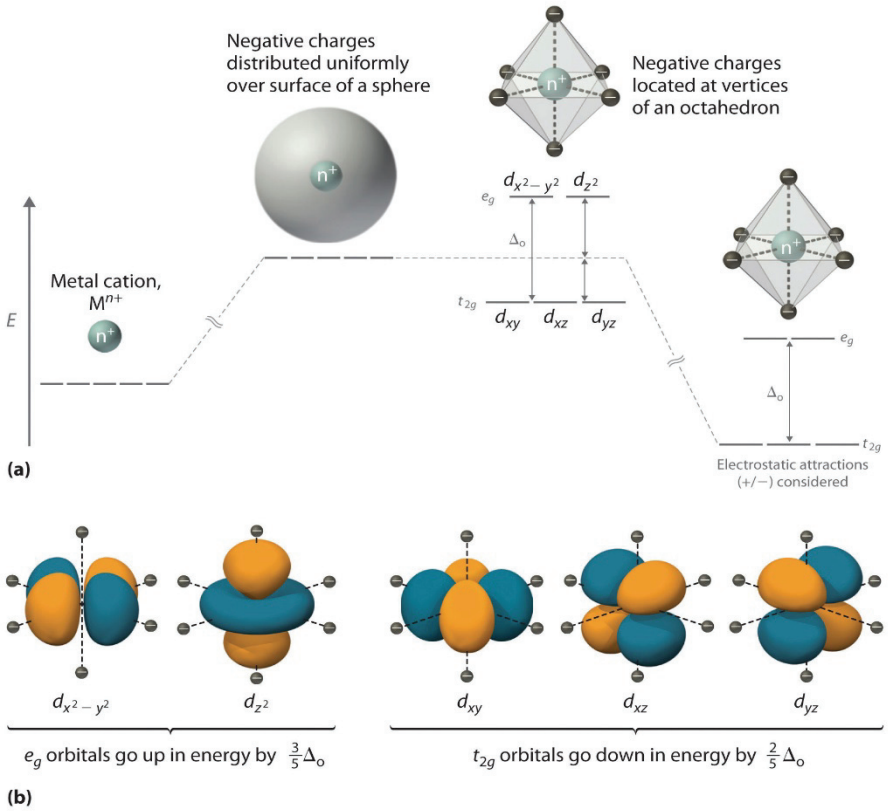

Figure 3-1: Distributing a charge of −6 uniformly over a spherical surface surrounding a metal ion causes the energy of all five d orbitals to increase due to electrostatic repulsions, but the five d orbitals remain degenerate. Placing a charge of −1 at each vertex of an octahedron causes the d orbitals to split into two groups with different energies: the $d_{x^2-y^2}$ and d_{z^2} orbitals increase in energy, while the, d_{xy}, d_{xz}, and d_{yz} orbitals decrease in energy. The average energy of the five d orbitals is the same as for a spherical distribution of a −6 charge, however. An attractive electrostatic interaction between the negatively charged ligands and the positively charged metal ion (far right) causes all five d orbitals to decrease in energy but does not affect the splitting of the orbitals. (b) Probability density (spatial distribution) of d orbitals. The picture is modified from ref. [99]

Transition G is metal centered and is referred to as d-d transition. These metal centered bands are forbidden in octahedral complexes for symmetry reasons and remain quite weak in lower symmetry molecules (ε= 1-100 $M^{-1}cm^{-1}$). Transition H is a ligand centered (LC) transition, specifically a π→ π* transition. These bands are very intense with molar absorbtivities of ~ $4.2x10^4$ $M^{-1}cm^{-1}$ in the iridium complexes discussed here. For the systems studied in this thesis LC bands other than π→ π* or an occasional n→ π* (n is non-binding orbital) are very high in energy. In the simple HOMO–LUMO model, when the spins are also taken into account, one obtains for the excited state configuration $^1\pi^1\pi^*$ four degenerate different situations. An excitation without a spin-flip is singlet ^{1}LC (or $^1\pi\pi^*$), while an excitation with a nonzero total spin, is triplet ^{3}LC (or $^3\pi\pi^*$) with three different possible spin orientations.

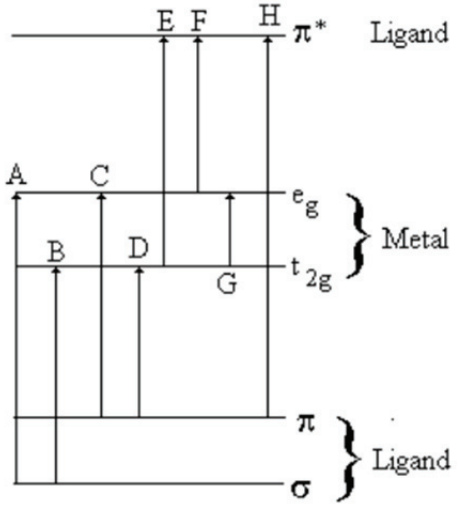

Figure 3-2: Simplified scheme of transitions between molecular orbitals typically encountered in inorganic spectroscopy.[100]

However, spectroscopic investigations show that the splitting between the excited singlet and triplet state (of LC) is usually significant (10^4 cm^{-1} (≈ 1.24 eV) for iridium complexes). Electron–electron interaction and the exchange integral explain this splitting of singlet-triplet states. This means that, the two electrons with the same spin orientation (the triplet state) have the tendency to avoid each other. Hence, the average electron–electron repulsion is smaller than in the singlet state with opposite spin orientation and thus the triplet has a lower energy than the singlet state. The d-orbitals and d-d* transitions are indirectly of importance for OLED materials. This is due to two different effects. On the one hand, the quantum mechanical mixing of d-orbitals of open-shell transition metal ions, such as Pt^{2+}, Ir^{3+}, or Os^{2+}, can induce the required SOC to make the formally forbidden triplet–singlet transitions sufficiently allowed (see the following). On the other hand, states which result from d-d* excitations often quench the emission efficiently, and therefore should not lie in a thermally accessible energy range of the emitting states. Usually, a description of d-d* states is carried out by use of group theory and the symmetry of the complex. An introduction to ligand field or crystal field theory can be found in most inorganic chemistry textbooks (*e.g.*, see Refs. [101-44]), whilst more detailed descriptions are found in refs.[102].

In the quantum mechanical picture, the Born-Oppenheimer (BO) Approximation gives a good initial guess for the molecular wave function (WF) of simple molecules by assuming that changes of electrons WF (ψ_0) are much faster than nuclear vibrational motions (χ). In other words, ψ can be computed in terms of three independent wave functions $\psi \sim \psi_0 \chi S$, which S describes the spin configuration. The most probable transitions between electronic states occur when the wave

function of the initial vibrational state χ_i most closely resembles the wavefunction of the final vibrational state χ_f (the Franck-Condon (FC) principle). For electronically allowed transitions, FC activity is the mechanism that gives rise to vibrational progression (or FC progression) in absorption, excitation spectra, or emission spectra. More precisely, the transition probability for electronic transitions is governed by matrix element for the interaction of light with the initial (i) and final (f) state electronic WFs $\langle\psi_i|\,\vec{D}\,|\psi_f\rangle$. This interaction in the dipole approximation is defined through electric dipole moment operator ($\vec{D} = -e\vec{r}$). However, the shape of the resulting absorption/emission bands is defined by the nuclear WF overlap, $\langle\chi_i|\chi_f\rangle$, called FC factor* depending on the symmetry species of the χ_i and χ_f.

In organometallic compounds containing heavy transitional metals (e. g. the third-row TM iridium) with electronic states more close in energy, the BO approximation breaks down give rise to different types of transitions in the system. When the electronic energies of two BO electronic states become very close, vibrations of the nuclei can induce symmetry-forbidden transitions. [103] This cannot be explained by means of the Franck-Condon principle, which governs only the distribution of intensity due to a non-vanishing transition moment over the various vibrational components of the band. The phenomenon can be understood by taking into account coupling of electronic and vibrational WFs and dependence of the electronic transition dipole moment on the nuclear geometry Q known as vibronic coupling (or Herzberg- Teller (HT) coupling).[103]

It is known that in the elements with high atomic number (e.g. third row TMs in periodic table e.g. Ir), electrons attain relativistic speeds inducing perturbations to the Hamiltonian of the system (subject of the relativistic quantum chemistry)[104]. In this relativistic regime the interaction between the electron-spin and the orbital angular momentum called spin-orbit coupling (SOC) is strong enough that must also be included in the atomic Hamiltonian. In fact, the SOC increases as the fourth power of the effective nuclear charge Z,[105] indicating that SOC interactions are significantly larger for heavy atoms e.g. Ir.

The emission properties of an organometallic complex are largely determined by the individual characteristics of the three sub-states of the lowest triplet term T_1. The sub-states do not represent “pure” states, but contain contributions from singlets and triplets of other

* The equilibrium positions of the potential surfaces of the final state (excited state (ES)) and the initial state (ground state (GS)) are shifted by ΔQ (Q is the configurational coordinate). This leads to a progression in the spectrum.

configurations due to configuration interaction (CI) and SOC. In particular, the mixed -in singlet components provide the required radiative rates and dictate the degree of allowedness of the optical transitions to the electronic singlet ground state. Further, specific interactions with higher-lying states lead to individual, but different, energy stabilizations of the sub-states. Thus, a splitting of the T_1 state, the ZFS, results[106-111]. Zero-field splitting (ZFS) is the removal spin microstate degeneracy for systems with S > 1/2 in the absence of an applied field.

3.2 Iron, the active centre of Myoglobin

Among the heme proteins, myoglobin is certainly the most studied and best known. Already in 1982 Frauenfelder et al. called it the hydrogen atom of biology[112]. Partially the interest in this protein comes from the fact that it represents a building block of hemoglobin, whose allosteric mechanisms are puzzling scientists since many years and is still not fully understood.

Myoglobin, the oxygen carrier in muscle tissue, is a small protein consisting of a single polypeptide chain of 153 amino acids and an iron porphyrin (heme) as active center. Heme, one of the best-known naturally occurring porphyrins, is the pigment in red blood cells, a cofactor of the protein hemoglobin. The protein is quite compact and 70 % of the polypeptide chain is folded in eight α-helices (A-H), connected by turns and loops[113]. The central iron can be found in the ferric or the ferrous redox state and it can bind a large variety of small molecules other than O_2, as during its physiological role, like CO, NO, CN, or water. Apart from a diatomic ligand and four nitrogen of the porphyrin ring, Fe is also coordinated to a histidine (His93). The unligated oxidized (ferric, Fe^{3+}) form of Myoglobin is also known as “met Myoglobin" or simply metMb and the unligated (refers to lack of the 6^{th} ligand) reduced (ferrous, Fe^{2+}) form of Myoglobin is called “deoxyMb". This terminology will be used from now on. Figure 3-3 shows an illustration of the heme group of Nitrosyl-Myoglobin (MbNO) and its surroundings. Myoglobin, as well as the other respiratory proteins, has the property of reversibly binding molecular oxygen[114]. The detachment of the diatomic ligand produces significant structural changes. This process has been studied extensively,[77,114-116] in order to understand which parameters control the ligand release.

It is of general consensus that the biological function of many proteins is controlled by conformational changes of different magnitudes. These structural changes, though crucial for protein function, are seldom characterized at the atomic level, which results in a poor understanding of the fundamental connection between structure, dynamics and function.

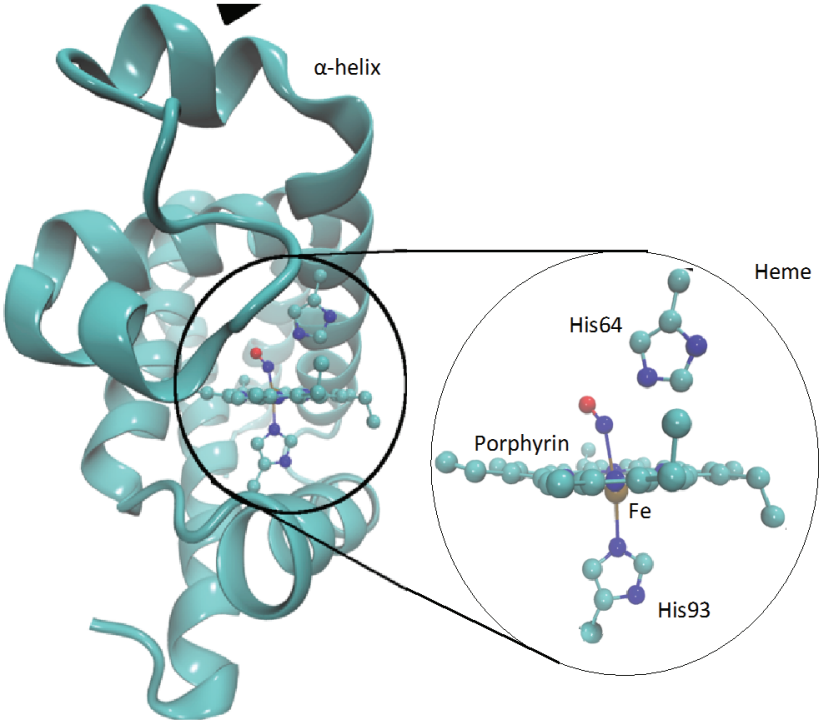

Figure 3-3: Schematic of heme and its close proximity at the center of Myoglobin.

In this sense Myoglobin (Mb) has played a central role in the investigation of protein dynamics. Despite its complex behaviour, reflected in many different functions apart from simply storing oxygen,[116-119] it serves as a model system of general significance. Some reasons why Mb is a good model include the vast characterization of the geometrical structure with respect to different ligands and its intrinsic reactivity[77] and the sensitivity of the iron-ligand bond to light exposure[120,121]. Thus, illuminating Mb with light of the appropriate wavelength can trigger the biological function of ligand-release. Mb also may increase the effectiveness of NO as a signaling molecule by enhancing the NO concentration gradients[122 116]. Another crucial role attributed to Mb is the ability to act as NO scavenger in heart and skeletal muscle[119,117,123]. In its deoxyMb form, Mb reversibly binds O_2 to yield oxymyoglobin (MbO_2), which will react irreversibly with NO yielding nitrite and metMb. This easy ligand substitution will facilitate the neutralization of the Cytochrome-C oxidase. The cycle continues with metMb being reduced to deoxyMb, which also binds to free NO molecules.

3.2.1 Geometrical structure and electronic configuration of the Myoglobin

Modern crystallographic techniques make it possible to determine the global structure of the protein with almost atomic resolution[124]. However, ideally one would prefer to determine the structure of the protein in its physiologically relevant environment. Hard X-ray absorption

spectroscopy at Fe K-edge revealed the bond length, angles and dihedrals by the analysis of the spectral resonances occurring above the ionization potential in both the X-ray absorption near edge

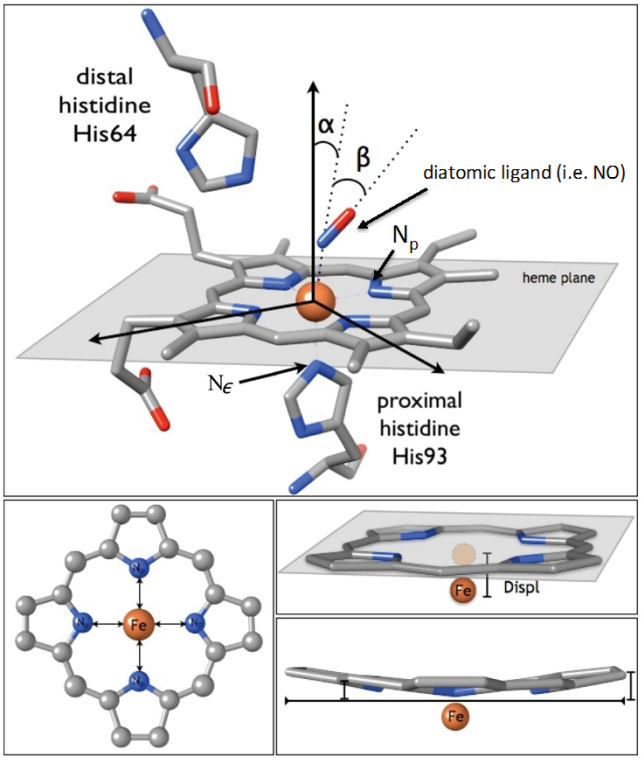

Figure 3-4: Schematics of the active center of myoglobin and the relevant structural parameters used in ref[43] to simulate the structure of heme in myoglobin. The upper panel shows the heme plane and angles (a and b) describing the ligand binding geometry. The lower left panel shows the Fe–Np distance and the lower right panels show the heme doming parameters. The picture is adapted from ref.[43].

structure (XANES) and the extended X-ray absorption fine structure (EXAFS) regions[43]. Some of the structural parameters necessary to describe the heme environment (Figure 3-4) are Fe-Np (distance of iron atom from nitrogen atoms of the porphyrin ring), Fe-Nε (distance of iron atom from nitrogen of proximal histidine, His93), Fe-L_1 (distance between the iron atom and the ligand closest atom), Displ (the Fe atom displacement out of the heme plane), α (tilting angle between the normal of the heme and vector between the iron center and the diatomic ligand), and β (bending angle between the vector of the diatomic ligand and the one connecting the ligand to Fe). In this thesis we mainly refer to the three bond distances defined in ref[43].

Apart from investigating the structure of Mb, massive research has been done to understand the biological functionality of Mb. It is known that the reactivity of Mb strongly depends on the

electronic structure of the active site. In fact, the ability of the heme to redistribute the charge and spin density of the iron plays an important role in the formation and stabilization of a variety of intermediates important for biological function[44,45]. The iron atom of the heme group may exist in three different oxidation states (ferrous, ferric and ferryl) and its valence 3d electrons are significantly delocalised into the porphyrin and ligand π^* orbitals[43]. The ferric species are: aquamet myoglobin (metMb) and cyanomyoglobin (MbCN). The ferrous ones are: the unligated myoglobin (deoxyMb) and the ligated species oxymyoglobin (MbO_2), nitrosy lmyoglobin (MbNO) and carboxymyoglobin (MbCO). In the following, more details of the electronic ground state are given for those of Mbs that have been studied in the course of this thesis.

3.2.1.1 MetMb

In metMb, the ferric iron center with a high spin electronic (S=5/2) configuration plays an important role in the reaction cycle with MbNO and MbO_2 (see above). Crystallographic studies showed that in horse metMb the heme structure is almost planar[125] (see also Figure 3-5). Note that a H2O molecule is bound to the ferric Fe in metMb. Horse metMb, as most of the myoglobins, contains two Trp residues (Trp7 and Trp14), in the α-helix A, which undergo Förster energy transfer to the heme[126-130]. Structural studies pointed out that Trp7 is ~20 Å far from the heme and partially exposed to the solvent, while Trp14 belongs to a strongly evolutionary preserved cluster and is located in a hydrophobic environment at ~15 Å from the heme [131, 132]. Electron transfer from these Trp amino acids to the Fe in metMb is discussed in chapter 5. The electronic structure of the heme in metMb has also been investigated in ref. [43,72]

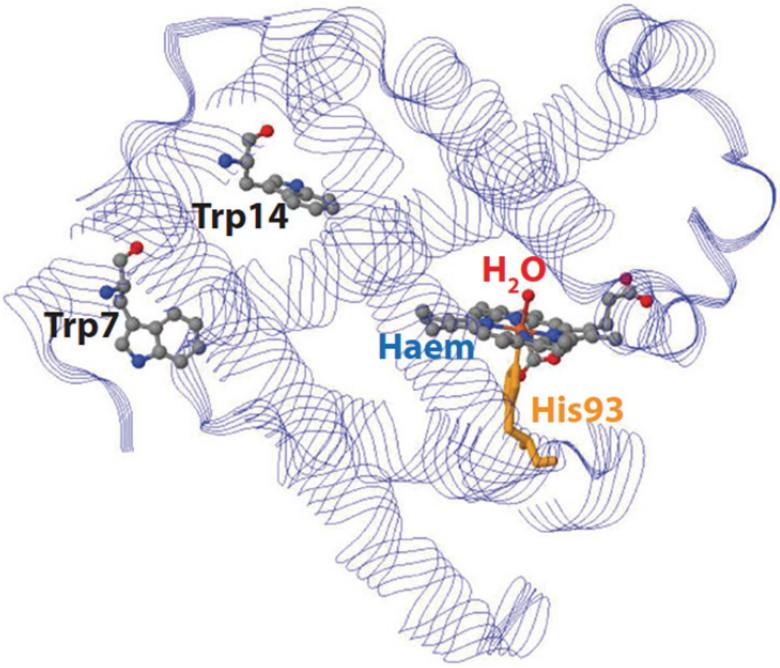

Figure 3-5: Molecular structure of metMb[125]

3.2.1.2 DeoxyMb

From all the studies about the geometrical structure of the different Mb forms, deoxyMb is probably the most controversial case. In deoxyMb, heme has only one axial ligand of distal histidine resulting in a pentacoordination (5C). This makes a unique geometry, and gives C4v symmetry to the iron environment. It is found that the heme in deoxyMb is non-planar referred to as domed heme. Many previous studies have reported an iron displacement from the heme plane in doxyMb[133-135]. Among them, the shortest value (0.2±0.02 Å) is reported by Lima *et. al* from the best fit to deoxyMb XAS spectrum[43]. They not only considered the displacement of the iron, but also the nitrogen atoms (0.03±0.01 Å) and nearest carbons (0.04±0.01 Å) in the heme plane, providing a more physical description of the doming. Their calculated[78] bond lengths for deoxyMb are: Fe-Np=2.075±0.009 Å and Fe-Nε=2.31±0.02 Å. Besides the doming, they found that the Fe–Nε distance is very sensitive to the experimental conditions e.g. pH, which makes their results most relevant to physiological conditions (298 K and pH 7).

In deoxyMb we have ferrous form (Fe^{II}) of iron with oxidation state of two. The ferrous deoxyMb has a high-spin (HS) ground state configuration. In addition, the HS configuration of iron in ferrous Mb[136] is responsible for the doming of the heme plane in deoxyMb[137,138] corresponding to non-planar square pyramidal (C_{4v}) symmetry. Figure 3-6 depicts the C_{4v} ground state. It is worth

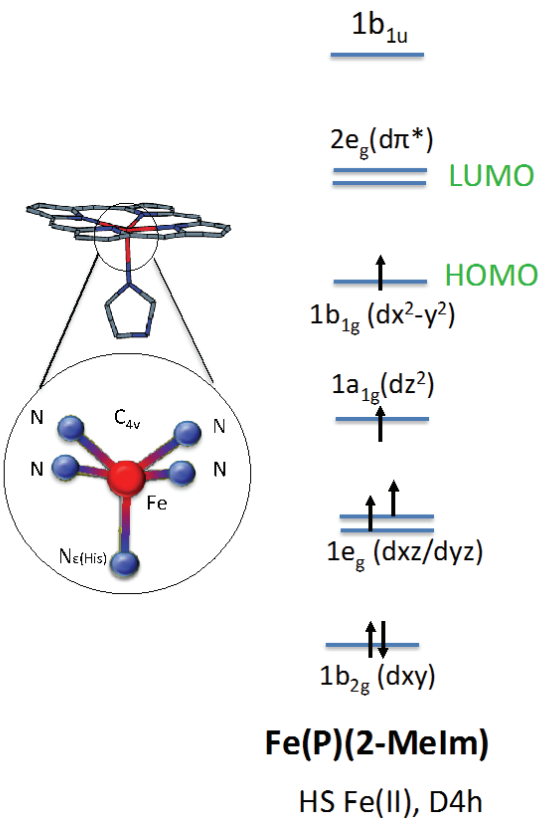

Figure 3-6: (left) the schematic molecular structure of five-coordinated iron porphyrin with the imidazole ligand. (right) orbital energy level diagram for deoxyMb and its model system Fe(P)(2-MeIm).

to note that the energy arrangement of 3d orbitals in a C_{4v} ligand field in deoxyMb is similar to that of the D_{4h} ligand field in MbNO (next section).

Several theoretical studies have been carried out to elucidate the electronic properties and out-of-plane displacement of the Fe^{II} in deoxyheme complexes in hemoprotein. The deoxy form of both myoglobin (Mb) and hemoglobin (Hb) has been well characterized with high-spin (HS) $3d^6$ ground-states.[139] They include a single axial imidazole ligand from the proximal histidine wherein the Fe lies ~0.2 Å below the porphyrin plane[43]. High-spin (S=2) states wherein the Fe atom lies significantly out of the porphyrin plane, is a general property of five-coordinate Fe^{II} porphyrin complexes. Hence, model systems consisting of iron porphine (FeP) with an axial nitrogenous ligand are good candidates for mimicking the deoxyheme electronic structure. Among the synthetic five-coordinate Fe^{II} porphyrins, a well-known HS complex is iron(II)(porphyrinato)(imidazole) as FeTPP(2-MeIm) with 2-methylimidazole as its axial ligand[140]; Fe lies ~0.42 Å above the porphyrin plane. This system represents a good model for deoxyMb and deoxyHb. Yet, another simpler model system for deoxyMb considering out-of-plane displacement

of Fe in LS configuration (by considering all possible low-lying states) is Fe(P)(2-MeIm). The out-of-plane displacement for Fe(P)(2-MeIm) is calculated[2] to be 1.3 Å shorter than that that of FeTPP (2-MeIm) which is so close to the recent experimental result of Lima et al.[43]. In this thesis, I refer to the electronic structure of Fe(P)(2-MeIm) as model for the electronic structure of the deoxyMb. The ground-state configuration of Fe(P)(2-MeIm) is calculated[2] (at C_1 symmetry) to be HS $(d_{xy})^2$ $(dz^2)^1$ $(d\pi)^2$ $(dx^2\text{-}y^2)^1$, in agreement with NMR experimental assignment[141]. As shown in Figure 3-6, the HOMO orbital for the Fe(P)(2-MeIm) model is the singly occupied $dx^2\text{-}y^2$ and the LUMO is calculated to be the $2e_g$ (π^*) orbital of the porphyrin ring. In this HS model system for deoxyMb, the anti-bonding dσ-orbitals, $(dz^2)^1$ and $(dx^2\text{-}y^2)^1$ are singly occupied, while they are not occupied in the low-spin (LS) configuration of the MbNO (see next section).

3.2.1.3 Nitrosyl Myoglobin

Here a brief introduction is presented on the geometrical and electronic structure of heme. Heme in the case of nitrosy lmyoglobin (MbNO), Figure 3-7, is planar and it has a 6-coordinated (6C) configuration with two axial ligand bonds to the diatomic molecule of nitric oxide (NO) and His93, respectively (Figure 3-4). Despite having a nitrogen bond to iron in all ligands, the heme has a tetragonal symmetry (D_{4h}) rather than octahedral (Oh)[*142]. The different nature of axial ligands imposes different bond lengths relative to the Fe-N_p. The calculated[78] bond lengths are: Fe-N_p=2.009±0.008 Å, Fe-NO=1.82±0.02 Å and Fe-Nε=2.15±0.03 Å. The structural refinements of MbNO in ref[43] appear to reflect large variations. For example, the NO alignment (angle α Figure 3-4) depends on the sample preparation conditions and specifically, the temperature (see Table 2 in ref[43]). Moreover, interactions with the distal pocket stabilizes local Fe–NO conformational minima, during the sample preparation and can influence the angle α by forcing a strained binding geometry on the NO.[143] With this method of sample preparation (section 3.III.4.a) the NO ligand will be bent by ~130° [43]. MbNO has the ferrous form (Fe^{II}) of iron with oxidation state of two. The ferrous complex of MbNO has a low-spin (LS) ground state. Figure 3-7, shows the simplified electronic configuration (orbital diagram) of the ground state of MbNO in D_{4h} symmetry[1,144].

[*] In fact it is generally assumed that the local symmetry of the heme environment in both deoxyMb (5C pyramidal) and MbNO (6C planar) can be approximated as D4h, assuming that the presence of a Jahn-Teller distortion causes a deviation from O_h symmetry. This is misleading, because the ground state of MbNO is not degenerate and cannot undergo a Jahn-Teller distortion.

The D_{4h} ligand field in MbNO splits the frontier 3d orbitals to d_{xy} (b_{2g}), d_{xz}, d_{yz} (e_g), d_{x2-y2} (b_{1g}), and dz^2 (a_{1g}) in order of increasing energy (Figure 3-7). Based on the involvement in either π-bond or σ-bonds these orbitals are considered dσ as combination of d_{x2-y2} (b_{1g}) and dz^2 (a_{1g}); and dπ as combination of d_{xz}, d_{yz} (e_g) and d_{xy} (b_{2g}) orbitals. In the low spin $3d^6$ GS, the b_{2g} and e_g orbitals are fully occupied. However, as for deoxyMb, to consider the mixing of 3d orbitals of Fe with ligands, one needs model systems for better understanding of the actual electronic configuration of MbNO. From the three model systems introduced in the literature (shown in Figure 3-7) Fe(NO)(TPP)[1], Fe(NO)(PP) and Fe(NO)(PP)Im[144], where PP is porphyrin, the model system of Fe(NO)(TPP) introduced by Olson *et. al* is oversimplified without considering the imidazole ligand (instead of His93). It is known that imidazole acts primarily as a sigma donor ligand, with essentially no backbonding ability[144]. Hence, including imidazole in the system reduces the HOMO-LUMO gap via destabilization of the dz^2 orbital, while dπ orbitals remain unperturbed. So, to a good approximation Fe(NO)PP(Im) represents an acceptable model for MbNO. Using this model, Graham *et. al* show that the dz^2 orbital has an antibonding interaction (σ bond) with the π^*_{NO} orbital of the axial ligand that accepts an electron from it the so called π-backbonding (Figure 3-7) whereas the bending of the ligand (130°) minimizes this interaction. Hence, the HOMO is a combination of π^*_{NO} and dz^2 (I call it dσ as it is shown that dz^2 has more contribution) and the

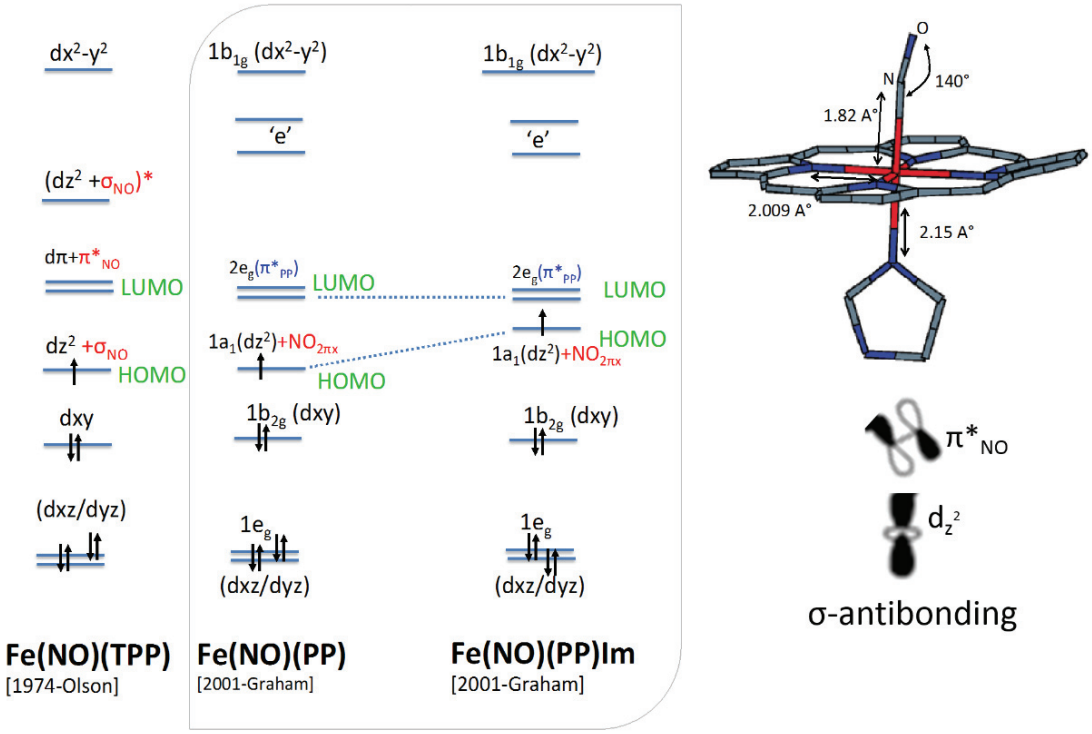

Figure 3-7: Schematic molecular diagram for Fe(NO)(TPP) ref [1], Fe(NO)(PP), and Fe(NO)(PP)Im from ref [144], where TPP is tetraphenylporphyrine, PP is porphyrin, and Im refers to imidazole.

LUMO orbital would be a combination of π^*_{NO} and $e_g(\pi^*_{PP})$ orbitals. Hereafter, I refer to the orbital diagram of the Fe(NO)PP(Im) model system when talking about electronic configuration of MbNO (see chapter 5).

3.2.2 Steady-state UV-VIS spectrum of MetMb, deoxyMb, and MbNO

In myoglobin, π-π^* transitions give rise to several absorption bands. In the absorption spectra Figure 3-8, depending on the nature of the diatomic ligand, a moderately intense pair of bands is located between 500 nm and 600 nm (called Q–bands). An intense band around 400-450 nm (called B or Soret band) and two moderately intense bands between 250 nm and 380 nm (called L and N bands respectively).[145] As shown in Figure 3-8 the shape of the Q–bands (number of the peaks and their relative intensity) is strongly influenced by the diatomic ligand coordinating the iron ion, which for the Soret band only the position of the peak is changing. The main absorbers in myoglobin in the 250-700 nm region are the heme and the tryptophan (Trp); as can be seen in Figure 3-8 all the absorption bands are due solely to porphyrin transitions, except the L band (250–300 nm) that is composed of a superposition of porphyrin and the tryptophan residues absorption. In this spectral region there are two other amino acids that absorb, namely phenylalanine and the tyrosine; however, the molar extinction coefficient of tryptophan is the largest (Figure 3-9), which makes it the main absorber in the 250–300 nm spectral region.[146] In nitrosyl ferrous heme complexes, photoexcitation of the system in the Q-band (π-π^* porphyrin transition[147]) opens up a photodissociation channel, which makes it an ideal

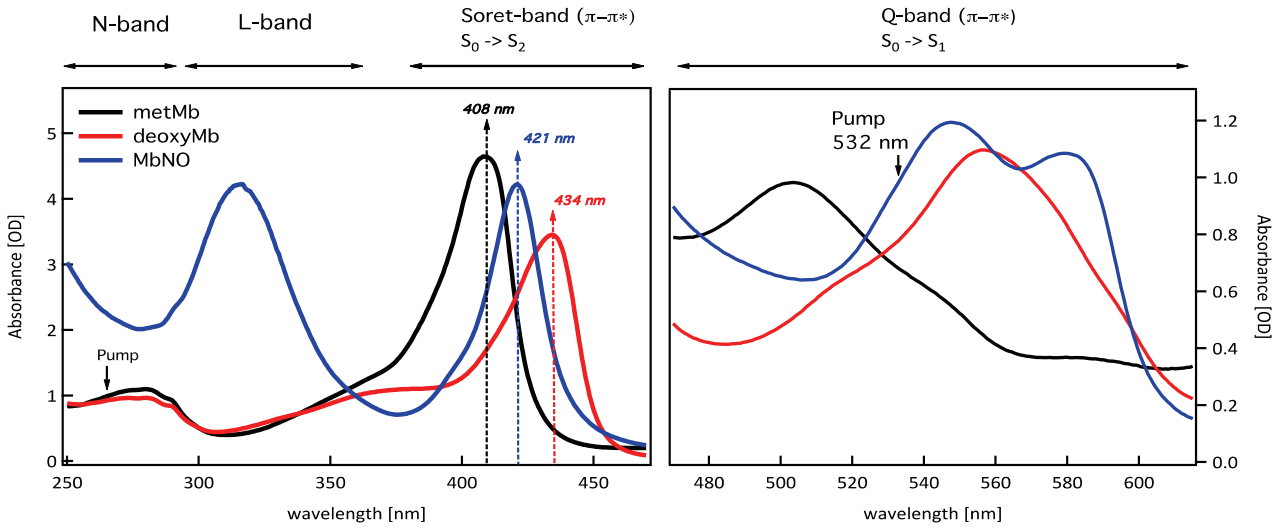

Figure 3-8: UV-Vis spectrum of metMb (black), deoxyMb (red) and MbNO (blue); optical path length=0.1 mm, concentration =1 mM

excitation band for investigating the ligand dynamics in MbNO. In the steady-state UV-VIS absorption spectra of MbNO (blue curve in Figure 3-8), the Soret-band in MbNO is located at 421 nm and its Q-band with two α and β peaks are at 548 nm and 581 nm, respectively. There is another important spectroscopic feature (not shown here) in the visible region at 757.5 nm, band III, sensitive to the iron−heme plane distance and therefore a good probe for the relaxation of the five-coordinate heme in Mb.[148] It is also important to know the exact position of Q-band and Soret-band for metMb (black curve) and deoxyMb (blue curve) in Figure 3-8 not only because they are involved in the process of synthesizing MbNO, but also because of monitoring integrity of the sample during the measurements. As slight exposure to air leads to fast transformation of MbNO to metMb. The main absorption bands in the UV-Visible characterizing metMb are the N-band at ~ 300 nm, the Soret-band at 400 nm, and the lowest energy the Q-band around 500 nm. In comparison, the main bands in deoxyMb are significantly red-shifted: the Soret going to 434 nm and the Q-band to about 556 nm. Tracking the position of the main absorption band provides a good probe of integrity of the MbNO sample during the experiment. Indeed, slow substitution of the NO ligand by the O_2 present in air can happen.

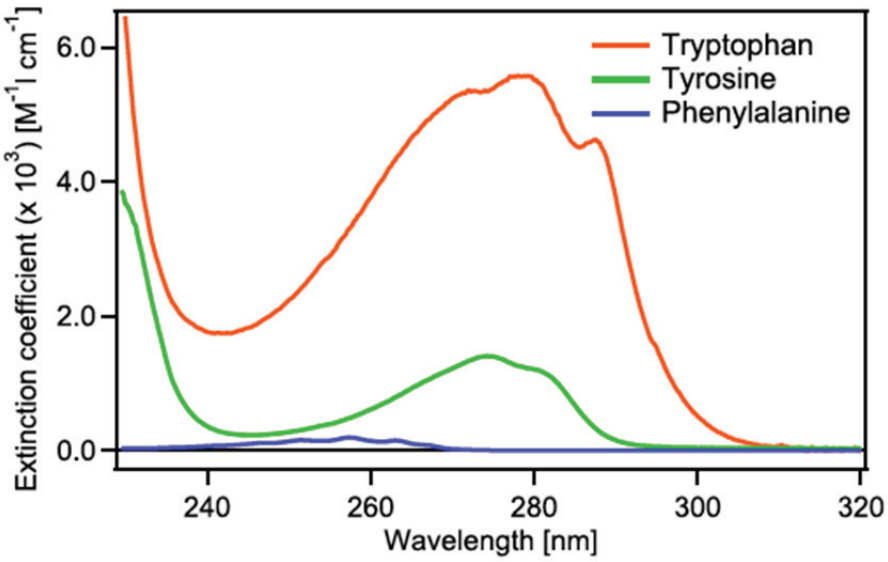

Figure 3-9: Lowest absorption bands of the aromatic amino acids. Reported extinction coefficients are from [146]

3.3 Iridium Cyclometalated Complexes

Since the 1990's, luminescent cyclometalated iridium (III) complexes were hot topic of research interest from different fields of chemistry, material science and physics due to their application in converting electric energy to light (organic light emitting diodes-OLEDs). The short

lifetime of their excited singlet state, wide color tunability and high phosphorescence quantum yield, make them very promising phosphorescence emitters for application in phosphorescence organic light-emitting diodes (PHOLEDs). PHOLEDs are efficient as both singlet and triplet harvesting devices[5,149-152]. Various phosphorescent light emitting materials have been synthesized and intensively studied worldwide.

The most widely used green emitting iridium (III) complex, fac-tris (2- phenylpyridine) iridium called $Ir(ppy)_3$ (ppy = 2-phenylpyridine, $C_{11}H_8N$), has shown a number of advantages such as ease of tuning emission energy by functionalizing the ppy ligand with electron donating and electron withdrawing substituents and high phosphorescent quantum efficiency at room temperature[153,61,154]. Among different types of tris-cyclometalated iridium complexes, neutral homoleptic complexes of the type $Ir(C\hat{}N)_3$, show the maximum quantum efficiency for phosphorescence emission (e.g. $Ir(ppy)_3$ ~100%)[5] and relatively high efficiency for OLED devices (~20%). Selective stabilization or destabilization of the HOMO and/or LUMO of the complex gives an effective strategy to tune the emission color. Watts et al[54,150-152,155] synthesized several substituted ppy-based neutral iridium complexes. Heteroleptic iridium complexes of the form $[(C\hat{}N)_2Ir(N\hat{}N)]^+$ are of particular interest because of their facile capacity to finely modulate the emission energy through independent modification of the cyclometalated and ancillary ligands[53]. Here, in particular I study the photophysics of the complexes $Ir(ppy)_3$ (**Ir1**), **Ir**$(ppy)_2$(pic) (**Ir2**), **Ir**$(ppy)_2(bpy)(PF_6)$ (**Ir3**) and **Ir**$(ppz)_3$ (**Ir4**) [phenylpyrazole (ppz)] both in the UV-Vis regime (Chapter 5) and X-ray regime (chapter 6). Only facial isomer[*58] of **Ir1** and **Ir4** were studied in the context of this thesis. As it is apparent from the chemical formulas, we can classify these complexes into homoleptic (tris) compounds (**Ir1**, **Ir4**) and heteroleptic (bis) compounds (**Ir2**, **Ir3**); neutral (**Ir1**, **Ir2**, and **Ir4**) and ionic (**Ir3**); as well as either pyridine base cyclometalated ligand or pyrazole base (**Ir4**). Of course there can be other classification that will be beyond the scope of this thesis. **Error! Reference source not found.** shows a schematic of the structure of these complexes. In the

[*] These complexes have two isomers, facial and meridional, the meridional isomers for both pyridyl and pyrazolyl-based cyclometalates show markedly different spectroscopic properties than do the facial forms. Isolated samples of mer-$Ir(C\hat{}N)_3$ complexes can be thermally and photochemically converted to facial forms, indicating that the meridional isomers are kinetically favored products. The meridional isomers are easier to oxidize, and the emission is broad and red-shifted relative to the facial forms. The solution photoluminescent quantum efficiencies of the meridional isomers and their emission lifetimes are significantly lower than the facial isomers of the same cyclometalating ligands. Hence, there is a preference to form the facial isomers at high temperatures (>200 °C).

following I introduce the reported frontier orbitals involved in the photophysics of each compound.

3.3.1 Geometrical Structure and Electronic Configuration

3.3.1.1 $Ir(ppy)_3$

In the facial tris-cyclometalated complexes, the three identical ligands surrounding the iridium atom create C_3 symmetry.[156] In **Ir1**, one carbon anion from phenyl and nitrogen from pyridine are coordinated to the metal (a). Iridium in the **Ir1** with their oxidation state of +3 [Ir(III)] in C_3 symmetry, has complete t_{2g} orbitals ($5d^6$) in the low spin configuration. DFT calculations of Hay[157] revealed that the HOMO in **Ir1** is principally composed of π orbitals of the phenyl anion ring and the metal d-orbitals albeit without taking spin-orbit coupling consideration into account. The pyridine is formally neutral and is the major contributor to the LUMO in the **Ir1** complex [157,158]. Hay calculated the HOMO-LUMO gap to be ~3.5 eV. Later in 2006, Nozaki using TDDFT introduced an orbital diagram for a model system of metal (M) bipyridine $M(bpy)_3$ with a higher symmetry of C_{2v} (the actual symmetry of **Ir1** is C_3) to explain the **Ir1** considering SOC. Figure 3-11 (left-bottom) shows the structure of the model system Nozaki used. In C_{2v} symmetry three dπ -orbitals are d_{y2-z2} (a_1), d_{xy} (a_2), and d_{xz} (b_1), and two dσ-orbitals are d_{x2} (a_1) and d_{yz} (b_2). The d_{xy} (a_2) in anti-bonding interaction with HOMO of bpy (with a_2 symmetry) is destabilized, while the d_{xz} (b_1) orbital in bonding interaction with the LUMO of bpy (b_1) is stabilized (so-called π-back donation as shown in Figure 3-11).

None of the π orbitals of bpy can interact with dy^2-z^2 (a_1) due to symmetric mismatch. Consequently, the lowest singlet excited state of this system is a metal to ligand charge transfer ^{1}MLCT: $a_2^* \rightarrow b_1^*$, which manifest itself as the peak at ~410 nm in the UV-Vis spectrum (see next section 3.3.2). The higher singlet excited state is $b_1 \rightarrow b_1^*$, whereas, $a_2^* \rightarrow b_1^*$ is predicted to be the lowest ^{3}MLCT state.

Studies of the temperature and magnetic field dependence of the emission of **Ir1**[159,160] showed that the emission is determined by the lowest triplet state ^{3}MLCT split into three sub-states, named I, II and III, with increasing energy[157] due to the zero-field splitting (ZFS) effect (§3.1.1).

The energy separation between the three sub-states is ΔE_{I-II} = 19 cm^{-1} and ΔE_{II-III} = 151 cm^{-1} for **Ir1** in $CHCl_3$,[160] and ΔE_{I-II} = 13.5 cm^{-1} and ΔE_{II-III} = 70 cm^{-1} for **Ir1** in THF.[159] These states have different SO mixing with singlet states, yielding very different pure radiative lifetimes, which are τ_{III} = 0.2 μs, τ_{II} = 6.4 μs and τ_{I} = 116 μs in $CHCl_3$, and τ_{III} = 0.75 μs, τ_{II} = 11 μs and τ_{I} = 145 μs in THF. Splitting smaller than kT = 200 cm^{-1} among these states tells us that the three sub-states are equally populated at RT and cannot be distinguished. Hence, given the stronger singlet character of the sub-state III, the fast emission from this sub-state is dominant and it would be the most likely to be observed in a luminescence experiment. HT coupling is assigned to the transition from sub-state I (I→0) which is claimed to be dominant below 10 K[159] At higher temperature, thermally populated higher lying states II and III give rise to the emission (II–III→0) through FC mechanisms.

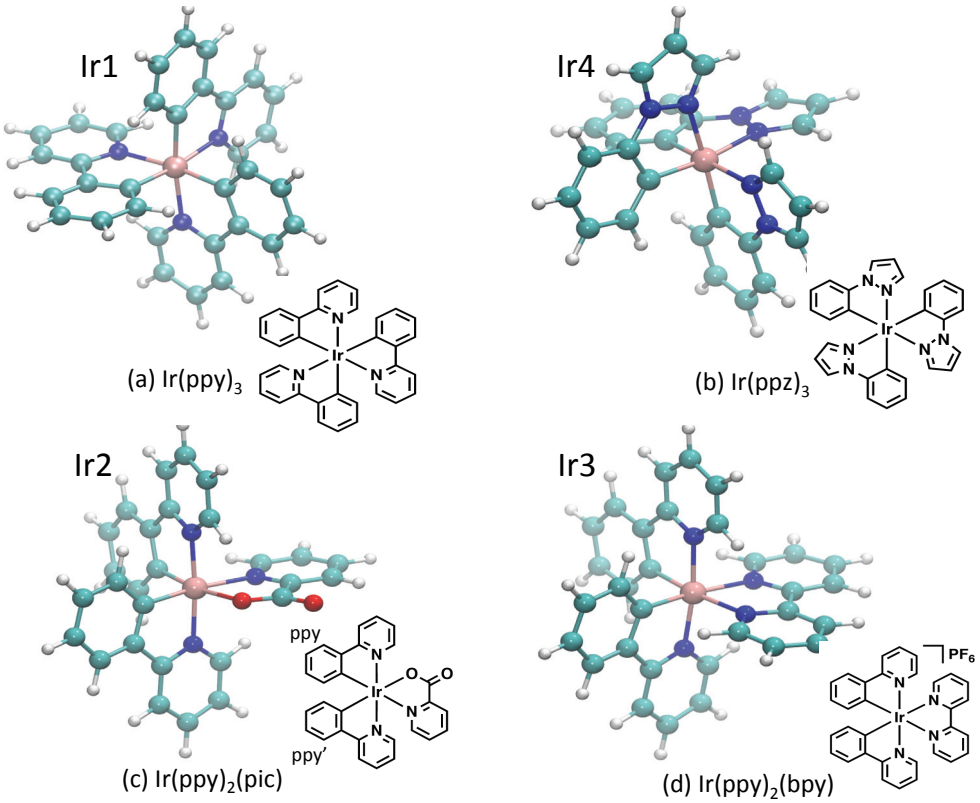

Figure 3-10 Schematic 3D and 2D representation of the four cyclometalated iridium complexes and their abbreviated names studied herein. Note that for the case of **Ir2**, calculations distinguishes the two ppy ligands according to the distortion of Ir-C and Ir-N bond length

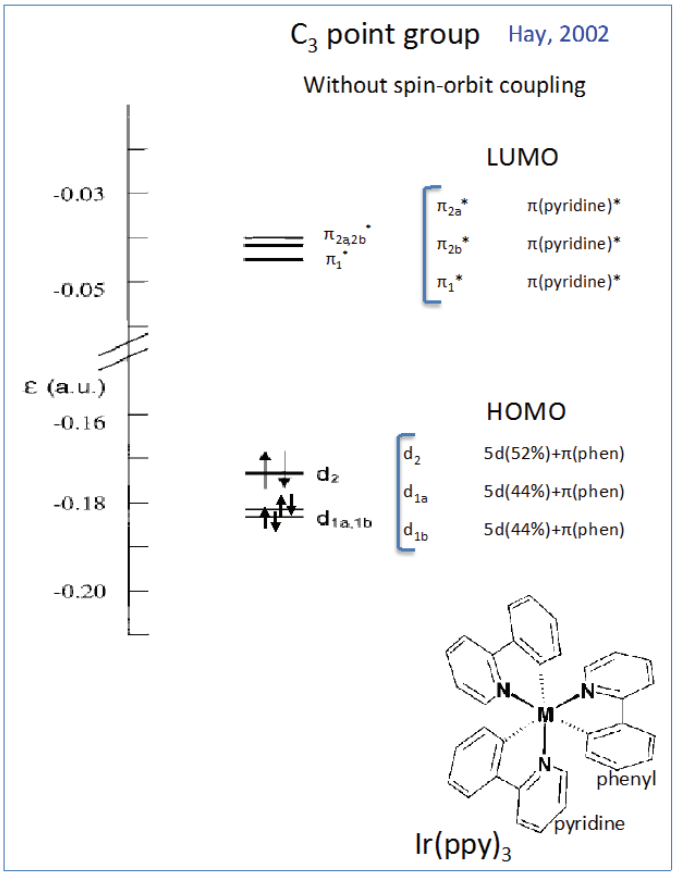

Figure 3-11: Electronic structure of the $Ir(ppy)_3$ complex for the ground state orbital energy. The orbital diagram calculated by Hay et al[157] without taking the spin-orbit coupling into account.

3.3.1.2 Ir (ppy) $_2$(bpy)

It is known that the substituents on the main ligands (e.g. pyridine) affect primarily the HOMO of the complex without significant impact on the LUMO[80]. In **Ir3**, the LUMO is largely localized on the N^N ancillary ligand as a result of the direct link between the two N-heterocyclic rings, which results in a lower LUMO relative to **Ir1** [161]. This smaller HOMO-LUMO band-gap is illustrated by a red shift of the maximum in the emission spectrum of **Ir3** (Figure 3-15). It is known that the symmetry of **Ir3** is restricted to C_2.[162] The HOMO is calculated (Figure 3-12) to be composed of a mixture of Ir dπ orbitals (t_{2g}) and phenyl π orbitals distributed equally among the two ppy ligands. For **Ir3** the LUMO is located on the bpy ligand.[163]

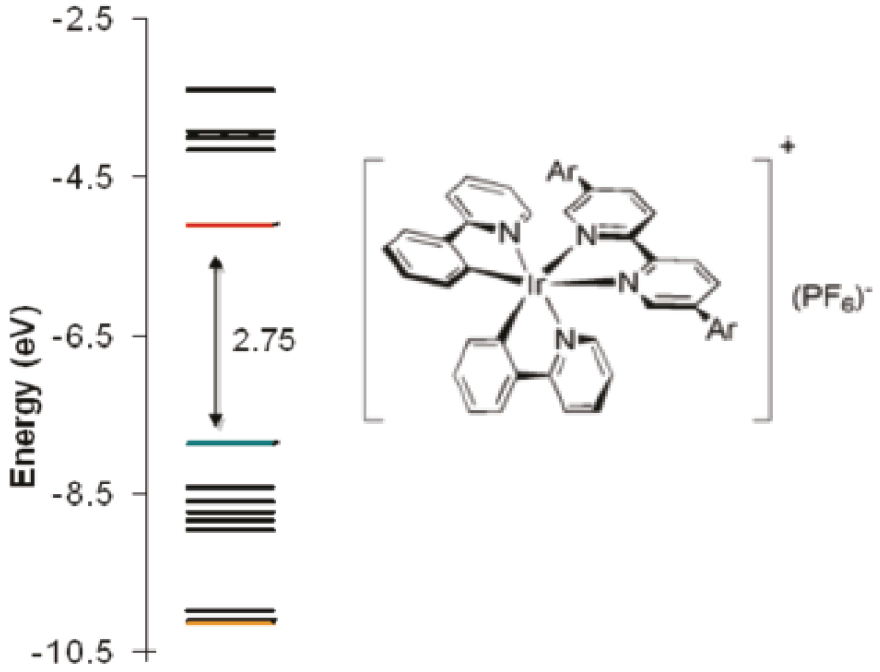

Figure 3-12: Calculated electronic structures for **Ir3** by DFT methods at their S_0-optimized geometries. Black indicates that the electron density is mostly localized on π(bpy) and π(ppy) with contributions from d(Ir). Orange and turquoise indicate the most energetic π(bpy) and π(ppy), respectively. In each of these cases, minor d(Ir) contributions may exist. Red indicates the LUMO, which is localized on π*(bpy)[53].

3.3.1.3 Ir(ppy)$_2$(pic)

In the case of the neutral bis-cyclometalated complex **Ir2**, with picolinate (pic) ligand, the HOMO is delocalized on the phenyl π orbitals of both ppy ligands[164] (). Minaev *et. al* showed that the HOMO has a large contribution (46%) from the 5dσ atomic orbital of the Ir ion and a minor one (8%) from the lone pair orbital of oxygen (Table 3-1). They also showed that in **Ir2**, they distinguish the two ppy ligands according to the distortion of Ir-C and Ir-N bond length. The ppy ligand that lies opposite to the Ir-O bond, called ppy' in **Error! Reference source not found.**, has shorter Ir-C and Ir-N bond. The LUMO is localized mostly on the ppy' ligand and has a strong bonding character for the phenylpyridine link. Thus the vertical HOMO→LUMO excitation includes besides the MLCT character also a large dose of interligand $\pi_{ppy} \rightarrow \pi_{ppy'}$ excitation.

Table 3-1: Molecular Orbital Energy Levels (a.u.) and Excited-State Transition Energy (eV) of the Ir(ppy)3 and Ir(ppy)2(pic) Complexes at the Ground S0 State Optimized Geometry. Main contributions are given in parentheses. Reported extinction coefficients are from[164]

Molecular orbitals	**Ir1**	**Ir2**
LUMO + 2	-0.050(ppy)	0.060(ppy)
LUMO+1	-0.050(ppy)	-0.064(ppy')
LUMO	-0.054(ppy)	-0.072(pic)
HOMO	-0.182(ppy + dσ)	-0.191(ppy2 + dσ)
HOMO-1	-0.182(ppy + dπ)	-0.211(dπ + π*OO)
HOMO-2	-0.182(ppy + dπ)	-0.224(dπ + pic*)
$E(T_1)$	2.532	2.459
$E(S_1)$	2.715(0.005)	2.516(0.003)
$E(S_2)$	2.768(0.002)	2.687(0.025)
$E(S_3)$	2.871(0.002)	2.821(0.009)
$E(S_4)$	2.963(0.024)	3.03(0.006)

3.3.1.4 $Ir(ppz)_3$

Thompson *et. al* showed that replacing the pyridyl ring with an N-pyrazolyl group significantly increases the emission energy of the complex by enhancing the LUMO energy [58, 51]. Hence, in **Ir4** the LUMO - predominantly phenyl in character - is delocalized among the three ligands (Figure 3-13) and affects the energies of the metal orbitals through π-backbonding. However, the pyridyl and pyrazolyl ligands do not contribute markedly to the HOMO in the tris cyclometalated forms. The

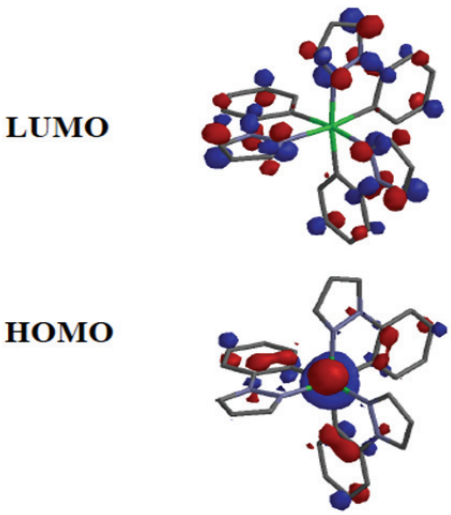

Figure 3-13: The HOMO pictures for both isomers consist of a mixture of phenyl and Ir orbitals for **Ir4**. The picture is adapted from ref. [58]

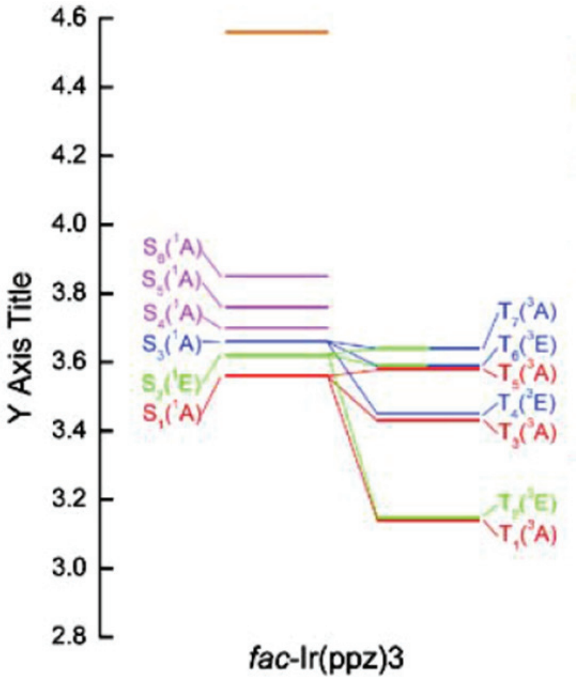

Figure 3-14: Schematic energy levels of excited states calculated by [165]

HOMO in **Ir4** is distributed equally among the three ppz ligands due to the C_3 symmetry of the complex and it is dominated by Ir-d orbital and minor contribution from the phenyl π orbitals, similar to related complexes.[58] It is important to realize that, comparing the energy of frontier orbitals calculated for **Ir1**[157] and Ir4[165] and lower-lying singlet and triplet states shows that the S_1 state (S, T denotes singlet and triplet excited states, and the index shows the energy order of the state) for **Ir1** lies ~ 0.1 eV below the T_3 and only two triplet state have been calculated to be lower than S_1. However, in the case of Ir4 Kim *et. al* calculated 4 triplet states below the lowest singlet state. In other words, in Ir4, a higher number of triplet states per energy interval are available for the internal conversion within the ^{3}MLCT manifold once the complex undergoes ISC from the ^{1}MLCT state (§5.2.4).

3.3.2 Steady State Spectrum of Cyclometalated Iridium Complexes

Steady-state absorption and emission measurements were carried out with a Shimadzu UV-3600 spectro-photometer and a Shimadzu RF-5301PC spectro-fluorimeter, respectively. The steady-state absorption and emission spectra of **Ir1-4** in $CHCl_3$ and/or DMSO (~ 1 mM) are shown in Figure 3-15. Below 320 nm an intense absorption band is observed in all compounds and can be attributed

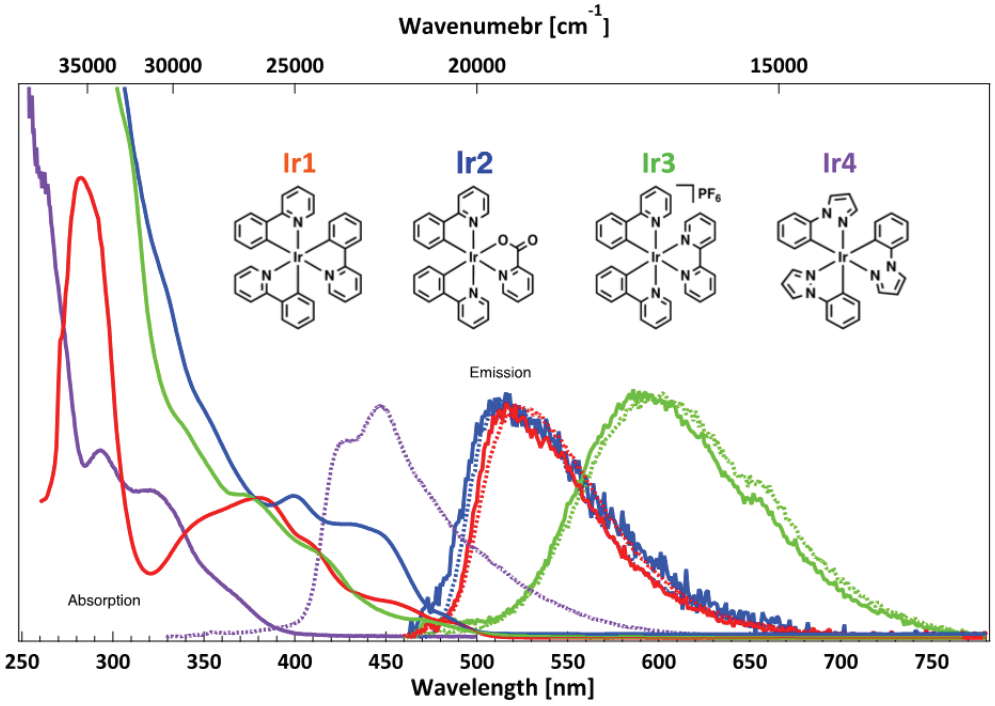

Figure 3-15: Absorption and emission spectra of **Ir1** (red), **Ir2** (blue), **Ir3** (green) in $CHCl_3$ (solid lines) and DMSO (dashed lines) and of **Ir4** (purple) in DMSO. Absorption spectra are normalized to the maximum of ^{1}MLCT band (see Table 3-2)

to the dipole-allowed $^1(\pi\rightarrow\pi^*)$ LC transitions. The overall absorption spectrum of Ir4 is blue shifted with respect to the other compounds. Absorption features at longer wavelengths have been generally assigned to $d\rightarrow\pi^*$ MLCT transitions of an electron from a d-orbital of the Ir ion to an anti-bonding π^* ligand orbital.[50] For complexes **Ir1-3**, ^{1}MLCT transitions lie around 350-430 nm, while ^{3}MLCT transitions are above 430 nm. There is a high degree of spin mixing for **Ir1-4** as reflected in the intensity ratio between the ^{3}MLCT and ^{1}MLCT absorption bands, which is larger than in $[Ru(bpy)_3]^{2+}$ and $[Fe(bpy)_3]^{2+}$ complexes, due to stronger spin-orbit coupling in Ir compared to Fe and Ru (first and second row transition metals, respectively. The degree of spin mixing varies quite significantly with ligand substitution; in a way that **Ir1** has the highest ratio of triplet to singlet intensity.

Main peaks of the UV-Vis absorption spectra of **Ir1-4** are listed in Table 3-2. The maximum of the ^{1}MLCT absorption band for **Ir1** is at 380 nm, and the ^{3}MLCT band peaks at 455 nm.[157,159,160] In particular, **Ir1** shows a well-defined ^{1}MLCT absorption band peaking around 380 nm, while ^{3}MLCT transitions are between 430 and 500 nm with a maximum around 455 nm.[157,159,160] Depending on the spacing between peaks of MLCT region (5 lowest energy peaks in Table 3-2), the lowest two

peaks (485 nm, 455 nm) with ~1350 cm^{-1} space can be vibrational progression within the ^{3}MLCT transition (indeed, Raman spectra of **Ir1** show a ligand vibration at ~1300 cm^{-1}).[166] The next bands (with ~2350 cm^{-1}) are most probably due to different electronic states or [157] [167].

Table 3-2: Photophysical properties (Experimental data) of **Ir1-4** measured in DMSO. Bold numbers are peak maxima. The stokes shift is with respect to the lowest triplet MLCT absorption.

	Absorption (nm)				Emission (nm)	Stokes-shift[§] (cm^{-1})
	^{1}LC	^{1}MLCT	[^{3}LC] / ^{3}MLCT			
Ir1	320	345, **375**, 410	**455**, 485	Exp.	520	2100
Ir2	262 264	330*, 360, 400 330, 350, 398	455, 485 440*, 484*	Exp.	506*, 514	2100
Ir3	256[§], 270[§]	300[§], 340, 375	420, 475**	Exp.	595	4380
	378 (ppy), 404(bpy)	409(ppy), 438(bpy)	[384,426] 456(bpy),461(ppy)	Calc.[162]		
Ir4	290	320	340	Exp.	445	
	244, 261, 292	321	366	Calc.[156]		

* In CH_2Cl_2 at room temperature, ref [168]
§ Ref [53]
** This peak is missing in ref [53]
§ Relative to the lowest triplet absorption

For the heteroleptic **Ir2** and **Ir3** the separation between singlet and triplet absorption is less clear-cut than for **Ir1**. In the former case, **Ir2**, the lowest absorption state is reported to be at 485 nm [168] corresponding to the predominantly triplet character[168] given its mirror image with the phosphorescence band. The prominent shoulder around 450 nm is probably the highly spin mixed ^{1}MLCT/^{3}MLCT peak, while peaks at shorter wavelength 400 nm and 360 nm are dominated by singlet character MLCT. In the case of **Ir3**, there are several broad features around 475 nm, 420 nm, 375 nm and 340 nm, again with the first being most probably due to the predominantly triplet state. The absorption features around 375 nm (and 404 nm, Table S1) have been attributed to a singlet inter-ligand transition (^{1}LLCT) of a π-electron in the ppy ligand to the bpy π^*-orbital.[162] ^{1}MLCT and ^{3}MLCT transitions are around 420 nm and 475 nm, respectively, and they include charge transfers to both ppy and to bpy ligands (Table 3-2). They are partially masked by more intense ^{1}ILCT transitions.[53,162] Finally, **Ir4** shows distinctly higher energy absorption bands than **Ir1-2-3**, mainly because the π^* orbitals of ppz are higher in energy than those of ppy.[58] Thus, ^{1}MLCT transitions correspond to the bands at 290 nm and 320 nm and the tail starting from 340 nm corresponds to the ^{3}MLCT absorption band.[51,58,169]

The steady state phosphorescence emissions of **Ir1** and **Ir2** consist of a similar broad and red-degraded* asymmetric band, with a maximum around 520 nm, that is not significantly solvent-dependent. The emission of **Ir2** is slightly broader than that of **Ir1**. Since the steady-state emission of **Ir1** is well established as being of ^{3}MLCT character,[159,160] this implies that the emission of **Ir2** also stems from a ^{3}MLCT state localized on the ppy ligands only. The phosphorescence of **Ir3** peaks more in the red (around 600 nm), is markedly broader and is also solvent-independent. However, Wu et al. reported a notable temperature-dependence: indeed, in ethanol at 77K, the phosphorescence of **Ir3** resembles that of **Ir1** and **Ir2**.[162] This behaviour can be related to the dual emission reported for heteroleptic Ir complexes containing ppy and bzq (=benzo[h]quinoline), as main cyclometalated ligands, and bpy and phen (=1,10-phenanthroline) as ancillary ligands, in which it appears that the band centred around 520 nm has ppy character, while the band centred around 600 nm has bpy (or phen) character.[54,55,170,171] Thus, in our case, the RT static emission of **Ir3** stems from a ^{3}MLCT state localized on the bpy ligand, whereas that of **Ir2** stems from a ^{3}MLCT state localized on ppy ligands. Finally, the ppz ligand confers **Ir4** the ability to emit a blue-shifted phosphorescence, compared to the other ppy-based complexes, with a maximum at 445 nm, a contour that suggests a vibronic progression with spacing of approximately 1170 cm^{-1} (corresponding to a known mode of the phenyl ring breathing at > 1000 cm^{-1} and Pyrazole ring breathing mode at > 1300 cm^{-1}). [172]

* It means with a long red tail.

Chapter 4 Picosecond Time-Resolved XAS Studies on Metalloproteins

This chapter presents the X-ray absorption studies of two metalloproteins namely Nitrosyl Myoglobin (MbNO) and aquoamet Myoglobin (MetMb) under physiological conditions (a solution of pH 7.0at room temperature and pressure), as introduced in chapter 2. Using the high-repetition rate picosecond laser pump/ X-ray probe set up (see §2.2.2), the photolysis of MbNO and subsequent ligand dynamics are discussed in the section 4.3. In the important case of MbNO the controversial reported time scales of ligand detachment/recombination determined via various spectroscopic technique, demands targeting Fe atom as the active site of the protein in physiological conditions for further investigations with ultrafast X-ray spectroscopic techniques. Here, on the ground of preliminary results of pump-probe measurement in our group[78], I present high quality pump-probe X-ray absorption signal measured at different time delays under physiological conditions. The detailed experimental results of the pump-probe measurement and analysis of the transient signal are presented in section 4.3.1 and 4.3.2, respectively. Based on the identified ground- state structure of MbNO under physiological conditions[78], results are interpreted in section 4.3.4.

Another aspect that will be discussed in this chapter, is the occurrence of electron transfer in MetMb upon photoexcitation of the Tryptophan (Trp) residue in the Mb. Recent optical studies of ferric myoglobin identified electron transfer (ET) as dominant mechanism in fluorescence quenching of one of the two Tryptophan (Trp) in the myoglobin[173]. Section 4.4 is devoted to the

investigation of Trp-mediated heme reduction in the ferric MetMb. Using a similar pump-probe setup (chapter 3), combining XAS with excitation in the ultraviolet regime, we aimed at observing the reduction of the Fe ions through a K-edge X-ray absorption spectrum shift toward lower energies. The result of the measurement is discussed in section 4.4.1.

4.1 A Review on the spectroscopic studies on ligand dynamics in MbNO

Diatomic molecules, such as CO, NO, and O_2 are the receptors that bind to and activate heme proteins. Among them, NO has been highlighted as a key biological messenger[7] whose level controls various physiological responses such as NO-synthases, message transduction (by soluble guanylyl cyclases),[8,9] NO transport and oxidation (by hemoglobin, myoglobin, nitrophorin)[10-12] and regulation of the NO/O_2 balance (by neuroglobin).[13,14] In all these cases, the heme group that binds the NO ligand is chemically identical and therefore variations in the reactivity and function are thought to be closely related to the spin, electronic configuration and geometric structure upon binding[15] and/or are suggestive of different steric and electronic interactions of the bound NO with neighbouring protein residues.[16] Consequently, there is great interest in understanding the nature of NO binding to heme proteins and its biochemical role.

The binding kinetics of NO in myoglobin has been studied by a variety of time-resolved spectroscopic techniques. Ligand dissociation from the heme iron was triggered by excitation into either the Soret or the Q-bands, while the ensuing dynamics were probed using transient absorption (TA) in the UV-Visible,[17-26] the near infrared (IR),[27-29] the mid-IR[16,29,30] or by resonance Raman spectroscopy.[26]

For UV-Vis and near-IR TA spectroscopy, the signals are dominated by the π-orbitals of the porphyrin, while mid-IR TA of the NO stretch mode is sensitive to the orientation of the NO dipole. Resonance Raman spectroscopy maps several vibrational modes of the porphyrin, but most studies have focused on the important Fe-Nε (on the Proximal Histidine) stretch vibration at 220 cm^{-1},[26,31,32,34,35,174] which is sensitive to the out-of-plane position of the iron with respect to the heme plane and to the strain the protein exerts on the heme through movements of the helices.[35]

All of these studies report multi-exponential recombination kinetics with time constants spanning from sub-ps to several hundreds of ps or even longer. Table 4-1 presents a compilation of these time constants, which vary somewhat with the spectroscopic observable. The shortest times (1-2 ps) have been attributed to vibrational relaxation, while the longer ones have been

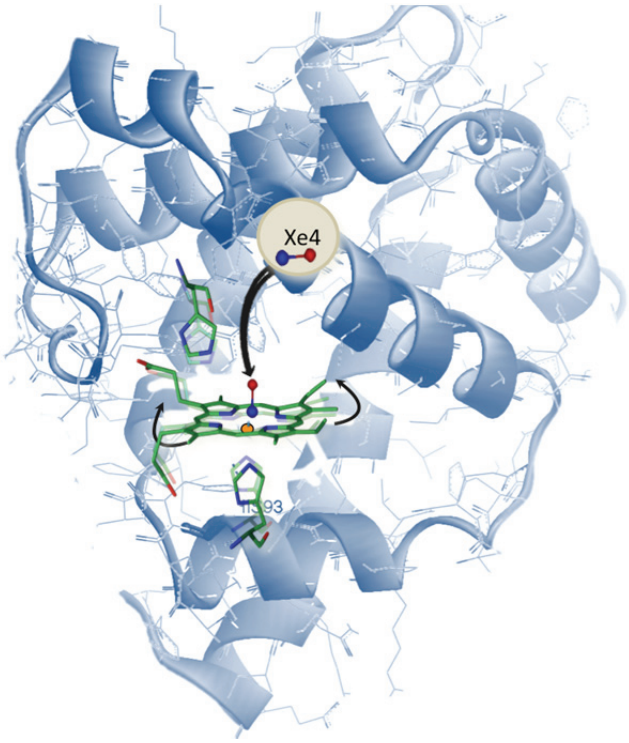

Figure 4-1: Schematic of active center in heme at the center of Myoglobin. The Xe4 site at the vicinity of the heme is also shown as docking site for the detached NO molecule.

attributed to geminate recombination (GR), with two main groups: 10-40 ps and 130-300 ps.[16,18,19,22-24,26,27,30] Based on temperature-dependent UV-Vis TA studies, Champion and co-workers argued that the transition state associated with the fast recombination kinetics (8-15 ps) has no barrier and is due to rebinding of NO from the centre of the distal pocket, very close to the iron.[23] A barrier-less recombination is thought to occur because the unpaired NO electron forms a transition state with the antibonding d_z^2-orbitals without structural distortions of the protein matrix.[23] The slow component in their work (170-200 ps) was assigned to recombination of NO from the more distant Xe4 pocket.[145] The rebinding occurs on a similar timescale as the structural fluctuations of the protein architecture[19,29,35] and therefore relaxation of the active site following dissociation gives rise to a small time-dependent barrier (~3 $kJmol^{-1}$ [23]). From their mid-IR TA studies, Lim et al[29,30] concluded in line with this that the slow recombination component (133 ps in their case) is due to the protein environment surrounding the distal side of the heme, and conformational relaxation of the protein after photolysis may raise the barrier to NO rebinding. In both cases (long and short component), it was hypothesized that NO binds to an out-of-plane iron (domed porphyrin), in agreement with theoretical calculations.[175-177]

More recent studies combining UV-visible, near-IR (in the region of band III-located in the near-IR at ~ 760 nm) TA and resonance Raman measurements,[26,27,31] showed that while the UV-visible TA results in the Soret and Q-band regions agree with those of refs [22,24], the resonance Raman results and the TA studies of Band III reveal an additional ~30 ps component (also reported in one of the mid-IR studies[16]). Yoo *et. al* also concluded[27] that GR leads to the formation of a transient 6-coordinated domed heme, with a rise-time corresponding to that of the τ_2 component in Table 4-1 and a decay of 30±10 ps, corresponding to the return to the planar form. Thus, the transition from domed to planar is not a prompt one (contrary to the reverse process[178]) and they attributed its time scale to the constraints that the protein exerts on the porphyrin. Indeed, from ps UV resonance Raman studies of MbCO, Mizutani and co-workers[35] found that upon photodissociation of CO, the signal of the Tryptophan situated on the A helix showed a prompt decrease of the amplitude, which recovers in ~50 ps and was attributed to changes in the protein tertiary structure that exerts strain on the heme-protein link. Negrerie et al[26] studied other heme proteins and found that the time scale of the primary domed-to-planar heme transition was ~15 ps for hemoglobin, ~7 ps for dehaloperoxidase (DHP) and ~6 ps for Cytochrome c (Cytc). They also attributed this timescale to the constraints exerted by the protein structure on the heme cofactor. They noted, however, that DHP and Cytc have similar time constants despite their different structure and heme linking, revealing that several factors, not only the protein strain, can influence the heme response kinetics. Similar time constants were reported using IR TA by Lim et al[28] for Cytc and for a model heme, microperoxidase-8 (Mp), but they attributed the faster ligand rebinding in Cytc compared to Mb to the fact that the former does not have a primary docking site (PDS)-like structure that slows down NO rebinding.

On the theory side, Franzen[175] calculated potential energy surfaces for the different spin states of a compound consisting of an imidazole (Im) ligand bound to iron-porphine (FeP) trans to the diatomic NO ligand (Im–FeP–NO): the electronic ground state (S=1/2) and the excited quartet (S=3/2) and sextet (S=5/2) states. For the planar geometry they found that the doublet is the most stable configuration, as expected in the ground state. The quartet is somewhat less binding while the sextet state is even less binding with a Fe-NO equilibrium distance above 2 Å. Franzen attributed the ~10 ps component to the S=5/2→S=3/2 relaxation and the >100 ps time scale to a

Table 4-1: Compilation of the time scales of NO recombination to the heme determined using various pump and probe schemes upon excitation of MbNO.

Probe	Excitation wavelength	τ_1(ps)	τ_2(ps)	τ_3(ps)	τ_4(ps)	Ref
UV-Vis TA[1]	574 nm		27.6 (52%)	279.3 (48%)		[18]
UV-Vis TA[1]	Times change with mutation	3-5	18.9 (41%)	126.4 (49%)	∞ (10%)	[17]
UV-Vis TA[2]	570 nm		9.1 (40%)	200 (50%)	∞ (10%)	[20]
UV-Vis TA[1]	564 nm	2-4	13 (40%)	148 (50%)	∞ (10%)	[26]
Res.Raman [2]	560-570 nm		30±10			[27]
Near-IR TA [3]	560-570 nm	2-4	27.5±5(42%)	293±30(33%)	∞ (25%)	[27]
Visible TA[3]	564 nm	2-4	12±3(40%)	205±30(37%)	∞ (23%)	[27]
Mid-IR TA	-	1,4 (35%)	42 (29%)	238 (36%)		[16]
Mid-IR TA	580 nm	5.3 (54%)		133 (46%)		[30]
UV-Vis TA[4]	400 nm	1.8 (42%)	13.8 (24%)	200 (34%)	∞ (<5%)	[22]
UV-Vis TA[4]	580 nm	1.1 (50%)	8 (30%)	170 (20%)		[22]
UV-Vis TA	400 nm		13.8 (41%)	200 (59%)		[23]
UV-Vis TA	580 nm		8 (60%)	170 (40%)		[23]
XAS	532 nm			192±44(75%)	1330(25%)	This work

1. Single wavelength detection at 480 nm (Soret band)
2. Single wavelength detection at 435 nm (Soret band)
3. Single wavelength detection at 615 nm (Q-bands)
4. White light continuum detection

sequential relaxation S=5/2→S=3/2→S=1/2 process. More refined calculations by Strickland and Harvey[176] found that the quartet state is the most likely state to be populated upon recombination. Contrary to refs [22,23,29,30], these calculations exclusively invoke intramolecular electronic relaxation, neglect the role of the environment and do not include the strain on the porphyrin.

Because the measured time constants somewhat vary with the observable (Table 4-1) and since the iron atom is the active site of the reaction, one would ideally like to probe it specifically. Time-

resolved X-ray techniques seem most appropriate since they can visualise the structure of the environment around the Fe atom. X-ray protein crystallography has been implemented on carboxy-myoglobin (MbCO) showing docking of the CO ligand at the Xe1 and Xe4 positions (Figure 3-3)[36-38]. However, solid samples are far from the physiological conditions under which proteins operate and it is desirable to investigate the ligand dynamics of heme proteins in physiological solutions, which can be flowed continuously to ensure the renewal of the sample and decrease the X-ray dose on it. Adapting such an approach, X-ray scattering studies of MbCO in solution with 100 ps resolution were recently reported,[40,41,179,180] but the spatial resolution is such that only tertiary structural changes can be probed. In addition, this approach does not deliver information about the electronic structure of the active site, which plays a central role in the biochemistry and reactivity of heme proteins[43,181]. The valence 3d electrons of the iron atom are significantly delocalised over the porphyrin ligand $\pi*$ orbitals and the ability of the heme to redistribute charge and spin density plays an important role in the formation and stabilisation of a variety of intermediates important for biological function.[43-45]

Time-resolved X-ray absorption spectroscopy (XAS)[46] offers the advantage of interrogating the electronic and geometric structure of the biochemically active centre of the system with atomic selectivity, i.e. the Fe atom. It was used to investigate the recombination of CO to myoglobin following its photo-dissociation from MbCO.[47,182,183] In this case, ligand recombination occurs in times up to milliseconds[184] and the transient XAS were recorded using alternating intervals of data acquisition for the laser-excited sample at 100 ps time delay and the unexcited sample, contrary to the pulse-to-pulse data acquisition where the unexcited and excited XAS are recorded in alternation.[49] The resulting transient reflects the formation of the DeoxyMb species,[47] indicating the absence of GR of CO at this time delay.

To investigate photo-induced processes in highly dilute media, such as proteins in physiological solutions, whose concentrations (1-4 mM) are one to two orders of magnitude lower than those of the metal complexes we investigated[49], a high-repetition rate ps XAS setup was originally developed.[47] Here, I demonstrate its implementation to address the nature of the recombination of NO to the heme Fe atom with 70 ps resolution. MbNO is excited at 532 nm into the Q band and the system is probed at the Fe K-edge near 7.12 keV. Our results show that upon dissociation of NO, the transient XAS spectrum deviates from the difference spectrum of the static DeoxyMb and MbNO spectra (expected in case of full dissociation of NO and full relaxation). This

deviation remains over hundreds of ps (transient XAS at 300 ps), pointing to a species that is intermediate between MbNO and Deoxy, but closer to the latter in terms of electronic and geometric structure. Our results are rationalized by the fact that the rate determining step to ligand rebinding is the diffusion of NO in the protein, presumably from the Xe4 pocket (~200 ps), as suggested in refs [22,23], forming the domed hexacoordinated species, which relaxes to the planar configuration in ~30 ps.[26,27] The experimental set-ups and sample preparation were described in chapter 3.

4.2 Ground state spectrum of MbNO and DeoxyMb

The electronic and geometric structures of MbNO and deoxyMb in physiological solutions have been studied by means of X-ray absorption spectroscopy at Fe K-edge[78]. The bond length, angles and dihedrals were extracted by the analysis of the spectral resonances occurring above the ionization potential in both the X-ray absorption near edge structure (XANES) and the extended X-ray absorption fine structure (EXAFS) regions. However, the electronic structure is obtained via the pre-edge region of the spectrum. Hence, the pre-edge region is in the focus of this thesis and the transient XAS signal of MbNO is interpreted based on the transient XAS.

From the simplified molecular orbitals of two model systems of ferrous nitrosyl heme (Fe(NO)TPP[1], and Fe(NO)PP(Im))[144] given in § 3.2.1.3, I choose the model system of Fe(NO)TPP since, although being simple, it includes the critical molecular orbitals of the system. It is known that imidazole acts primarily as a sigma donor ligand, with essentially no backbonding ability[144]. Hence, adding imidazole to the system only reduces the HOMO-LUMO gap via destabilization of the dz^2 orbital (HOMO), while the other 3d orbitals remain unperturbed. So, to a good approximation Fe(NO)TPP with HOMO (σ_{NO}+$1a_{1g}(dz^2)$) and LUMO (π^*_{NO}+ $e_g(\pi^*_{PP})$) orbitals can be considered as a model system for ferrous nitrosyl heme. Figure 4-2 compares the schematic molecular orbital of Fe(NO)TPP (model system for MbNO) with the model system[2] of Fe(PP)Im for high-spin ferrous deoxyMb. Based on these schemes I can introduce main features of the normalised static Fe K edge spectra of deoxyMb and MbNO in Figure 4-3[43,78]. Key features labelled as (A) in the pre-edge, (B, C, and D) in the XANES range and (E) for the EXAFS part.

Generally speaking, pre-edge features in the XAS of Myoglobin previously have been assigned to be predominantly 1s → 3d (bound-bound) transitions. Pre-edge features in the XAS of Myoglobin with/without different diatomic axial ligands (CO, NO, O_2, CN/metMb, deoxyMb) are

predominantly 1s → dσ and 1s → dπ-π*$_{ligand}$ transitions (for MetMb the ligand refers to porphyrin), while 1s→ dπ transitions also weakly contribute for MbO_2, metMb and deoxyMb.

In general, 1s → 3d bond-bond transitions are dipole forbidden. However, distortion of the symmetry in heme based proteins like Mb make them partially allowed. Previous XAS investigations on Fe complexes have demonstrated the sensitivity of the magnitude of Fe 3d–4p mixing to the Fe–X (where X is the diatomic ligand) bond length.[136] In other words, the shorter the Fe-X bond is (with more deviation from the ideal Oh symmetry), the more the overlap is between 3d orbitals and 4p orbitals of Fe atom. Therefore, despite the dominant Fe d contribution to the valence molecular orbitals in heme[43], the bond-bond transitions draw their intensity from the 1s-4p dipole transition moment. In the presence of a specific ligand field the Fe d orbitals split into dπ and dσ with different degrees of overlap with 4p orbitals of Fe (§3.1.1). Therefore, the 1s → dπ and 1s → dσ

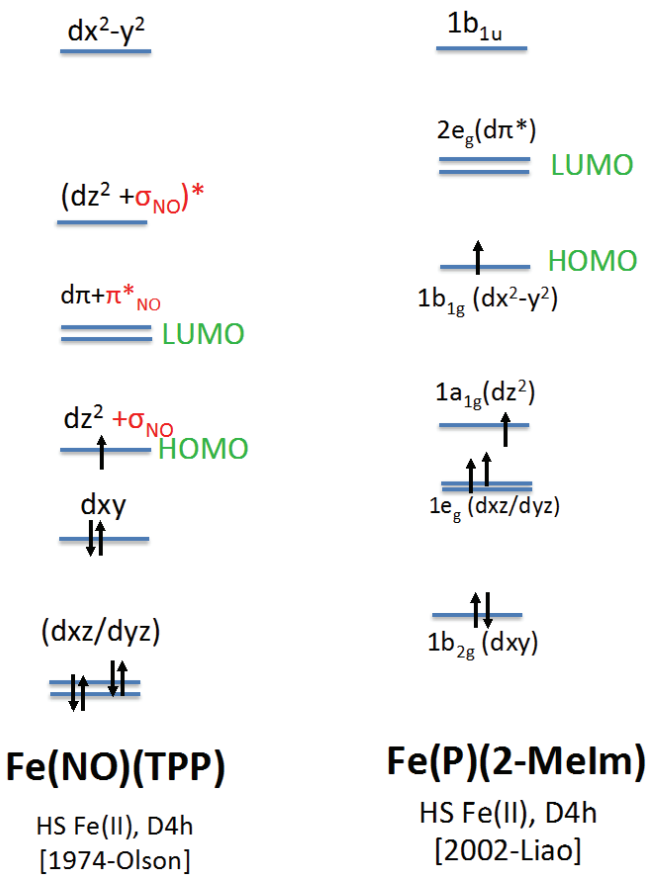

Figure 4-2: Comparing the schematic molecular orbital of Fe(NO)TPP (model system for MbNO) (left) with Fe(PP)Im (model system for high-spin ferrous deoxyMb) (right). Adapted from refs [1] and [2], respectively.

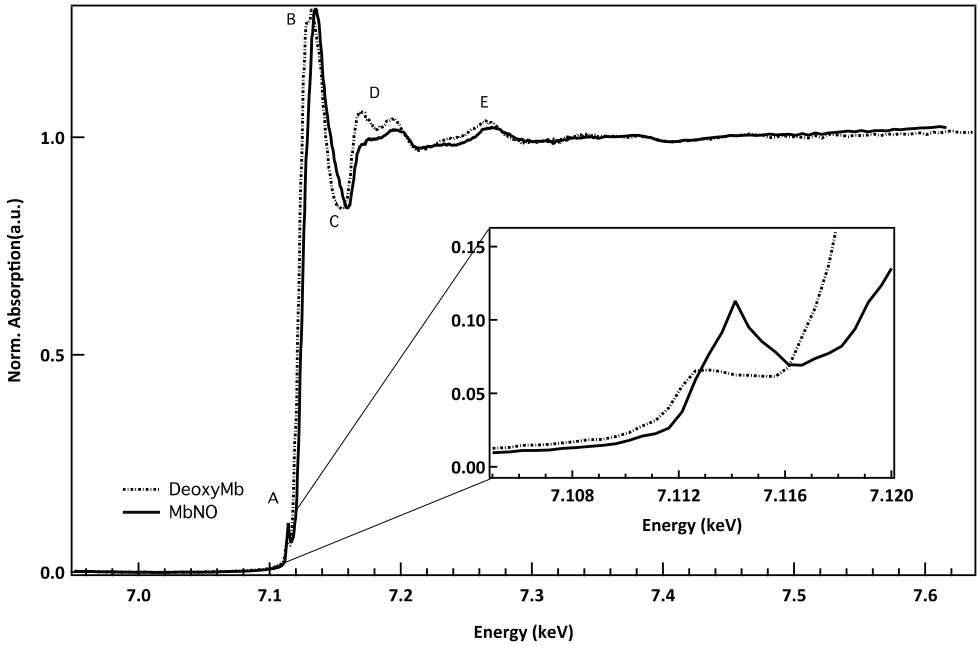

Figure 4-3: The steady-state Fe K-edge absorption spectra of MbNO and deoxyMb. The inset is a zoom into pre-edge region.

transitions will have different quadrupole/dipole characteristics. While the 1s →dσ transitions are very weak and arise from the quadrupole moment, the 1s →dπ transition borrows intensity by significant mixing with 4p orbitals. Along with 1s→3d transition, there is another typical feature at higher energy on the rising edge of the XAS spectra. This feature, characteristic of the K-edge spectra of transition metal complexes, is a dipole-allowed 1s → 4p transition. This feature is only visible experimentally for the complexes with reduced 3d–4p mixing at lower energy (MbO_2 and MbCN) while it is concealed in the XAS of MbNO.[43] Its appearance in the experimental spectrum is a sensitive probe of the edge position, but also the distribution of 4p character throughout the valence space. In summary, there are three typical pre-edge features that we should take into account studying the XAS of myoglobin complexes.

In particular, in the pre-edge region (7108-7122 eV), feature A at 7.114 keV in MbNO (inset Figure 4-3), is dominated by two distinct transitions of 1s → dσ and 1s → 3dπ - π_{NO}* character with small energy separation (weak π-backbonding for Fe–N–O due to singly occupied π_{NO}* orbital (HOMO) in the NO molecule)[43]. However, with the limited energy resolution (1 eV) of the XAS these two peaks cannot be resolved experimentally because they are quite close in energy, therefore the core-hole broadening causes them to be overlapped (Figure 4-4). Finally, the third peak corresponding to the 1s→4p transition is predicted by TD-DFT calculations at 6 eV below the

E_0 (=7.125.3 keV in MbNO) that is concealed by the rising edge in the experimental spectrum (Figure 4-4).

In the case of deoxyMb, the experimental static X-ray absorption spectrum shows one single broad pre-edge peak at 7.111 keV that is shifted by ~3 eV toward lower energies with respect to the MbNO pre-edge (Figure 4-4) which is a typical distinction of high spin and low spin ferrous systems.[185,186] [43]. Likewise feature A in MbNO is attributed to two distinct 1s → dσ and 1s → dπ transitions. However, in the absence of the 6th ligand and for the high-spin configuration of the deoxy, one expects less overlap of 3d/4p orbitals and less dipole moment characteristic. On the other hand, the different symmetry (square pyramidal) in the deoxy form (C4v) with respect to MbNO (D4h), leads to d-p mixing of the dz^2 orbital which results in significant dipole characteristic and intensity gain of the 1s→dσ transition. The overall effect results in a weaker and broader pre-edge peak for deoxyMb (Figure 4-4).

The separation between these peaks has been confirmed by simulations to be ~1.5 eV[43], which is smaller than our present resolution in the XAS. Moreover, because they are quite close in energy, the core-hole broadening causes them to be overlapped. Distinguishing these two features requires separate recording of high-energy resolution fluorescence detection (HERFD) via resonant X-ray emission spectroscopy (RXES) measurement.

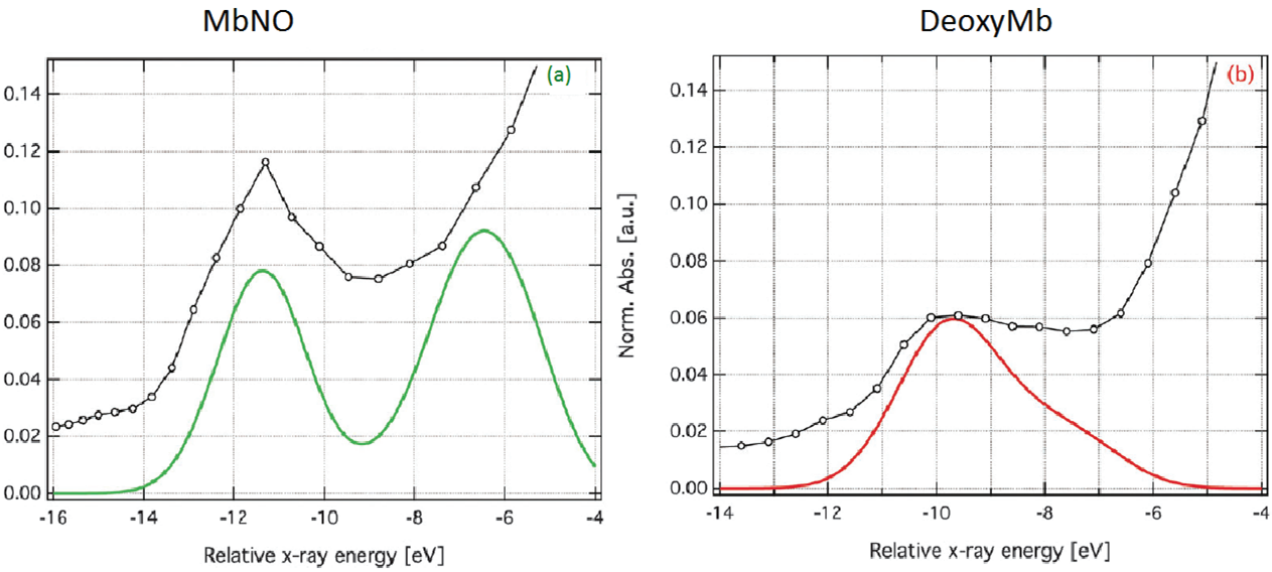

Figure 4-4: The pre-edge spectrum calculated using TD-DFT within the approximation of the BP86 functional for MbNO in green (a) and DeoxyMb in red (b) along with their static XAS spectra (adapted from ref. 19b). The horizontal axis is relative to the ionization energy E_0 (defined as the maximum of the first derivative of the edge region in the XAS spectra, also called edge-jump) for MbNO and DeoxyMb to be 7.1253 keV and 71226 keV respectively.

Before introducing multiple-scattering resonances in XANES region of Figure 4-3, it is interesting to compare the E_0 (corresponding to the ionization potential) in MbNO and deoxyMb both as a ferrous species. It has been shown that using E_0 to determine the oxidation state of the iron is not accurate. This is well evidenced in the inset of Figure 4-3, despite being ferrous, the value of the E_0 in deoxyMb lies about 2.7 eV lower than that of MbNO. This shift is due to the elongation of the Fe-Np distances in the high-spin state of DeoxyMb.[184] To explain this, we have to look at the qualitative bonding schemes proposed for metaloporphyrins that includes strong porphyrin-to-metal sigma donation and a back π donation from the dπ metal orbitals to the ligand π* orbital.[187] In the ferrous species, the porphyrin as a conjugated system becomes a weak π-acceptor with strong delocalization of the iron 3d electrons into the porphyrin and axial ligand π* orbitals[43]. On the other hand, the chemical bonding of the NO to Fe in MbNO modulates the charge transfer from the iron atom into an empty π* orbital of the NO through the mechanism of π-backbonding and σ-donation. Free nitric oxide has the S=1/2 ground state, with the unpaired electron in the π^* orbital. The σ-donation from this σ orbital of NO is only possible into dz^2 orbital of Fe, mainly because of its orientation and geometry, additionally the dxz, dyz; dx^2-y^2 orbitals of Fe are fully occupied, while dz^2 is singly occupied. Besides, the π-backdonation from the occupied dxz and dyz orbitals of iron into the empty π^* orbitals of NO is also present.[188] However, in the absence of the 6th ligand in deoxyMb the π-backbonding to and σ-donation from NO molecule is missing.

In Figure 4-3, label B is the maximum of the X-ray absorption spectrum in the XANES region about 9 eV above the edge (the defined position of E_0). This feature lying already in the continuum has been assigned to a multiple-scattering (MS) resonance[43]. The interplay between the MS process and the local geometrical structure in the XANES is very complex, making a complete analysis of a particular feature with selected structural parameters difficult. Features C, D and E are all due to the specific geometry of the Myoglobin under study. While C and D are very close to each other and can be assigned to MS effects, feature E is already in the EXAFS regime and therefore contains mainly single scattering contribution from the nearest N atom in the first coordination shell.

4.3 Time-resolved XAS of MbNO: Experimental Results

Study of the ligand dynamics of MbNO in physiological conditions (pH=7, low concentration, continuous flow of the sample) using our high repetition rate picosecond laser pump/X-ray probe setup[189], first was included in the Ph.D. thesis of Fred A. Lima.[78] The signal-to-noise ratio obtained in this study lifted uncertainties in the conclusions about the dynamics of the system. The importance of understanding ligand recombination dynamics in MbNO upon physiological conditions led us to conduct further investigations with direct probing of the Fe atom. The set of measurements described below bring in a number of improvements (in particular, the statistics) to ascertain the trend observed in ref. 76 and derive unambiguous conclusions. The results presented here confirm the results of the ref. 76 by improving the signal to noise ratio (S/N), in particular the deviation with the static difference spectrum. It is important to note that this work has a distinct data acquisition strategy compare to ref. 76 (discussed in 4.3.2), yet the similarity of the results obtained are evidence for the accuracy of our UV pump – x-ray probe techniques.

The experiment was carried out using a quartz glass double funnel capillary (Hilgenberg GmbH), with a wall thickness of 10 to 20 µm, a length of 85 $\pm$ 5 mm and an optical path length of 300 µm that was carefully chosen for our 4 mM concentration sample. The sample was circulated and flowed through the nozzle at a rate of ~80 ml/min[*]. An efficient cooling system was used to keep the sample reservoir at standard room temperature to prevent sample degradation. Due to geometry considerations, we did not use an I_0 APD detector, but used a silicon photodiode to monitor I_0 in the transmission signal. Indeed, for the present dilute samples, the latter is a good representation of I_0, as it does not show any recognizable pattern of Fe K-edge absorption. The focused X-ray spot-size was 30µm diameter, which implies a probe volume of 2.12 x 10^{-4} mm^3 considering the 0.3 mm optical path length. The laser fluence was 26 mJ/cm^2 (530 mW at 520 kHz repetition rate) focused into a 70 µm diameter spot. The quartz capillary is totally transparent at 532 nm and the X-ray transmission (through 10 µm thickness) is ~90% near the Fe K-edge. Moreover, in order to avoid sample damage and deposition of sample on the wall of the quartz capillary, the latter was displaced vertically after each scan using a motorized stage. The transient signal at 70ps is the result of ~14h measurements and for 300ps is the result of ~15h.

[*] Cross-sectional area of the flow channel= 0.07 mm^2

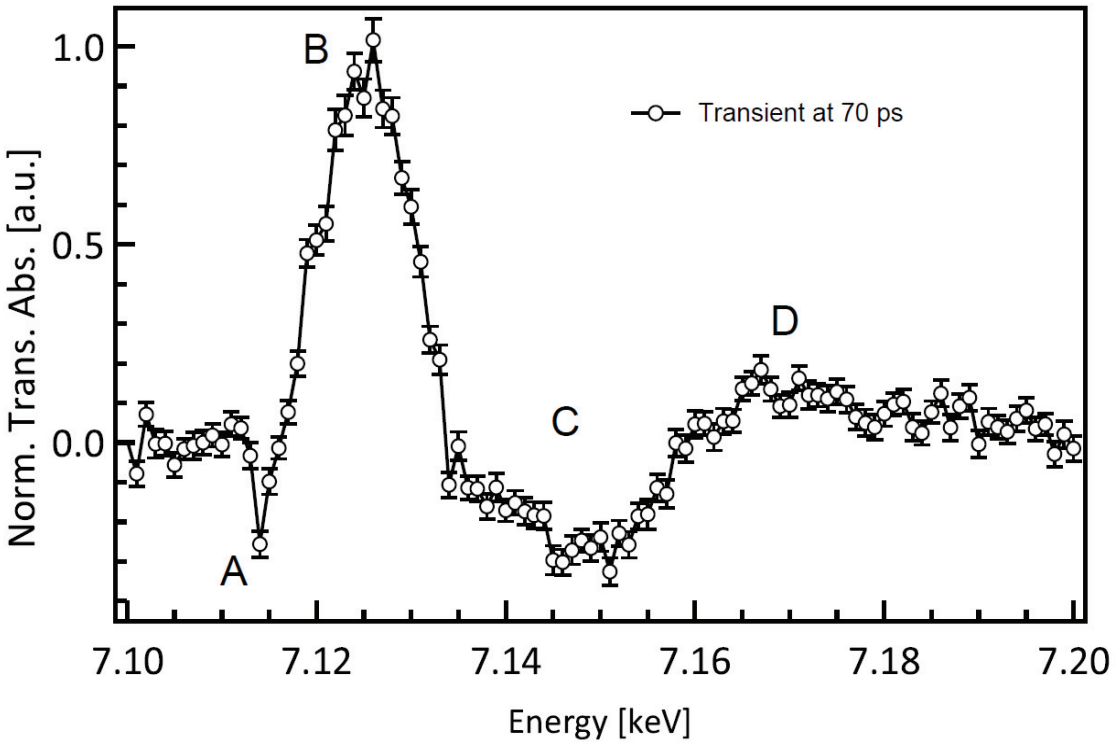

Figure 4-5: The transient spectrum recorded 70 ps after excitation of the 4mM MbNO at 532 nm (under physiological conditions). Important features are labelled A-D.

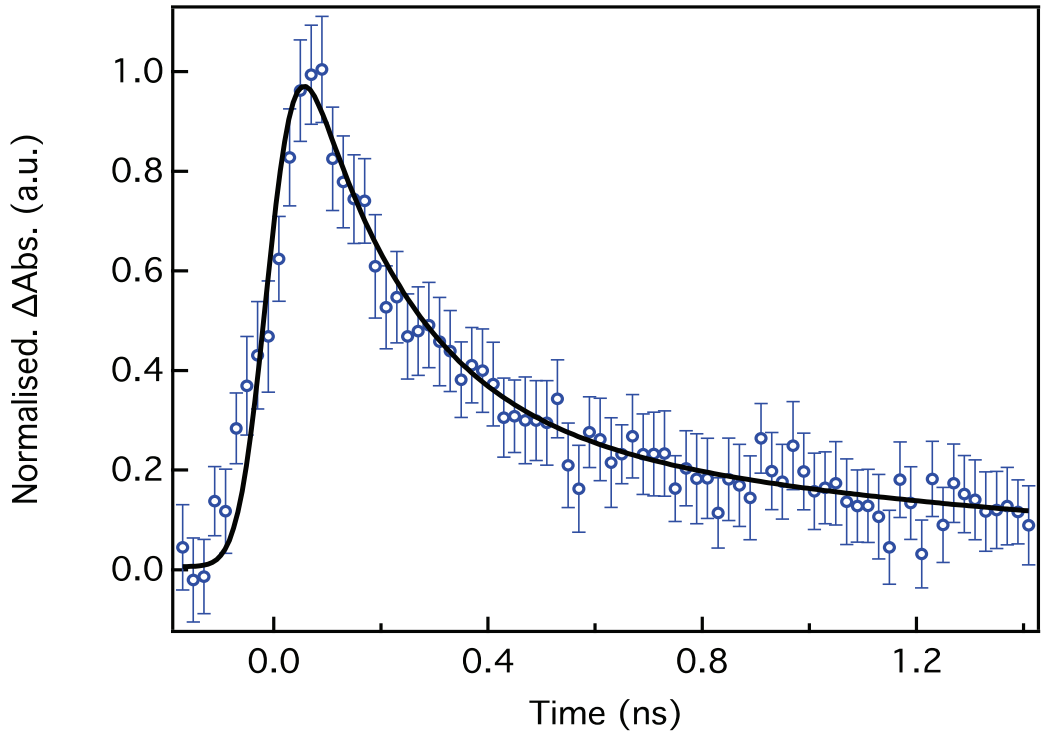

Figure 4-6: Kinetic trace of the maximum Fe K-edge absorption spectrum signal of MbNO upon 523 nm excitation. Fitted time scales are τ_1=192±44 ps (75%), τ_2=1330±688 ps (25%).

4.3.1 **TR-XAS Result of MbNO at different delay times**

Figure 4-5, shows the measured transient spectrum at 70 ps after excitation of the Q-band (532 nm) of the porphyrin. The transient (excited - unexcited) spectrum is composed of four principle characteristics; a small negative feature at 1.708keV (labelled A), a large positive feature around 7.125 keV (labelled B), a broad minimum around 7.150keV (labelled C) and a small positive feature with a maximum around 7.165keV (labelled D). The dynamics of these transient features have been probed using a time-scan of the strong spectral feature at 7.125 keV.

This kinetic trace of the maximum feature in the transient is shown in Figure 4-6. It is best fitted with a bi-exponential function convoluted with a Gaussian function of 70 ps width, representing the X-ray pulse duration[190]. The fit yields decay times (pre-exponential factors) of τ_3=192±44 ps (75%) and τ_4=1330±688 ps (25%) (labels are based on Table 4-1). The 70 ps resolution hinders us from resolving the short decay times τ_1,τ_2 < 40 ps in Table 4-1) but the reported time constants are in good agreement with most optical studies. Considering that the short component in our case integrates all first three decay times in the optical studies (Table 4-1), the ratio of the pre-exponential factors agrees* well with these studies. This also shows that the methodology of using a high repetition rate laser to excite the system does not lead to sample damage compared to the 1 kHz repetition rate used in all previous laser-only studies. This is important for future optical pump/X-ray probe studies of hemoproteins in solution, either by X-ray scattering or X-ray spectroscopy.

Figure 4-7 compares the transient signal at 70ps to the transient spectrum at 300 ps time delay. Within the limits of the signal to noise ratio, the two normalised experimental transients are identical except for small deviations in the pre-edge, the edge and the post-edge regions. Moreover, the transient signal at 1 ns (red curve in Figure 4-8) was measured to crosscheck the signal of our time traces and to confirm that it is not an electronic offset. The transient signal at 1ns is very weak due to the decay of almost all excited state species to the ground state but agrees well with the other two transients. In the presented result specially for the transient signal at 70 ps time delay (Figure 4-7) there seems to be a sudden drop at ~7.145

* This agreement with optical studies is valid for the ratio between the integrated area of each component of the bi-exponential fit (0.754 and 0.245 for 192 ps and 1330 ps components, respectively).

keV beyond the error bars, prompted me to check once again all of our experimental data to know where it comes from. Results of this analysis are presented in the following section.

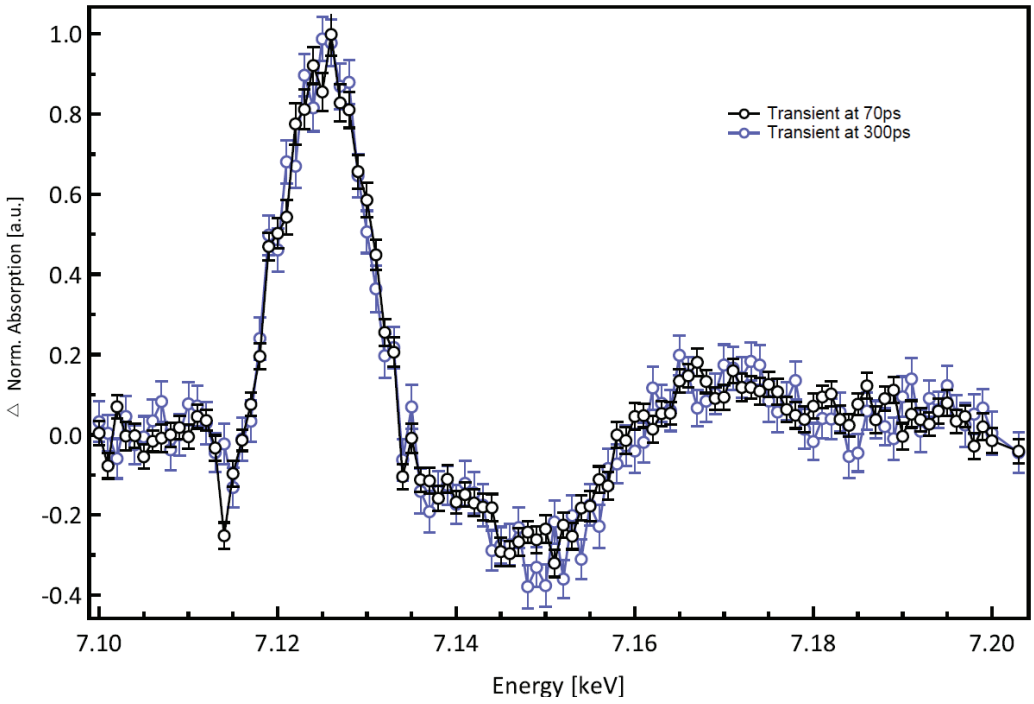

Figure 4-7: comparison of transient spectra of MbNO at 70 ps (black) and 300 ps (blue) time delays after excitation at 532 nm

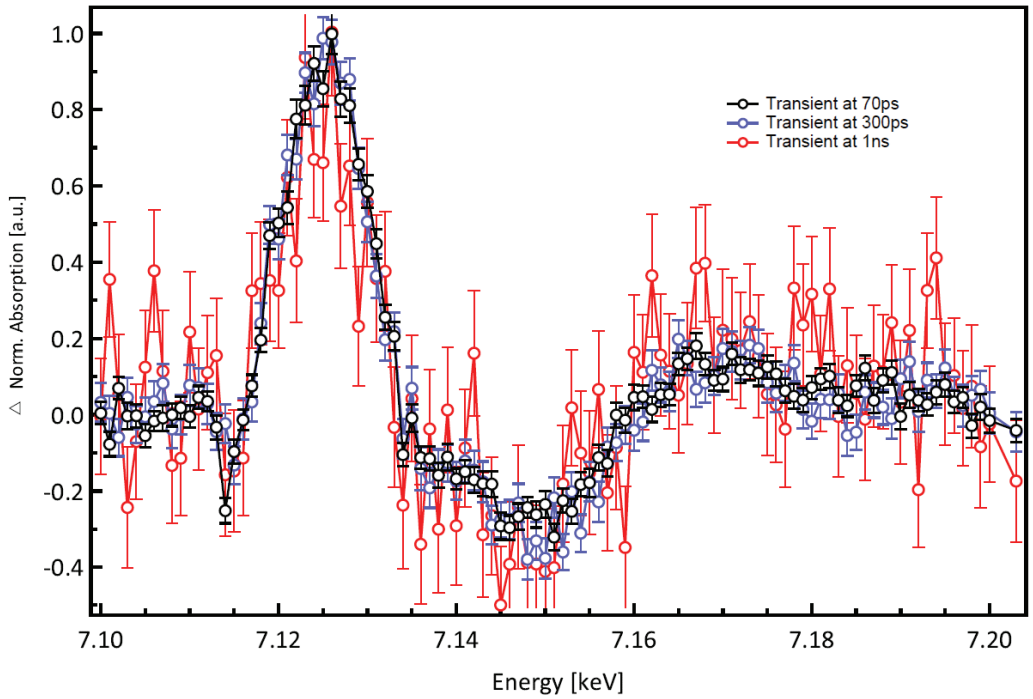

Figure 4-8: Comparison of transient spectra of MbNO at 70 ps (black) and 300 ps (blue), and 1 ns (red) time delays after excitation at 532 nm.

4.3.2 Analysis of the Results

The special data acquisition strategy that I used for the measurements requires extra care in comparison to what has been explained as a typical data analysis method in Chapter 3. As mentioned earlier, in order to avoid sample damage and its deposition on the wall of the quartz capillary, the latter was displaced vertically after each scan using a motorized stage. In addition, in Table 4-2, it is shown that 102 data points of the spectrum were measured in 4 different sets labeled ei (i=1-4) list, each including ~25 data points with a 4 eV step size but different energy ranges (keV): e1 (7.1, 7.2); e2 (7.101, 7.201); e3 (7.102, 7.202); e4 (7.103, 7.203). Figure 4-9 represents these datasets constructing the whole spectrum. A loop is defined as a set of 19 different spots on the capillary, i.e. the capillary is shifted vertically 19 times in front of the X-ray spot. This way, we only measured each spot on the capillary during ~80 sec before moving to the next spot. Repeating this pattern for 8 loops at fixed time delay of 70 ps (for 300 ps time delay see Table 4-2), we collected 294 scans in 14 hours for the full spectrum from both fluorescence APD's without causing sample degradation and its deposition on the capillary wall and also avoiding burning the capillary wall with laser.

Along with special data acquisition strategy, the indirect monitoring of I_0 via transmission detector demands different treatment of the data. Instead of correcting (i.e., dividing by I_0) each individual scan for fluctuations in I_0, we kept the uncorrected data after making sure that there are neither glitches nor unexpected changes in I_0. Moreover, to avoid introducing noise to the weak transient signal, only the averaged transient signal was normalized to the averaged edge-jump (the averaged edge-jump is obtained from the I_0 corrected averaged unpumped fluorescence signal). However, in case of strong transient signal normally each individual scan is normalized to its corresponding edge-jump of the unpumped fluorescence signal. Analyzing the transient signal at 70ps time delay Figure 4-5, the following points are observed:

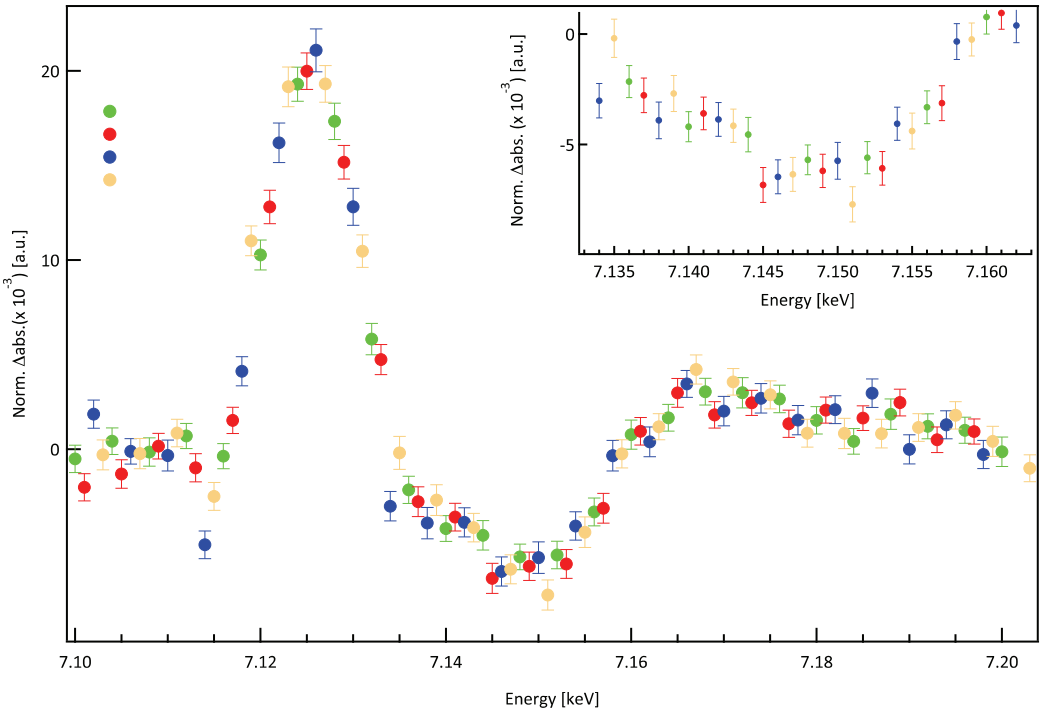

Figure 4-9: Representation of different sets of data points to make a full spectrum of the transient at 70 ps and 300 ps time delay. Energy points of set e1 are shown in green, set e2 in red, set e3 in blue and set e4 in points yellow. Note that not all datasets have been measured a similar number of times (details in Table 4-2). Therefore, to count the total number of scans for the whole spectrum we consider the number of scans of e4 that has been measured less than or equal to others. Additionally, this number is multiplied by two since we have averaged the signal of two fluorescence APD (number of full spectra in Table S2). The inset shows a better contribution of different data sets around 7.145 keV. The small difference in the size of error bars is due to the different number of scans for each dataset.

Table 4-2: Details of the data acquisition for this work. ei (i=1-4) is the set of data points for energy scans. Each eiset includes ~25 data points with 4 eV step size but different start and end points. These sets together cover the whole energy range of the spectrum (in keV): e1 (7.1,7.2); e2 (7.101,7.201); e3 (7.102,7.202); e4 (7.103,7.203). A loop is defined as measuring the energy list of 19 different spots on the capillary. The number of full spectra is e4 multiplied by two since we have averaged the signal of two fluorescence APD.

Signal	**Scan number per set**				**Number of full spectra**
	e1	e2	e3	e4	
70 ps	175*	166	147	147	147 x 2= 294
	10 loops	9 loops	8 loops	8 loops	
300 ps	163	162	163	161	161 x 2= 322
	9 loops	9 loops	9 loops	9 loops	

* Note that, each energy list has different contribution to the total averaged scan number. The e1 has the highest proportion of while the rest has 26.2 %, and 23.1 %, respectively. This leads to smaller error bar for the e1 data points compare to that of e3 lists.

a) The sudden drop at 7.145 eV is comparable to a similar drop around 7.10 eV where the signal is zero on average. Moreover, the fact that the confidence interval for these error bars is less than 90%, infers that 10% of the actual data points could be out of the error bar. Additionally, the following checks were done to make sure that the drop at 7.145 eV is due to statistics.

The data was sorted scan by scan and scans that had points lying outside 3σ (i.e. 46 scans) and 2σ (i.e. 172) were excluded (for more details see Table 4-3). Figure 4-10-b and Figure 4-10-c show the average transients obtained by excluding the scans that had values deviating by > 3σ and 2σ, respectively, from the average signal, where σ is standard deviation. These Figures show no meaningful difference compared to Figure 4-10-a, even though in Figure 4-10-c, the number of scans reduces by 41% (122 scans) of the total 294 scans.

b) The transient data at 70 ps was measured using two different samples (A and B). In , we compare the transient of sample A (blue curve) to that of sample B (red curve) and also to the average (black curve). Note that including all the 294 scans; although error bars are comparable, the drop reduces by 30% of its size for the transient of both samples.

c) Figure 4-12 shows the transient XAS obtained here from averaging 294 scans (14 hours) and ref.2 of measurements at 70 ps time delay from 51 scans (5 hours), as well as the static difference

d) 2σ, respectively, from the average signal, where σ is standard deviation. These Figures show no meaningful difference compared to Figure 4-10-a, even though in Figure 4-10-c, the number of scans reduces by 41% (122 scans) of the total 294 scans.

e) The transient data at 70 ps was measured using two different samples (A and B). In , we compare the transient of sample A (blue curve) to that of sample B (red curve) and also to the average (black curve). Note that including all the 294 scans; although error bars are comparable, the drop reduces by 30% of its size for the transient of both samples.

f) Figure 4-12 shows the transient XAS obtained here from averaging 294 scans (14 hours) and ref.2 of measurements at 70 ps time delay from 51 scans (5 hours), as well as the static difference spectrum. Comparing these two signals that were recorded using different data acquisition strategies (see above), the results are identical, despite the larger error bars in ref.2. In

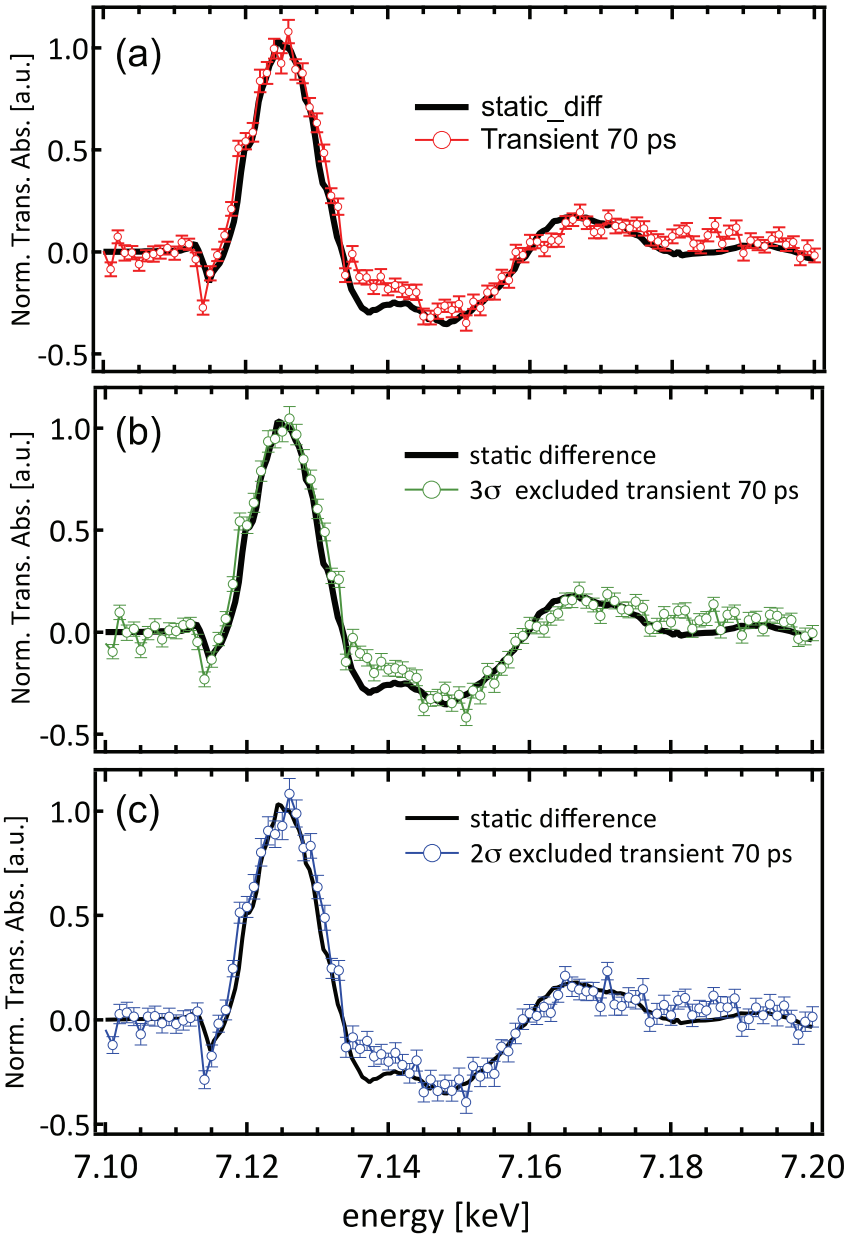

Figure 4-10: Averages of the scans: (a) all scans; (b) scans excluding those with points deviating by >3σ (c) those having points deviating by >2σ. The size of the error bars should decrease by excluding 3σ and 2σ outliers. But, on the other hand, it depends on how many scans have been excluded. From Table 4-3, it is apparent that by excluding 172 scans from 294 total scans for 2σ outliers the error bars will increase by a factor of 1.3 (size of error bar$\propto 1/\sqrt{N}$, where N is the number of scans). For example at 7.126 keV, the size of the error bar increases by a factor of 1.28 for the signal shown in (c) compare to the signal of (a), which is not so clear in the figure. Note that, this at the end does not change the conclusion that sudden point-to-point jumps (at *e.g.* 7.137 or 7.145 keV) in the data is statistics and does not have any physical meaning. Moreover, such a jump also has occurred at 7.10 keV which the signal should be zero.

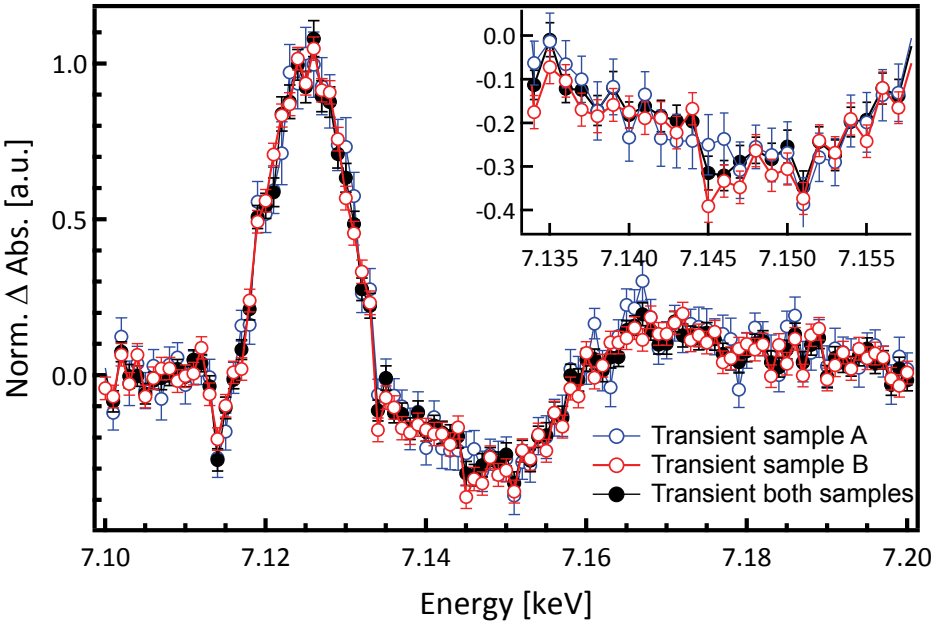

Figure 4-11: Transient signal (black) averaged over 294 scans for two measured samples compared to the transient signal (blue) average over 203 scans of sample A, and 91 scans of sample B (red). Note that although the error bars are comparable, the drop at 7.145 keV shrinks by 30% of its size in the red curve and it is almost absent in the blue trace.

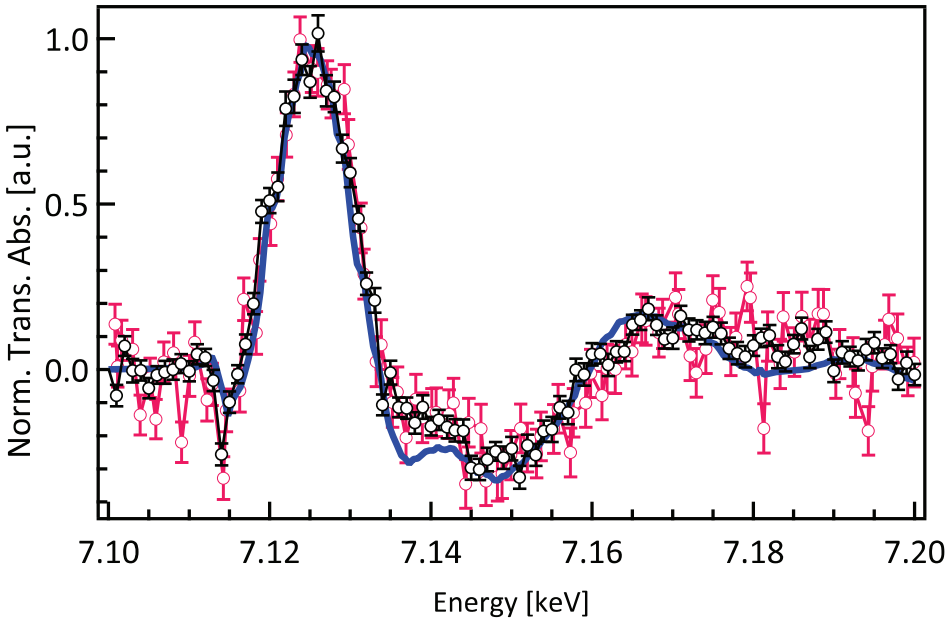

Figure 4-12: Comparison of the TR-XAS signal at 70 ps time of the different series of measurements: ref. 76 (red), this work (black). The static difference spectrum is given in blue

Table 4-3: Statistical analysis of the transient signal at 70 ps time delay with our special method of measurement. Here, σ is the standard deviation from average value; ei (i=1-4) is the set of data points for energy scans, including ~25 data points in 4 eV steps but different energy ranges (keV): e1 (7.1,7.2); e2 (7.101,7.201); e3 (7.102,7.202); e4 (7.103,7.203). A loop is defined as the collection of set e1 on 19 different spots on the capillary. The number of full spectra is e4 multiplied by two since we have averaged the signal of two fluorescence APD.

Signal at 70ps This work		Scan number in each ei list				Full spectrum
		e1	**e2**	**e3**	**e4**	
All scans		175 10 loops	166 9 loops	147 8 loops	147 8 loops	147x2=294
3σ	Outliers	17	30	18	23	46*
2σ	Outliers	96	93	82	86	172*

* This is the number of excluded scans. The total scan number subtracted by the number of remained scans for both APD's, e.g. 294-248=46.

both series, the transient signal level at 70 ps corresponds to less than 2 % of the steady-state absorption. The transients in both series show the same trends and in particular, the deviation with the static difference around 7.145 keV. It is important to note that despite having different data acquisition strategies, their identical result guarantees the reproducibility of the measurement. Therefore, we conclude that the results and in particular, the deviation of the experimental transients from the static difference spectrum in the region of 7.14 keV is correct.

The data presented here for 70 ps time delay and its signal-to-noise ratio (S/N) are the result of 294 averages of the transient spectrum including 102 points, taken over 14 hours. We calculate two types of error estimation for our data. The first type is the propagated standard error* calculated for the 520 000 shots per point per scan per second recorded separately during the measurement of one scan. The standard deviation of this "standard error" upon averaging all the scans is the "noise" (half the size of the error bar) we report in our data. The second type of error is calculated from the statistical deviations from scan to scan over the entire averaged set of scans. Note that since we are not counting photons, we do not assume shot-noise in our experimental results. However, in total fluorescence yield detection with limited solid angle and the very low concentration of the sample used, we reach the photon-counting regime. However, to verify that despite the 14 hours of measurements, we are still at the shot-noise limit, we calculate the second

* The "Standard error" estimates how repeated measurements on the same setup tend to be distributed around the "averaged value" and can be defined as the square root of the estimated error variance of the measured value (here, is Intensity of the pumped/unpumped/difference signal).

type of error. These two error bars are similar in size for the present study, which means we had little scan-to-scan sources of noise, and the experiment was close to shot noise.

The total number of incoming X-ray pulses for the averaged spectrum (at 70 ps and 300 ps) is about 5 x 10^8 incoming X-ray pulses per data point with 2 x 10^4 photons per pulse (considering 1.04 MHz repetition rate of incident X-ray beam at SLS). Hence, in total for the averaged transient signal with 102 data points there were 5 x 10^{10} X-ray shots. From the absorption coefficient obtained from the normalized static X-ray absorption spectrum $\Delta A^{F}_{norm} = 2\%\ (1.2\ \%\ \text{for}\ 300\ \text{ps})$, the edge-jump of ΔA^{F}_{edge} =25% in the normalized averaged unpumped fluorescence signal, and the value of the fluorescence yield (ε_F) at Fe K-edge ≈ 34% (0.333 ± 0.006) obtained from experimental data according to ref. [191], we can calculate the number of fluorescence photons detected per data point:

$$I_F^p - I_F^{unp} = \Delta A^F_{norm} \times \Delta A^F_{edge} \times I_0 \times \varepsilon_F = 2 \times 10^{-3} \times 0.25 \times 2 \times 10^4 \frac{ph}{pulse} \times 0.333$$

$$= 3 \frac{ph}{pulse}$$

where I_F^p and I_F^{unp} are the X-ray fluorescence intensities from the pumped and unpumped sample. This corresponds to $\cong 5 \times 10^6 \frac{photon}{data\ point}$.

Error! Reference source not found. shows the transient XAS signals and the error bars at 70 ps and 300 ps time delays. The error bars are the result of averaging the scans described in Table 4-4. The absolute amplitude of the signal at 300 ps is of course weaker than at 70 ps, however for the comparison to be meaningful we normalized the two transients to maximum in **Error! Reference source not found.**. The point here is that the spectra at 70 and 300 ps are identical (to within error bars) and deviate in the same way from the static difference near 7.14 keV. The ratio of the transient signal level to the static signal is lower for 300 ps (0.012), due to the fact that the population of intermediates is smaller (the recombination time scale of the system is ~200 ps, see Table 4-1). Likewise, for the case for 70 ps transient signal I performed a similar statistical analysis on the averaged signal at 300 ps time delay. Details of excluding values deviating more than 3σ and 2σ from the average signal, are tabulated in Table 4-5. Averaged remaining scans after excluding both 3σ and 2σ outliers show no meaningful difference compared to the signal including all scans. Comparing values in Table 4-5

Table 4-4: Statistics of the two series of measurements. The signal-to-noise ratio (S/N) is defined as the division of signal level to half the error bar and is given for an energy of 7.126 keV.

Series	*Time delay*	*Scan number*	*Data acquisition (sec /scan/point*	*Transient signal / edge-jump of static signal*	*S/N*
Ref .2	70 ps	51	3.5 (100 points)	2%	15.4
This work	70 ps	294	3 (102 points)*	2.3 %	19.5
This work	300 ps	322	3 (102 points)*	1.2 %	16.8

Note that the value of ~3 sec/point/scan is from ~80 sec and 25 data points for each dataset of Table 4-2. To calculate measuring time for each full spectrum, it multiplies by 4 (four datasets) and to calculate the total time of measurement it multiplies by 147 scans for each APD.

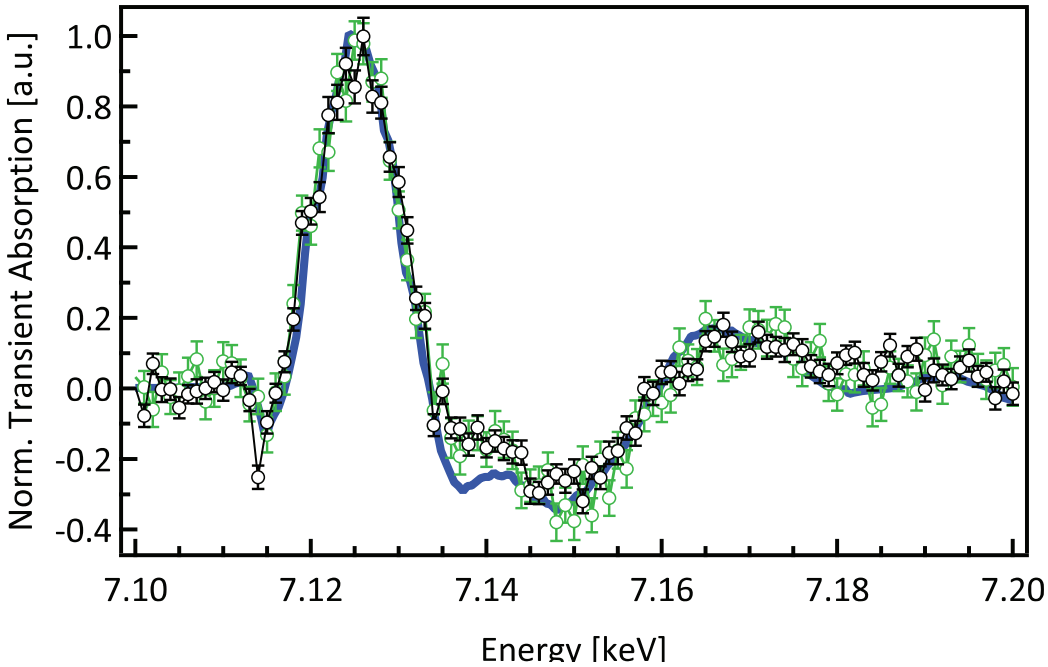

Figure 4-13 Comparison of transient spectra of MbNO at 70 ps (black) and 300 ps (green) time delays after excitation at 532 nm, and the static difference spectrum (blue). The transients have been normalised to the maximum at 7.125 keV.

with their equivalents in Table 4-4, the averaged transient signal at 300 ps delay time shows overall less deviation from averaged values for each data point leading to less standard error Table 4-4 for 300 ps signal. However, less standard error does not bring better S/N for 300 ps averaged signal. While the obtained S/N for the transient at 70 ps is 19.5, it turns out to be 16.8 for the 300 ps case. This is due to the lower transient signal level for 300 ps compare to 70 ps case that is

reflected also in their ratios to the static signal (Table 4-3). Again this is as a result of the smaller population of intermediate species which have relaxed to the ground state within ~200 ps (recombination time scale of the system, see Table 4-1).

Table 4-5: Statistical analysis of the transient signal at 300 ps time delay with our special method of measurement. Similar definitions to Table 4-3.

Signal at 300ps This work		Scan number per set				Full spectrum
		e1	**e2**	**e3**	**e4**	
All scans		163	162	162	162	162x2=324
		10 loops	9 loops	9 loops	9 loops	
3σ	Outliers	4	0	5	7	14
2σ	Outliers	13	19	10	10	38

Table 4-5 gives the details of the scans at 70 ps and 300 ps time delays compared to ref.2. The signal-to-noise ratio (S/N) has improved by a factor of 1.3 compare to what has been reported[78], which resulted from: a) the longer data acquisition time; b) the minimization of sample damage using a lower laser power (0.53 W vs 2 W); c) a shorter scan time (80 sec for ~25 data points of each ei) on each spot of the capillary but more frequently measured (in the conventional method each scan of ~100 data points takes 2-3 minutes with a higher probability of sample damage); d) a higher flow rate of the sample in a longer closed loop; e) an efficient cooling of the sample; f) a closer positioning of APD's, i.e. larger solid angle for data collection.

4.3.3 **Simulation of the transient signal at 70 ps**

Ideally we would like to derive the structure of intermediate species from our transients, however the most notable changes occur in the XANES region (up to ~50 eV above the edge) and are small, which makes a quantitative analysis very challenging. The weakness of the signal (i.e. the deviation from the static difference spectrum) is an important aspect of the domed 6-coordinated intermediates, since the only difference between the deoxy form and the ligated domed species is the presence of NO near the Fe atom. Since the iron is surrounded by only light elements with weak photoelectron backscattering efficiency, they do not contribute efficiently to the XANES modulations. However, simulations are helpful to see if the observed transient trends are confirmed by theory. Despite the limitations of multiple scattering theories in explaining the

XANES region, we did simulations of the static difference spectrum (taking the simulated spectra from ref.[43]) and of the domed ligated species.

Both simulated transient XAS spectra (Figure 4-14) were calculated using the multiple scattering theory implemented within the FDMNES package[192]. A self-consistent potential of radius 6.0 A around the absorbing atom was used in each case. The interaction with the X-ray field was described using the electric quadrupole approximation. Following the calculation, many body effects and the core hole lifetime broadening were accounted for using an arctangent convolution[193].

The structure used for the intermediate was obtained using a DFT(B3LYP*)[194-197] geometry optimization of the FeP(Im)(NO) complex in the quartet state using the ORCA quantum chemistry package[198] (P is a porphine ring and Im is an imidazole group). A def2-TZVP basis set[199,200] was used for all atoms. To account for the weak π–π interactions, the calculations were supplemented with Grimme's D3 dispersion correction with the Becke–Johnson damping scheme[201,202].

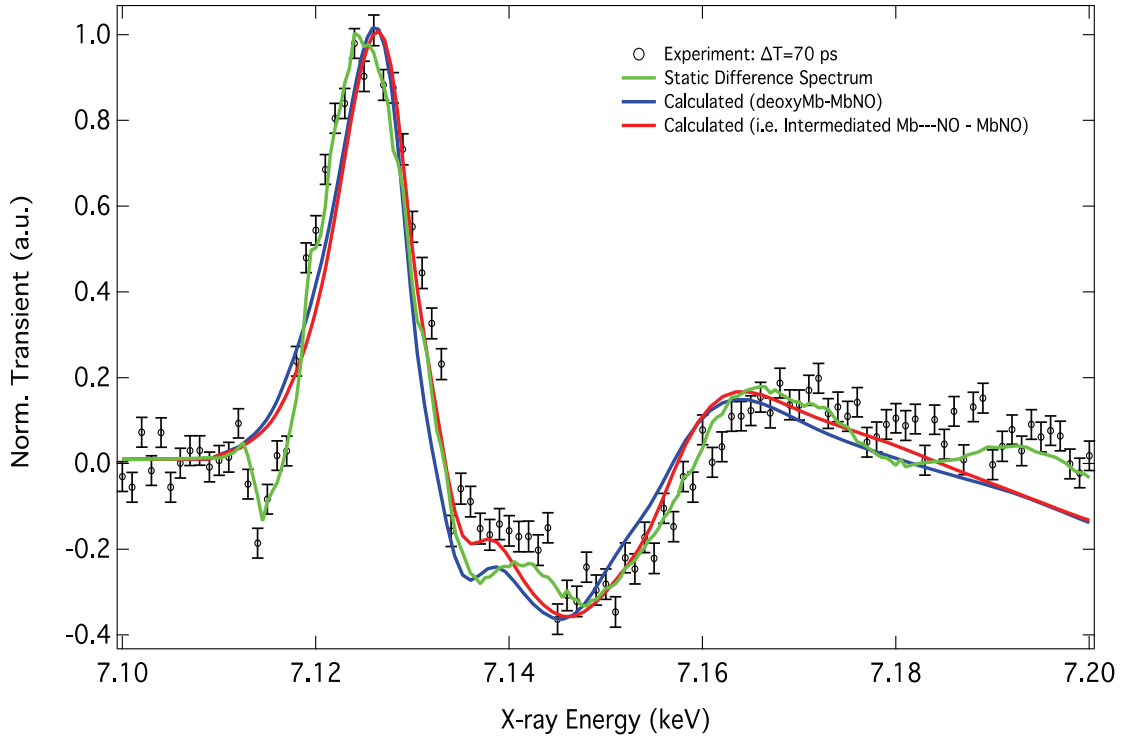

Figure 4-14: Simulations of the difference static spectrum (deoxy minus MbNO, blue line) and the transient spectrum (domed ligated minus MbNO, red line) along with the experimental transient spectrum at 70 ps (black points) and the experimental static difference spectrum (green line).

The structure of the quartet state is very similar to deoxyMb, the Fe-N bond to the proximal histidine is 2.30 Å (2.31 Å for deoxyMb in ref. [43], the Fe-Np bond distances in the porphyrin ring

are 2.06 Å ((2.31 Å for deoxyMb in ref. [43]). The displacement of the iron atom from the plane of the porphyrin ring (indicative of doming) is 0.15 Å (0.2 Å in deoxyMb). Finally, Fe-NO distance of the FeP(Im)(NO) complex in the quartet state is 2.45 Å.

4.3.4 **Discussion and Interpretation**

Based on the interpretation of the static spectra given in section 4.2, it is possible to qualitatively assign the principle features of the transient as follows (using the same labelling as in Figure 4-5): the negative feature A arises from a bleach of the high spin configuration of the iron in deoxyMb. Visible photoexcitation of the system in the Q-band is associated to a π-π^* porphyrin transition triggers the photo-dissociation channel[147]. Involving only porphyrin orbitals, Q-band π-π^* excitation does not directly change the electronic configuration of the Fe valence electrons. However, the HOMO and LUMO orbitals will be affected strongly upon detachment of NO ligand. As deduced from the static XAS (4.2), in the ground state (GS) we have 1s→dσ and 1s→dπ-π^*_{NO} transitions. The detachment of the NO ligand involves a low-spin (LS) to high-spin (HS) transition of the iron (and doming of the heme). One would expect these peaks to decrease in intensity because of partially occupation of dσ (d_{x2-y2}) in the HS deoxy form (Figure 4-2). In Figure 4-15, a zoom into the pre-edge region shows the deviation of the transient signal from the static difference. If ligand photo-dissociation were the only outcome of the reaction (conversion of the MbNO only to the deoxyMb, such as the case of MbCO[183 189]), the transient XAS spectrum would be identical to the static difference spectrum weighed by the photolysis yield. To reconstruct the transient spectrum, we should subtract the XAS of ES MbNO* (here deoxyMb) from the GS MbNO, that implies a transition from the LS to HS electronic configuration (§ 3.2.1.2 and § 3.2.1.3). This transition accompanies a depletion of the dπ orbitals at lower energy than the HOMO in MbNO, which manifest itself as a small positive feature in the transient XAS at the energy slightly lower than 7.114 keV (the pre-edge feature in the XAS of MbNO), see Figure 4-15. However, owing to the weak nature of the quadrupole transition moment this component is not remarkable in the transient spectrum. However, simultaneously there is a change from tetrahedral D4h symmetry in LS ferrous MbNO to the square pyramidal coordination symmetry (C4v) in the photolyzed species. For which one expects an increase in the 3d/4p orbital mixing that can enhance the intensity of 1s→dπ with higher dipole moment characteristic.

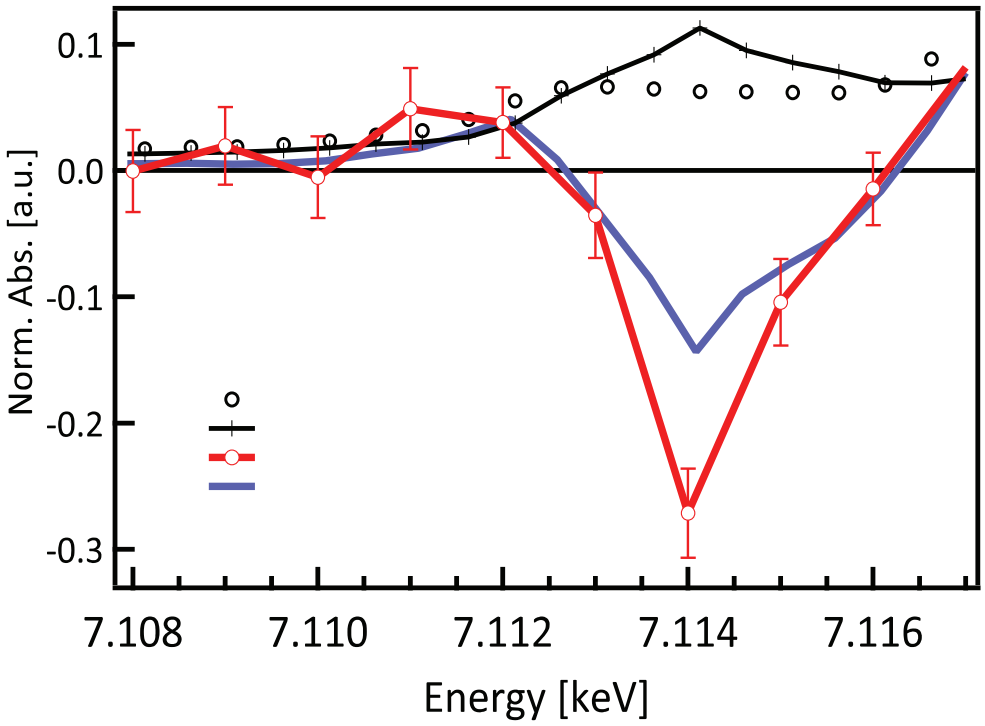

Figure 4-15: Zoom into the pre-edge and post-edge of XAS for MbNO (black solid line) and deoxyMb (dotted), along with static difference spectrum (blue) and experimental pump-probe signal (red) at 70 ps time delay.

The main transient feature (B) at 7.125 keV (Figure 4-5) arises from the edge-shift associated with formation of deoxyMb. This shift is due to the elongation of the Fe-Np distances in the high-spin state of deoxyMb.[184] The fact that this feature does not show any change compared to the static difference spectrum points to a similar oxidation state of the intermediate with the DeoxyMb and the ligated form MbNO. This, in retrospect, shows that on this time scale (70-300 ps) any changes in the pre-edge region associated with the intermediate species are merely due to an electronic changes within the d-orbitals and not an oxidation state change.

Finally the region between 7.14 and 7.16 keV is very sensitive to the ligand binding, as discussed in ref.[43], and the fact that it is negative in the transient, reflects the decreased absorption of deoxyMb-like species at these energies (Figure 4-5). In summary: (i) The transient species has a somewhat similar geometric and electronic structure to deoxyMb; (ii) Our pulse width integrates the signals of the short components (<40 ps), representing over 50% of the total signal (Table 4-1). This implies that at 70 ps time delay, we are mostly detecting domed ligated species. The fact that the transients are basically similar at 70 and 300 ps (Figure 4-8), further supports this conclusion.

The most obvious interaction that would account for the intermediate species is between the

iron and the NO ligand and is, of course, weaker than in MbNO, as it bears several common features with deoxyMb. Based on previous studies, we conclude that it is the domed NO-ligated form[23,26,27,175,176]. Ideally, we would like to derive its structure from our transients, however the most notable changes occur in the XANES region (up to ~50 eV above the edge) and are small, which makes a quantitative analysis very challenging. The weakness of the signal (i.e. the deviation from the static difference spectrum) is an important aspect of the above conclusion, since the only difference between the deoxy form and the ligated domed species is the presence of NO, which does not contribute strongly to the backscattering of the photoelectron in the above edge region. It is a dilemma that proof of the domed ligated form lies in the weakness of the deviation it shows compared to the deoxy form. Nevertheless, bearing in mind the limitation of multiple scattering theories in the XANES region, we performed simulations of the static difference spectrum (taking the simulated spectra from ref. [43]) and of the domed ligated species just to see if the observed trends are confirmed by theory. Figure 4-14 shows that this is indeed the case, as the deviation from the static difference spectrum becomes larger in the 7.14 keV region in the case of the domed ligated form. Again we insist that these calculations cannot be used to extract the structure of the latter, due to limitations of the theory.

We can now rationalize the three types of time scales (typically: <10 ps, 20-30 ps, ~200 ps) that were reported in laser-only studies and in the present one. Champion et al[23,145] explain the <10 ps time constant as reflecting geminate recombination (GR) to the domed configuration due to nearby NO's, while the 200 ps is attributed to the more distant NO's located in the Xe4 position. This is supported by the conclusions of Lim et al[29,30] and Kholodenko et al[24], who argued that the long component is determined by the relaxation of the protein.

Our results show that the entire kinetics up to ~300 ps reflect the same intermediate species, which we identify as the domed ligated heme, relaxing in ~30 ps back to the planar configuration, according to ref.[26]. Thus, we conclude that the 200 ps time scale for the diffusion of NO (probably from the Xe4 position) to the Fe atom is the rate-limiting step for the formation of the domed species that has a lifetime of 30 ps.[26] Even with a higher time resolution, we would not detect the latter as the rise time of the intermediate is longer than it decay time, so that the former appears as a decay in the kinetics, which is our case.

Kruglik et al's[26] resonance Raman experiment is specifically sensitive to the 30 ps component, which was missed in most IR or UV-visible transient absorption studies (Table 4-1). Interestingly,

they report a rise of this component of ~10 ps, i.e. they detect the fast rising component of the domed ligated form, due to GR, amounting to about 50% of the entire recombining population (τ_2 in Table 4-1). The rest of the domed species are covered in the 200 ps component because, as mentioned above, the rise is slower than the decay. Kruglik et al[26] associate the 30 ps relaxation of the domed ligated to the constraints exerted by the protein on the porphyrin, while from DFT calculations of the model system Im-FeP-NO, Franzen[175] finds that for an Fe-doming of 0.2 Å (typical of the domed deoxy species), the highest excited state accessible upon NO recombination to the Fe atom is the sextet state, which has an equilibrium distance of 2.85 Å, where it crosses the potential curves of the doublet (ground) state. The more recent calculations by Strickland and Harvey[176] rather suggest that the quartet state is more likely to be populated upon recombination with an equilibrium distance of 2.93 Å. However, more important here are Franzen's conclusions of a sequential cascade among spin states, which are invalidated by the similarity of our 70 and 300 ps transient spectra, unless the relaxation from a high spin to a low spin state is on the order of 100s ps or longer, which is unlikely. Thus both effects may contribute simultaneously. Finally, the >1 ns component in the present XAS study and in previous optical studies (Table 4-1) is most probably due to proteins that have lost the NO ligand to the surrounding solvent. Figure 4-16 summarizes the results of the present and previous investigations [22,23,26,29,30].

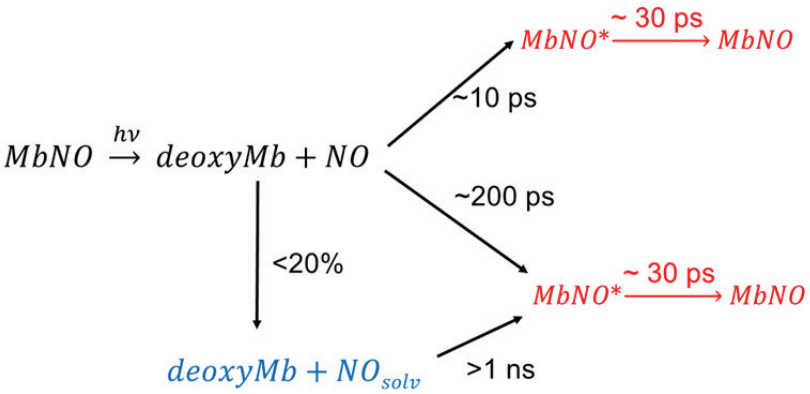

Figure 4-16: Recombination of NO to the myoglobin heme after photolysis. DeoxyMb is the domed unligated protein. The MbNO* represents the domed ligated form after recombination and NO_{solv} represents the NO ligands that have escaped to the solvent.

4.4 Charge Transfer from Tryptophan to Fe(III) in MetMb

Tryptophan (Trp) is commonly used to study protein structure and dynamics, such as protein folding, as a donor in fluorescence resonance energy transfer (FRET) studies.

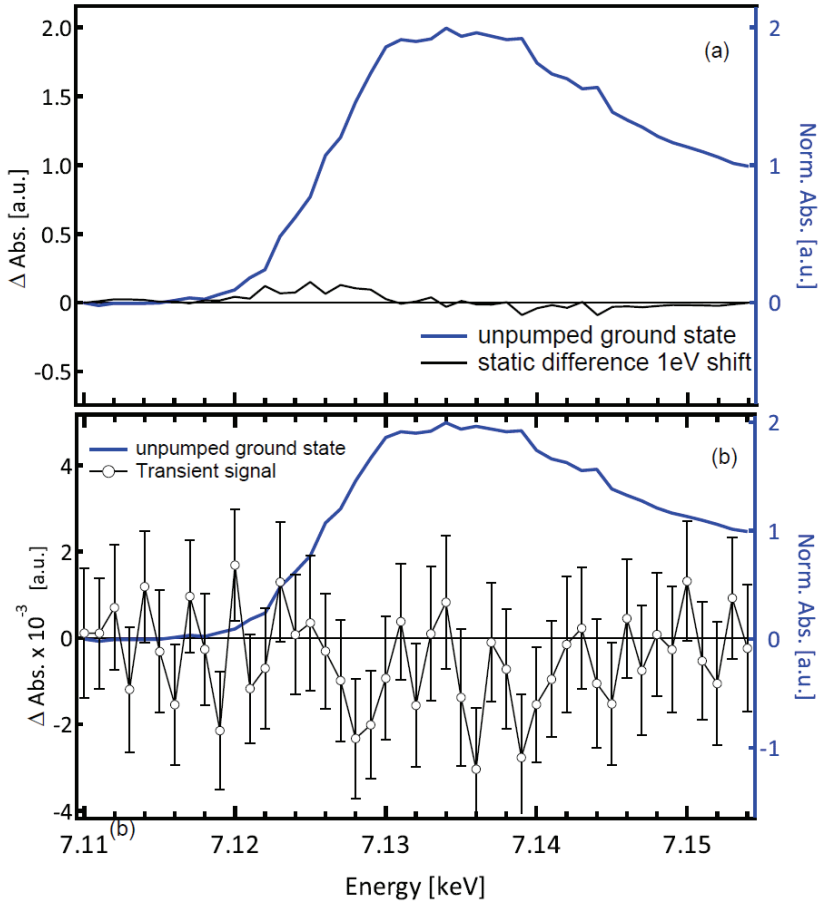

Figure 4-17: (a) The transient spectrum of metMb, excited at 266 nm and recorded in fluorescence mode, detected by the APD detectors. (b) The difference signal between ground state and a spectrum shifted by 1eV. Note that the transient spectrum in both cases is scaled to the edge jump of the fluorescence signal, and the experimental data is 2 orders of magnitude weaker than the static difference.

There are two Trps present in Mb (Trp7 and Trp14) at different relative distances to the porphyrin (~13.5 Å and 8 Å respectively). Their fluorescence is quenched on time scales of 20 to 30 ps and 110 to 140 ps, respectively [131,132,203]. While the fluorescence of Trp7 has been approved to be quenched by FRET, recent optical studies of ferric myoglobin identified electron transfer (ET) as dominant mechanism in fluorescence quenching of Trp14[173]. This raises the question whether such ET pathways occur in a larger class of metalloproteins. Ferric Mbs are ideal to address the Trp-heme interaction because heme ground state recovery is complete in < 10 ps after photoexcitation [204-207]. Addressing this query motivates the study of Trp-mediated heme reduction in both ferric and ferrous heme via the direct method of X-ray absorption spectroscopy. Using a pump probe scheme by combining X-ray absorption spectroscopy with excitation in the ultraviolet regime, the reduction of the heme via excitation of the Tryptophan (Trp) amino-acid residue in ferric Mb (metMb) was investigated.

4.4.1 Experimental Results and Analysis

The time-resolved XAS of metMb was measured using our high-repetition rate setup.[47] The metMb sample was excited using 10 ps laser pulses with 520 kHz repetition rate. The sample has been excited at 266 nm to excite mainly the tryptophan with the highest molar extinction coefficient in the range of 250–300 nm in Myoglobin [146] (see Figure 3-8). The laser fluence used was 5 μJ/cm^2. XAS transients were recorded 80 ps after laser photo-excitation. Monochromatic x-rays are focused on the sample to a spot of approximate dimensions of 50 x 50 μm^2 at the sample position, approximately 40 cm from the exit of the KB mirror unit. The fluorescence signal was recorded by two large-area APDs positioned perpendicular to the incoming x-ray beam to minimize scattering.

A sheet jet of 100μm thickness was used as sample delivery system. The 4mM metMb solution was recirculated in a closed loop system. The sample was flowed continuously at about 60 ml/min and cooled to reduce foaming, which remained a major issue. According to discussion with Prof Lin Chen, the best way to prevent generation of foam is to use polypropylene glycol 2000 (3-5 drops in every 20 mL batch of Mb). A secondary flow-loop was used to monitor the UV-Vis spectrum of the sample, ensuring its integrity during the experiment. The transient in the time-resolved XAS signal presented here is composed of the total fluorescence yield signal of 95 individual scans each about 2 minutes (43 data points) that corresponds to a total 5.3 x10^{12} ph/point.

Figure 4-17, shows the result of the measurement. The transient spectrum has been scaled to the edge jump of the fluorescence signal. One can see that the spectrum shows no signal larger than the error bar at the K-edge energy (7.125 keV). The most probable reason for zero signal is the presence of other amino acids inside the pocket of the protein which absorb photons at 266 nm (**Error! Reference source not found.**) and basically hindered the excitation of Trp14. Looking at the sequence of amino acids inside the Mb, we can count up to two tyrosine (Try) with an extinction coefficient of 1000 M^{-1}cm^{-1} and sixteen phenylalanine (phen) residues with an extinction coefficient of 100 M^{-1}cm^{-1}.[208] In total the ratio of Trp14 extinction coefficient to the other amino acids including the Trp7 is 5000/8600 which explains the lower probability of excitation. **Conclusion**

The present study demonstrates the feasibility of picosecond X-ray absorption spectroscopy at high repetition rates on hemoproteins in physiological solutions. Importantly, no radiation

damage by either laser or X-ray is observed. Furthermore, we conclude that the domed MbNO* species is the only initial product of recombination, which is populated in 200 ps (due to recombination from distant NOs) and relaxes in ~30 ps. The latter time scale is governed by the constraints exerted by the protein on the porphyrin. This work paves the way to an investigation of the short time dynamics using ultrafast XAS and X-ray emission (XES) at X-ray Free Electron Lasers to address the nature of the electronic and spin state of the intermediate and its geometric structure. In summary: (i) The transient species has a somewhat similar geometric and electronic structure to deoxyMb; (ii) Although our pulse width integrates the signals of the short components (<40 ps), representing over 50% of the total signal (Table 4-1), the transient is unchanged between 70 ps and 300 ps.

What we are saying here is that many of these features (pre-edge and main edge) point to a species that is close to but not identical to deoxyMb. The resemblance with the latter is a crucial point, because this is what leads to the conclusion of a domed ligated species. The other crucial point is that it persists on a time scale similar to the recovery time of the system. This can best be rationalized by the occurrence of a domed ligated species that is formed in a short time once the NO is in the vicinity of the Fe atom, but that rises on the time scale of NO migration in the protein (ca. 200 ps), which represents the rate-limiting step.

Chapter 5 Photoluminescence Up-conversion Studies on Iridium Complexes

Ultrafast photoluminescence up-conversion (PLUC) is a powerful tool to study intra-molecular electronic-vibrational and spin relaxation processes in TM complexes.[66,67,209-211] Ultrafast luminescence studies of Ir-complexes have been performed with monochromatic detection to investigate the excited states relaxation.[84,209,210,212] These studies focussed on homoleptic systems, like the representative ppy-based complex **Ir1**, which shows a very high luminescence efficiency at room temperature (RT).[59] Under 400 nm excitation of its singlet metal-to-ligand-charge-transfer (^{1}MLCT) state, the observed signal of **Ir1** was assigned to phosphorescence from the ^{3}MLCT manifold.[210] Within the time resolution of these experiments (220 fs), the luminescence was found to rise instantaneously and then decay with three time constants of ~0.2 ps, 3 ps and > 1 ns, where the femtosecond dynamics are attributed to electronic relaxation to the lower electronic ^{3}MLCT sub-states via internal conversion (IC) and intra-molecular vibrational redistribution (IVR)-population equilibration of sub-states. Energy Vibrational Redistribution (EVR) cooling with energy transfer to the solvent is responsible of picosecond luminescence decay leading to the long-lived phosphorescence component.

Almost all the above-mentioned studies of **Ir1** were carried out with monochromatic detection only,[84,210,213] that hinders a full visualization of the relaxation cascade. However, a polychromatic detection PLUC[214] allows a more complete visualization of the cascade among excited states. Our femtosecond photoluminescence up-conversion setup, with broadband detection capability and ≤ 120 fs time resolution, is ideal to capture the contours of the transient

fluorescence signals, and even phosphorescence ones, with very low luminescence quantum yield ($\geq 10^{-7}$).[66] Henceforth, in order to investigate more in detail these relaxation steps and to study the effects of ligand substitution on the ultrafast relaxation of Ir-complexes, using our PLUC setup, I studied various Ir-complexes differing by their coordination ligands. This chapter presents the results of femtosecond photoluminescence up-conversion study of $Ir(ppy)_3$ (**Ir1**), $Ir(ppy)_2(pic)$ (**Ir2**), $Ir(ppy)_2(bpy)$ (**Ir3**) and $Ir(ppz)_3$ (Ir4) (ppy= phenylpyridine; ppz= phenylpyrazole; pic= picolinate; bpy= bipyridine) in Chloroform ($CHCl_3$) and/or Dimethylsulfoxide (DMSO). The use of two different excitation wavelengths 400 nm (section 5.1.1) and 266 nm (section 5.2.1), and polychromatic probing in steps of ~120 fs, brought new insight into the relaxation cascade and the states therein involved in the photophysics of **Ir1**. The role of the ligand architecture in the photo-physics of Ir complexes is investigated upon visible excitation of **Ir1-4** complexes. Indeed, the effect of symmetry reduced on the electronic relaxation is investigated through the measurement of the heteroleptic complexes **Ir2** and **Ir3**, differing from **Ir1** by substitution of one ppy by a pic or bpy ligand respectively. In addition, more insight obtained (section 5.3) using the time correlated single photon counting (TCSPC) technique as a complementary study to investigate the evolution of the system in **Ir1** and **Ir4** in the gap between ps regime with PLUC and the microsecond steady state studies. I finally compare the relaxation dynamics of **Ir1** with that of the ppz-based complex **Ir4** to shed light on the kinetics of non-radiative relaxation channels occurring in blue-emitting systems.

5.1 Sub-nanoseconds PLUC studies of Ir1-3 - Visible Excitation

Understanding the photophysics behind ^{1}MLCT excitation in these compounds is a key step to unravel the more complicated case of their UV excitation. The ^{1}MLCT band in pyridine-based compounds lies in a range accessible with the 2nd harmonic (400nm) of our pumping laser. However, **Ir4** does not absorb at this wavelength, so I could only excite it at 266 nm (see Figure 3.15).

5.1.1 Experimental Results

Figure 5-1 shows the normalized time-wavelength (t-λ) plots of the luminescence of **Ir1**, **Ir2** and **Ir3** complexes in both $CHCl_3$ and DMSO upon excitation at 400 nm. **Ir4** does not absorb at 400 nm, and can only be excited at 266 nm (see below). The peak at 460 nm and at zero time delay is due to the Raman scattering signal of the solvent. The (t- λ) plots of **Ir1** appear qualitatively similar

in the two solvents, despite their different polarity. The kinetics of the **Ir2** and **Ir3** signals are overall faster than those of **Ir1**, while differences appear between the behaviour of the former two, which also show a solvent dependence. Figure 5-2 shows the transient luminescence spectra extracted from Figure 5-1 at t = 0, 200 fs, 2 ps and 100 ps. The peak position of the t = 0 spectrum is approximately the same (520-530 nm) for all samples, and it appears very close to the steady-state emission for **Ir1** and **Ir2** spanning all the range of 450-700 nm. Consequently, only the ppy ligand is involved at early times in **Ir1-2-3**. The subsequent evolution of the emission involves a drop in intensity that is significant in <200 fs for **Ir2** and **Ir3**, and then continues on a picosecond time scale mainly affecting the blue side of the emission. On the contrary, for **Ir1** the maximum of the emission signal at 200 fs undergoes a red shift of ~700 cm^{-1} in $CHCl_3$ and ~1000 cm^{-1} in DMSO with an appreciable rise between 550- 600 nm in DMSO, followed by an intensity drop of about 50% in 100 ps. In **Ir2**, a similar shift is observed (around 700 cm^{-1} in both solvents), but a larger portion of the luminescence (60% in $CHCl_3$ and 80% in DMSO) decreases in 100 ps compared to

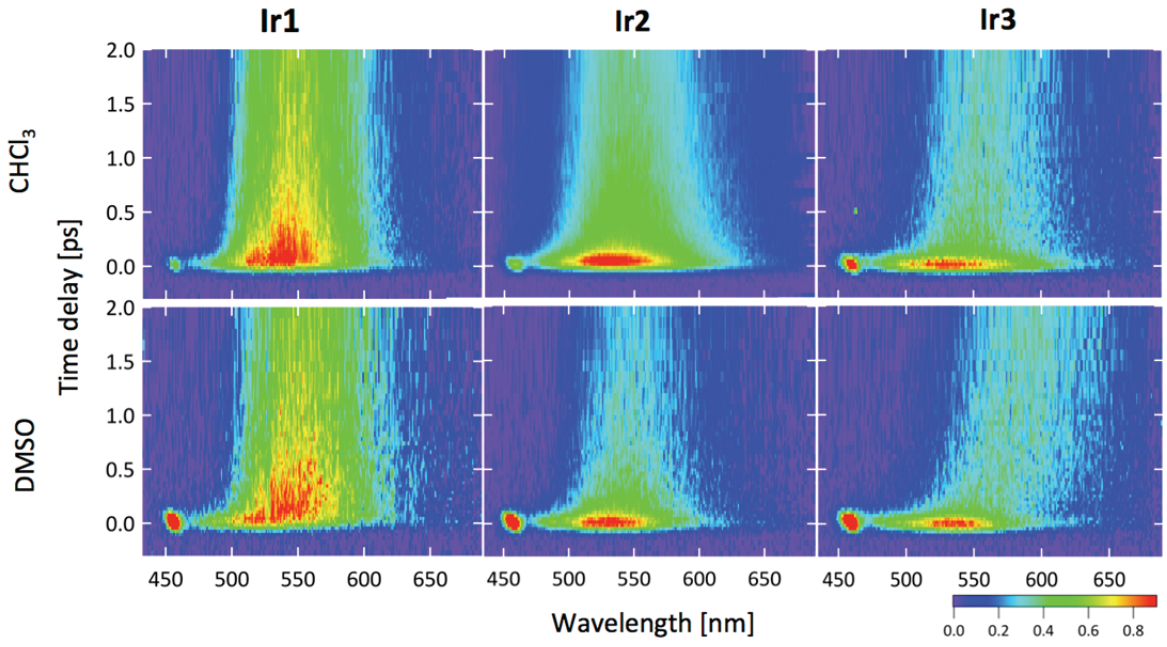

Figure 5-1: Luminescence 2D plots of **Ir1** (left), **Ir2** (centre) and **Ir3** (right) in $CHCl_3$ (top) and DMSO (bottom). Plots are shown up to 2 ps time delay and normalized to the maximum of the luminescence signal.

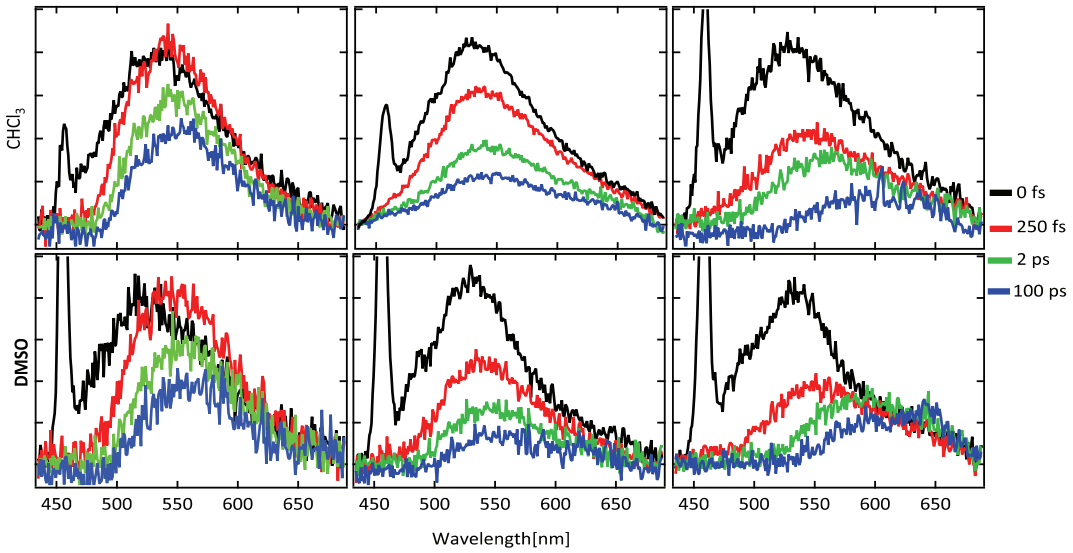

Figure 5-2: Luminescence transient spectra of **Ir1** (left), **Ir2** (centre) and **Ir3** (right) in $CHCl_3$ (top) and DMSO (bottom) at 0 fs (black), 200 fs (red), 2 ps (green) and 100 ps (blue) time delay. The peaks at around 460 nm and 0 fs correspond to the Raman scattered signal.

Ir1. **Ir3** shows an intensity drop that is similar to **Ir2** but with a faster overall dynamics: a dramatic quenching (55%) of the blue side of the signal is already evident within 200 fs, and at longer times a new emission band appears with a maximum around 600 nm. Finally, on the time scale of hundreds of ps to infinite times, the times, the **Ir1** and **Ir2** spectra evolve as the observed 100 ps transient spectrum is broader than and red shifted by ~1250 cm^{-1} with respect to the steady state spectrum (Figure 2.IV.5).

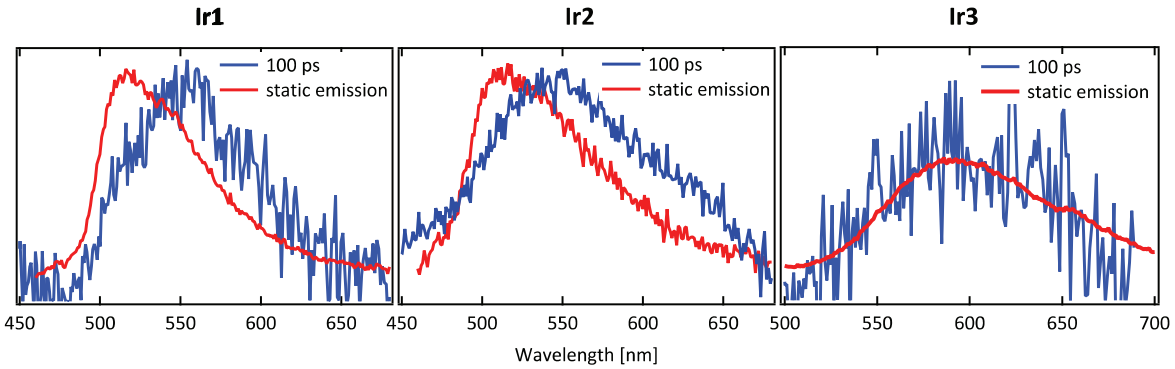

Figure 5-3: Comparison of the steady-state emission spectrum with the transient spectrum at 100 ps for **Ir1**, **Ir2** and **Ir3** in $CHCl_3$.

5.1.2 **Analysis of the results**

The basics and theory behind the applied algorithms for the treatment of time- and spectrally-resolved data, namely Singular Value Decomposition (SVD) technique and Global fitting (GF) together with the information they can provide is discussed in the (§2.4.3).

In order to disentangle the various spectral contributions in the spectra, singular value decomposition (SVD) is carried out after subtraction of the Raman signal, of the (t-λ) data for **Ir1**, **Ir2** and **Ir3** (Figure 5-1) as well as a global fit of the recorded kinetic traces. The resulting decay-associated spectra (DAS) are shown in Figure 5-4 for complexes **Ir1-2-3** and their decay constants are summarized in Table 5-1.

For each complex, the overall kinetics can be described by the characteristic time constants of $\tau_1 \leq 80$ fs, $\tau_2 = 0.9\text{-}1.6$ ps, and $\tau_3 > 1$ ns. The DAS associated to the shortest constant (DAS_1) is centred around 490 nm for **Ir1** and 530 nm for the other complexes, independent of the solvent. It appears that the blue wing of the DAS_1 extends to 465 nm (21500 cm^{-1}) (Figure 5-4) in which the lower amplitudes below <500 nm is due to the loss of efficiency in the detection (§2.4.1), so a relatively flat signal up to 500 nm can be considered. The observed shift in DMSO (Figure 5-2) and the appreciable rise of the signal between 550 and 600 nm are reflected in the DAS traces (where DAS_1 becomes negative). Likewise for **Ir2** and **Ir3**, the strong intensity drop at early times is also reflected in the DAS (note that these have been multiplied by 0.3 to fit them in Figure 5-4).

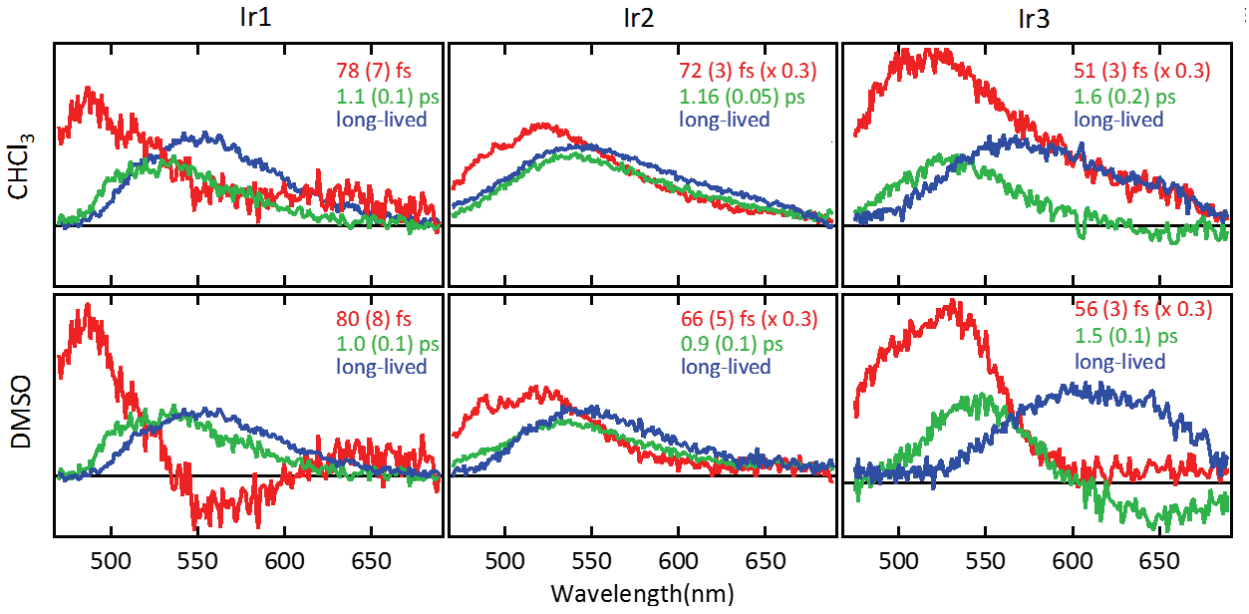

Figure 5-4: DAS curves (DAS_1 in red, DAS_2 in green and DAS_3 in blue) obtained via SVD of the 2D data reported in Figure 5-1.

Table 5-1: Time constants obtained from the SVD analysis of the emission of **Ir1**, **Ir2** and **Ir3** in $CHCl_3$ and DMSO excited at 400 nm. The third column for each time scale is the peak position.

Sample		$\tau_{1,VIS}$ [fs]		$\tau_{2,VIS}$ [ps]		$\tau_{3,VIS}$ [ps]	
$CHCl_3$	Ir_1	78 ± 7	485 nm	1.1 ± 0.1	528 nm	> 1 ns	547 nm
	Ir_2	72 ± 3	521 nm	1.2 ± 0.1	540 nm	> 1 ns	540 nm
	Ir_3	51 ± 3	516 nm	1.6 ± 0.2	524 nm	> 1 ns	560 nm
DMSO	Ir_1	80 ± 8	486 nm	1.0 ± 0.1	536 nm	> 1 ns	554 nm
	Ir_2	66 ± 5	515 nm	0.9 ± 0.1	535 nm	> 1 ns	550 nm
	Ir_3	56 ± 3	530 nm	1.5 ± 0.1	547 nm	> 1 ns	607 nm

For all complexes, DAS_2 has its maximum around 520 - 540 nm. In the case of **Ir3** in DMSO, it has negative values between 600 nm and 700 nm, which correspond to the rise of the 650 nm band (blue trace in Figure 5-2), and is not that clear in $CHCl_3$.

The long-time decay, whose spectral distribution is represented by DAS_3, cannot be accurately measured by our up-conversion set up. DAS_3 for **Ir1** and **Ir2** in both solvents peaks in the range of 540 - 550 nm i.e. to the red of the steady state emission (Figure 3.15) but for **Ir3**, it lies above 550 nm and shows a solvent-dependence with steady-state emission.

5.1.3 **Discussion of the results of fs, ps, and ns studies**

The early time signal, upon 400 nm excitation, is in all cases centred at 500-530 nm shifts slightly to the red in the first 200 fs (Figure 5-2), showing a significant ultrafast intensity loss in the blue part of the spectrum. Indeed, the DAS_1 traces of all three **Ir1-2-3** complexes in both solvents are found at somewhat lower wavelengths.

The DAS_1 at < 500 nm for **Ir1** with a maximum at 485 nm has to be emission from a low ^{3}MLCT state between ~440-455 nm (21980 cm^{-1}) but not the lowest at ~485 nm (20620 cm^{-1}). In the literature, this peak in the steady state absorption spectrum has been assigned to be predominantly ^{3}MLCT state spin-mixed with singlet (Table 3-2) as illustrated by its higher absorption than the lowest pure triplet levels. In particular Hay[157] assigned a T_3 (^{3}A) and T_1 (^{3}A) character to the states at 2.79 eV (485 nm) and 2.59 eV (455 nm), respectively (T is triplet and A is the symmetry representation)[*]. However, Samuel *et. al* observed a 180 fs decay (IRF = 222 fs) at

[*] Surprisingly they calculated more singlet fraction for 485 nm (0.69) than for 455 nm (0.11), which can be due to mixing more with ^{3}LC states than to ^{1}MLCT.

480 nm and 490 nm (upon 400 nm excitation of **Ir1**) that they attributed it to emission from vibrationally hot sub-state III with higher SOC, shorter lifetime, and faster dissipation of vibrational energy via IVR compare to the ultrafast luminescence (230 fs) they observed in 500-560 nm window. Now, with better time resolution (~150 fs in the visible) we observe decay at 80 fs in the range 470-500 nm. The faster kinetic hints not only to be a hotter sub-state III, but also coming from higher electronic triplet state (455 nm) with more significant singlet character. I conclude that this state (absorption at ~440-455 nm) is populated by ISC < 80 from ^{1}MLCT and decays (with IC) within ^{3}MLCT manifold to reach the lowest ^{3}MLCT. This ultrafast cascade agrees with the retarded rise of the signal that is present in the range of 550-600 nm at 1 ps (although the rise of the signal occurs at lower energy than the static emission which can be explained by dual emission, see below). Despite the clear conclusion of Thompson et al[59] about the absence of fluorescence (due to the fast ISC (<100fs)[210, 212]) in cyclometalated Ir complexes, the characteristic of this band yet has to be investigated. Theoretical calculations can explain better whether this state is a pure singlet or a higher lying triplet mixed with singlet character. Note that that the Raman peak was subtracted prior analysing the data, so the amplitude of the DAS_1 below 500 nm is not contaminated by Raman peak. On the other hand, similar to this ultrafast peak at 485 nm, a blue-shifted ultrafast feature is observed at ~450 nm upon ^{1}LC excitation of **Ir1** (see section 5.2) that is attributed to the emission from a higher spin-mixed state absorbing at 410 nm (section 5.2.3). We will see later that, exciting the sample into ^{1}LC populates all the states including the band at ~450 nm (and the lowest ^{3}MLCT) in <80 fs which later vibrationally relaxes within the lowest triplet state in ~300 fs. However, exciting the sample into ^{1}MLCT, this vibrational relaxation (~300 fs) is missing for the band at 485 nm. Because, it's absorption at 455 nm has a higher degree of triplet character, implies faster (<80 fs) electronic relaxation (via IC) to the lowest ^{3}MLCT.

The peak of DAS_1 (at 80 fs) in particular for **Ir1**, in the region between 500-540 nm, coincides with the steady state phosphorescence of **Ir1** (520 nm), so it is associated to the lowest ^{3}MLCT state. Applying the Stokes shift of ~2100 cm^{-1} (Figure 3.15) this emission is coming from the absorption state at ~485 nm that has been populated within 80 fs by IC from the higher triplet state at 455 nm absorption (Figure 3.15). This band (500-540 nm) later shows two more decay time scales at 1 ps and longer than 1 ns, which has been assigned to vibrational cooling to the solvent and phosphorescence emission of the relaxed lowest ^{3}MLCT[210]. However, Samuel *et. al* observed a 230 fs decay in the range 500-560 nm (exc. 400 nm) calling it an equilibration within

the three sub-states of the ^{3}MLCT. This time scale is absent in our result of ^{1}MLCT excitation due to the fact that these sub-states are very close lying (<100 cm^{-1})[159,160] and our set-up would not be able to resolve them.

In the case of **Ir2** and **Ir3**, the DAS of the shortest-lived component shows a maximum near 520 nm, making them most likely ^{3}MLCT states. However, unlike **Ir1**, the emission from these complexes undergoes a strong reduction (almost 50%) in the first 200 fs with no rise in the red part of the spectrum (Figure 5-4). The corresponding DAS_1 (Figure 5-4) are broader and red-shifted with respect to the DAS_1 of **Ir1** and have a much larger amplitude (around 70%) with respect to DAS_2 and DAS_3. For **Ir2-3**, we attribute it to a higher lying state of the ^{3}MLCT manifold that has a larger singlet character. Such short-lived emissions from higher lying ^{3}MLCT states have been reported in the case of Re[215] and Os[211] complexes. The strong loss of emission intensity in the first 200 fs can be explained by the fact that upon cascading from higher to lower energy triplet states, the singlet character of these states dramatically decreases, implying a strong decrease of the radiative rate. The strong loss of emission intensity in the first 200 fs can be explained by the fact that upon cascading from higher to lower energy triplet states, the singlet character of these states dramatically decreases, implying a strong decrease of the radiative rate.

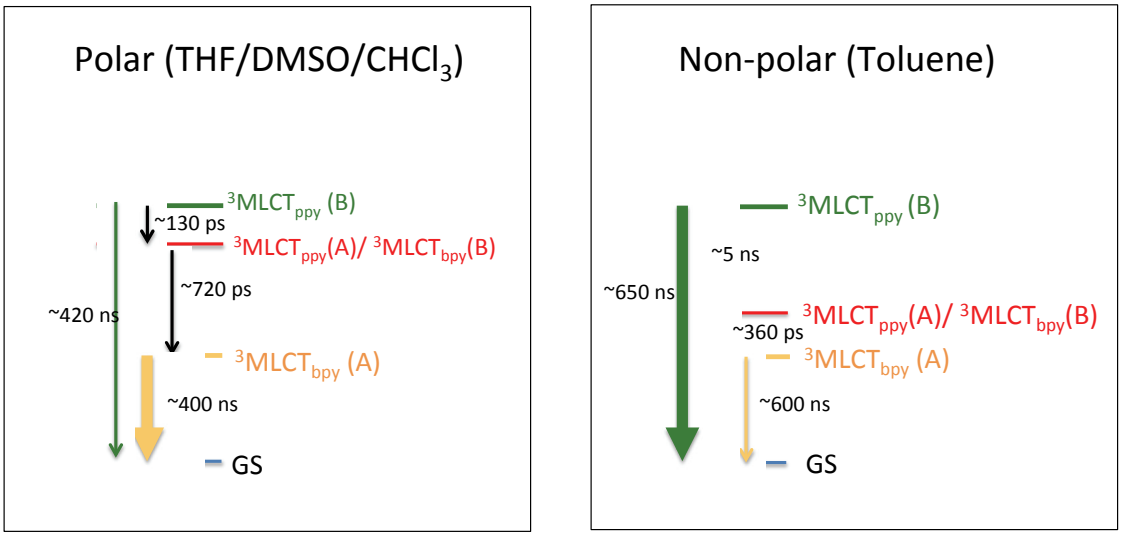

Figure 5-5: Proposed relaxation mechanism for **Ir3** by Wu et al.[162] Thickness of flashes shows the intensity. The intermediate state is a mixture of triplet from both ppy and bpy but with different symmetry than the main lowest triplet states of each ligand.

Finally, DAS_2 shows quite similar time constants τ_2 (0.9 to 1.4 ps) in all three complexes (Table 5-1), and it is shifted by a typically 700 cm^{-1} from DAS_1, which for **Ir1** this shift is even larger ~ 1920 cm^{-1}

(Figure 5-4). This red shift is larger than kT and it confirms the cascading scenario from higher lying triplets in all of them. As mentioned in the analysis section, in the case of **Ir3**, DAS_2 has negative values in the range 600-700 nm corresponding to the rise of the band peaking at 650 nm. This can be explained by the relaxation mechanism under 355 nm proposed by Wu et al. As shown in Figure 5-5, in their model following an ultrafast (<30 ps) population of $^3MLCT_{ppy}$ and $^3MLCT_{bpy}$ [which due to lack of temporal resolution they could not define a direct relaxation from ^1LLCT or a cascade through ^1MLCT (most probably according to the 266 nm results of **Ir1** (see section 5.2) it is a cascade process involving IVR, IC, ISC; perhaps a UV excitation experiment will lift the ambiguity), the former decays to an intermediate state while the latter is populated from that intermediate state (Figure 5-5). This intermediate state is a combination of $^3MLCT_{ppy}$ and $^3MLCT_{bpy}$ with different symmetry than the main lowest triplet states of each ligand. In a polar solvent (THF/ DMSO) the band at 520 nm (coming from $^3MLCT_{ppy}$) undergoes a fast (130 ps) decay to the intermediate state, while the $^3MLCT_{bpy}$ is only populated later (720 ps) in agreement with negative amplitudes of the negative DAS_2. However, in the nonpolar solvent (Toluene/ $CHCl_3$) the decay of $^3MLCT_{ppy}$ (~ 520 nm) state is delayed by 5 ns due to its larger energy gap with the intermediate state, and a rise time of 360 ps is observed for $^3MLCT_{bpy}$ (> 600 nm). This delayed rise time of 360 ps is out of our

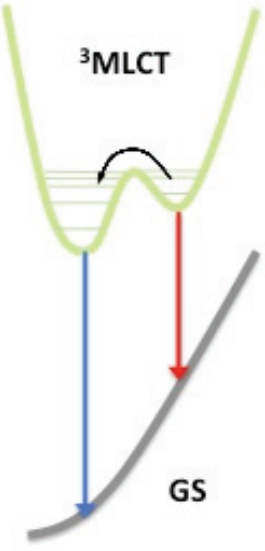

Figure 5-6: Schematic topographical representation of dual luminescence of red and blue emission in the relaxation process from the lowest 3MLCT state to the to the curved ground state surface of the lowest triplet state. The higher-lying minimum would emit in the red due to the curvature of the ground state while the lower energy minimum would emit in the blue reaching to the deeper region of the ground state surface potential.

detection time window so only the decay of this band is detected populating at very early steps (as they show up in the t=0 signal). As already pointed out for **Ir1-2**, the red shift (~ 1250 cm^{-1}) of the

maximum of DAS_2 (~536 nm) and DAS_3 (~554 nm) in DMSO with respect to the steady-state emission peak is remarkable and it is absent in the case of **Ir3** (Figure 5-4). A somewhat similar behaviour of the emission peak is also reported by Yersin et al.[160] In their temperature-dependent studies of the steady-state spectra of **Ir1** at low (LT) and room temperature (RT), Yersin and coworkers[50,159,160] observe an emission at 530 nm (at 1.5 K) that they attribute to sub-state I (the lowest triplet state splits into three sub-states due to ZFS effect, see §3.3.1.1), which is characterized by a Herzberg-Teller (HT) vibrational coupling with the ground state, i.e. the 0-0 transition is missing. Then, this emission shifts to blue at 30 K due to the emission from thermally populated sub-state II and III (§3.3.1.1) and because of higher SOC which carry significant allowedness with respect to their 0-0 transitions to the electronic GS than sub-state I and characterised by Franck-Condon (FC) emissions. At RT the shape changes for the liquid phase accompanying a red shift of the maximum. These considerations are not applicable here since we are at RT and in the short time domain. Rather, here mentioned results can be rationalised by invoking a mechanism of dual luminescence with the red component dominating at early times of the order of 100's ps, while the bluer component stemming from a lower energy conformation which is populated at infinite times. This is schematically depicted in Figure 5-6. The higher lying minimum would emit in the red due to the curvature of the ground state, while the lower energy minimum would emit in the blue, as it samples a deeper region of the ground state surface. The hypothesis of dual emission is not new. Dual phosphorescence mechanisms, based on double-well potentials or the availability of other triplet states closer in energy to the lowest lying ^{3}MLCT, have been proposed to explain the RT emission of various Ir-based complexes.[216-219] Recently, Kleinschmidt et al have shown that different minima can be found for the triplet state of lowest energy of **Ir1**, corresponding to slightly different structural configurations.[220] This result makes it reasonable to represent the lowest lying ^{3}MLCT state by a double-well potential surface as shown in Figure 5-6.

As already mentioned for **Ir1** and **Ir2**, the ^{3}MLCT emission involves the ppy moiety. The fact that it decays to another minimum over extended times (100s ps to infinite times) implies that the relaxation from the blue emitting minimum to the red one is slow and therefore the barrier from one configuration to the other is larger than kT. Given the similarity of the time-zero spectra of **Ir1-2-3**, I previously concluded that the ppy moiety is involved at early times in **Ir3**. However, at later times the bpy moiety is responsible for the steady-state ^{3}MLCT emission, which is populated

on a ps time scale (Figure 5-4). Therefore, a ppy to bpy Inter-ligand Energy Transfer (ILET) occurs. King et al. have proposed that the large Stokes shift in **Ir3** in liquid solution occurs because of a large distortion of the bpy ligand in the corresponding ^{3}MLCT excited state, induced by solvent relaxation,[54] however this explanation is not needed since the ppy and bpy related emission bands are at their characteristic energies, as observed in various transition metal complexes.

5.1.4 **Summary**

I measured broadband femtosecond luminescence after optical excitation at 266 nm and 400 nm to investigate the ultrafast photo-physics of $Ir(ppy)_3$ (**Ir1**), of two closely related heteroleptic ppy-based compounds (**Ir2** and **Ir3**) and of a ppz-based complex $Ir(ppz)_3$ (**Ir4**). The series of performed measurements here provide an extensive picture of the molecular photo-cycle of the prototype **Ir1** complex and provide the first observation of various ultrafast relaxation processes occurring in Ir complexes upon alteration of their ligand architecture.

After excitation of the molecules into the ^{1}MLCT band by 400 nm photons, a 80 fs ISC populates the ^{3}MLCT manifold. Phosphorescence is then emitted from the lower lying ^{3}MLCT state. Upon excitation of **Ir1** at 266 nm, promoting the molecule to the ^{1}LC state, I observe a double relaxation process: the ^{3}MLCT manifold can be populated through a cascade from the ^{1}LC to the ^{1}MLCT band via IC, and then ISC, or via direct ISC from ^{1}LC state. The broadband detection capability of our set-up extending into the UV allows for the first experimental observation of the transient ^{1}LC (centered at 330 nm) and ^{1}MLCT emission (between 410 and 500 nm) of **Ir1**. These early dynamics are complicated in the heteroleptic complexes **Ir2** and **Ir3** by an ultrafast relaxation to the lowest lying ^{3}MLCT state via an ultrafast IC through the ^{3}MLCT states of higher energy. This effect is related to the symmetry breaking that characterizes **Ir2** and **Ir3** with respect to **Ir1**, which induces a large energy splitting of the ^{3}MLCT states.

The successive dynamics of the Ir complexes are controlled by depopulation of the sub-state III of the lower lying ^{3}MLCT state via IC into the other two sub-states. These ps dynamics turn out to be not significantly altered by the symmetry breaking, except for **Ir3**. In this case, indeed, the data provide the first direct evidence of an Inter-ligand Energy Transfer (ILET) driven by solvation, which transfers the excitation initially localized on the ppy ligand to the bpy ligand in a few ps after photo-excitation.

What concerns the non ppy-based complex Ir4, I show that that the timing of the mechanism that quenches its phosphorescence at RT is limited to the nanosecond regime. This timescale is in agreement with the idea of thermal activation of a non-radiative channel of structural character, probably involving an Ir-N bond breaking and a rotation of the complex after photo-excitation.

5.2 Sub-nanoseconds PLUC studies of Ir1 - UV Excitation

The photophysics of large polyatomic molecules obeys the Kasha rule[62] according to which, they luminesce with appreciable yield only from the lowest excited state of a given multiplicity. The mechanisms involved along the relaxation pathways leading to this luminescence consist of intramolecular vibrational redistribution (IVR), internal conversion (IC) and intersystem crossing (ISC). IVR was specifically investigated in gas phase molecules such as Anthracene.[63,64] It was found to strongly vary with excess excitation energy, in other words, with increasing density of states (DOS). When dealing with electronically excited states, the DOS increases dramatically, as well as the couplings between electronic states. One may ask how fast can energy redistribution be in this extreme regime of DOS and intramolecular couplings? Because cascading among electronic states implies structural changes in the molecule, one anticipates the vibrational motions of the molecule to be the limiting factor. Here, using femtosecond photoluminescence up-conversion spectroscopy[214] upon 266 nm excitation of the ligand-centred (LC) absorption band **Ir1** we directly clock the relaxation cascade leading to the lowest triplet metal-to-ligand charge transfer (^{3}MLCT) state that lies ~1.6 eV lower in energy. I find that the relaxation cascade proceeds at a time scales of ≤ 10 fs, which is faster than some of the highest frequency modes of the system. The participation of the latter modes in conical intersections[221] and their overdamping to low frequency intramolecular modes is invoked.

5.2.1 Experimental Results of PLUC on Ir1-UV Excitation

Applied set-up for ultrafast PL up-conversion is described in §2.4.1 and in refs[214,222]. When operated for 266 nm excitation, it has a time resolution of ~150 fs in the ultraviolet (as inferred from the Raman peak of the solvent, Figure 5-8), while its detection limit corresponds to an emission quantum yield as low as ~10^{-6} [67]. This combination allows for the observation of the transient fluorescence from high-lying, dipole-allowed electronic transitions. For instance, the estimated pure radiative lifetime (~1 ns) of the deep UV-absorbing (<270 nm) Charge-Transfer-To-Solvent (CTTS) states of aqueous iodide prompted us to attempt and successfully detect their

fluorescence with a lifetimes as short as 60 fs.[222] However, the same experiment on the CTTS states of aqueous ferrous $[Fe(CN)_6]^{4-}$ did not correspond to pure radiative lifetimes of the order of ~1 ns - the same

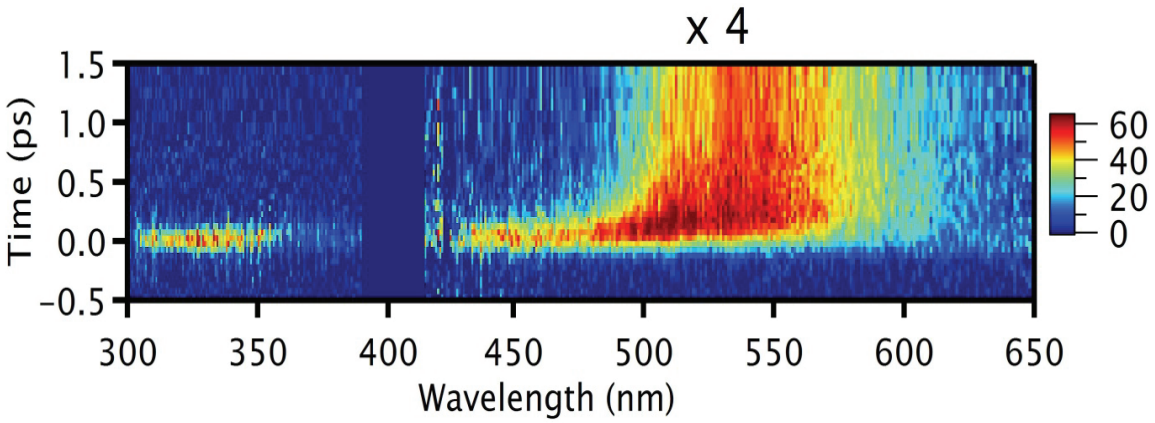

Figure 5-7: Time-wavelength plot of the 266 nm-excited emission of **Ir1** in DMSO in the first 1.5 ps after photo-excitation (no further variations are observed at longer times). The intensity of the data in the visible spectral region has been multiplied by 4 for the sake of clarity. The actual intensity ratio between UV and VIS emissions at time zero can be seen in Figure 5-8.

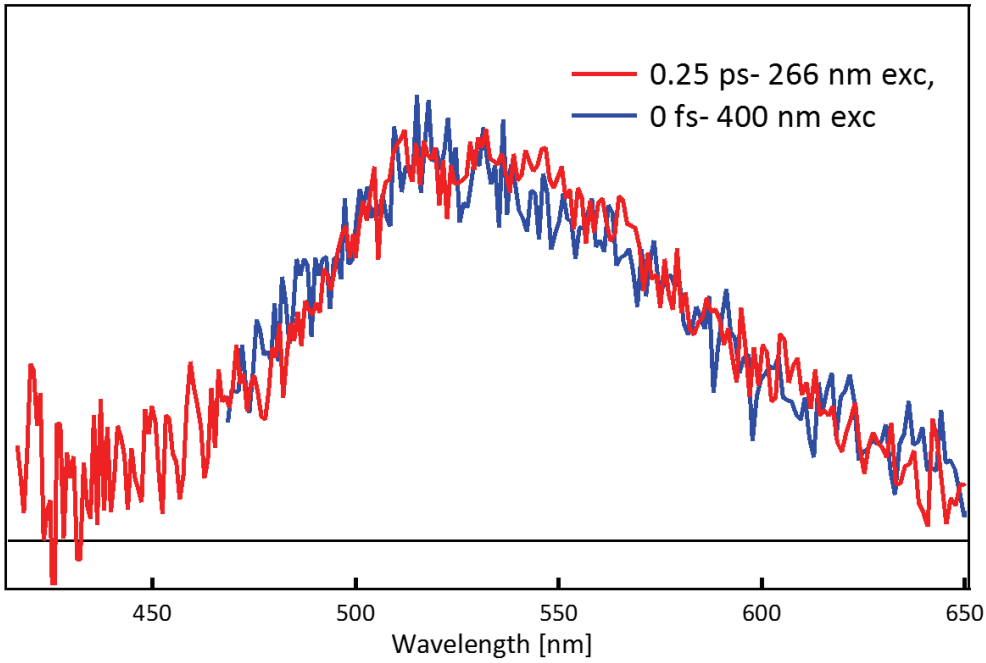

Figure 5-8: Fluorescence detected at a delay of t=0.25 ps after 266 nm excitation (red curve), as compared to that observed at time zero after 400 nm excitation (blue curve) in **Ir1** in DMSO.

reasoning as in the case of CTTS emission of aqueous iodide should be applicable. Figure 5-7 shows the time -wavelength (t-λ) plot of the luminescence of **Ir1** in DMSO upon 266 nm excitation of the

LC band. The emission range between 390 nm and 415 nm is excluded because of contamination by a strong scattering peak resulting from the pump and gate pulses. The remarkable feature of Figure 5-7 is the presence of a t=0 emission spanning from ~310 nm till ~550 nm, i.e. a range of ~1.5-1.6 eV. The emission in the <480 nm region is very short-lived while at longer wavelengths, further spectral evolution occurs (especially around 500 nm) within a ps, eventually leading to the long-lived phosphorescence. Figure 5-9 compares the emission spectrum at t=0 to the steady-state absorption spectrum. Figure 5-7 and Figure 5-9 show that a band at ~330 nm dominates the emission, while a broad and 4 times weaker signal shows up at λ>420 nm. Also, the 330 nm band appears as a mirror image of the LC absorption band of the complex, suggesting that it represents an LC emission. Further confirmation is provided by its comparison with the steady-state emission of the ppy ligand in solution (red trace in Figure 5-9) and apart from a small shift with respect to the emission of the complex, the two bands are very similar. Also the decay kinetics of the fluorescence is measured at 330 nm using single- wavelength detection and In Figure 5-10, it is compared to the Raman peak obtained under identical excitation conditions. Using the cross-correlation provided by the latter and by deconvolution, I found that the LC emission decays in 70±20 fs. This is significantly shorter than the lifetime of ~1 ns of ppy ligands in solution.[223] Further insight into the 266 nm-excitation induced intramolecular dynamics comes from the time-gated emission spectra shown in Figure 5-11. Just as in Figure 5-7, it can be seen that the fluorescence rapidly decays at wavelengths <500 nm while it slightly rises at >500 nm, so that the 250 fs transient exhibits a single band only, peaking at ~520 nm.

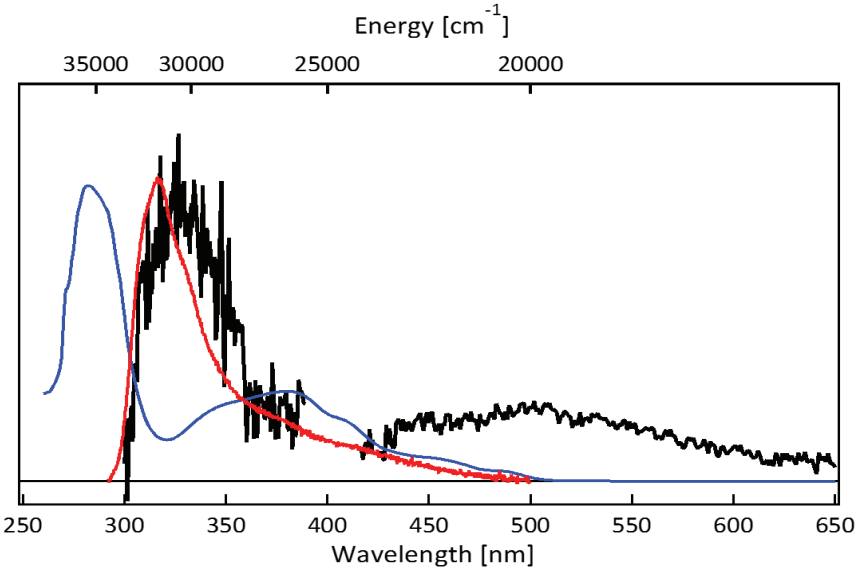

Figure 5-9: Time-zero emission spectrum (black) upon excitation at 266 nm of **Ir1** in DMSO, along with the normalized steady-state absorption spectrum (blue). The red trace shows the steady state emission spectrum of the ppy ligand dissolved in DMSO solution and excited at 266 nm.

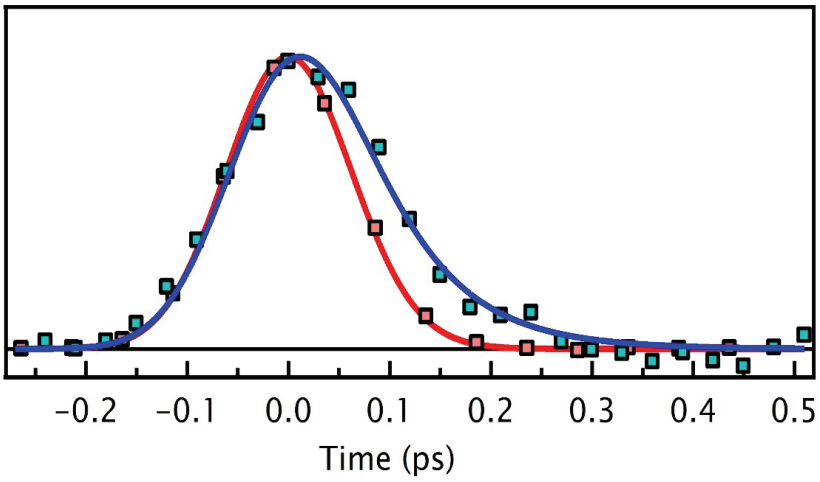

Figure 5-10: (Green squares) Fluorescence kinetic trace of the LC emission of $Ir(ppy)_3$ in DMSO measured in single-wavelength detection mode at 330 nm upon 266 nm excitation. (Red squares) Instrument response function of the set-up (IRF=150 fs from a gaussian fit) as measured by a trace of the Raman signal of the solvent. The continuous blue line is a fit by a convolution of the IRF with an exponential decay having a time constant of 70±20 fs.

This band later undergoes a further, minor decay on the blue side and by 2 ps, it is centred at ~540 nm where it remains thereafter. The 266 nm-excited emission at 250 fs time delay is identical to the spectrum obtained at t=0 under 400 nm (Figure 5-8), implying that the extra features in the <470 nm region are only fed by the UV excitation. Therefore, the 266 nm-excited fluorescence at

t=0 covers the entire range up to the main band at 520-540 nm, whereas only the latter can be observed upon 400 nm excitation.

The 520-540 nm emission coincides with the steady-state phosphorescence from the lowest ^{3}MLCT state, whose absorption band is the weak feature at 485 nm (20620 cm^{-1}) in Figure 3.15. This implies an absorption-emission Stokes shift of ~2100 cm^{-1}. Using the same Stokes shift, I find that the higher energy transient emission at ~450 nm, observed only upon UV excitation, can be attributed to the state whose absorption lies at 410 nm (Figure 3.15). It is not clear if this state is a singlet or a higher lying triplet but in either case, it must be strongly spin-mixed, as witnessed from its absorption intensity, which is higher than that of the predominantly triplet MLCT bands on its red side.

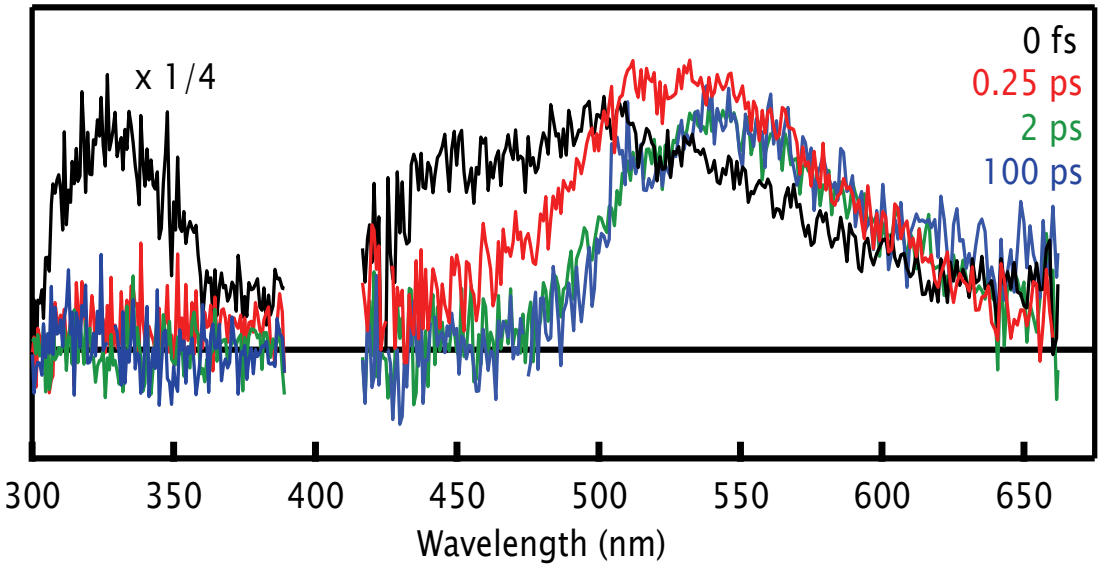

Figure 5-11: Luminescence spectra of Ir1 in DMSO at 0 fs (black), 200 fs (red), 2 ps (green) and 100 ps (blue) time delay upon 266 nm excitation. The data between 390 and 420 nm are not considered because of the presence of a strongly fluctuating background.

5.2.2 **Analysis of PLUC Results of Ir1-UV Excitation**

A singular value decomposition (SVD) of the (t-λ) data is carried out in combination to a global fit (GF) of the corresponding kinetic traces, which are standard approaches to better disentangle the various spectral contributions in time-resolved data. The results are identical in both cases. The basics and theory behind applied algorithms for the treatment of time- and spectrally-resolved data, SVD technique and GF were explained already in section 3.IV.3. Here, I present the

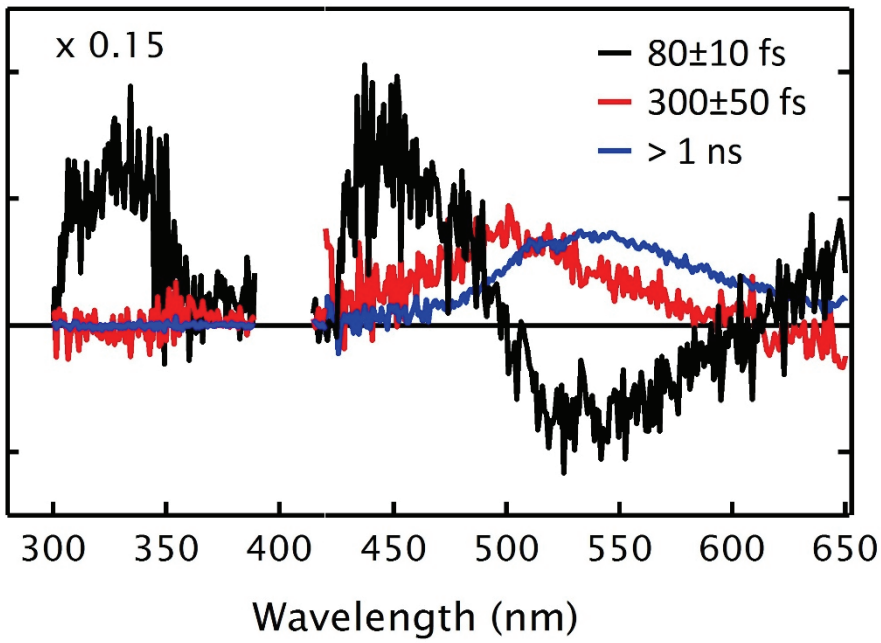

Figure 5-12: Decay associated spectra (DAS) obtained by a singular value decomposition (SVD) of the time-wavelength emission data of Ir1 in DMSO (Figure 5-7) upon 266 nm excitation. The time constants associated to the three spectra are reported in the legend. The UV portion of the DAS has been multiplied by 0.15.

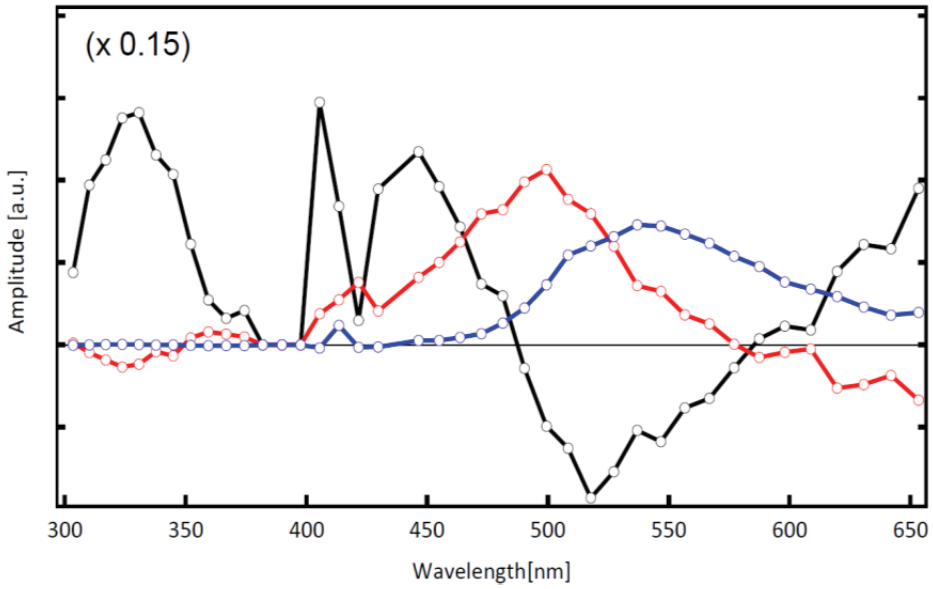

Figure 5-13: Global Fit of the time traces extracted from the time-wavelength plot (Figure 5-7). The extracted decay times are 72±10 fs (black) and 300±25 (red). The blue trace accounts for the long-lived component, which was set to 1 ns. These time constants are also confirmed by the fit of kinetic traces shown in Figure 5-14.

results of the SVD (Figure 5-12) and GF (Figure 5-13) analysis. Both approaches show that the overall kinetics can be described by the characteristic time constants of $\tau_1 \approx 80$ fs, $\tau_2 \approx 300$ fs, and $\tau_3 > 1$ ns and the resulting decay-associated spectra (DAS) are shown in Figure 5-12. The time con-

stants are further confirmed by fitting the kinetic traces at three characteristic wavelengths as shown in Figure 5-14, with the results of fits given in Table 5-2. The ~80 fs DAS fully confirms the trends of Figure 5-7, Figure 5-11 and in that it reproduces the spectral profile of the LC emission at 330 nm, along with the MLCT emissions down to ~450 nm. The ~80 fs time constants coincides with the decay lifetime derived from the kinetic trace of the LC emission (Figure 5-10) and of the states emitting up to ~450 nm (Figure 5-7). At longer wavelengths, the 80 fs DAS becomes negative, which means that it contributes to the rise of population in the region of the long-lived ^{3}MLCT emission (>1 ns DAS in Figure 5-12), but also partly to that of the ~300 fs DAS. Thus, the arrival of the population in the lowest MLCT state and its departure from the LC state are identical within the uncertainty of these measurements.

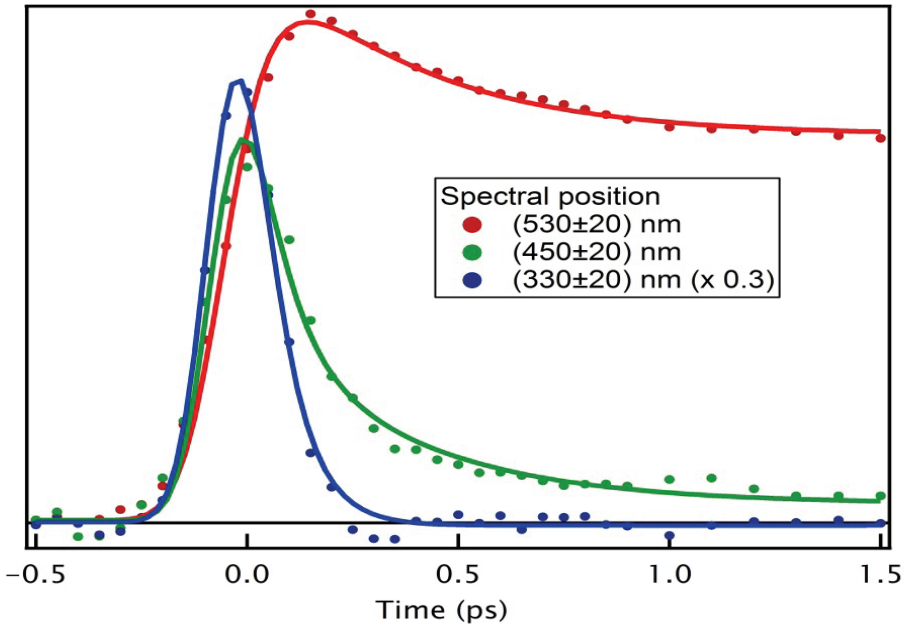

Figure 5-14: Kinetic traces extracted from time-dependent emission data of 266 nm-excited Ir1 (Figure 5-7) by spectrally integrating the signal in three different windows (330±20, 450±20, 530±20 nm). Data are fitted by a multi-exponential relaxation function convoluted with the instrumental response function (IRF) of the setup. The table reports the time constants obtained by the fit and the associated amplitudes (normalized in such a way to sum up to one at each spectral position). Negative amplitudes correspond to a rise of the signal.

Table 5-2: time constants extracted from the fit of the kinetic traces in Figure 5-13

Time constants (ps)	Amplitudes 530 nm	Amplitudes 450 nm	Amplitudes 330 nm
0.072±0.010	-0.89	0.72	1.00
0.35±0.10	0.74	0.26	0.00
1000 (fixed)	1.14	0.02	0.00

5.2.3 Discussion - An intramolecular electronic relaxation at sub-vibrational time scale

These observations can only be rationalized by assuming that the LC decay is the rate-limiting step of the entire ensuing cascade, which itself must be extremely fast (an upper limit of 10 fs is estimated). Thus, the LC state decays to the manifold of near-resonant MLCT states and the subsequent intramolecular relaxation therein proceeds in < 10 fs. The ~70-80 fs component appears as a decay of the intermediate states (350 to 500 nm) because they are decaying on a much shorter time. It should be stressed that the region between the LC and the lowest ^{3}MLCT state is characterized by a very high density of strongly spin-mixed MLCT states (over 100),[157,224] and this number explodes when including the vibrational degrees of freedom. The 300 fs DAS reflects the kinetics retrieved in the 450-500 nm region. This DAS is exclusively positive, close to the steady-state emission and is largely populated within 80 fs, like the > 1 ns DAS. If it were the emission band of another, intermediate MLCT state, its decay would have been reflected as a rise of the >1 ns component, but this is not the case. Therefore, we conclude that it reflects a vibrational relaxation process within the lowest ^{3}MLCT state, which narrows and shifts to the red. The ~300 fs time scale is close to the 230 fs component reported by Samuel and co-workers[210] in their monochromatic photoluminescence up-conversion studies of Ir1 upon 400 nm excitation. They attributed it to an equilibration within the three sub-states of the ^{3}MLCT, but I rule out this explanation based on the fact that these sub-states are very close lying (<100 cm^{-1})[159,160] and our set-up would not be able to resolve them.

The overall relaxation cascade inferred from the present results is schematically shown in Figure 5-15. Upon fs excitation of the LC state at 266 nm, decay to the manifold of close lying spin-mixed MLCT states occurs in ~70 fs, thereafter intramolecular electronic-vibrational relaxation proceeds at extremely short times (< 10 fs) leading to population of the lowest ^{3}MLCT state in high

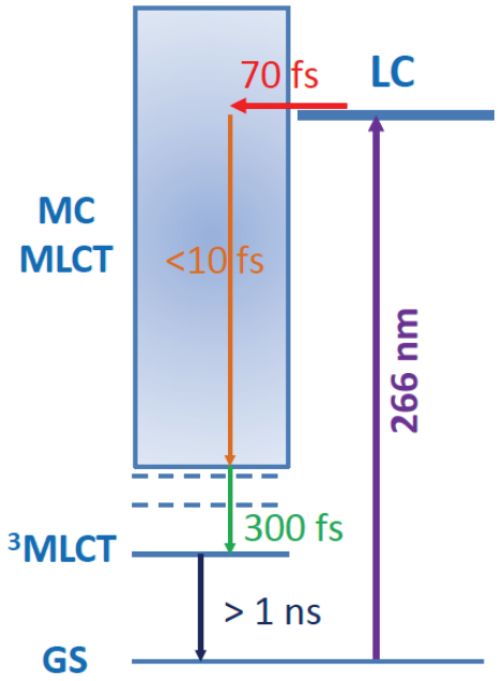

Figure 5-15: Intramolecular relaxation cascade of Ir1 upon 266 nm excitation of the LC state. Relaxation to the manifold of metal-centered (MC) and metal-to-ligand-charge-transfer (MLCT) states occurs in 70 fs. IVR/IC within the latter occurs in < 10 fs leading to formation of the vibrationally hot lowest ^{3}MLCT state, which relaxes in ~300 fs. Radiative decay back to the ground state ensues in >> 1 ns. The dashed lines represent high vibrational levels of the lowest ^{3}MLCT state.

vibrational levels. Vibrational relaxation within this state requires ~300 fs followed by the radiative decay to the ground state on much longer time scales (>> 1 ns). In another study, with monochromatic detection, Samuel et al[213] investigated the relaxation cascade of the heteroleptic iridium complex bis(2-(9,9-dibutylfluorenyl)-1-isoquinoline(acetylacetonate) iridium(III), denoted as Ir(dbfliq)$_2$acac, which has a low lying LC band peaking at 370 nm with a wing extending beyond 400 nm and three distinct singlet bands between 450 and 570 nm. They excited at 400 nm and concluded that the $L_1 \rightarrow S_3$ process is very fast, based on the lack of an observable rise-time in the S_3 kinetics and the small energy difference between the states. The decay from the highest MLCT singlet state (S_3 to S_2) was reported to occur in <20 fs, while IC from S_2 to S_1 and ISC from S_1 to T_1 were found to be substantially slower (65 and 75 fs, respectively). This relaxation cascade is somewhat different to the case reported here, in the sense that the LC decay is very much faster, while relaxation within the lower states slows down. However, the fact that some steps occur in <20 fs is a common feature to the present and previously reported cases.[225] The speed at which these relaxation processes occur is impressive, in view of the energy range they cover (here, ~1.6

eV). As mentioned above, they were already hinted to from indirect measurements on TM complexes,[225] on organic molecules,[226] and on biological chromophores in proteins such as rhodopsin where, within the 20 fs resolution of their experiment, Polli et observed a stimulated emission with a Stokes shift of about 0.7 eV with respect to the pump energy.[227] The sub-10 fs time scales invoked here and in these examples is below the period of most of the highest frequency modes of the systems under study. Factors such as high density of states (i.e. very small energy gaps) and strong electronic and spin-orbit couplings obviously play an essential role in favouring the ultrafast relaxation. Also, it was shown by theory that conical intersection (CI's), mediated by high frequency modes, enable much faster internal conversion processes than avoided surface crossings, when energy dissipation to a bath is included, e. g. here this would be to the bath of intramolecular degrees of freedom in addition to the solvent.[228] As a matter of fact, CIs were invoked to explain the observations in rhodopsin.[227] However, the occurrence of relaxation via CI's implies a change of coordinates in going from one state to the other, i.e. conformational distortions. Therefore, the highest frequency modes must be strongly overdamped and transfer their energy very efficiently to low frequency modes while promoting IC/ISC through conical intersections. These result do not mean that the system is cold in such a short time scale, but simply that it is cold with respect to the high frequency Franck-Condon modes, which are those dominating the optical transitions. The redistributed energy goes to the low frequency modes, which are often optically silent.

5.2.4 **UV Excitation of Ir4**

Upon 266 nm excitation of **Ir4** in DMSO, only a very weak emission at 450 nm (maximum of the **Ir4** steady state emission) is observed that requires long integration times in order to measure the single wavelength kinetic traces shown in (Figure 5-16). In the case of **Ir4**, the lack of (t-λ) plot for this system makes the identification of the relaxation cascade uneasy. The signal recorded at 450 nm (maximum of its steady-state emission) shows a rise time of 140 fs, which probably reflects population of the ^{3}MLCT state. Given the sub-kT splitting of the ^{3}MLCT sub-states (60 cm^{-1})[59], it is most likely dominated by sub-state III as in the other complexes. The origin of the 530 fs decay is unclear, but it could be relaxation of a higher ^{3}MLCT with a stronger radiative transition rate, which overlaps with the 450 nm emission, like in the other complexes. In fact, comparing the energy of frontier orbitals calculated by TDDFT for **Ir1**[157] and **Ir4**[165] and lower-lying singlet and triplet states shows that the S_1 state for **Ir1** lies ~ 0.1 eV below the T_3 and only two triplet state

have been calculated to be lower than S_1. However, in the case of **Ir4** Kim *et. al* calculated 4 triplet states below the lowest singlet state. Additionally, the energy gap between the two triplets above and below the lowest singlet, T_3 and T_2, in **Ir1** is ~ 0.2 eV. This is higher than that between T_5 and T_4 ~ 0.13 eV in **Ir4**. Probably, the higher density of triplet states (with overall smaller energy gap between them with respect to **Ir1**) increases the probability of IC cascading in the ^{3}MLCT manifold for **Ir4**.

The **Ir4** phosphorescence signal has a lifetime of 1.6 ns in DMSO at RT, *i.e*. about two orders of magnitude shorter than that of **Ir1** (170 ns). This effect is not present at LT, for which a lifetime of tens of µs has been measured.[59] Therefore, the strong quenching at RT can be attributed to the thermal activation of a non-radiative channel to the ground state as reported in the case of Copper complexes.[229] On this point, according to refs [59,60], the calculated energy barrier to the non-radiative state for **Ir4** has a value comparable to the Ir-N bond strength between the Ir ion and a ppz ligand. Therefore at RT, thermal energy would be sufficient to cause the rupture of this bond after excitation. A rotation of the ppz ligand would then stabilize the complex into a trigonal bipyramidal geometry, leading to a five-coordinate species with a triplet metal-centred (^{3}MC) character.[59]

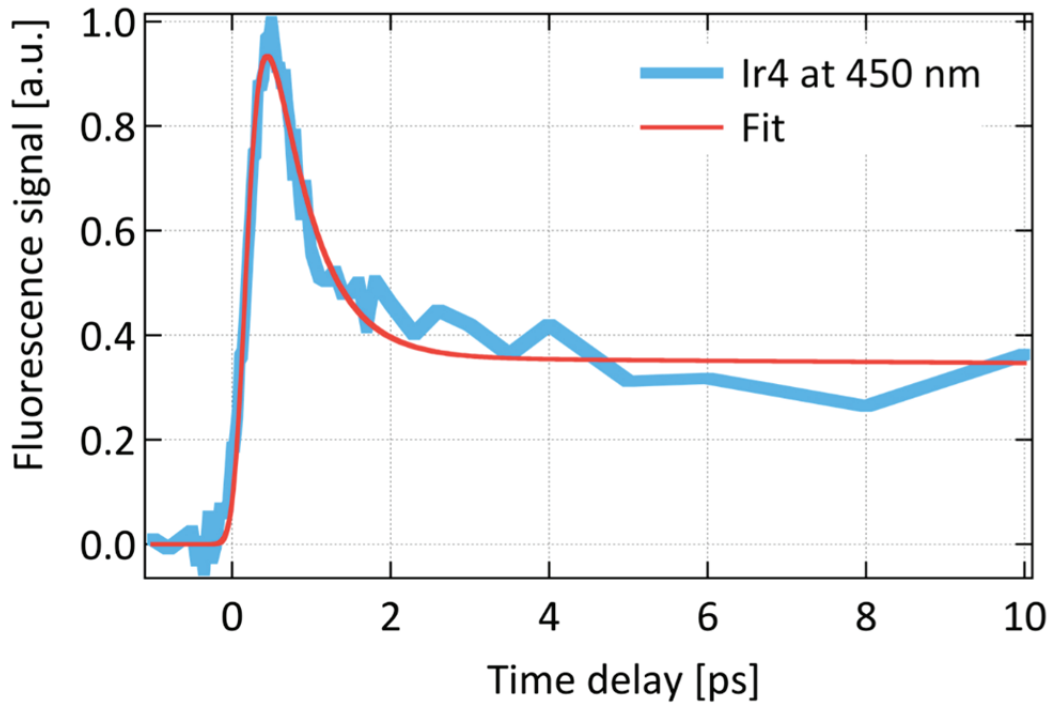

Figure 5-16: Kinetic trace of the emission of **Ir4** in DMSO at 450 nm, upon 266 nm excitation.

5.2.5 **Summary**

The observation of a clear-cut, short-lived emission of the initially excited high-lying ^{1}LC state in a TM complex provides us with an unambiguous clocking of the ensuing intramolecular dynamics, which is found to occur in < 10 fs. In this respect, due to its notably longer lifetime, the LC state in the present system provides a “bottleneck” to the intramolecular relaxation compared to these extremely short decay times. The fact that large energy ranges of the cascade can be crossed at sub-vibrational time scales is attributed to the participation of high frequency modes, probably through conical intersections, and to their overdamping by dissipation to the lower frequency modes of the system.

5.3 Nanosecond TCSPC studies for Ir1 and Ir4

The nanosecond-resolved photoluminescence lifetimes of **Ir1** and **Ir4** are recorded in DMSO. For **Ir1** in DMSO a lifetime of 170 ± 30 ns was found across the entire profile of its emission band (Figure 3.15). Reduction of the lifetime of **Ir1** at RT from 1.6 μs to 45 ns in aerated CH_2Cl_2 and to 36 ns in aerated 2-Methyltetrahydrofuran (2-MeTHF) have been previously reported.[59,212] This lifetime shortening is related to oxygen quenching occurring in aerated solutions.[230] The ppy-based complexes **Ir2** and **Ir3** behave similar to **Ir1**, as previously reported.[231-233]

In the case of **Ir4**, the multi-exponential fit (convoluted with a Gaussian IRF) of its kinetic trace (Figure 5-17-b) yields an IRF limited rise (140 ± 50 fs), followed by two decays with time constants of 530 ± 80 fs (78%) and a long one that is fixed at 1.6 ns (22%), according to the nanosecond-resolved measurements (Figure 5-17-b). In contrast, **Ir4** luminescence decays faster with respect to ppy-based compounds. Figure 5-17 shows the photoluminescence emitted at 450 nm at RT by **Ir4** in an aerated solution of DMSO, decaying with a time constant of 1.6 $\pm$ 0.1 ns. The strong decay of the **Ir4** phosphorescence is temperature-dependent, as it is not present at low temperatures.[59]

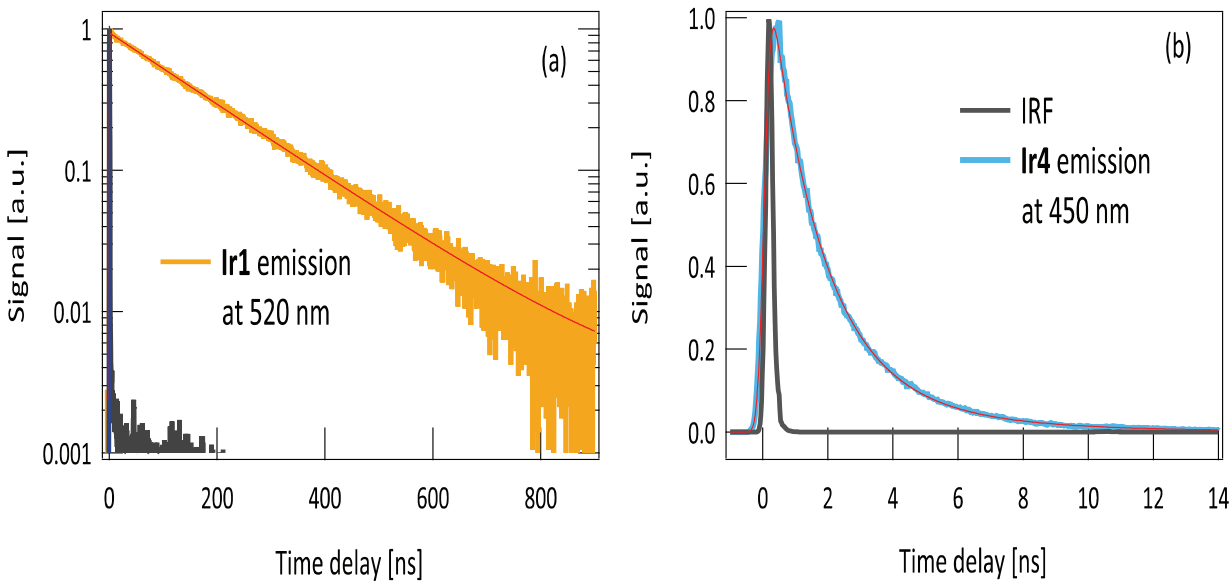

Figure 5-17: (a) Nanosecond-resolved signal at 520 nm emitted by **Ir1** in DMSO. The red line shows the fit of the data with an exponential decay function. (b) Nanosecond-resolved signal emitted by **Ir4** at 450 nm. The red line shows the fit of the data with a function obtained by the analytical convolution of an exponential decay with the IRF (assumed to be gaussian) of the instrument.

Chapter 6 Static and Time-resolved Complex X-ray Absorption Spectroscopy of Tris-Cyclometalated Iridium Complexes

Despite extensive optical studies on the cyclometalated iridium compounds aiming to unravel their remarkable "triplet harvesting" character for PHOLED and OLED applications, there is a lack of studies to directly probe the iridium as the active site of these complexes. Almost all X-ray studies on the iridium complexes focused on defining the geometric structure of the cyclometalated iridium complexes via X-ray crystallography or diffraction. However, Kim *et. al* conducted XAS study on iridates (iridium oxides) powder samples at the L_2 and L_3 edges of Ir investigating the strength of spin-orbit coupling (SOC)[68]. Another XAS survey was done on relatively complicated system of a NDI-PMI-Ir catalyst triad to investigate the oxidation state change during the catalytic mechanism upon photoexcitation of PMI, which provided direct evidence of $Ir^{+3} \rightarrow Ir^{+4}$ oxidation state change.[69]

The severe lack of element specific X-ray absorption spectroscopy (XAS) and time-resolved X-ray absorption spectroscopy (TR-XAS) studies on this important class of organometallic compounds prompted us to study the ground state of four different iridium cyclometalated complexes Ir1 (**Ir1**), $Ir(ppy)_2(pic)$ (**Ir2**), $[Ir(ppy)_2(bpy)]^+$ (**Ir3**), and $Ir(ppy)_3$ (**Ir4**) by means of XAS (§ 6.1). To our knowledge, this is the first systematic study of these tris-cyclometalated iridium complexes in solution via x-ray absorption spectroscopy providing more insight about the electronic (§ 6.1.1.2) and geometrical structure (§ 6.1.1.1) of the ground state and the triplet-excited state. We have successfully measured (§ 6.2) the structural and electronic changes upon

laser-excitation of tris-cyclometalated Iridium complexes **Ir1** and **Ir4** by time-resolved X-ray absorption spectroscopy (TR-XAS) at the Ir L_3-edge both in dichloromethane (DCM) and dimethylsulfoxide (DMSO). In addition, we followed the kinetics of their excited state population after visible excitation (§ 6.2.3).

6.1 The ground state of cyclometalated Iridium complexes

The photophysics of transition metal complexes has received significant attention due to their potential applications in photocatalysis and solar energy conversion or as emitters in organic light-emitting diodes or devices (OLEDs). Especially for the case of the latter, the focus of this research has been upon the heavier (4th or 5th row) transition metals with partially filled d-shells, such as iridium and platinum. The reason for this arises from the spin statistics of excited state formation after electrical excitation. Indeed, because only 25% form singlet states (S_1), and in order to achieve high efficiency one must ensure that the T_1 state (75% of the excited state) is effectively coupled to the molecular ground state (S_0). This is achieved through strong spin-orbit coupling (SOC) between the two states.

Second-generation phosphorescence-based OLEDs (PHOLEDs) overcame this limitation by doping the host layer with metal-organic emitters.[5] Through exploiting the large SOC of the metal centre, it becomes possible to also harvest the triplet excitons and consequently achieve almost unity quantum efficiency. However, to date the only phosphorescent materials found practically useful are iridium and platinum complexes. This is because alternative complexes, based upon more abundant metal ions, tend to have smaller SOC and therefore exhibit much lower $T_1 \rightarrow S_0$ radiative rates. In such cases the emission decay times are too long, and non-radiative processes, saturation and/or triplet-triplet annihilation effects lead to quenching of the excited states, reducing the device efficiency.[50] The experimental procedure for the static and the picosecond XAS experiments along with the theoretical methodology has already been described in (§ 2.2).

6.1.1 X-ray absorption spectra of cyclometalated iridium complexes at Ir- L_3 edge

I studied two homoleptic and two heteroleptic forms of cyclometalated iridium complexes by means of steady-state XAS at the L_3-edge of the iridium (origin of the core electron is the $2p_{3/2}$ state- see § 2.1.3) in its Ir(III) oxidation state. The homoleptic compounds introduced (§ 3.3.1) are **Ir1**, and **Ir4**, while the heteroleptic compounds are **Ir2**, **Ir3**. The measurements were carried out in the total fluorescence-yield mode, using 1.5-3.5 mM solutions in DCM and DMSO according to

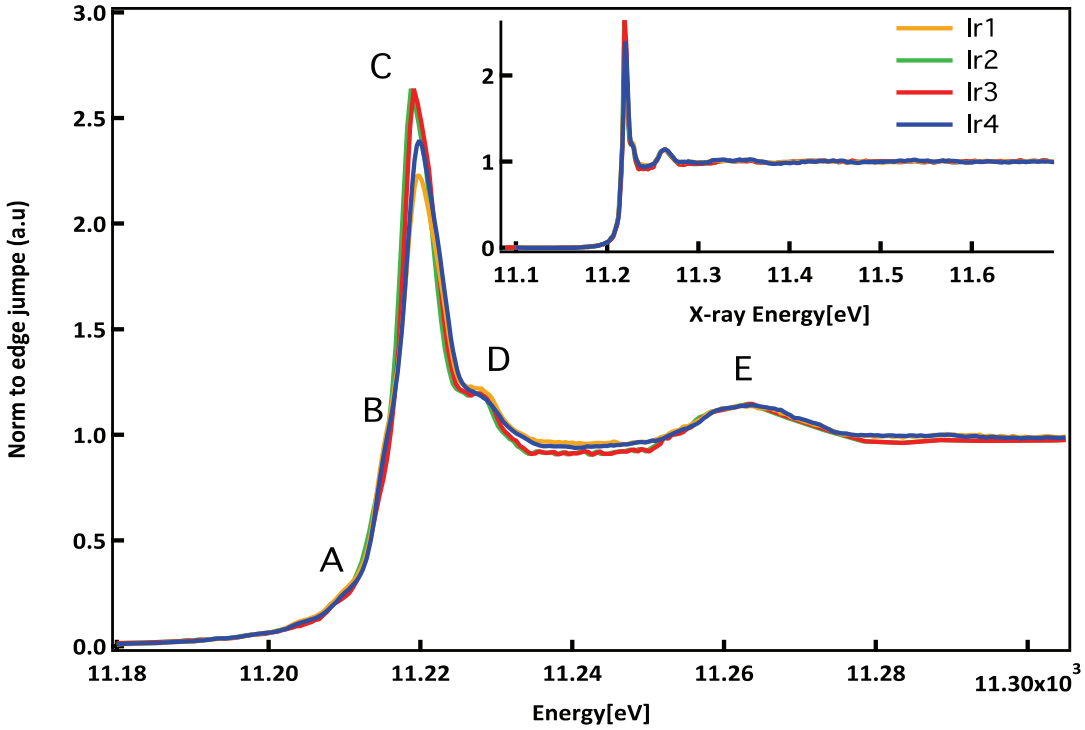

Figure 6-1: Zoom into the normalized ground state X-ray absorption spectra of 1.65 mM solution of **Ir2** (green)**, Ir3** (red) in DMSO and 1.651 mM solution of **Ir1** (yellow), and 3.11 mM solution of **Ir4** (blue) in DCM recorded in total fluorescence yield mode at the Ir L_3-edge. Labels correspond to below edge region (A, B, and C), above edge region multiple scattering (D and E). The inset shows the whole range of the spectra, which is fairly structure less in the EXAFS part.

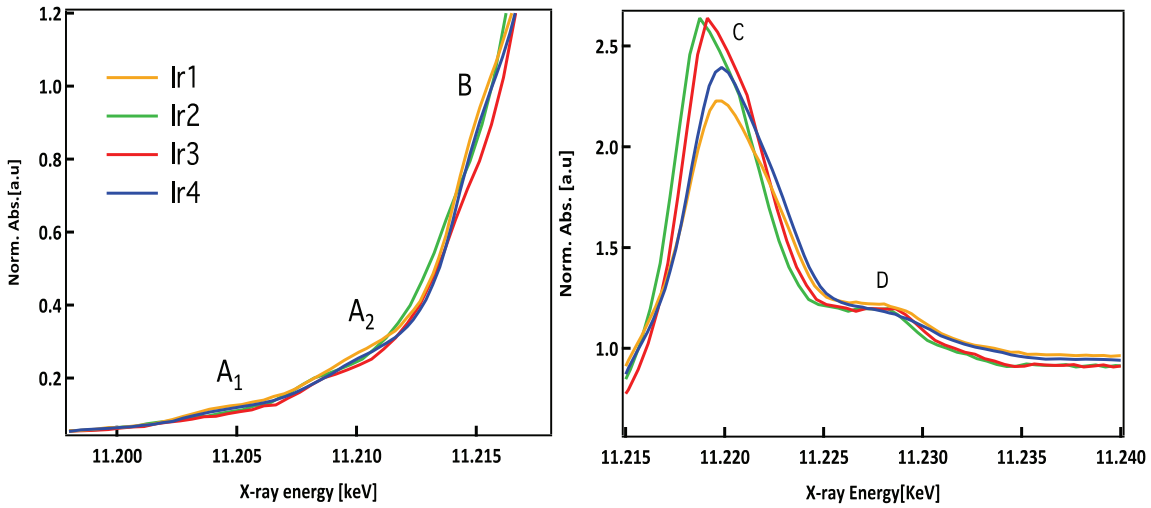

Figure 6-2: Zoom into the pre-edge region (left) and the white-line peaks (right) of ground state XAS spectra of the four complexes as shown in Figure 6-1. Features A and B in the low energy shoulder of the white-line can be a signature of additional electronic transitions from metal core-ligand charge transfer (MLCT). Note that in the left panel, **Ir3** and **Ir2** do not show feature B. Also, **Ir3** has shifted by ~1 eV to the higher energy with respect to **Ir2**.

their highest solubility at standard condition (room temperature and pressure) exposed to air. The samples were continuously flown through a sheet jet (0.5 mm path length) to avoid damage caused by x-ray irradiation. Several successive scans were averaged together in order to improve the signal-to-noise (S/N) ratio. The whole set of steady-state spectra of the four different forms of cyclometalated Iridium complexes is shown in Figure 6-1. The background subtraction and spectra normalization were performed using the ATHENA package[234]. The EXAFS part of each spectrum is normalized to one.

In other words, the spectrum is normalized to the edge as described in (§ 6.1.1). The range of 11.10 keV to 11.65 keV covers both XANES and EXAFS regions (§ 2.I). The ionization potential (E_0) is estimated (§2.1) from the first derivative of the static X-ray absorption spectra for **Ir1** and **Ir4** complexes to be at 11218 eV (within 1 eV energy resolution). In analogy, the E_0 values are estimated for both of **Ir3** and **Ir2** to be at 11229 keV (within our 1 eV energy resolution). Several features appear below and above the edge (E_0) in the spectra: (i) a weak pre-edge (A) at 11.210 keV, (ii) a more intense pre-edge feature (B) at 11.213 keV, (iii) the white-line (C) at ~ 11.220 keV, and multiple scattering features (D and E) at 11.227, 11.263 keV, respectively. The inset of Figure 6-1 shows the whole range of the spectra, which is fairly structure-less in the EXAFS part, E> 60 eV above the edge.

In the following we will assign the main features of the ground state XAS spectra shown in Figure 6-1. Figure 6-2-left shows the zoom into the pre-edge region with main weak resonance around 11.215 keV (feature B). It is interesting to note that the spectra of both **Ir1** and **Ir4** appear to show feature B, while it is not apparent in the spectra of the other two complexes. Considering the energy of feature B relative to the energy of the white line (WL), this resonance is consistent with a 2p-5d (t_{2g}) transition as observed in $[Os(bpy)_2dcbpy]^{2+}$.[235] However, in this case Os (II) has a vacancy in the 5d(t_{2g}), which does not hold for Ir(III). A similar effect was also recently observed for a series of rhenium complexes[236] and is discussed in more detail below. It will be shown later that they may correspond to transition from the core level $2p_{3/2}$ to the lowest-lying unoccupied valence π^* orbitals of pyridine or pyrazole ligands (§ 3.3.1) with MLCT character. In fact, the $5d^6$ configuration of Ir(III) in the low spin state of these complexes corresponds to fully occupied $d\pi$ (t_{2g}) orbitals in the ground state. According to (§ 3.3.1) unoccupied $d\sigma$ orbitals of Ir(III) sit higher in energy, well above the HOMO orbitals. Therefore, one should not expect any bound-bound transitions in the pre-edge region. Moreover, there are two features at lower energy labeled as features A_1 and A_2

that their origin is not clear yet.

TM complexes with an empty or partially occupied metal d-shell exhibit a strong white line (WL) due to the dipole allowed transitions from the $2p_{1/2,3/2}$ core orbitals into unoccupied valence d-orbitals[237]. In the case of Ir (III) with full ($d\pi$) t_{2g} orbitals, the WL at the L_3-ege corresponds to a transition from $2p_{3/2}$ to $5d\sigma$ (e_g) orbitals. Figure 6-2-right zooms into the edge-region reflecting the electronic structure and shows distinct differences in the intensity of the WL. Compared to **Ir1**, the WL intensity of **Ir4** is somewhat larger indicating a larger contribution of Ir 5d character in the region. This increase in WL intensity for **Ir4** is accompanied by a decrease in the above-ionization resonance at 11.227 keV (feature D). The spectra of both **Ir2** and **Ir3** are very similar to each other, and red shifted in comparison with the other two. Additionally, the WL intensity in the heteroleptic complexes is higher than in the homoleptic ones. This is indicative of an increase in electron density on the Ir with larger contribution of Ir 5d character in the region.

In Figure 6-2-right, identical above-edge multiple scattering resonances, features D and E, for all the samples indicate that the bond lengths and angles in the first coordination sphere of the Ir are all rather similar within the present signal to noise ratio (S/N). High quality EXAFS spectra would probably differentiate between **Ir1**, **Ir4** and **Ir2** and **Ir3**.

6.1.1.1 EXAFS analysis for Ir1 and Ir4

The EXAFS analysis allows extracting the local geometric order around an absorbing atom of a sample as comprehensively discussed in (§2.1). In this thesis, the EXAFS analysis is carried out for the **Ir1** and **Ir4** complexes in DMSO solution.

As explained in (§ 2.1), in the normal scheme of EXAFS analysis with FEFF9 we give two input files of experimental data and atomic structure of a model system. For the latter, xyz coordinates of the crystal structures of **Ir1**[238] and **Ir4**[156] determined by X-ray crystallography, were used to generate the fine structure $\chi_{fit}(k)$. FEFF9 using the ARTEMIS interface[234] generates single- and multiple scattering paths between the absorber atom (here Ir) and the neighboring atoms at a half-path distance of R_γ^0 up to a maximum path length of R_γ^{max} (generated SS paths are tabulated in Table 6-1). Among all scattering paths computed by FEFF9, only those six paths with the largest amplitudes are reported in Table 6-1. The Ir-C and Ir-N single scattering (SS) paths both have degeneracies of N_γ= 1 and different positions in the crystallographic data. This is due to the crystallographic structure that I have used as an input file, which has a methyl attached to one of the ppy

ligands in **Ir1**. However, I compensated by manually subtracting the difference between the position of each C and N atoms of the shell from the respective reference C or N atom in that shell.

Based on Equation 2.10, to model EXAFS as a sum of scattering paths, ARTHEMIS refines the parameters $N_\gamma, S_0^2, \Delta R$, ΔE_0, and σ_γ^2 (Table 6-2) for each path. These parameters refer to: path degeneracy, amplitude in %, the deviation from the input half path length R_γ, deviation from the input edge-position* (the maximum of the first derivative in the spectrum), and the squared rms fluctuations in path length σ_γ^2 or Debye-Waller factor (see § 0). The scattering amplitudes and phase-shifts are calculated by FEFF9. Each of these parameters has typical range (§2.1) of value, as the number of parameters we can extract is limited to $N \approx \frac{2\Delta k\, \Delta R}{\pi}$.[239] Hence, to avoid overfitting the signal, it is always recommended to keep the number of independent parameters as low as possible, while maintaining a meaningful analysis. Using common half-path lengths and similar amplitudes for all Ir-N and all Ir-C scattering paths in the first two shells, as well as similar σ and ΔE_0 parameter for C and N atoms reduces the number of independent fit parameters to 6 for both samples of **Ir1** and **Ir4** (Table 6-2).

EXAFS fitting is typically done in R-space to retrieve distances R (bond length) and coordination number ignoring the contribution of higher shells. In the fitting procedure, the reduced measured data χ is first transformed to k-space converting the incident X-ray energy to the photoelectron wave vector k (Equation 2.9). Then, using a Hanning-function for the Fourier-transform (FT) window, all fits were performed in the R-space range 1.3-4.8 Å (Figure 6-3), with a k -weight of 2 and 3. From Figure 6-3 (top) it can be seen that the In k-space the EXAFS looks similar in both **Ir1** and **Ir4**. Figure 6-3 (bottom), Fourier transforming (FT) the χ(k) in the range of 4.6-13.8 $Å^{-1}$ for both **Ir1** and **Ir4** shows three distinct peaks (whose origin will be explained in the following structural analysis). Interestingly, already by FT we can see differences in the distances between the first peak and second peak for **Ir1** and **Ir4**, which refers to longer bonds in the latter. Note that these peaks include both SS and MS contributions. However, for fitting, to isolate SS from significant MS contributions (due to the (C_3) symmetry of the complex),

* The EXAFS analysis does not rely on an accurate calibration of χ(E), as the edge-position (E_0) can be included as a fit parameter. Here E_0 is treated as an independent variable for the EXAFS fitting.

Table 6-1: Paths generated by FEFF9 using ARTEMIS and parameters used for the fitting models of Ir1 (upper panel) and Ir4 (bottom panel). $\boldsymbol{N_\gamma}$ is path degeneracy, DW is Debye-Waller parameter, and amplitudes are in %. Ir is the absorbing atom. N_{paths} is the number of single scattering paths between the absorber atom and a neighbor atom. Multiple scattering pathways are given in Appendix B. The contribution of the respective pathways to the EXAFS function is presented in the Figure 6-4. The Input cif files are given in Appendix B.

N_{paths} Ir1	N_γ	R_γ	Amplitude	Pathway	Distance Parameter For ref. atom	DW parameter
3	1	2.194	100	$Ir \leftrightarrow C_{123}$ $Ir \leftrightarrow C_{122}$ $Ir \leftrightarrow C_{121}$	$\Delta R_{Ir-C_{123}}$	σ_{Ir-C}
3	1	2.0318	100	$Ir \leftrightarrow N_{13}$ $Ir \leftrightarrow N_{12}$ $Ir \leftrightarrow N_{11}$	$\Delta R_{Ir-N_{13}}$	σ_{Ir-C}
N_{paths} Ir4	N_γ	R_γ	Amplitude	Pathway	Distance Parameter For ref. atom	DW parameter
3	1	2.0156	100	$Ir \leftrightarrow C_1$ $Ir \leftrightarrow C_{10}$ $Ir \leftrightarrow C_{19}$	ΔR_{Ir-C_1}	σ_{Ir-C}
3	1	2.0206	99.42	$Ir \leftrightarrow N_1$ $Ir \leftrightarrow N_3$ $Ir \leftrightarrow N_5$	ΔR_{Ir-N_1}	σ_{Ir-C}

Table 6-2: All the independent parameters used for fitting the EXAFS of **Ir1** and **Ir4**. Parameters are $N_\gamma, S_0^2, \Delta R,\ \Delta E_0$, and σ_γ^2, where each respectively refers to: path degeneracies, amplitude in %, the deviation from the input half path length R_γ, deviation from the input edge-position* (the maximum of the first derivative in the spectrum), and the squared rms fluctuations in path length σ_γ^2 (see § 2.1).

Model	Ir1			Ir4		
Parameters	Guess	Uncertainties	Initial	Guess	Uncertainties	Initial
ΔR_{Ir-C} (Å)	-0.011	± 0.072	0.0000	0.068	± 0.038	0.0000
ΔR_{Ir-N}(Å)	-0.005	± 0.030	0.0000	-0.067	± 0.037	0.003
σ^2_{Ir-C}	0.0002	± 0.002	0.0030	-0.0002	± 0.002	0.0030

the lower limit of the k-range is set at relatively high energy (corresponding to higher energy photoelectrons). Hence, for first shell analy sis including only SS, the k-range is set to 4.6-13.8 Å^{-1} for **Ir1** and **Ir4**, respectively. The fitting result yielded a reduced chi-square of χ^2_υ< 29 for **Ir1** and χ^2_υ< 37 for **Ir4** (Table 6-3) for which the typical value for a good fitting is between to 10-50.

* The EXAFS analysis does not rely on an accurate calibration of χ(E), as the edge-position (E_0) can be included as a fit parameter. Here E_0 is treated as an independent variable for the EXAFS fitting.

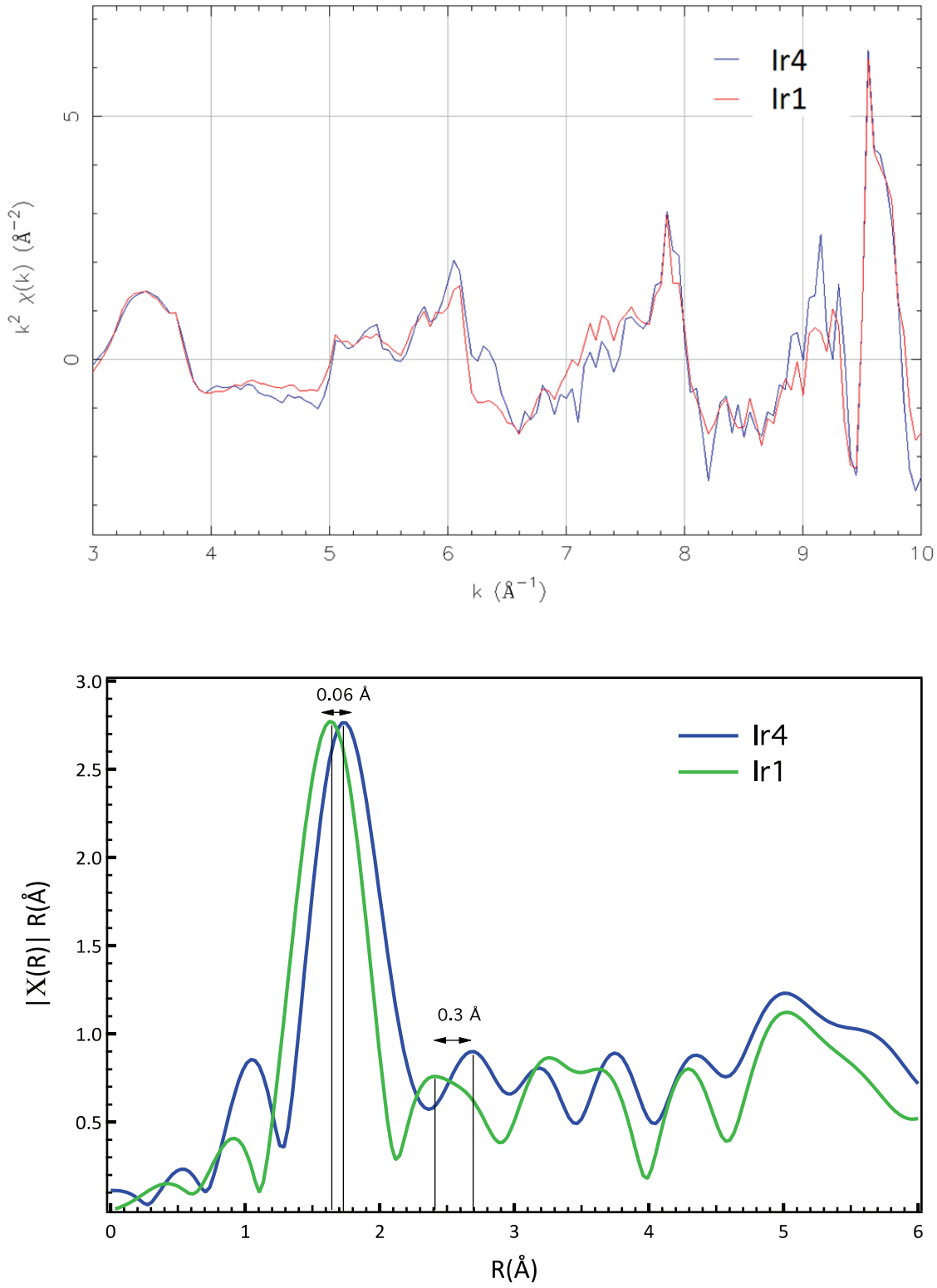

Figure 6-3: (top) Comparison of the extracted fine structure as a function of the photoelectron wave vector k in the range 4.6-13.8 Å^{-1} for **Ir1** (red) and **Ir4** (blue) in DMSO solutions using a k-weight of 2. (bottom) Fourier transform of the extracted EXAFS shown in (top). The R-range for both samples is 1.30-4.30 Å, and the trace for **Ir1** (green) is multiplied by a factor of 9.2 to be have same height of peak with **Ir4** (blue).

In Figure 6-4, data and resulting fits for **Ir1** is shown in R-space together with the contributing single scattering paths. For obtaining a satisfying agreement for R_Y^{max}~4.3 Å with a minimal number of free fitting parameters, six scattering pathways of first shell were found to be sufficient (the second shell SS paths contribution are shown in the picture). The paths are listed in (Table 6-1). In the case of **Ir1**, the main peak at 1.65 Å has equal contributions from all single-scattering paths 1-6 from the absorber Ir atom to the next three surrounding N and C atoms in the first shell. According to our model (Table 6-1) only ΔR and the amplitudes ($\boldsymbol{S_0^2}$) differ between N and C while they share the other two variables ΔE_0, and σ_{Ir-c}^2). Hence, unsurprisingly, in **Ir1** there is no discrimination between N and C in the fit except that N has higher amplitude.

Comparing **Ir1** and **Ir4** in Table 6-3 (see Appendix B), it is found that the Ir-C distances in **Ir4** is 13 pm longer than in **Ir1**, while the Ir-N distance elongates by ~ 3 pm (Table 6-3) in **Ir4**. This illustrates the reduced π–backbonding in the **Ir4** complex, which leads to an elongation of the Ir-C/N bond. Note that in the present EXAFS analysis the Ir-N bond length is estimated to be similar to Ir-C bond in **Ir1**, which is not the case for **Ir4.** The EXAFS features are quite weak and we could only locate the position of atoms in the first shell neighborhood of Ir. Identical above-edge resonances, feature D in Figure 6-2, for all the samples indicates that the atoms and bond distances in the first coordination sphere with the Ir are rather similar within the present signal to noise ratio (S/N). Moreover, the relative interatomic distances for Ir-C (and Ir-N) obtained by EXAFS analysis for **Ir1** and **Ir4** differs from the crystallographic/diffraction data and quantum chemistry calculations (see § 6.1.1.2). In fact all the crystallographic/diffraction data were measured with powder and not in the solution. In addition, with the available energy resolution in k–space at SLS and its FT, we do not have the accuracy to reach any better result.

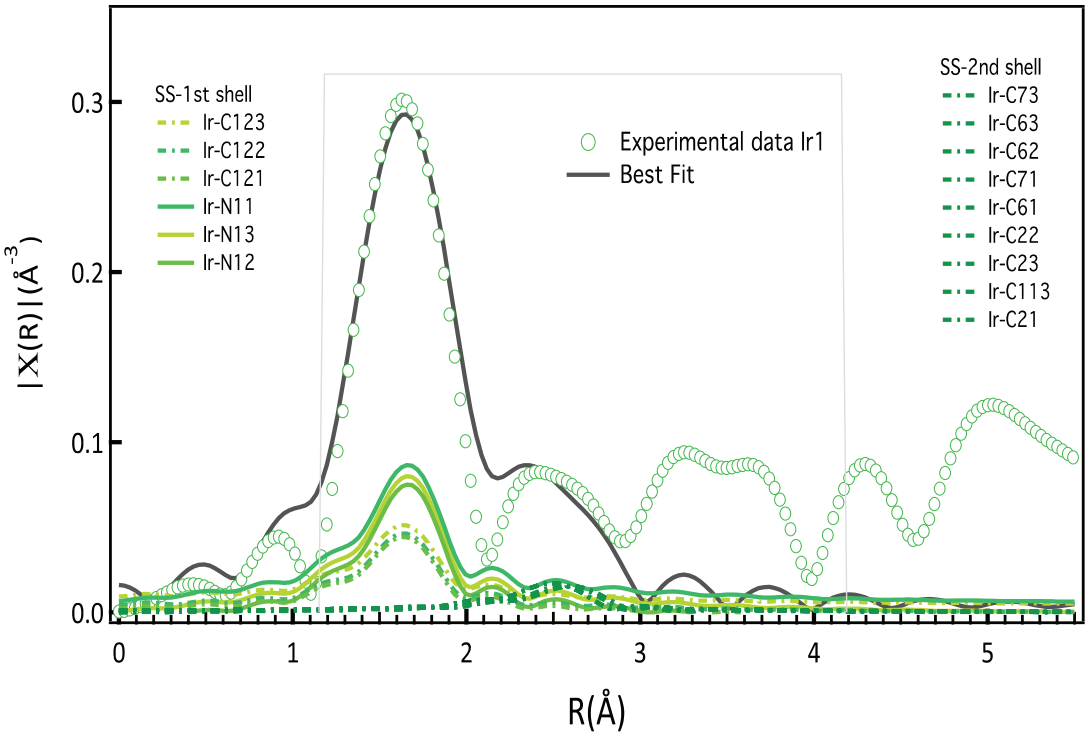

Figure 6-4: Experimental data (open circles) compared with the scattering paths included in the EXAFS of **Ir1** together with the best fit. The paths are shown for the first shell single scattering and second shell single scattering. The K-range is 4.6-13.8 Å^{-1} and R range is 1.3-4.3 Å. The peaks of Nitrogen atoms and Carbon atoms are offset vertically for better visibility.

Table 6-3 The EXAFS fitting goodness is given as the Reduced Chi-square (χ_v^2) parameter. The distance values are only for the first shell and not phase –shift corrected.

	Ir1	**Ir4**
Reduced Chi-square	29	37
R-factor	0.34	0.36
Distance Ir-C (Å)	1.65	1.78
Distance Ir-N (Å)	1.65	1.68, 1.74*

* One of the N atoms was closer to Ir atom

Nevertheless, with the high quality EXAFS spectra (taking several scans) it might be possible to differentiate between **Ir1**, **Ir4**. In any case, we should remember the EXAFS region in these complexes in solution is quite featureless.

6.1.1.2 Analysis of the XANES region

Figure 6-5 shows L_3-edge spectra calculated using the FEFF9 package[240] compared to the experimental spectra presented in (§ 6.I.1). The main structural parameters for the optimized geometries of ground states for all the complexes are shown in Table 6-4 and are depicted in . The overall agreement between the simulated and experimental spectra is good, and the simulated

spectra capture the three main features occurring at 11.22 keV, 11.227 keV and 11.263 keV (indicated by dashed lines in Figure 6-5). The first one corresponds to the WL, composed of dipole allowed 2p-5d transitions, while the latter two are above the ionization threshold and consequently are multiple scattering resonances primarily sensitive to structure. The experimental trends, namely an increase in the WL line strength and a decrease in the above-ionization resonance at 11.227 keV for **Ir4** compared to **Ir1**, are reproduced by the calculations. The former effect reflects the difference in the covalency* of the two ligands and consequently impacts the distribution of 5d orbitals density of states within the valence electronic structure and is discussed in more detail below. The latter effect (weaker D feature) in **Ir4** reflects the structural changes between **Ir1** and **Ir4** and in particular the shorter Ir-N bond distance for **Ir4** (in Table 6-4)†. It is noted that in both cases this resonance is calculated to be weaker than observed experimentally, which is a manifestation of the muffin-tin approximation.

Table 6-4: Selected bond distances (Å) for the four complexes in the ground state (S_0) compared to those determined using X-ray diffraction. Second (row in the table) corresponds to the Ir-N bond of the ancillary ligand in complexes. The bond distances of the long-lived ^{3}MLCT states for **Ir1** and **Ir4** are also shown (T_1).

		Ir1			**Ir4**		**Ir3**		**Ir2**
		X-ray[241]	PBE(S_0)	PBE(T_1)	PBE(S_0)	PBE(T_1)	X-ray[242]	PBE(S_0)	PBE (S_0)
Bond length	Ir-N	2.13	2.15	2.14	2.12	2.10	2.06	2.06	2.05
	Ir-N						2.15	2.16	2.16
	Ir-O								2.17
	Ir-C	2.02	2.02	2.01	2.02	2.04	2.02	2.02	2.01
Bond Angle	C-Ir-N						80.7	80.2	80.7
	N-Ir-N		79.2	79.5	78.9	79.5	76.4	75.9	
	O-Ir-N								76.7

* Here it means the bond strength due to the degree of π-back donation.

† In Table 6-4, the XANES analysis gives quite a different bond length for Ir-C (shorter) than Ir-N for both samples. Also, it yields longer Ir-N bond for **Ir4** relative to **Ir1,** which is not the case for the EXAFS analysis (Table 6-3). However, the stronger π-back donation in **Ir1** is more consitent with having shorter Ir-N bond in **Ir1** as I conclude from EXAFS result in Table 6-3.

In the case of **Ir3** and **Ir2** (Figure 6-5-b) the calculations indicate, as observed experimentally, that the spectra of the two complexes are almost identical. This is because the main change, in the first coordination sphere of the Ir is the exchange on N for O and, as discussed earlier, XAS has limited ability to distinguish atomic species within Z±1. It is therefore unsurprising that the spectra are so similar. However, importantly the Ir-N and Ir-O bond lengths in the two complexes are almost identical.

The edge region of the XANES spectrum was calculated using TDDFT[243] within the approximation of the BP86 functional[244]. We considered excitations only from the 2p core levels of iridium. The calculations used a TZVP basis set and accounted for scalar relativistic effects using the ZORA approximation[245]. Figure 6-5 compares the calculated WL region of the spectra to the experimental data. For all complexes we observe a broad and rather featureless resonance as a consequence of the large lifetime broadening associated with the Ir 2p core hole (5.5 eV). Interestingly, as previously noted, the experimental spectra of **Ir1** and **Ir4** appear to show (the second derivative of the spectra is used to locate the energy of this peak) a resonance at 11.213 keV (1 eV resolution), respectively. This is not observed in the calculated spectrum with 5.5 eV broadening. Figure 6-6-inset shows the calculated spectra with a reduced core-hole broadening (1.5 eV). In the case of **Ir1,** resonances become visible (shown with an arrow), one is predominately a metal ($2p_{3/2}$)-to-ligand charge transfer (MLCT) excitation (feature B) and the other a $2p_{3/2}$→ 5d transition (feature C). Figure 6-7 shows the density difference plots (i.e. $\Delta\rho = \rho_{GS} - \rho_{ES}$). Similar resonounces are also observed for **Ir4**. However, for **Ir4**, π-backbonding is weaker, this weakens feature B also it is closer* to the main transition of $2p_{3/2}$→ 5d in WL and not resolved in the calculation. The contribution of 5d orbitals in the molecular orbitals of d_2, d_{1a}, and d_{1b} are calculated for the **Ir1** [**Ir4**][157,165] to be 52% [50.2%], 44% [47.8%], and 44% [47.8%] which shows overall stronger π-backdonation in the **Ir1**. Probably the weaker π-backdonation in **Ir4** is due to the higher energy of the π* orbitals in ppz compared to ppy (pyrazole destabilized LUMO) (§ 3.III.1.4). This difference in π-back donation of 5d electrons is also reflected in the intensity of the WL. In the simple picture, the weaker π-back donation for **Ir4**, causing a lesser contribution of d-orbitals to the ligand-valence π*-

* Indeed, the second derivative of the experimental static XAS dataat 11.213 keV gives an energy difference of $\Delta E_{E_0-B} \approx 5\text{eV}$ between feature B and E_0 for both samples.

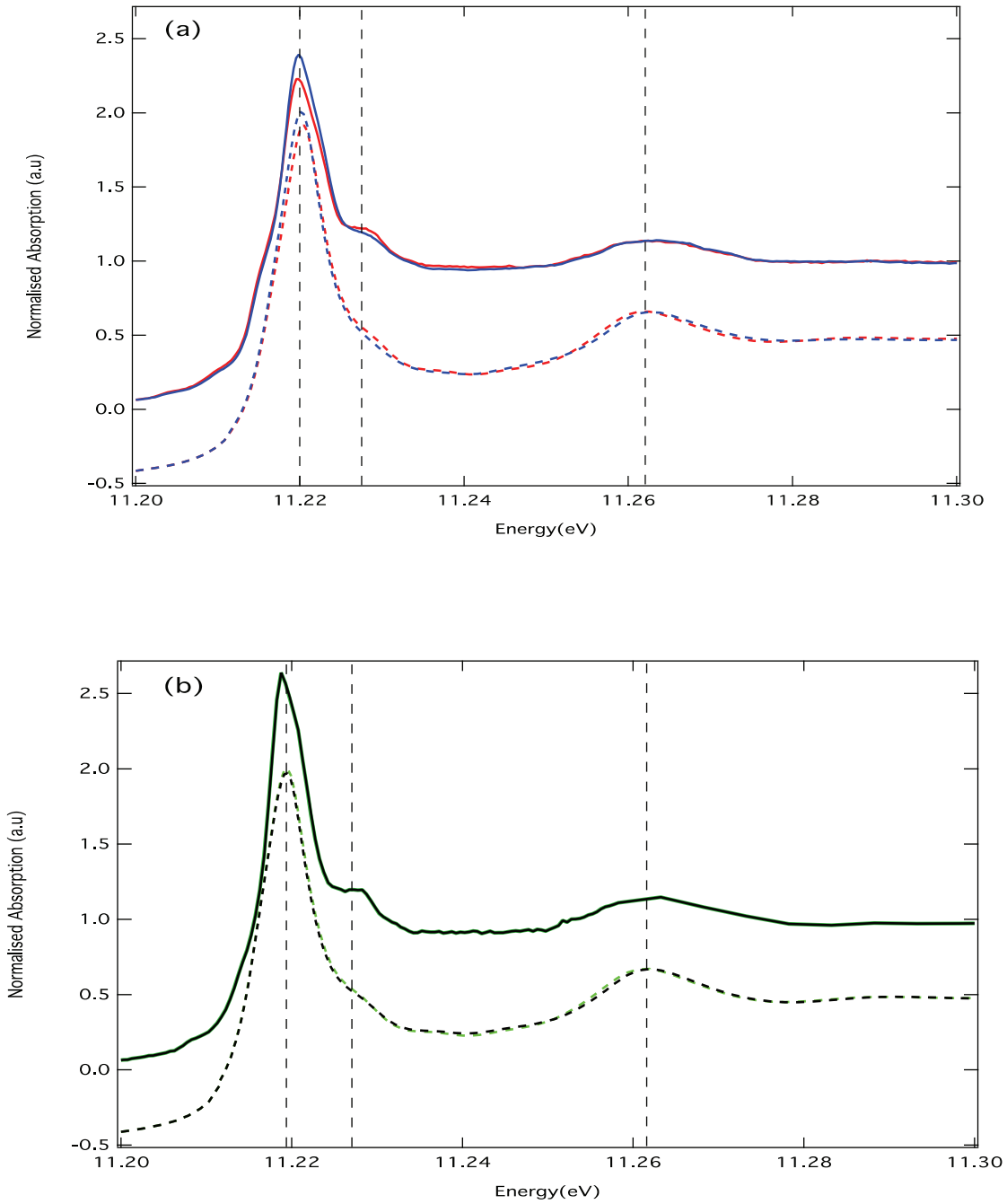

Figure 6-5: (a) Ir L_3-edge experimental spectrum (solid line) for **Ir1** (red), **Ir4** (blue) compared to their simulated spectra (dotted lines). (b) Ir L_3-edge spectrum for **Ir2** (green), **Ir3** (black) compared to their simulated spectra (dotted lines).

orbitals. This weakens the shoulder and there is less d-density of states in the d-orbitals (they have spread and mixed into the ligand-valence orbitals). However, other mechanism namely configuration interaction (CI) are involved in determining the intensity of the WL in complexes

having the π-back donation. In particular, a final state mixing mechanism that redistributes intensity from the main e_g peak into the π* orbitals.[246]

In the case of **Ir3** and **Ir2** the transitions are dominated by metal centred transitions $2p_{3/2}$ → 5dπ (Table 6-5), which are close in energy and form one strong resonance. This is due to the reduced covalency of the bpy and pic ligands compared to ppy and ppz leading to purer d-transitions. This also reduces the MLCT transitions in heteroleptic compared to homoleptic complexes.

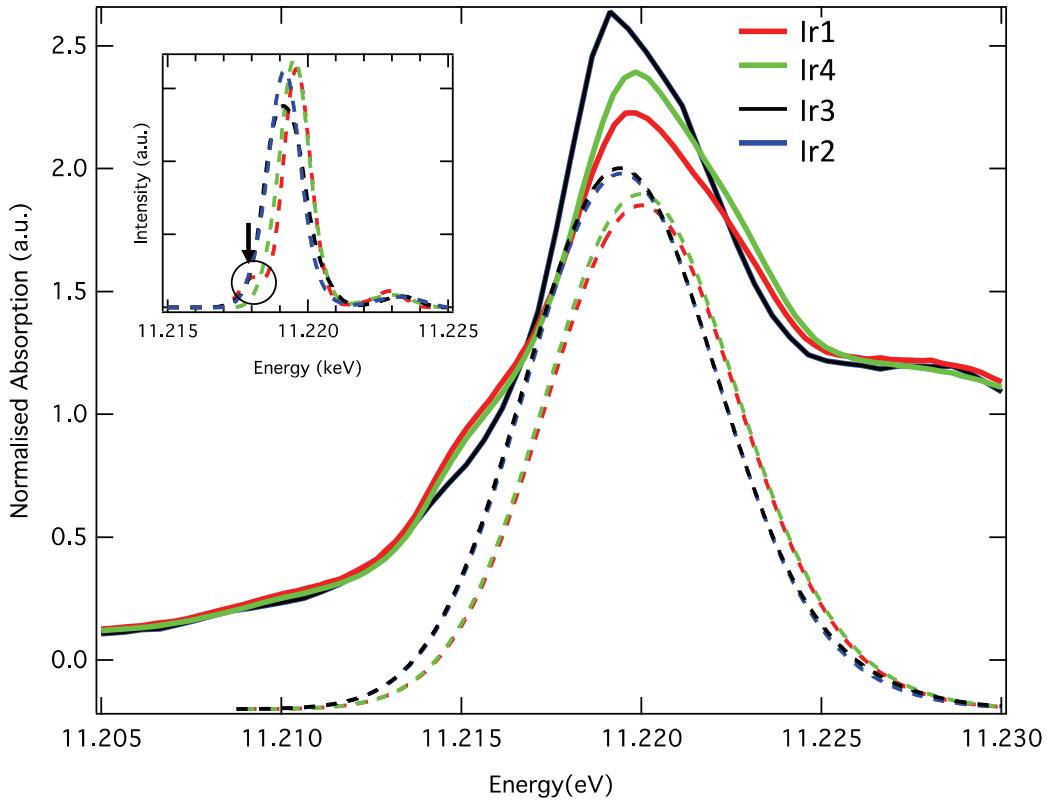

Figure 6-6: A zoom of the Ir L3-edge WL line of **Ir1** (red), **Ir4** (green), **Ir3** (black) and **Ir2** (blue) compared to the simulations using TDDFT (dotted lines). Inset: The spectra computing using TDDFT with a reduced core-hole lifetime broadening of 1.5 eV, the feature shown by an arrow is the M(core)LCT peak.

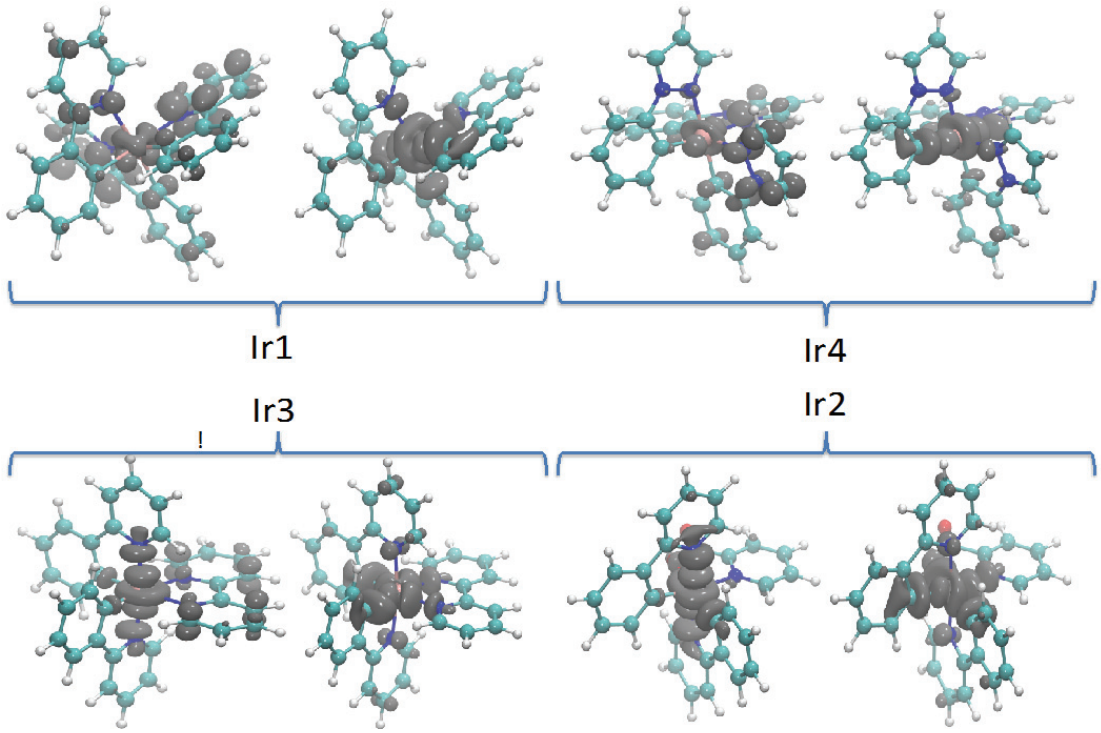

Figure 6-7: The difference densities ($\Delta\rho = \rho_{GS} - \rho_{ES}$). For each sample the left molecule $\Delta\rho$ is associated with the pre-edge transition of M(core)LCT, while the right molecule shows $\Delta\rho$ associated with the main transition of WL ($2p_{3/2}$→ 5d).

6.2 Picosecond Time-Resolved X-ray Absorption Spectroscopy

6.2.1 Experimental conditions

Two cyclometalated iridium samples of **Ir1** and **Ir4** were studied in two series of laser/X-ray pump/probe experiments; the first was in dichloromethane (DCM), a non-polar solvent, while the second series was conducted in the polar solvent of dimethylsulfoxide (DMSO). The differences in the experimental conditions of the two series of experiments are summarized in Table 6-5. To minimize sample damage, the solution was flown through the jet nozzle using peristaltic pump (flow rate of ~60 ml/min) creating a sheet of solution with 500 μm thickness. The low boiling temperature (~40° C) and high vapor pressure of DCM together with the considerable heat load by the high-repetition rate pump laser system created jet instabilities, which introduced fluctuations in the signal. Therefore, DMSO with much a higher boiling point (180°C) and low vapor pressure was chosen for the second set of measurements.

In the case of DCM solvent, the samples were exposed to air while for the second series of experiments in DMSO, we measured under nitrogen inert atmosphere. During the very first measurements on **Ir1** and **Ir4**, both changed color to dark green and blue respectively within 20

minutes, which is caused by the oxidation of Iridium exposed to oxygen. Therefore, we add 20% Methanol (MeOH) to the solution in order to close the loop of electron exchange with reduction of Ir by MeOH. Optical studies[59] in aerated conditions obtained a lifetime of 36 ns for the triplet state of the **Ir1** limited by oxygen quenching in these type of highly effective water oxidant catalysis[247]. Hence, 520 kHz repetition rate (RR) was an appropriate choice for the recovery of the excited sample. However, the lifetime of the lowest triplet state of **Ir1** is reported to increase to 1.6 μs in the absence of oxygen.[59] In order to isolate the sample from Oxygen quenching, the sample was circulated in the sheet jet placed inside a chamber under N_2 over-pressure. Moreover, samples were degassed and bubbled with N_2 for about 1 hour before measurements. Enhancement of the lifetime prompted us to work at 260 kHz to give enough time for the recovery of the irradiated sample. Absorption at 355 nm will excite the sample to ^{1}MLCT state (Figure 3.III.6). The low achievable concentration of <2 mM (very low solubility) together with the low damage threshold of laser power resulted in limited excitation yield, f(t), of this sample. The magnitude of the measured transient $\Delta A_{norm}(E,t)$ is directly proportional to the excitation yield f(t). I assumed that we have one-photon excitation that each absorbed photon leads to an excited molecule, so according to the experimental parameters mentioned in Table 6-5 the number of photons on the sample is calculated to be:

$$N_{ph} = \frac{Laser\ power}{RR.hv} = 5 \times 10^{12}$$

Table 6-5: Experimental condition for TR-XAS experiments. A is spot-size, P is power, E is Energy, F is fluence, C is concentration, RR is repetition-rate, d is the sample thickness. **Ir1** and **Ir4** refer to **Ir1** and **Ir4** respectively.

		80% DCM + 20% MeOH Aerated condition	**80% DMSO+ 20% EtOH Degassed / N_2 overpressure**
Sample	C-Ir1	1.65 mM	1.75 mM
	C-Ir4	3.11 mM	3.12 mM
Laser-Pump (355 nm) X-ray Probe	P_{pump}	1.5 W	760 mW
	E_{pump}	2.88 μJ	2.11 μJ
	F_{pump}	58 μJ/cm^2	16 μJ/cm^2
	A_{pump}	66 x 75 μm^2	80 x 100 μm^2
	RR_{pump}	520 kHz (half RR of X-ray probe)	260 kHz
	A_{probe}	30 x 22 μm^2	45 x 35 μm^2

Knowing the extinction coefficient of **Ir1** at this wavelength ($\varepsilon = 9.2 \times 10^3$ M^{-1} cm^{-1}) and using Equation 2.21 an excitation yield of ~ 2% is obtained which implies that the level of transient signal will be low.

6.2.2 **Experimental Results**

By means of picosecond X-ray absorption spectroscopy (XAS) it has been successfully measured the transient spectrum (pumped sample spectrum–un-pumped sample spectrum) at the Ir L_3-edge of both **Ir1** and **Ir4** probed 150 ps after laser excitation. Upon optical excitation a Metal to Ligand Charge Transfer (MLCT) occurs, the change of oxidation state is observed by the edge shift. The time-resolved Ir L_3-edge transients of **Ir1** and **Ir4** in DCM recorded in the range 11.20-11.30 keV are shown in Figure 6-8. The upper panels show ground state (GS) X-ray absorption spectra of **Ir1** in green and **Ir4** in blue (§ 6.1.1), and the transient spectra in DCM recorded 150 ps after laser excitation (lower panels). In cases of strong transient signal normally each individual scan is normalized to its corresponding edge-jump of the unpumped fluorescence signal. For both samples, the transient signal level at 150 ps corresponds to less than 4.3 % of the steady-state absorption signal level (Table 6-6). However, here for easier comparison the transient spectra are normalized to the first maximum. The transients shown in the lower panel of Figure 6-8 are result of a total of 266 scans for **Ir1** and 269 scans for **Ir4** each scan takes ~3 minutes (all parameters are summarized in Table 6-6). The obtained signal-to-noise ratio (S/N) which is defined as the ratio of signal level to half the error bar at the highest peak of the transient (11.219 keV) is 7.8 for **Ir1** and 7 for **Ir4**.

In Figure 6-9-upper panel, within our X-ray probe temporal resolution of 70 ps, in agreement with the small differences in the GS spectra of **Ir1** and **Ir4** (see (6.1.1), the transient spectra are identical within the error bars. For both samples the only significant changes are those observed around the WL (features A, B and C in Figure 6-8). In both cases, features B (at 11.219 keV) and C (at 11.223 keV) are typical of an edge shift (E_0 = 11.218 keV for the GS, see §6.1.1) to higher energy as a result of oxidation state change (here Ir+3 to Ir+4).

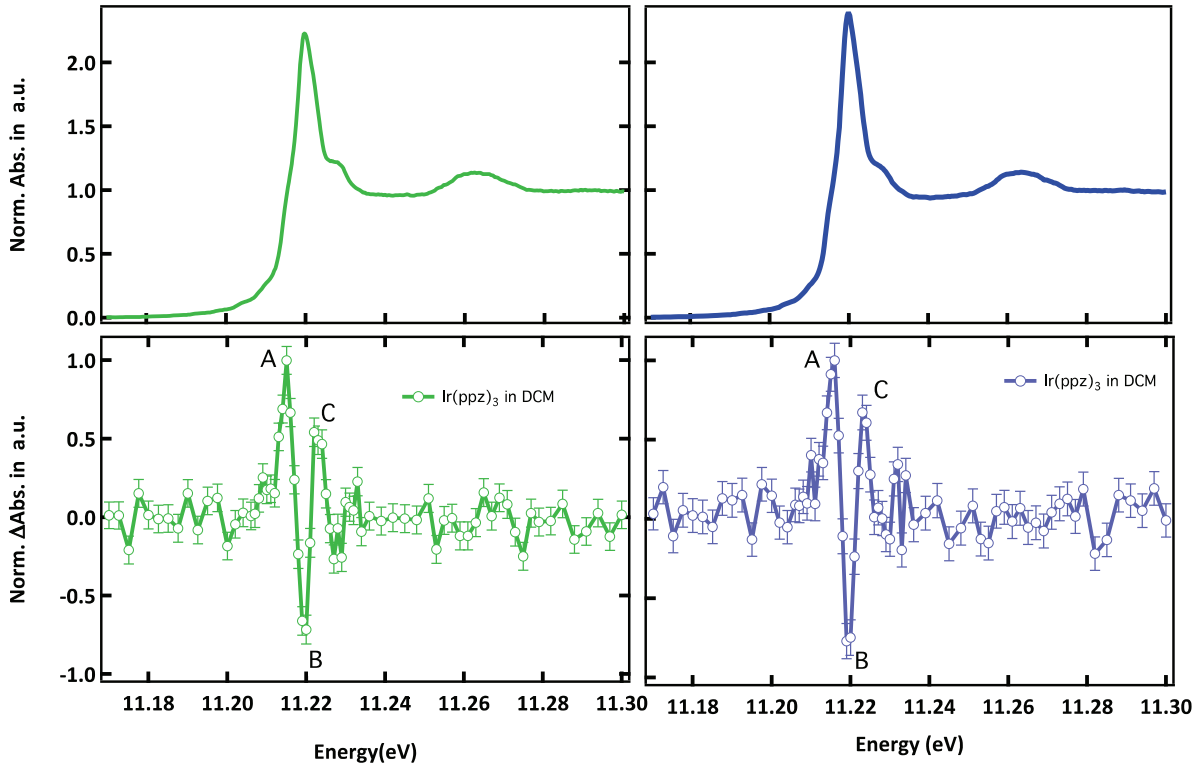

Figure 6-8 Comparison of transient spectra of **Ir1** (green) and **Ir4** (blue) measured in DCM at 150 ps time delay after excitation at 355 nm, together with their static difference spectrum (in green and blue, respectively). Transients have been normalised to the maximum at 11.215 keV. The signal to noise ratio for **Ir4** is ~8 and for **Ir1** is ~ 7.

Table 6-6 Statistics of the two series of measurements. The signal-to-noise ratio (S/N) is defined as the division of signal level by half the error bar and is given for an energy of 11.215 keV. Values in paranteses refere to equivalents in DMSO. Tr/St is the ratio of the signal level between transient (when normalized to the edge jump) and static spectrum.

Solvent	Scan num-ber	No. Data points	Signal level (Tr/St)	S/N (at 11.22 keV)
Ir1	226 (321)	70 (56)	3.6 %	8
Ir4	269 (123)	70 (56)	4.3 %	7

As mentioned earlier (§3.3.1), the GS of **Ir1** and **Ir4** has full-occupied dπ orbitals in the $5d^6$ low-spin configuration. The WL in the GS reflects transitions from $2p_{3/2}$ to 5dσ (e_g) having a shoulder at lower energy (~ 5 eV below 11.218 keV) that we assigned to be the M(core)LCT (§ 6.1.1.2). While upon laser excitation, in the valence excited state we have a transfer of electron density from the dπ orbitals to π* orbitals of the ligand (ppy or ppz), creating a photo-induced vacancy in dπ

orbitals that opens up a new channel for absorption. This photo-induced vacancy in the valence band manifests itself as the increased absorption of the excited state (ES) in resonance A at 11.215 keV (Figure 6-8). Note that feature A in the transient locates at 11.215 keV, and the pre-edge in the GS is at 11.213 keV. However, electronic charge transfer is not the only reason behind the trend in the transient spectrum, and one should also look at intramolecular bond length changes between GS and ES (see § 6.2.4).

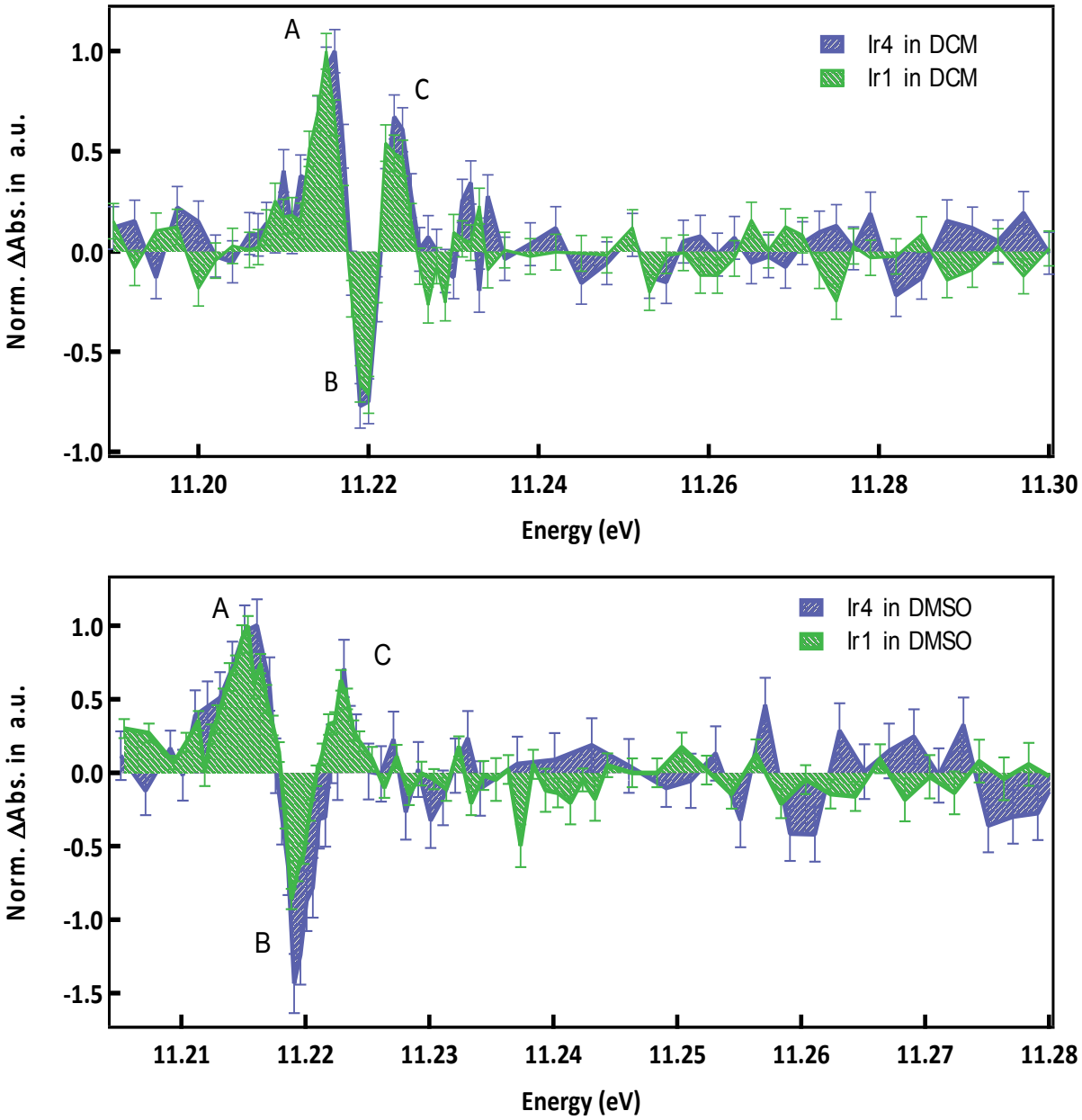

Figure 6-9: Comparison of transient spectra of **Ir1** in green and **Ir4** in blue both measured in DCM (top) at and in DMSO (bottom) 150 ps time delay upon excitation of 355 nm. The transients have been normalised to the maximum at 11.215 keV. Main features labelled A-C, see the text.

In DMSO (Figure 6-9-lower panel), feature B is intensified and broadened by ~ 1 eV) in **Ir4** relative to that of **Ir1**. Qualitatively we can say that the more negative value indicates less absorption in the ES of **Ir4** with respect to **Ir1** in DMSO. However, being spectrally broader could also reflect more structural differences in the ES of the two samples in the polar solvent DMSO. Moreover, comparing the transient signal for each sample in DCM and DMSO (Figure 6-10) shows that in both cases the negative peak B at 11.22 keV is deeper in DMSO. Yet, a rather low S/N in DMSO inhibits an ambiguous interpretation and higher S/N (at least comparable with the S/N in DCM) is demanded to better quantify these differences between the transient signals for both solvents.

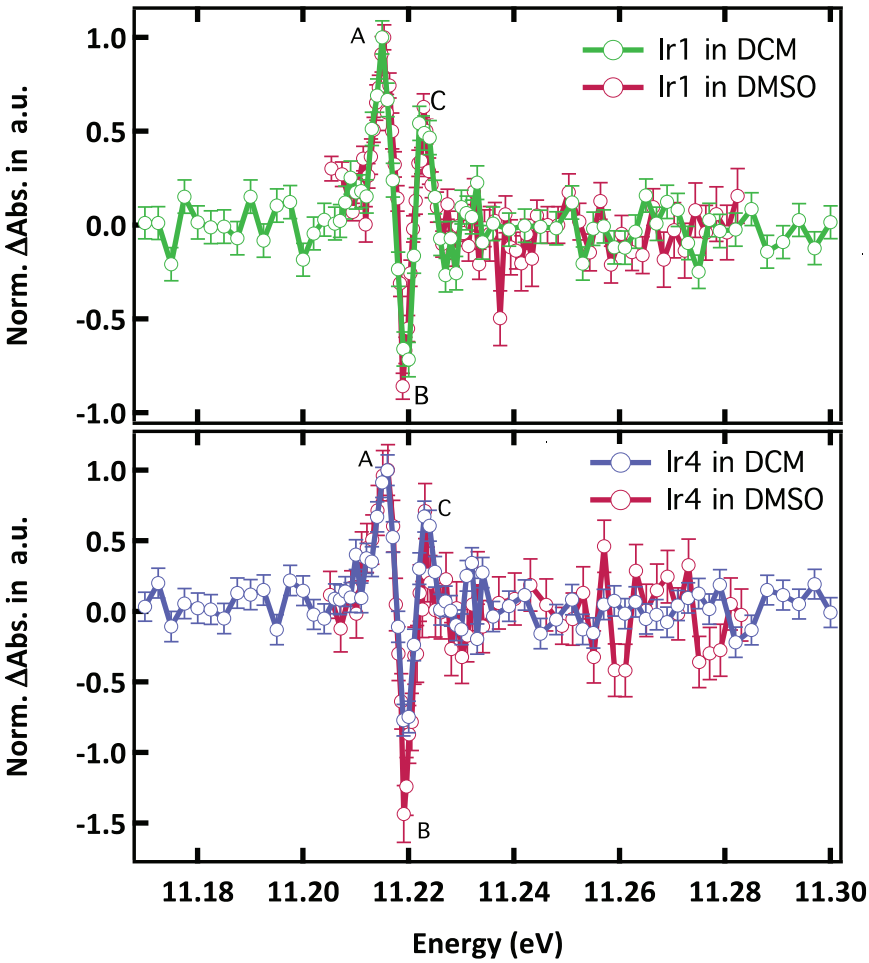

Figure 6-10: (top) Comparison of the transient spectra of **Ir1** measured in DCM (green) and in DMSO (dark red) at 150 ps time delay upon excitation of 355 nm. (bottom) Similar to top panel for **Ir4** in blue. The transients have been normalised to the maximum at 11.215 keV. Main features labelled A-C, see the text.

6.2.3 **Excited state decay in Ir1 and Ir4**

We have monitored the kinetics of the excited state for both samples in DCM, recorded at the maximum transient signal (here at 11.22 keV) and scanned the time delay of the x-ray pulse from 2 ns before to 280 ns after laser excitation. The decay in **Ir4** follows a bi-exponential function, while in the case of **Ir1** a single exponential function is sufficient to describe the decay. Table 6-7 summarizes the time scales and their amplitude for both samples. The upper panel of Figure 6-11 shows the whole range we scanned and lower panel zooms into the first 10 ns. As tabulated in Table 6-7, a double exponential is used to reproduce the data. The former function gives a time scale very close to 36 ns obtained from optical measurement[59] under aerated conditions, and the long time scale is kept fixed at 1.6 μs according to the similar value reported[59] by optical measurements*. In the case of the **Ir4** using a two exponential function correspond to any of the time scales known from optical measurements on this complex (Table 5-1)**.** The second time scale with large uncertainty is comparable with τ_1 obtained with single exponential yields τ_1 =0.77 $\pm$ 0.31 ns and τ_2 =187.59 $\pm$ 73.2 ns.

Table 6-7: Results of best fit parameters for the decay of the transient signal in **Ir1** and **Ir4** with 70 ps temporal resolution of the X-ray probe beam provided at Swiss Light Source. Amplitude of the signal at t=0 is 3.5 for **Ir1** and 2.36 for **Ir4**. For the best-fit result the offset is set to 0.

In DCM	τ_1 (ns)	Amp.	τ_2 (ns)	Amp.
Ir1	36.87 ± 11.5	2.10 ± 0.20	1600 (fix)	0.83 ± 0.19
Ir4	0.77 $\pm$ 0.32	1.45 $\pm$ 0.29	187.59 $\pm$ 73.2	0.95 $\pm$ 0.10
Ir4**	0.33 $\pm$ 0.27	1.09 $\pm$ 0.43	6.08 $\pm$ 2.88	1.35 $\pm$ 0.32

** In the range of -2.0 ns to 6.0 ns.

* Note that the error bars are under estimated, and the bump in the signal <1 ns is an artefact due to the jittering of the triggering system that looks like a rise in the signal.

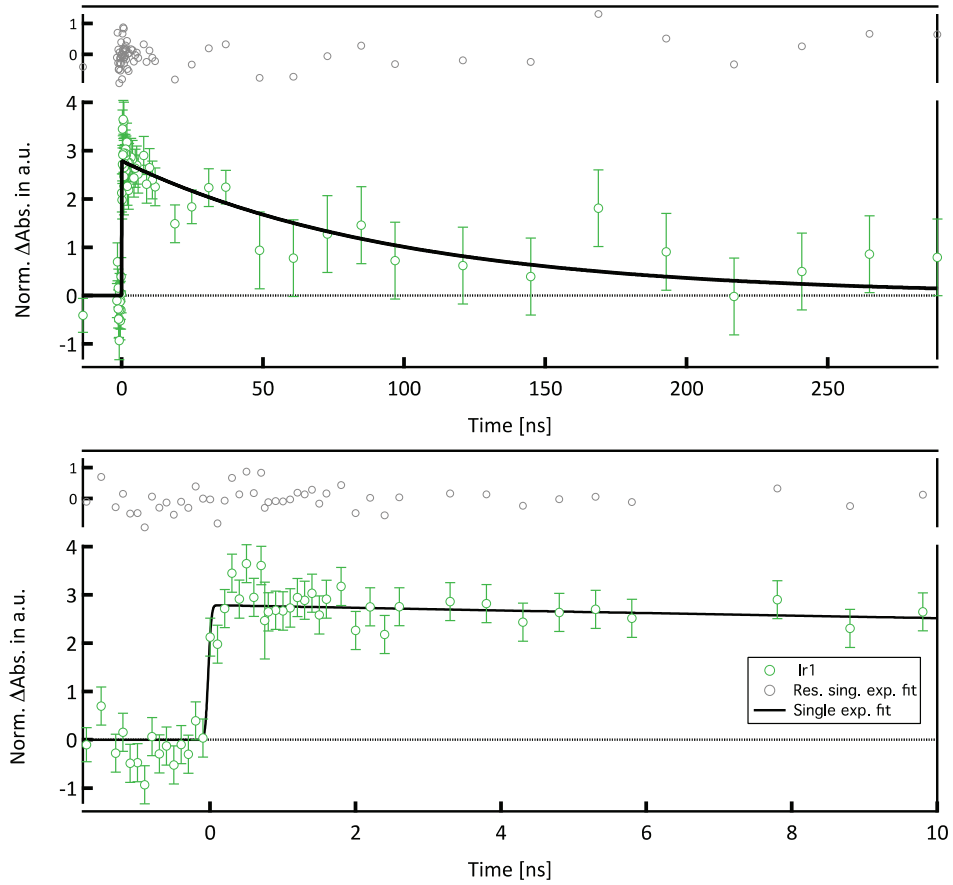

Figure 6-11: Kinetic trace of the maximum Ir L_3-edge absorption spectrum signal of Ir1 upon 355 nm excitation measured at 11.215 keV. Best Fit with mono- (single) exponential decay function in black line yield time scale of τ_1=98 ± 13.8 ns (100%).

The origin of τ_1 is not clear as it does not tial for **Ir1**. Moreover, the data in **Ir4** has been fitted in the shorter range < 6ns (Figure 6-12- bottom) to check if the trend reveals different time scales. It is observed that the huge uncertainty of $\boldsymbol{\tau_1}$ **=** 0.327 ± 0.266 makes it comparable with $\boldsymbol{\tau_1}$ obtained fitting the long range.

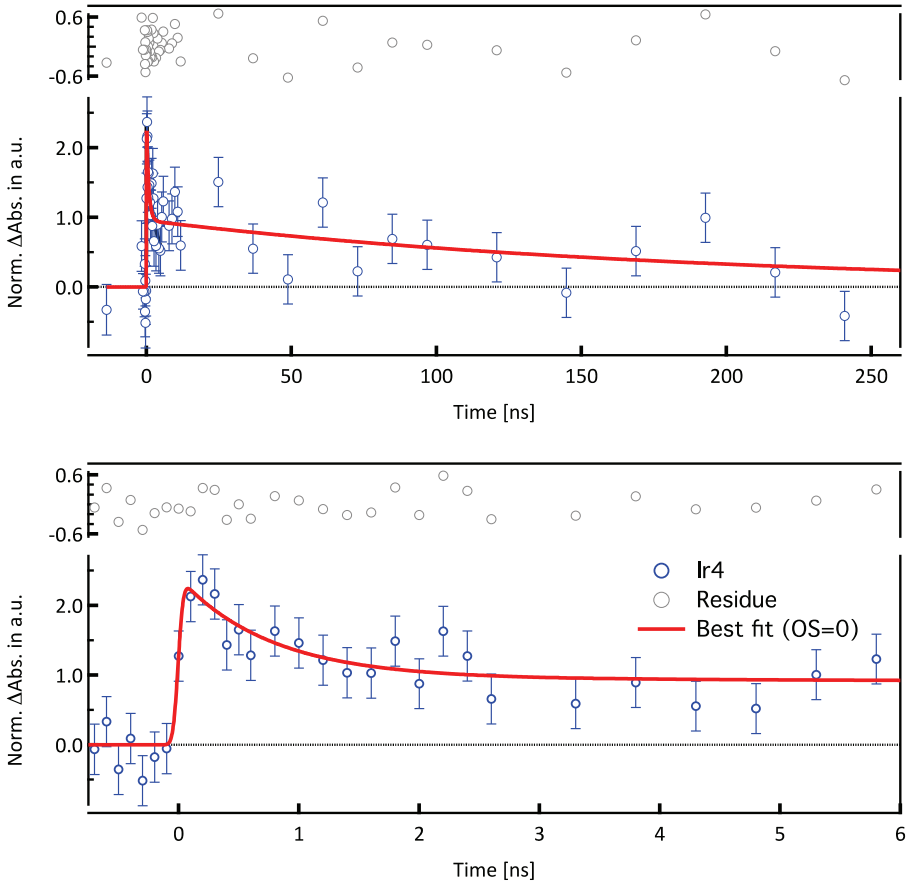

Figure 6-12: Kinetic trace of the maximum Ir L_3-edge absorption spectrum signal of **Ir4** upon 355 nm excitation measured at 11.215 keV. Best Fit with bi-exponential time scales are τ_1=0.77 ± 0.32 ns (6%), τ_2=187.59 ± 73.2 ns (40%). Upper panel shows the result of spanning the whole range of -2.0 to 250 ns, while lower panel zooms into first 6 ns.

6.2.4 **Data Analysis and discussion**

The transient spectrum ΔA, can be described as the difference between the X-ray absorption spectrum (XAS) of the excited state (ES) $\mu^*(E)$ and the ground state (GS) $\mu(E)$:

$$\Delta A(E) = g.\left(\mu^*(E) - \mu(E)\right)$$

g is the scaling factor substitutes the excitation yield f in Equation 2.21. In (§ 6.2.1) the excitation yield has been estimated for these ps XAS studies to be ~2% for **Ir1** in DCM. A qualitative experimental analysis is that first the transient spectrum is compared to the difference signal $\Delta A'_{calc}$ between a hypothetical ES and the GS-XAS. As mentioned earlier, the negative feature in the transient signal around the energy position of the WL, indicates a shift toward higher energy in the ES spectrum due to oxidation state change from Ir+3 to +4. To verify this assumption, I

considered a chemical shift of ΔE for the excited state $\mu^*(E+\Delta E)$ and subtracted it from GS-XAS, which leads to the following calculated signal:

$$\Delta A'_{calc.}(E) = g.\left(\mu^*(E+\Delta E) - \mu(E)\right)$$

Assuming different values for the chemical shift of ES and calculating the $\Delta A'_{calc}$, reveals that best matching value would be 1-1.2 eV (Figure 6-13). In this regards, Clancy *et. al* [68] have argued that the increase of ionization state in iridates results in three changes in the XAS spectrum of the complex at the L_3-edge: a blue shift of the WL toward higher energies by ~ 1.3 eV for each additional 5d hole; the integrated intensity of the WL monotonically increases by a factor of ~2 from $5d^7$ to $5d^5$; the width of the WL varies by 30%-50% between different iridium valence states. Therefore, at this point better agreement between experimental data and $\Delta A'_{calc}$is obtained with 1.2 eV in the range of 11.218 keV-11.222 keV. However, out of this range $\Delta A'_{calc}$ deviates from the experimental data in particular in the first positive feature (labeled A), as expected. The transient spectrum of **Ir1** shows more features than a mere shift of the absorption edge from the oxidation state change. The deviation between the calculated spectrum and the transient data in the region of 11.205 keV-11.218 keV imposes that the main peak of pump-probe signal in both cases shows not only an edge-shift (Ir^{3+} → Ir^{4+}), but also a potential change (broadening) of the WL width in the pumped sample.

It is apparent from Figure 6-10 that the transient signal for both samples in both solvents shows significant changes only around the WL (feature B). These reflect a re-organization of the electronic structure on the Ir following photoexcitation. Indeed, as shown by the optimized structures in Table 6-4, the absence of any significant above edge changes in the XAS spectra is because of the small structural reorganization of these complexes in the excited state, a highly desirable property for OLEDs. Note that the same argument also applies for **Ir4** due to their identical above-edge region of X-ray absorption spectra and transient signal. In both cases around the edge we observe a derivative profile consistent with a blue shift of the absorption spectrum suggesting a decrease in an electron density on the Ir upon photoexcitation. This is accompanied with an additional feature at 11.215 keV from the opening of a new absorption channel ($2p \rightarrow 5d(t_{2g})$), consistent with depletion of the Ir 5d orbitals upon photoexcitation.

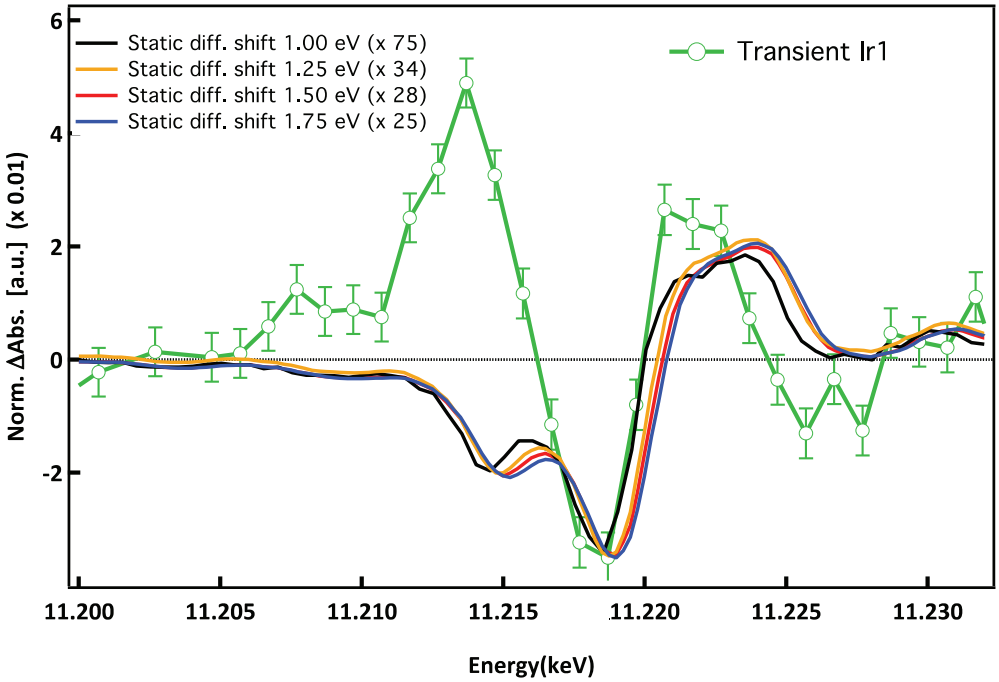

Figure 6-13: The transient signal of **Ir1** in green line is compared to a calculated static difference spectrum with energy shifts of +1 eV (black), 1.25 eV (orange), 1.5 eV (red), and 1.75 eV (blue) with respect to the ground state spectrum. The best agreement lies between 1.0 eV and 1.25 eV. Here the transient is normalized to the edge-jump in the static signal.

Figure 6-14 shows the transient spectra compared to the computed transient spectra. The calculations reproduce the blue shift of the absorption spectrum mainly due to Ir+3→Ir+4 with a minimal structural change of 0.02Å bond elongation, indicating a transfer of electron density away from the Ir, consistent with the MLCT excitations. The calculations also reproduce the new feature, arising from a hole in the HOMO created by photo excitation, opening of a new absorption channel (2p→ 5d(t_{2g})). The valence molecular orbitals corresponding to this transition are shown in the inset and consistent of a mixed Ir 5d-π*.

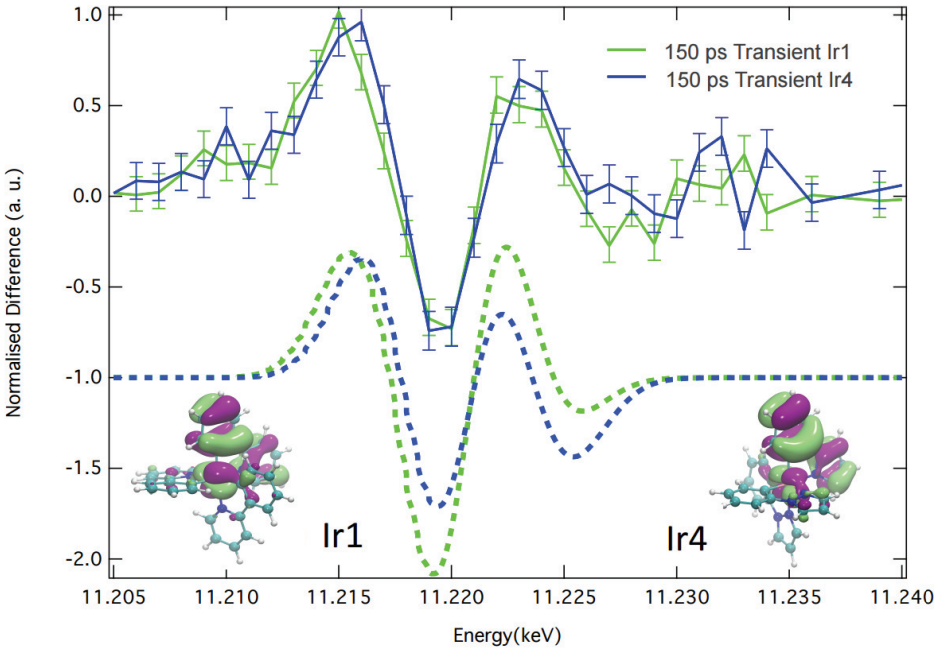

Figure 6-14: Calculated transient signal for transient spectra of **Ir1** in green (dashed line) and **Ir4** in blue (dashed line) at 150 ps time delay after excitation at 355 nm. Solid line shows experimental data. The transients have been normalised to the maximum at 11.215 keV. Inset: Molecular orbitals of the photoexcited complex corresponding to the transition from $2p_{3/2}$ to the HOMO (Ir 5d-π*). Purple stands for positive and green stands for negative change of electron density upon photoexcitation of the sample, respectively.

6.2.5 **Summary**

In this chapter, I presented the studies of the ground state (GS) of four different iridium cyclometalated complexes **Ir1**, **Ir2**, **Ir3**, and **Ir4** using X-ray absorption spectroscopy (XAS) at the Ir L_3-edge in DCM and DMSO solution. The XAS results probing directly the iridium site provide insight into the electronic and geometrical structure of the GS of these complexes. There are four main features in the XAS spectra: a pre-edge feature at ~11.213 keV; the white line (WL) at ~11.220 keV; and two multiple scattering features (at 11.227 keV and 11.263 keV). The geometric and electronic structures of the samples are retrieved investigating the above ionization resonances (E>11.22 keV) and the WL (including the pre-edge and edge) region of the XAS spectra, respectively. Calculated L_3-edge spectra using the FEFF9 package[240] for the edge and above-edge region of the four samples gives a good overall agreement between simulated and experimental spectra, capturing the main features of WL and the two multiple scattering resonances. The calculations correctly show a higher WL strength and weaker above-ionization resonance for **Ir4** than for **Ir1**. In the case of the heteroleptic **Ir3** and **Ir2** compounds, the calculations yield very similar spectra and almost identical Ir-N and Ir-O bond lengths in the two complexes, pointing to

the limited ability of XAS to distinguish the effect of substituting N for O. Moreover, the XANES analysis of the spectra provide detailed information about bond lengths and angles for the first shell single scattering paths. Contrary to EXAFS analysis for **Ir4** and **Ir1**, according to these results, the Ir-N bond length decreases in the order of **Ir1**> **Ir4**> **Ir3**> **Ir2**. However, the Ir-C bond length is found to be similar for all samples.

The electronic structure of the ground state of **Ir1**, **Ir2**, **Ir3** and **Ir4** in solution was studied by analyzing the pre-edge and the WL of the experimental XAS spectra. The origin of the WL at the L_3-edge of Ir(III) is a transition from $2p_{3/2}$ to $5d\sigma$ (e_g) orbitals. The WL intensity of **Ir4** is larger than that of **Ir1**, reflecting the stronger π-back donation in the latter. Higher WL intensity for **Ir4** is accompanied by a decrease in the above-ionization resonance at 11.227 keV. Weaker resonance at this energy points to slightly longer bond lengths in **Ir4**. The spectra of both **Ir3** and **Ir2** are very similar with stronger WL absorption at slightly lower energy in comparison to the other two samples, which also implies weaker π-back donation in them. In addition, only XAS spectra of **Ir1** and **Ir4** show a pre-edge feature corresponding to a transition from the $2p_{3/2}$ core level to the lowest-lying unoccupied valence π^* orbitals of the pyridine or pyrazole ligands. The edge region of the XANES spectrum was calculated (using TDDFT[243]) to be a broad and rather featureless resonance for all the complexes. A shoulder due to a resonance of predominantly metal ($2p_{3/2}$)-to-ligand charge transfer excitation becomes apparent in the simulated spectrum of **Ir1** when using an (unreasonably small) core-hole broadening (1.5 eV). This is not the case for **Ir4** owing to the smaller π-back donation. This shoulder is indistinguishable for the calculated spectrum in **Ir4** due to the weaker π-back donation of 5d electrons. In the case of **Ir3** and **Ir2**, the transitions are dominated by metal centred transitions $2p_{3/2} \rightarrow 5d\pi$, which are close in energy and form one strong resonance.

Probing the X-ray absorption of **Ir1** and **Ir4** samples (in DCM and DMSO) at the Ir L_3-edge, 150 ps after optical excitation in a metal-to-ligand charge transfer (MLCT) band, we observed a typical feature due to the change of the oxidation state of Ir from +3 to +4. Moreover, the transient signal for both samples (in both solvents) shows a positive feature at 11.215 keV. This feature corresponds to the photo-induced vacancy in $d\pi$ orbitals that opens up a new channel for absorption in the valence molecular orbital, which manifests itself as the increased absorption of the excited state (ES). The TDDFT calculations reproduce the blue shift of the absorption spectrum, indicating a transfer of electron density away from the Ir, consistent with an excited state of MLCT

character. The calculations also reproduce the new feature, arising from a hole in the valence MO created by photoexcitation, opening a new absorption channel ($2p \rightarrow 5d(t_{2g})$). Moreover, comparing the transient signals obtained in the polar solvent (DMSO) and the non-polar solvent (DCM), shows essentially identical spectra for **Ir1** and **Ir4** in the latter, while they are clearly distinct in the former. The transient signal in DMSO shows spectrally broader and deeper negative feature for **Ir4**. Clearly, the obtained S/N ratio of ~8 for **Ir4** (~7 for Ir1) limits us from driving any ambiguous conclusion about the difference between the excited state absorption in DCM and DMSO. Moreover, to gain further insight into the origin of this difference, one should first measure the static spectrum of samples in DMSO and compare their ground state in both solvents.

Chapter 7 Conclusions and Outlook

In this thesis, I presented different experimental studies on two classes of transition metal compounds. The ultrafast dynamics of Fe-based metalloproteins, first and foremost Myoglobin (Mb) in nitrosy lmyoglobin (MbNO), building block of heme proteins, were studied by using the advantages of the high-repetition rate picosecond laser pump/X-ray probe scheme suitable for dilute solutions under physiological conditions. In particular, I deliver results of pump-probe measurements on MbNO in physiological solutions, where we directly interrogate the active centre of the protein, delivering insight into its electronic and geometric structure. Second, I focused on the ultrafast dynamics of Iridium-based organometallic compounds, namely tris-cyclometalated iridium complexes famous for their high performance in the fields of phosphorescent organic light emitting diodes (PHOLED). Using our photoluminescence up-conversion (PLUC) setup with <150 fs temporal resolution, we were able to detect at intramolecular electronic relaxation at sub-vibrational time scales upon UV excitation of the archetypal $Ir(ppy)_3$ (**Ir1**) complex. Using the same PLUC setup, other tris-cyclometalated iridium complexes (pyridine based homoleptic and heteroleptic complexes and a pyrazole based homoleptic complex) were studied under visible light excitation to follow their femtosecond relaxation dynamics in solution. Finally, systematic studies on the electronic and geometric structure of four different tris-cyclometalated iridium complexes using X-ray absorption spectroscopy (XAS) were presented. Moreover, by means of picosecond laser pump/X-ray probe experiments I could investigate directly for the first time the structural changes in photoexcited **Ir1** and **Ir4** in solution after singlet metal-to-ligand charge transfer (^{1}MLCT) photoexcitation. The results widen our understanding of the photophysics of these metal complexes.

7.1 Picosecond X-ray absorption spectroscopy on MbNO

Diatomic ligands in hemoproteins and the way they bind to the active centre are central to the protein's function. The importance of understanding ligand recombination dynamics in MbNO upon physiological conditions led us to conduct investigations with direct probing of the Fe atom. Using picosecond Fe K-edge X-ray absorption spectroscopy (XAS) with direct sensitivity to the Fe-NO binding, we probe the NO-heme recombination kinetics at different delays (70 ps and 300 ps) following 532 nm photoexcitation of nitrosy lmyoglobin (MbNO) in physiological solutions (pH=7, low concentration, continuous flow of the sample). With the improved S/N of the measurements described in chapter 4 we observed deviations of the ps transient from the static difference spectrum. The transient XAS spectra at 70 ps and 300 ps are identical but they weakly deviate from the difference between the static spectra of deoxyMb and MbNO demonstrating the formation of an intermediate species. From the results presented (namely the pre-edge and main edge features in the transient spectra), we conclude that the domed MbNO* is the initial species generated by ligand – metal recombination. This intermediate is identified as a 6-coordinated domed species, which is populated on a time scale of ~200 ps (due to recombination from distant NOs) and relaxes in ~30 ps. It is important to note that this work used distinct experimental conditions and data acquisition strategy compared to ref.[78], yet the similarity of the results obtained are evidence for the accuracy of our UV pump–X-ray probe techniques. Importantly, no radiation damage by either laser or X-ray is observed, as the reported time scales agree very well with previous optical studies at lower repetition rates.

7.2 Photoluminescence up-conversion studies on tris-cyclometalated iridium complexes

I presented a broadband femtosecond luminescence study of the ultrafast photo-physics of $Ir(ppy)_3$ (**Ir1**), of two closely related heteroleptic ppy-based compounds $Ir(ppy)_2(pic)$ (**Ir2)** and $[Ir(ppy)_2(bpy)]^+$ (**Ir3**) and of a ppz-based complex $Ir(ppz)_3$ (**Ir4**) upon excitation at 400 nm and 266 nm. This study provides the first extensive picture of the ligand dependence on the photo-cycle of these complexes.

Here, using femtosecond fluorescence up-conversion spectroscopy[214] upon 266 nm excitation of the ligand-centered (LC) absorption band of **Ir1**, we directly clock the relaxation cascade leading to the lowest triplet metal-to-ligand charge transfer (^{3}MLCT) state that lies ~1.6 eV lower in

energy. We find that the relaxation cascade proceeds at a time scales of ≤ 10 fs, which is faster than some of the highest frequency modes of the system.

In the overall relaxation mechanism we infer from the present results that a decay to the manifold of close lying spin-mixed MLCT states occurs in ~70 fs after excitation of the LC state at 266 nm. Thereafter intramolecular electronic-vibrational relaxation proceeds on extremely short timescales (< 10 fs) leading to population of the lowest ^{3}MLCT state in high vibrational levels. Vibrational relaxation within this state requires ~300 fs followed by the radiative decay to the ground state on much longer time scales (>> 1 ns). The LC decay is the rate-limiting step of the entire ensuing cascade, which itself must be extremely fast (upper limit of 10 fs). The fact that large amounts of electronic energy are converted to vibrational energy on sub-vibrational time scales is attributed to the participation of high frequency modes, probably through state crossing at conical intersections, and to their overdamping by dissipation to the lower frequency modes of the system. The observation of a clear-cut, short-lived emission of the initially excited high-lying ^{1}LC state in a TM complex provides us with an unambiguous clocking of the ensuing intramolecular dynamics, which is found to occur in < 10 fs. In this regard, theoretical support to explore the high density of MLCT states and possibly cuts of their potential energy surfaces along high frequency coordinates will be helpful to understand how or why this fast relaxation proceeds.

Upon 266 nm excitation of **Ir4** in DMSO, only a very weak emission at 450 nm (maximum of the **Ir4** steady state emission) is observed. In the case of **Ir4**, the lack of (t-λ) plot for this system makes the identification of the relaxation cascade difficult. Nevertheless, an ultrafast (with 140 fs rise time and 530 fs decay time) cascade leading to the steady state emission is observed, which we propose to be similar to that of the other complexes studied here, i.e. a relaxation within the manifold of higher lying ^{3}MLCT states. Finally, we discuss the strong quenching of the ^{3}MLCT lifetime in going from low to room temperature and conclude that it is caused by thermally activated non-radiative relaxation to the ground state.

For **Ir1, Ir2,** and **Ir3**, the emission upon 400 nm excitation is dominated by intermediate ^{3}MLCT states at early times, which are related to the ppy moiety. The shortest timescale in the kinetic of system, <100 fs, is assigned to relaxation from low lying ^{3}MLCT state with singlet mixture. The ~1 ps component reflects the emission to intermolecular vibrational cooling by energy transfer to the solvent. At later times (>100s ps), the emission evolves to the steady-state showing evidence of dual emission with different time behaviours for each luminescence component. In **Ir1-2**, this

evolution is due to a double-well minimum of the lowest emitting ^{3}MLCT state involving the ppy moiety. For **Ir3**, the final emission involves the bpy moiety, pointing to the occurrence of a ppy to bpy ILET on the picosecond time scale.

The nanosecond-resolved photoluminescence lifetimes of **Ir1** and **Ir4** were recorded in DMSO. For **Ir1** in DMSO a lifetime of 170 ± 30 ns was found across the entire profile of its emission band, which is due to oxygen quenching occurring in aerated solutions.[230] A similar behaviour, decrease of lifetime by oxygen quenching has previously been reported for the ppy-based complexes **Ir2** and **Ir3**.[231] In contrast, **Ir4** luminescence decays faster (1.6 $\pm$ 0.1 ns) than the ppy-base compounds.

7.3 Steady-state and time-resolved X-ray absorption studies of the tris-cyclometalated iridium complexes

The studies of the ground state (GS) of four different iridium cyclometalated complexes **Ir1**, **Ir2**, **Ir3**, and **Ir4** by means of XAS at the Ir L_3-edge in DCM and DMSO solution presented in Chapter 6 delivers experimental data probing directly the iridium site, and it provides insight into the electronic and geometrical structure of the GS of these complexes. The investigation of the above ionization resonances (E>11.24 keV) and around the white line (WL) (including the pre-edge and edge) region of these XAS spectra yields information about the geometric structure and provides information about the electronic structure, and in particular the contribution of Ir 5d orbitals throughout the valence orbitals. The above-edge resonances of all four spectra are quite similar, which is a manifestation of the Z$\pm$1 sensitivity of XAS.[75] The overall similarity of the above-edge multiple scattering resonances at 11.227 keV and 11.263 eV, for all the samples indicate that the bond lengths and angles in the first coordination sphere of the Ir are all rather similar within the present signal to noise ratio (S/N).

The electronic structure of the four different iridium cyclometalated complexes in solution was studied by analyzing the features present in the WL of the XAS spectra. The WL at the L_3-edge of Ir with full ($d\pi$) t_{2g} orbitals corresponds to a transition from $2p_{3/2}$ to $5d\sigma$ (e_g) orbitals. The near-edge region of the spectra, which reflects the electronic structure, shows distinct differences among the complexes studied. Compared to **Ir1**, the WL intensity of **Ir4** is larger, indicating a larger contribution of Ir 5d character in the region. This increase in WL intensity for **Ir4** is accompanied by a decrease in the above-ionization resonance at 11.227 keV. The spectra of both **Ir3** and **Ir2** are very similar with higher WL intensity, and red shifted in comparison to the other two. This is

indicative of an increase in electron density on the Ir with larger 5d character in the region. Interestingly, the spectra of both **Ir1** and **Ir4** appear to show a shoulder on the red side of the WL, while it is not apparent in the spectra of the other two complexes. This feature corresponds to a transition from the $2p_{3/2}$ core level to the lowest-lying unoccupied valence π^* orbitals of pyridine or pyrazole ligands with MLCT character. However, the existence of such transitions remains open for debate since Ir(+3) has only occupied t_{2g} orbitals ($5d^6$) in the GS low spin configuration. The observed shoulders might in fact stem from experimental artefacts. Only resonant X-ray emission spectroscopy (RXES, including high-energy resolution fluorescence detected (HERFD) and X-ray Emission Spectroscopy (XES)), can lift this ambiguity. A detailed information about the nature and the strength of the orbital mixing between ionic metal centers and the organic parts of the samples in the ground state can be offered by measuring XES and RXES, which can lead to more accurate simulation of the excited state X-ray absorption spectra. Moreover, measuring the RXES map around L_3-edge and detecting the L-α_1, L-α_2 emission lines, can give more insight on the influence of different ligands on the Ir(+3) $5d^6$ orbitals.

The L_3-edge spectra calculated using the FEFF9 package[240] for the edge and above edge region show overall good agreement with the experimental data for all the complexes, capturing the three main features: the WL at ~11.22 keV, and multiple scattering resonances at 11.227 keV and 11.263 keV. The calculations correctly showed a higher WL strength and weaker above-ionization resonance for **Ir4** than that of **Ir1**. In the case of the heteroleptic **Ir3** and **Ir2** compounds, the calculations yield very similar spectra and almost identical Ir-N and Ir-O bond lengths in the two complexes, as observed experimentally. This is because of the limited ability of XAS to distinguish the effect of substituting N for O.

The edge region of the XANES spectrum was calculated using TDDFT[243] within the approximation of the BP86 functional[244]. For all complexes we observe a broad and rather featureless resonance as a consequence of the large lifetime broadening associated with the Ir 2p core hole (5.5 eV). In the calculated spectra of **Ir1** with a reduced core-hole broadening (1.5 eV), resonance become visible, being predominately a metal ($2p_{3/2}$)-to-ligand charge transfer (MLCT) excitation. This shoulder is indistinguishable for the calculated spectrum in **Ir4** due to the weaker π-back donation of 5d electrons. In the case of **Ir3** and **Ir2** the transitions are dominated by metal centred transitions $2p_{3/2} \rightarrow 5d\pi$, which are close in energy and form one strong resonance.

By means of picosecond X-ray absorption spectroscopy (XAS) we have successfully captured the transient spectrum (pumped sample spectrum–un-pumped sample spectrum) at the Ir L_3-edge of both **Ir1** and **Ir4** probed 150 ps after laser excitation. Upon optical excitation a metal-to-ligand charge transfer (MLCT) band, we observed a change of the oxidation state of Ir from +3 to +4.

In DCM, the transient spectra are almost identical for both **Ir1** and **Ir4** within the error bars and the temporal resolution of 70 ps. For both samples the only significant changes are those observed around the WL. The photo-induced vacancy in dπ orbitals opens up a new channel for absorption in the valence molecular orbital (MO), which manifests itself as the increased absorption of the excited state (ES) at 11.215 keV. The calculations reproduce the blue shift of the absorption spectrum, indicating a transfer of electron density away from the Ir, consistent with the MLCT excitations. The calculations also reproduce the new feature, arising from a hole in the valence MO created by photo excitation (HOMO (5d(t_{2g})+π^*_{phen}) to LUMO ($\pi^*_{pyridine}$)), opening a new absorption channel (2p$\rightarrow$ 5d(t_{2g})).

Apendix A Raman Spectra of Ir1, 3, 4

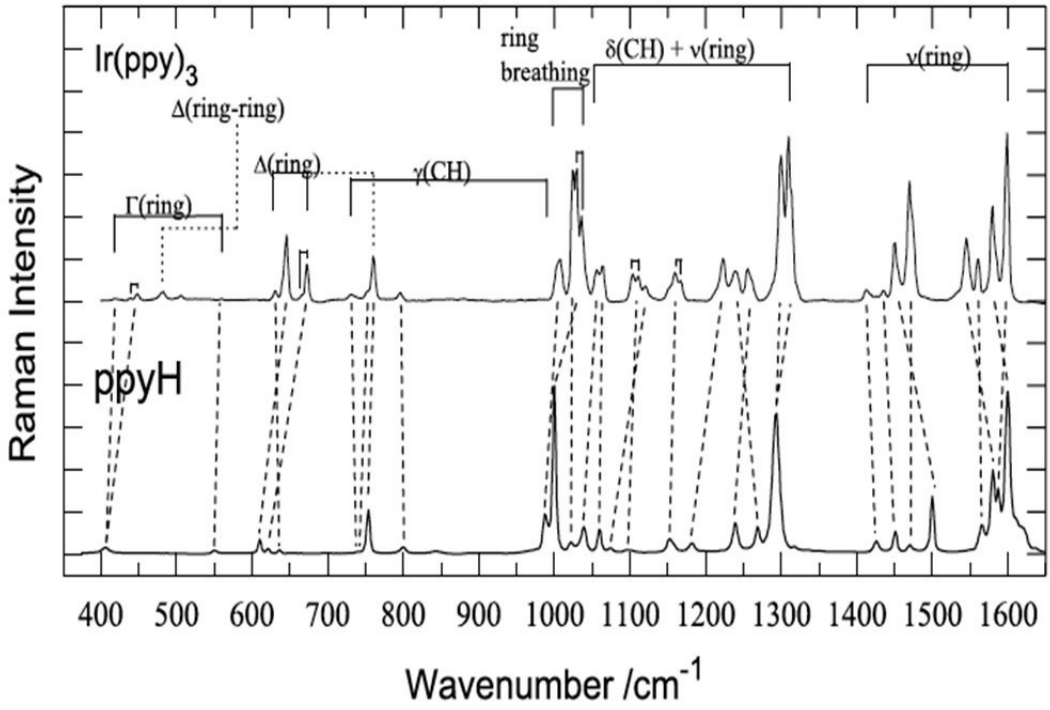

Figure A-0-1: Raman spectra of $Ir(ppy)_3$ (**Ir1**) and ppyH recorded at excitation wavelength 632.8 nm, with assignments in range of 1700–400 cm^{-1}. Symbol ν denotes stretch, δ, γ in-plane and out-of-plane bending and Δ, Γ for in-plane and out-of-plane deformation of phenyl or pyridyl ring. Adapted from ref. [166]

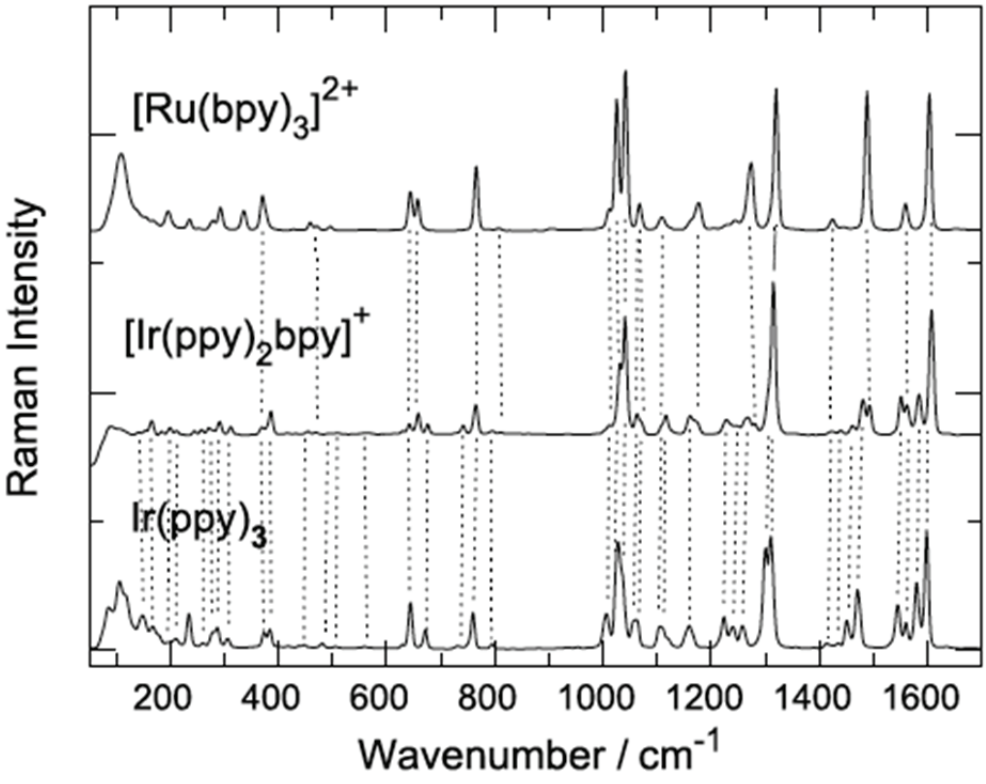

Figure A-0-2: Raman spectra of $Ir(ppy)_3$, $[Ir(ppy)_2bpy]^+$ and $[Ru(bpy)_3]^{2+}$ excited at wavelength 1064 nm.[166]

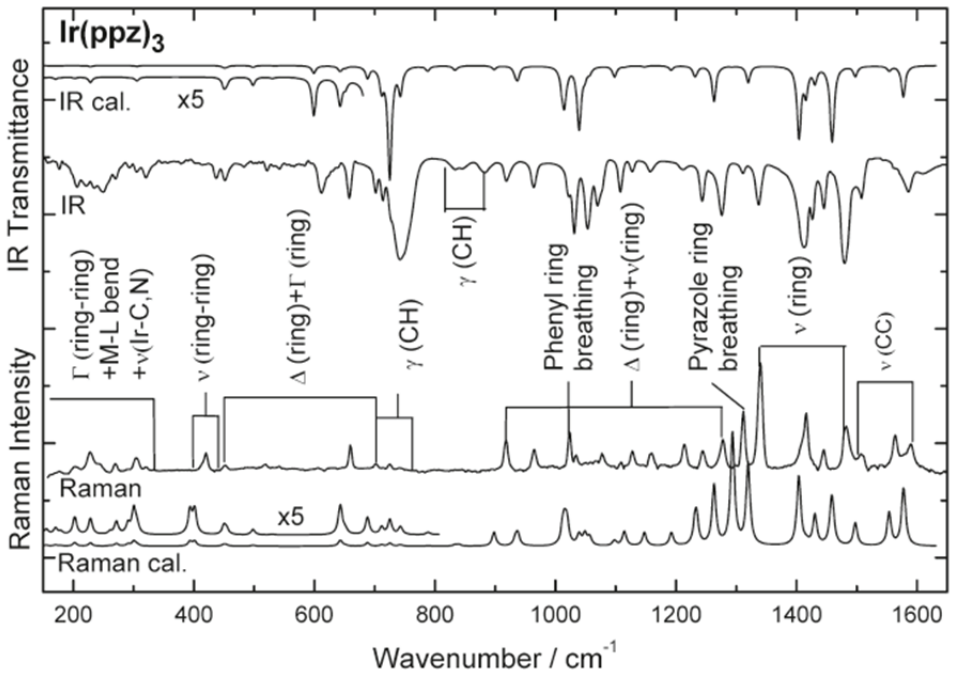

Figure A-0-3: Experimental and calculated (B3LYP/6-31G*) infrared and Raman spectra of Ir(ppz)3 in the wave-number range 150-1650 cm^{-1}.[172]

Appendix B EXAFS Analysis- ARTEMIS

B-1 Ir1

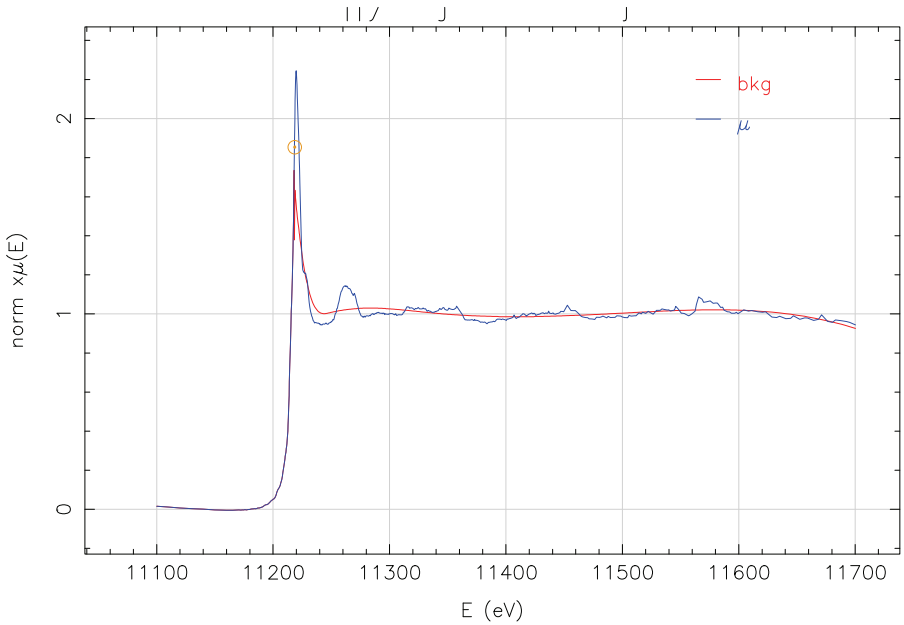

Figure B-0-1: The edge-jump normalized Ir L_3-edge spectrum of [Ir(ppz)$_3$] (blue). The red line represent the background determined with ATHENA (see §2.2.4.1).

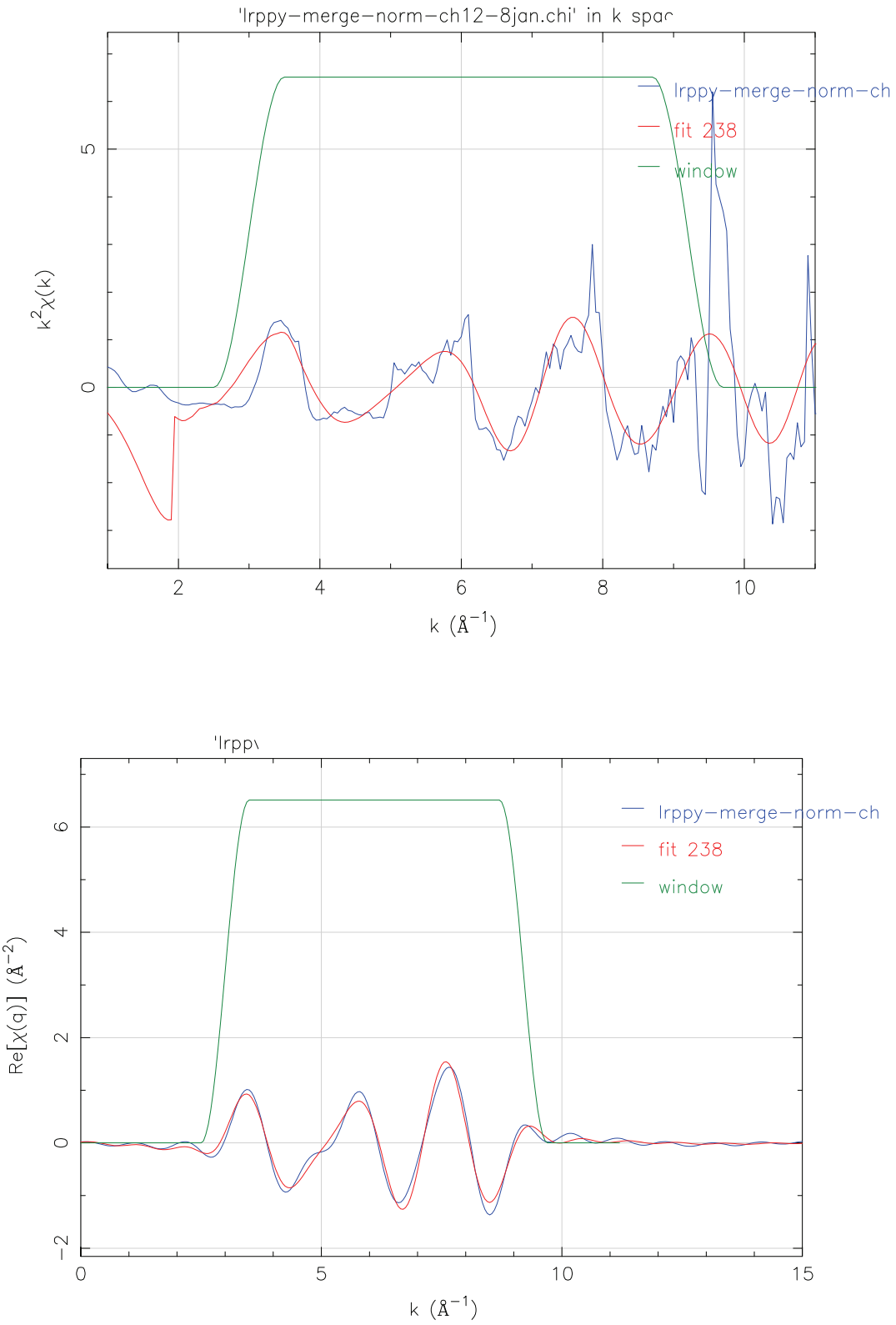

Figure B-0-2: EXAFS signal of Ir1 in k space (Top) and q space (back Fourier transform). (Bottom)

Table B-1 Paths generated by FEFF9 using ARTEMIS and parameters used for the fitting models of **Ir1**.

Nr.	N_γ	R_γ	Amplitude	Pathway	Distances Parameter	DW parameter
1	1	2.0156	100	$Ir \leftrightarrow C_1$	ΔR_{Ir-C}	σ_{Ir-C}
2	1	2.0206	99.42	$Ir \leftrightarrow C_{10}$	ΔR_{Ir-C} – 0.005	σ_{Ir-C}
3	1	2.0273	98.65	$Ir \leftrightarrow C_{19}$	ΔR_{Ir-C} - 0.0117	σ_{Ir-C}
4	1	2.1178	100	$Ir \leftrightarrow N_1$	ΔR_{Ir-N}	σ_{Ir-N}
5	1	2.1208	99.67	$Ir \leftrightarrow N_3$	ΔR_{Ir-N} - 0.003	σ_{Ir-N}
6	1	2.1349	98.11	$Ir \leftrightarrow N_5$	ΔR_{Ir-N} - 0.0171	σ_{Ir-N}
7	1	2.9173	40.08	$Ir \leftrightarrow C_6$	ΔR_{Ir-C}	σ_{Ir-C}
8	1	2.9201	39.98	$Ir \leftrightarrow C_1$	ΔR_{Ir-C} - 0.0028	σ_{Ir-C}
9	1	2.9285	44.515	$Ir \leftrightarrow N_4$	ΔR_{Ir-N}	σ_{Ir-N}
10	1	2.9326	44.351	$Ir \leftrightarrow N_2$	ΔR_{Ir-N} - 0.0041	σ_{Ir-N}
11	1	2.9336	39.504	$Ir \leftrightarrow C_{15}$	ΔR_{Ir-C} - 0.0163	σ_{Ir-C}
12	1	2.9474	43.762	$Ir \leftrightarrow N_6$	ΔR_{Ir-N}	σ_{Ir-N}
13	1	3.1112	33.808	$Ir \leftrightarrow C_{11}$	ΔR_{Ir-C}	σ_{Ir-C}
14	1	3.1170	33.639	$Ir \leftrightarrow C_2$	ΔR_{Ir-C} - 0.0028	σ_{Ir-C}
15	1	3.1193	33.573	$Ir \leftrightarrow C_{20}$	ΔR_{Ir-C} - 0.0028	σ_{Ir-C}

B-1-1 Input file for Ir1

```
TITLE C34 H26 Ir N3
 TITLE Aidan R. McDonald
 TITLE Probing the mer- to fac- Isomerization of Tris-Cyclometalated Homo- and
 TITLE Heteroleptic (C,N)3 Iridium(III) Complexes

 HOLE 4   1.0   *  Ir L3 edge  (11215.0 eV), second number is S0^2
 *        mphase,mpath,mfeff,mchi
 CONTROL  1     1    1    1
 PRINT    1     0    0    0
 RMAX       7.0
 *CRITERIA    curved   plane
 *DEBYE       temp     debye-temp
 NLEG       4
 POTENTIALS
 *    ipot   Z  element
      0   77   Ir
      1   77   Ir
      2   7   N
      3   6   C
      4   1   H

 ATOMS                    * this list contains 123 atoms
 *   x         y         z      ipot  tag           distance
   0.00000   0.00000   0.00000  0 Ir1           0.00000
   0.83692   0.70013  -1.69926  3 C123_1        2.01943
  -1.18492   1.61564  -0.33725  2 N13_1         2.03176
   1.20479  -1.64998   0.13019  2 N12_1         2.04717
```

-1.12094	-1.39061	-1.05246	3	C122_1	2.07316
1.11036	1.19992	1.27941	3	C121_1	2.07596
-0.86098	-0.48763	1.90001	2	N11_1	2.14222
0.27909	1.89576	-2.18489	3	C73_1	2.90612
-0.84385	2.40164	-1.41494	3	C63_1	2.91239
0.81140	-2.77084	-0.56023	3	C62_1	2.94105
-0.48108	-2.64634	-1.22652	3	C72_1	2.95616
0.71114	1.14340	2.64384	3	C71_1	2.96698
-0.38082	0.22431	2.96865	3	C61_1	3.00137
2.36091	-1.69542	0.81726	3	C22_1	3.01931
-2.22200	1.99630	0.44189	3	C23_1	3.01956
2.62889	-0.92016	1.29870	4	H22_1	3.07317
1.91064	0.15777	-2.41566	3	C113_1	3.08397
-2.46810	1.44463	1.17684	4	H23_1	3.09248
-1.81913	-1.40456	2.10026	3	C21_1	3.11338
-2.41524	-1.28400	-1.57899	3	C112_1	3.15836
2.18044	2.06534	0.97880	3	C111_1	3.15880
-2.13085	-1.90399	1.35397	4	H21_1	3.16211
2.32810	-0.63753	-2.10898	4	H113_1	3.20535
2.47940	2.12437	0.07891	4	H111_1	3.26598
-2.89103	-0.46938	-1.46603	4	H112_1	3.27530
-0.63238	-0.88438	-3.89046	4	H51_1	4.03952
-1.54933	3.58725	-1.65852	3	C53_1	4.24494
0.74942	2.51970	-3.34213	3	C83_1	4.25210
1.62261	-3.90637	-0.56159	3	C52_1	4.26708
0.06216	4.03838	1.43726	4	H54_1	4.28697
-2.28945	0.72911	-3.57012	4	H41_1	4.30336
-1.10453	-3.69172	-1.91919	3	C82_1	4.30489
1.35828	1.89755	3.62738	3	C81_1	4.31318
-2.94025	3.15257	0.21213	3	C33_1	4.31611
3.17395	-2.80519	0.86373	3	C32_1	4.32309
-0.93317	0.03828	4.22457	3	C51_1	4.32658
2.37003	0.77741	-3.57674	3	C103_1	4.36056
-2.37331	-1.65786	3.33844	3	C31_1	4.41886
-3.02957	-2.33474	-2.26080	3	C102_1	4.44303
2.82759	2.84848	1.95526	3	C101_1	4.46454
1.22886	4.43550	-0.41283	4	H84_1	4.62106
-0.93317	-0.36169	-4.62408	3	C51_2	4.73115
-2.58112	3.97184	-0.84013	3	C43_1	4.81077
2.80024	-3.91639	0.14764	3	C42_1	4.81677
1.79397	1.95086	-4.04516	3	C93_1	4.83606
-1.92121	0.58994	-4.43631	3	C41_1	4.87031
2.40466	2.72040	3.27658	3	C91_1	4.89070
-2.36237	-3.52643	-2.44120	3	C92_1	4.89653
-1.92121	-0.91336	4.41234	3	C41_2	4.89837
1.07755	-2.16516	-4.31381	4	H81_1	4.94550
0.35384	3.33002	-3.64293	4	H83_1	4.94825
-1.30870	4.13140	-2.40247	4	H53_1	4.95510
1.36011	-4.67305	-1.05527	4	H52_1	4.98005
-0.65426	-4.52279	-2.02752	4	H82_1	4.99945
1.07755	1.84174	4.53484	4	H81_2	5.01178
-0.89671	-4.18650	2.60978	4	H96_1	5.01416
-0.63238	0.56097	4.95819	4	H51_2	5.02974
3.97240	-2.80197	1.37879	4	H32_1	5.05293
-3.67308	3.38368	0.77127	4	H33_1	5.05328
3.09192	0.38924	-4.05831	4	H103_1	5.11677
-3.04416	-2.32257	3.44973	4	H31_1	5.15382
-4.55356	0.14597	2.46796	4	H112_2	5.18141
-0.15295	4.81651	1.93590	3	C54_1	5.19325
-3.91006	-2.22955	-2.60108	4	H102_1	5.19857
2.11299	-2.68391	4.01032	4	H93_1	5.26790
-1.06442	3.83804	3.45478	4	H44_1	5.27248

```
 -4.97649   -1.76804   -0.17492  4 H23_2         5.28413
 -3.77151   -3.70710    0.23065  4 H33_2         5.29340
 -3.53453    1.90614    3.60300  4 H102_2        5.39517
 -4.40043    1.99916   -2.44781  4 H31_2         5.41777
 -0.50478   -4.94387    2.19020  3 C96_1         5.43080
  1.34735    5.34671   -0.66097  3 C84_1         5.55334
 -5.31374    1.58058   -0.35204  4 H21_2         5.55500
  4.28778    3.54825    0.68994  4 H13B_1        5.60813
  1.79397   -2.27427    4.80349  3 C93_2         5.60929
  3.93777    3.79725    1.57077  3 C131_1        5.69144
 -0.81650    4.69666    3.12868  3 C44_1         5.70210
 -5.02935    0.96058    2.58091  3 C112_2        5.73395
 -5.07128    1.33444   -2.33652  3 C31_2         5.74090
 -5.22259   -2.31971    0.56003  3 C23_2         5.74196
 -4.50434   -3.47599    0.78980  3 C33_2         5.74416
  3.09192   -0.71266    4.79034  4 H103_2        5.74589
 -2.04153   -5.28839    0.94046  4 H86_1         5.74625
 -3.04233    4.78968   -0.99401  4 H43_1         5.76063
  3.35442   -4.68736    0.14296  4 H42_1         5.76575
  2.11299    2.36049   -4.83833  4 H93_2         5.78326
 -5.62546    1.08115   -1.09834  3 C21_2         5.83276
  1.35828   -2.22097   -5.22127  3 C81_2         5.83432
  2.85129    3.21554    3.95392  4 H91_1         5.83978
 -2.77253   -4.23300   -2.92821  4 H92_1         5.84633
 -4.41502    2.01132    3.26272  3 C102_2        5.84664
 -2.28945   -1.05253    5.27853  4 H41_2         5.84913
 -1.18474   -5.60000    1.20755  3 C86_1         5.84994
  2.37003   -1.10082    5.27191  3 C103_2        5.88404
 -0.38082   -0.54773   -5.88000  3 C61_2         5.91772
  2.26612    4.94351   -2.42034  4 H94_1         5.95245
  0.76036   -5.37461    2.58321  3 C106_1        6.01145
  1.23250   -4.91632    3.26831  4 H106_1        6.03085
  3.58958    4.71455    1.54024  4 H13A_1        6.12245
 -2.37331    1.33444   -5.51021  3 C31_3         6.14620
  0.74942   -2.84311    5.50652  3 C83_2         6.24233
  1.95257    5.64544   -1.85885  3 C94_1         6.25610
  0.21165    6.08906    1.44479  3 C64_1         6.26170
  0.35384   -3.65343    5.20572  4 H83_2         6.36964
  4.65784    3.74502    2.23417  4 H13C_1        6.38061
  0.71114   -1.46681   -6.20481  3 C71_2         6.41537
  0.90437    6.35130    0.19261  3 C74_1         6.41825
 -3.04416    1.99916   -5.39892  4 H31_3         6.51244
 -5.52338    0.58994   -3.41042  3 C41_3         6.51818
 -6.58361    0.16421   -0.89809  2 N11_2         6.64661
  2.85129   -3.53895   -4.89473  4 H91_2         6.67925
 -6.25967   -1.93905    1.33918  2 N13_2         6.68856
 -3.53453   -2.22955   -5.24565  4 H102_3        6.70676
  1.91064   -0.48119    6.43299  3 C113_2        6.72796
 -6.32365    1.06720    2.05439  3 C122_2        6.73409
 -5.15514    0.72911   -4.27661  4 H41_3         6.73769
 -4.86347   -4.29525    1.84205  3 C43_2         6.74505
 -0.63056   -6.72730    0.59231  3 C76_1         6.78270
  2.40466   -3.04381   -5.57207  3 C91_2         6.78934
 -1.06442   -4.16145   -5.39387  4 H44_2         6.89525
  1.32729   -6.48188    1.96301  3 C116_1        6.90144
 -5.08222    3.20302    3.44313  3 C92_2         6.92412
 -5.15514   -1.05253    4.57204  4 H41_4         6.97043
END
```

B-1-2 Fitting data sheet for [Ir1]

Data sheet containing all fitting paramters for EXAFS fit presented in chapter 6.x.x in figure 6.x.x.

==========

Independent points	**10.910156250**
Number of variables	10.000000000
Chi-square	35.086170070
Reduced Chi-square	38.549611750
R-factor	0.005418197
Measurement uncertainty (k)	0.004140303
Measurement uncertainty (R)	0.005890426
Number of data sets	1.000000000

Guess parameters +/- uncertainties (initial guess):

amp_c	**0.4598810**	**+/-**	**0.1384760**	**(1.0000)**
enot_c	13.0183370	+/-	2.7472340	(0.0000)
delr_c	0.0142370	+/-	0.0178450	(0.0000)
ss_c	-0.0130560	+/-	0.0041040	(0.0030)
amp_n	1.5472630	+/-	0.9508040	(1.0000)
enot_n	-6.9010430	+/-	8.9985400	(0.0000)
delr_n	-0.0249900	+/-	0.0783480	(0.0000)
delr_c2	0.0297990	+/-	0.0498090	(0.0000)
delr_c3	0.1232540	+/-	0.0554470	(0.0000)

Set parameters:

ss_n = 0.003

Correlations between variables:

delr_c2 and delr_c3	**-->**	**0.9665**
enot_n and delr_n	-->	0.9228
amp_n and ss_n	-->	0.9128
enot_c and delr_c2	-->	0.9041
enot_c and delr_c3	-->	0.8842
amp_c and ss_c	-->	0.7139
delr_n and enot_c	-->	0.6765
enot_n and enot_c	-->	0.6693
enot_c and ss_c	-->	-0.6540
enot_n and ss_c	-->	-0.6240
delr_n and ss_c	-->	-0.6204
delr_n and delr_c3	-->	0.6144
ss_c and delr_c2	-->	-0.6076
ss_n and ss_c	-->	-0.5867
delr_n and delr_c2	-->	0.5867
amp_n and enot_c	-->	0.5821
enot_n and delr_c3	-->	0.5802
enot_n and delr_c2	-->	0.5631
ss_c and delr_c3	-->	-0.5304

amp_n and ss_c	-->	-0.5264
amp_n and delr_c2	-->	0.5251
ss_n and delr_c	-->	0.5221
amp_n and delr_c3	-->	0.5083
amp_n and delr_n	-->	0.4584
enot_n and amp_c	-->	-0.4218
enot_n and delr_c	-->	-0.4149
ss_n and enot_c	-->	0.4018
ss_n and delr_c2	-->	0.3897
delr_n and delr_c	-->	-0.3850
amp_n and delr_c	-->	0.3415

All other correlations are below 0.25

=====Dataset>>[Ir1]-deglitch-then merge.chi<<==========

Athena data file -- Athena version 0.8.061

Saving Ir4-deglitch-then-merge as chi(k)

Background parameters

. E0=11218.317 Eshift=0.000 Rbkg=1.000

. Standard=0: None

. Kweight=2.0 Edge step=1.000

. Fixed step=yes Flatten=yes

. Pre-edge range: [-98.249 : -30.000]

. Pre-edge line: -0.00073778 + 6.6159e-08 * E

. Normalization range: [60.949 : 478.612]

. Post-edge polynomial: 1.0047 + -8.1768e-07 * E + 3.538e-11 * E^2

. Spline range: [0.000 : 481.944] Clamps: None/Strong

Forward FT parameters

. Kweight=0.5 Window=hanning Phase correction=no

. k-range: [2.500 : 7.500] dk=1.00

Backward FT parameters

R-range: [1.000 : 3.000]

. dR=0.00 Window=hanning

Plotting parameters

. Multiplier=1 Y-offset=0.000

k-range	**2.500 - 9.200**
dk	1.000
k-window	Hanning
k-weight	1,2,3
R-range	1.000 - 3.600
dR	0.000
R-window	Hanning
fitting space	R
background function	none
phase correction	none

R-factor for this data set = 0.00542

R-factor with k-weight=1 for this data set = 0.00243

R-factor with k-weight=2 for this data set = 0.00541

R-factor with k-weight=3 for this data set = 0.00841

===== Paths used to fit Ir4-deglitch-then-merge.chi

FEFF0: Path 1: [C123_1] ..

r	**2.033637**
degen	1.000000
S02	0.459881
e0	13.01833
dr	0.014237
ss2	-0.013056
3rd	0.000000
4th	0.000000
ei	0.000000

FEFF1: Path 2: [N13_1] ..

r	**2.006810**
degen	1.000000
S02	1.547263
e0	-6.901043
dr	-0.024990
ss2	0.005529
3rd	0.000000
4th	0.000000
ei	0.000000

FEFF0: Path 3: [C19_1] ..

r	**2.006810**
degen	1.000000
S02	1.547263
e0	-6.901043
dr	-0.040390
ss2	0.005529
3rd	0.000000
4th	0.000000
ei	0.000000

FEFF1: Path 4: [C122_1] ..

r	2.034237
degen	1.000000
S02	0.459881
e0	13.01833
dr	-0.038963
ss2	-0.013056
3rd	0.000000
4th	0.000000
ei	0.000000

FEFF1: Path 5: [C121_1] ..

r	2.033637
degen	1.000000
S02	0.459881
e0	13.01833
dr	-0.042363
ss2	-0.013056
3rd	0.000000
4th	0.000000
ei	0.000000

FEFF1: Path 6: [N11_1] ..

r	2.007010
degen	1.000000
S02	1.547263
e0	-6.90104
dr	-0.13519
ss2	0.005529
3rd	0.000000
4th	0.000000
ei	0.000000

FEFF1: Path 7: [C73_1] ..

r	2.935899
degen	1.000000
S02	0.459881
e0	13.01833
dr	0.029799
ss2	-0.013056
3rd	0.000000
4th	0.000000
ei	0.000000

FEFF1: Path 8: [C63_1] ..

r	2.935899
degen	1.000000
S02	0.459881
e0	13.01833
dr	0.023499
ss2	-0.013056
3rd	0.000000
4th	0.000000

ei	0.000000

FEFF1: Path 9: [C62_1] ..

r	**2.935899**
degen	1.000000
S02	0.459881
e0	13.01833
dr	-0.005201
ss2	-0.013056
3rd	0.000000
4th	0.000000
ei	0.000000

FEFF1: Path 10: [C72_1] ..

r	**2.955899**
degen	1.000000
S02	0.459881
e0	13.01833
dr	-0.000301
ss2	-0.013056
3rd	0.000000
4th	0.000000
ei	0.000000

FEFF1: Path 11: [C71_1] ..

r	**2.935899**
degen	1.000000
S02	0.459881
e0	13.01833
dr	-0.031101
ss2	-0.013056
3rd	0.000000
4th	0.000000
ei	0.000000

FEFF1: Path 12: [C61_1] ..

r	**2.935799**
degen	1.000000
S02	0.459881
e0	13.01833
dr	-0.065601
ss2	-0.013056
3rd	0.000000
4th	0.000000
ei	0.000000

FEFF1: Path 13: [C22_1] ..

r	**3.139054**
degen	1.000000
S02	0.459881
e0	13.01833
dr	0.123254
ss2	-0.013056
3rd	0.000000

4th	0.000000
ei	0.000000

FEFF1: Path 14: [C23_1] ..

r	**3.142854**
degen	1.000000
S02	0.459881
e0	13.01833
dr	0.123254
ss2	-0.013056
3rd	0.000000
4th	0.000000
ei	0.000000

FEFF1: Path 16: [C113_1] ..

r	**3.142554**
degen	1.000000
S02	0.459881
e0	13.01833
dr	0.058554
ss2	-0.013056
3rd	0.000000
4th	0.000000
ei	0.000000

FEFF1: Path 18: [C21_1] ..

r	**3.142554**
degen	1.000000
S02	0.459881
e0	13.01833
dr	0.029154
ss2	-0.013056
3rd	0.000000
4th	0.000000
ei	0.000000

FEFF1: Path 19: [C112_1] ..

r	**3.142554**
degen	1.000000
S02	0.459881
e0	13.01833
dr	-0.015846
ss2	-0.013056
3rd	0.000000
4th	0.000000
ei	0.000000

FEFF1: Path 20: [C111_1] ..

r	3.142954
degen	1.000000
S02	0.459881
e0	13.01833
dr	-0.015846
ss2	-0.013056
3rd	0.000000
4th	0.000000
ei	0.000000

B-2 Ir4

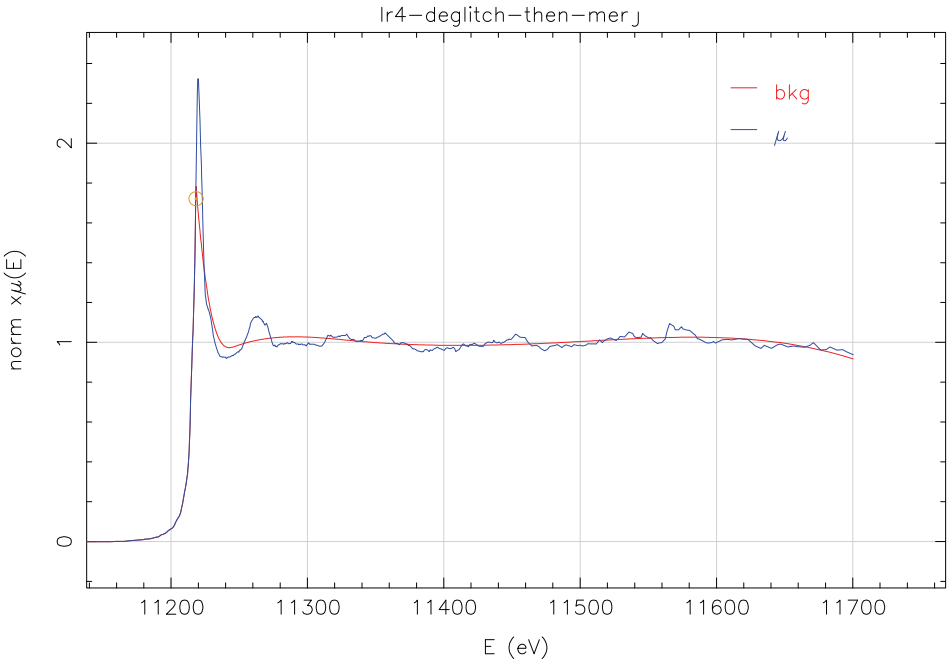

Figure 0-3: The edge-jump normalized Ir L_3-edge spectrum of [Ir(ppz)$_3$] (blue). The red line represent the background determined with ATHENA (see § 2.2.4).

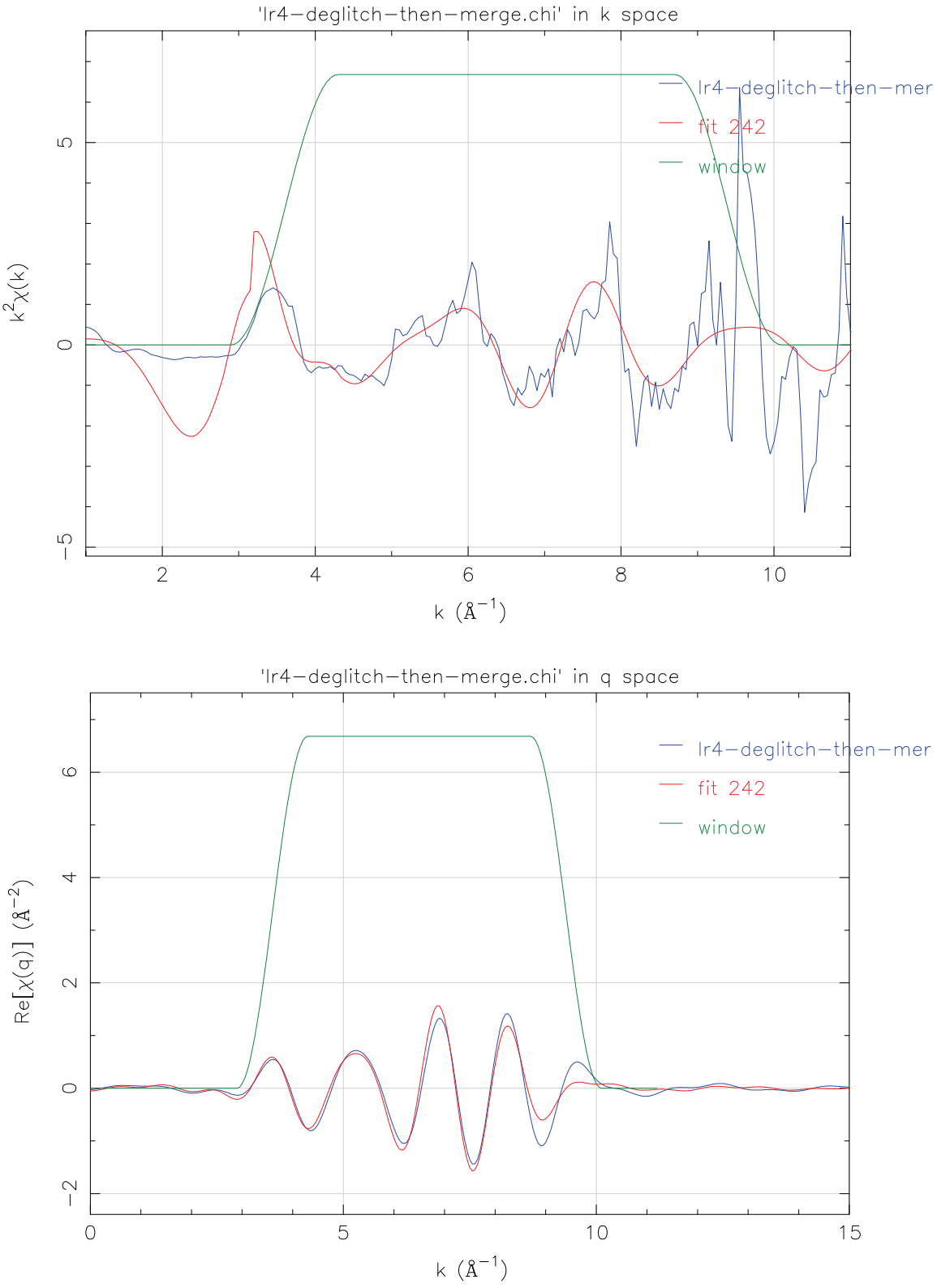

Figure 0-4: EXAFS signal of **lr4** in k space (Top) and q space (back Fourier transform). (Bottom)

Nr.	N_γ	R_γ	Amplitude	Pathway	Distances Parameter	DW parameter
1	1	2.194	100	$Ir \leftrightarrow C_{123}$	ΔR_{Ir-C}	σ_{Ir-C}
2	1	2.0318	100	$Ir \leftrightarrow N_{13}$	ΔR_{Ir-N}	σ_{Ir-N}
3	1	2.0472	98.250	$Ir \leftrightarrow N_{12}$	ΔR_{Ir-N} - 0.0154	σ_{Ir-N}
4	1	2.0732	84.776	$Ir \leftrightarrow C_{122}$	ΔR_{Ir-C} - 0.0532	σ_{Ir-C}
5	1	2.0760	84.508	$Ir \leftrightarrow C_{121}$	ΔR_{Ir-C} - 0.0566	σ_{Ir-C}
6	1	2.1422	88.287	$Ir \leftrightarrow N_{11}$	ΔR_{Ir-N} - 0.1102	σ_{Ir-N}
7	1	2.9061	36.736	$Ir \leftrightarrow C_{73}$	ΔR_{Ir-C2}	σ_{Ir-C}
8	1	2.9124	36.529	$Ir \leftrightarrow C_{63}$	ΔR_{Ir-C2} - 0.0063	σ_{Ir-C}
9	1	2.9411	35.603	$Ir \leftrightarrow C_{62}$	ΔR_{Ir-C2} - 0.035	σ_{Ir-C}
10	1	2.956	35.126	$Ir \leftrightarrow C_{72}$	ΔR_{Ir-C2} - 0.0301	σ_{Ir-C}
11	1	2.9670	34.789	$Ir \leftrightarrow C_{71}$	ΔR_{Ir-C2} - 0.0609	σ_{Ir-C}
12	1	3.0014	33.746	$Ir \leftrightarrow C_{61}$	ΔR_{Ir-C2} - 0.0954	σ_{Ir-C}
13	1	3.0158	33.321	$Ir \leftrightarrow C_{22}$	ΔR_{Ir-C3}	σ_{Ir-C}
14	1	3.0196	33.210	$Ir \leftrightarrow C_{23}$	ΔR_{Ir-C3} - 0.038	σ_{Ir-C}
16	1	3.0840	31.396	$Ir \leftrightarrow C_{113}$	ΔR_{Ir-c3} - 0.0647	σ_{Ir-C}
18	1	3.1134	30.608	$Ir \leftrightarrow C_{21}$	ΔR_{Ir-C3} - 0.0941	σ_{Ir-C}
19	1	3.1584	29.450	$Ir \leftrightarrow C_{112}$	$\Delta R_{Ir-C}3$ - 0.1391	σ_{Ir-C}
20	1	3.1584	29.440	$Ir \leftrightarrow C_{111}$	ΔR_{Ir-C3} - 0.1391	σ_{Ir-C}

B-2-1 Input file for [Ir4]

```
* title      C27 H21 Ir N6
* title      Arnold B. Tamayo
* title      Synthesis and Characterization of Facial and Meridional
* title      Tris-cyclometalated Iridium(III) Complexes
* space = P -4 21 c
* a =       23.1250  b =          23.1250  c =          8.8540
* alpha = 90.0       beta =      90.0       gamma =  90.0
* core =  Ir1         edge =     L3
* atoms
* ! elem   x        y        z       tag       occ
*   Ir   0.74884   0.02054   0.88343  Ir1         1.00000
*   N    0.77840   0.10340   0.94990  N1          1.00000
*   N    0.77550   0.14320   0.83630  N2          1.00000
*   N    0.66340   0.02960   0.96720  N3          1.00000
*   N    0.62960  -0.01740   0.93430  N4          1.00000
*   N    0.78020  -0.02250   1.08040  N5          1.00000
*   N    0.83540  -0.04270   1.06350  N6          1.00000
*   C    0.73220   0.06730   0.69630  C1          1.00000
*   C    0.70750   0.05110   0.55800  C2          1.00000
*   H    0.69390   0.01340   0.54720  H2          1.00000
*   C    0.70250   0.08910   0.43530  C3          1.00000
*   H    0.68570   0.07620   0.34590  H3          1.00000
*   C    0.72180   0.14480   0.44560  C4          1.00000
*   H    0.71900   0.16970   0.36340  H4          1.00000
*   C    0.74520   0.16310   0.57730  C5          1.00000
*   H    0.75750   0.20120   0.58700  H5          1.00000
*   C    0.75090   0.12510   0.69860  C6          1.00000
*   C    0.79750   0.19480   0.88630  C7          1.00000
*   H    0.80150   0.22830   0.82920  H7          1.00000
*   C    0.81250   0.18850   1.03320  C8          1.00000
*   H    0.82710   0.21700   1.09690  H8          1.00000
*   C    0.80160   0.13010   1.07040  C9          1.00000
```

```
*  H    0.80920   0.11290   1.16330  H9         1.00000
*  C    0.71220  -0.05200   0.79960  C10        1.00000
*  C    0.73410  -0.09380   0.70230  C11        1.00000
*  H    0.77250  -0.09080   0.67230  H11        1.00000
*  C    0.70180  -0.13980   0.64750  C12        1.00000
*  H    0.71870  -0.16630   0.58200  H12        1.00000
*  C    0.64520  -0.14650   0.68910  C13        1.00000
*  H    0.62360  -0.17740   0.65210  H13        1.00000
*  C    0.62040  -0.10740   0.78590  C14        1.00000
*  H    0.58220  -0.11200   0.81670  H14        1.00000
*  C    0.65290  -0.06060   0.83780  C15        1.00000
*  C    0.57680  -0.01040   0.99930  C16        1.00000
*  H    0.54590  -0.03590   0.99220  H16        1.00000
*  C    0.57710   0.04040   1.07630  C17        1.00000
*  H    0.54690   0.05600   1.13250  H17        1.00000
*  C    0.63250   0.06490   1.05390  C18        1.00000
*  H    0.64520   0.09990   1.09340  H18        1.00000
*  C    0.82890  -0.00280   0.81280  C19        1.00000
*  C    0.85580   0.00510   0.67260  C20        1.00000
*  H    0.83700   0.02650   0.59850  H20        1.00000
*  C    0.91000  -0.01810   0.64100  C21        1.00000
*  H    0.92610  -0.01330   0.54560  H21        1.00000
*  C    0.93990  -0.04830   0.74980  C22        1.00000
*  H    0.97630  -0.06320   0.72780  H22        1.00000
*  C    0.91660  -0.05670   0.88960  C23        1.00000
*  H    0.93670  -0.07690   0.96370  H23        1.00000
*  C    0.86180  -0.03400   0.91850  C24        1.00000
*  C    0.85360  -0.06750   1.19320  C25        1.00000
*  H    0.88940  -0.08480   1.20920  H25        1.00000
*  C    0.80980  -0.06280   1.29690  C26        1.00000
*  H    0.80980  -0.07600   1.39620  H26        1.00000
*  C    0.76560  -0.03420   1.22230  C27        1.00000
*  H    0.73040  -0.02450   1.26590  H27        1.00000
* ---------------------------------------------------------------------
```

B-2-2 Fitting data sheet for [Ir4]

Data sheet containing all fitting paramters for EXAFS fit presented in §6.1.1.1 in Figure 6-4.

```
=============================================================
```

Independent points	**10.910156250**
Number of variables	7.000000000
Chi-square	493.381700285
Reduced Chi-square	126.179535737
R-factor	0.116926152
Measurement uncertainty (k)	0.005725403
Measurement uncertainty (R)	0.008145556
Number of data sets	1.000000000

Guess parameters +/- uncertainties (initial guess):

amp_c	**7.0318750**	**+/-**	**3.4973390**	**(1.0000)**
enot_c	10.8566450	+/-	5.2422150	(0.0000)
delr_c	0.1022430	+/-	0.0555460	(0.0000)
ss_c	0.0009750	+/-	0.0049770	(0.0030)
amp_n	8.2287590	+/-	4.4082610	(1.0000)
enot_n	0.0691890	+/-	7.9053560	(0.0000)
delr_n	0.1695000	+/-	0.0701760	(0.0000)

Set parameters:

ss_n = 0.003

Correlations between variables:

enot_c and enot_n	**-->**	**0.9429**
delr_c and delr_n	-->	0.9038
amp_c and amp_n	-->	0.8857
delr_c and ss_c	-->	0.8577
ss_c and delr_n	-->	0.8470
enot_n and delr_n	-->	0.7637
enot_c and delr_n	-->	0.6971
amp_c and delr_c	-->	0.6413
enot_c and delr_c	-->	0.6191
amp_c and ss_c	-->	0.5679
delr_c and enot_n	-->	0.5592
ss_c and enot_n	-->	0.3848
delr_c and amp_n	-->	0.3299
enot_c and ss_c	-->	0.3260
amp_c and delr_n	-->	0.3256
amp_n and enot_n	-->	-0.3047

All other correlations are below 0.25

=====Dataset>>[Ir(ppz)$_3$]-deglitch-then-merge.chi<<==========

Athena data file -- Athena version 0.8.061

Saving Ir4-deglitch-then-merge as chi(k)

Background parameters

. Element=Ir Edge=L3

. E0=11218.079 Eshift=0.000 Rbkg=1.000

. Standard=0: None

. Kweight=2.0 Edge step=1.000

. Fixed step=yes Flatten=yes

. Pre-edge range: [-98.598 : -52.693]

. Pre-edge line: -0.00076369 + 6.8595e-08 * E

. Normalization range: [87.460 : 482.311]

. Post-edge polynomial: 0.0086715 + 0.00017085 * E + -7.3609e-09 * E^2

. Spline range: [0.000 : 481.687] Clamps: None/Strong

Forward FT parameters

. Kweight=0.5 Window= Hanning Phase correction=no

. k-range: [3.000 : 7.000] dk=1.00

Backward FT parameters

. R-range: [1.000 : 3.000]

. dR=0.00 Window=Hanning

Plotting parameters

. Multiplier=1 Y-offset=0.000

k-range	**2.500 - 9.200**
dk	1.000
k-window	Hanning
k-weight	1,2,3
R-range	1.000 - 3.600
dR	0.000
R-window	Hanning
fitting space	R
background function	none
phase correction	none

R-factor for this data set = 0.11693

R-factor with k-weight=1 for this data set = 0.10854

R-factor with k-weight=2 for this data set = 0.11932

R-factor with k-weight=3 for this data set = 0.12291

===== Paths used to fit Ir4-deglitch-then-merge.chi

FEFF0: Path 1: [C1_1] ..

r	**2.117843**
degen	1.000000
S02	7.031875
e0	10.856645
dr	0.102243
ss2	0.000975
3rd	0.000000
4th	0.000000
ei	0.000000

FEFF0: Path 2: [C10_1] ..

r	2.117843
degen	1.000000
S02	7.031875
e0	10.856645
dr	0.097243
ss2	0.000975
3rd	0.000000
4th	0.000000
ei	0.000000

FEFF0: Path 3: [C19_1] ..

r	2.117843
degen	1.000000
S02	7.031875
e0	10.856645
dr	0.090543
ss2	0.000975
3rd	0.000000
4th	0.000000
ei	0.000000

FEFF0: Path 4: [N1_1] ..

r	2.287300
degen	1.000000
S02	8.228759
e0	0.069189
dr	0.169500
ss2	0.003000
3rd	0.000000
4th	0.000000
ei	0.000000

FEFF0: Path 5: [N3_1] ..

r	2.287300
degen	1.000000
S02	8.228759
e0	0.069189
dr	0.166500
ss2	0.003000
3rd	0.000000
4th	0.000000
ei	0.000000

FEFF0: Path 6: [N5_1] ..

r	2.287300
degen	1.000000
S02	8.228759
e0	0.069189
dr	0.152400
ss2	0.003000
3rd	0.000000
4th	0.000000
ei	0.000000

B-3 EXAFS result Ir4

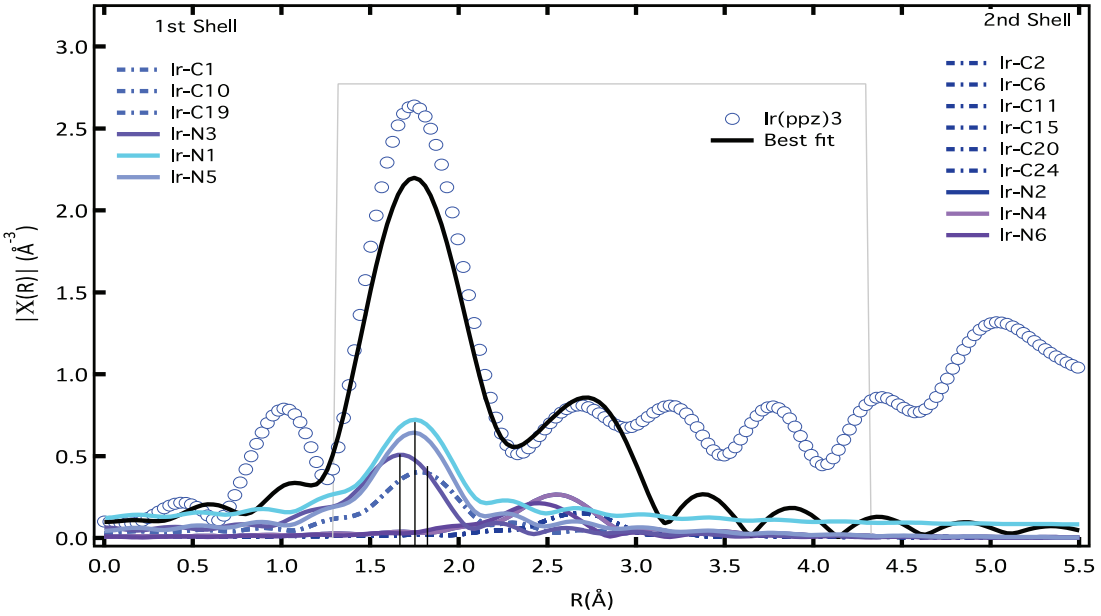

Figure 0-5: Experimental data (open circles) compared with the scattering paths included in the EXAFS of **Ir4** together with the best fit. The paths are shown for the first shell single scattering and second shell single scattering. The K-range is 4.6-13.8 $Å^{-1}$ and R range is 1.3-4.3 Å. The peaks of Nitrogen atoms and Carbon atoms are offset vertically for better visibility.[71]

Abbreviations

APD	Avalanche Photo Diode
ASC	Avoided surface crossing
BBO	Beta Barium Borat Crystal
BO	Born-Oppenheimer
bpy	bipyridine
CCD	Charge-Coupled Device
$CHCl_3$	Chloroform
CI	Conjugation Interaction
CT	Charge Transfer
CTTS	Charge Transform to Solvent
Cyt C	Cytochrome C
DAQ	Data Acquisition
DAS	Decay Associated Spectra
DCM	Dichloromethane
DFT	Density functional theory
DHP	Dehaloperoxidase
DMSO	Dimethyl sulfoxide
DOS	Density of states
ES	Excited State
EVR	Energy Vibrational Redistribution
EXAFS	Extended X-ray Absorption Fine Structure
FC	Franck-Condon
FDMNES	Fine difference method for near-edge structure
Fe	Iron
FeP	Iron porphyrin
FRET	Fluorescence resonance energy transfer
Fs	Femtosecond
FWHM	Full Width Half Maximum
GF	Global Fitting
GR	Geminate Recombination
Hb	Hemoglobin
HERFD	High energy resolution Florescence Detected
HOMO	Highest Occupied Molecular Orbital
HT	Herzberg-Teller
IC	Internal Conversion
ILCT	Intra-ligand charge transfer
ILET	Inter-ligand Energy Transfer
Im	Imidazole
Ir	Iridium
Ir1	Tris[2-phenylpyridine]iridium(III)
Ir2	bis(2- phenylpyridinato-N, C2')(picolinate)Iridium(III)
Ir3	bis(2- phenylpyridinato-N, C2')(2,2'-bipyridine)Iridium(III)
Ir4	Tris[2-phenylpyrazole]iridium(III)

IRF	Instrument Response Function
ISC	Inter-system crossing
IVR	Intra-Molcular Vibrational Redistribution
LC	Ligand Centred
LLCT	Inter-ligand charge transfer
LUMO	Lowest Occupied Molecular Orbital
Mb	Myoglobin
MbCN	Cyanomyoglobin
MbCO	Carboxymyoglobin
MbNO	Nitrosy lmyoglobin
MbO2	Oxymyoglobin
MetMb	Aquametmyoglobin
MLCT	Metal to Legend Charge Transfer
MO	Molecular Orbital
Mp	Microperoxidase
MS	Multiple Scattering
NLO	Non-Linear Optics
nm	Nanometer
NO	Nitricoxide
Ns	Nano Second
O_h	Octahedral Array
OLED	Organic Light Emitting Diodes
PDS	Primary Docking site
PHOLED	Phosphorescent Organic Light Emitting Diodes
Pic	Picolinate
PLUC	Photoluminescence up-conversion
PoD	Pluse on Demand
ppy	Phenylpyridine
ppz	Phenylpyrazole
Ps	Pico Second
RT	Room Temperature
RXES	Resonance X-ray Emission Spectroscopy
S/N	Signal to Noise ratio
SAS	Species Associated Spectra
SLS	Swiss Light Source
SOC	Spin-orbit coupling
SVD	Singular Value Decomposition
TCSPC	Time Correlated Single Photon Counting
TDDFT	Time Dependent Density Functional Theory
THF	Tetrahydrofuran
TM	Transition metal
TA	Transient Absorption
TRP	Tryptophan
WF	Molecular Wave Junction
WL	White Line
XANES	X-ray Absorption near edge Structure

XAS	X-ray Absorption Spectroscopy
XES	X-ray Emission Spectroscopy
ZFS	Zero-field Splitting

References

(1) B, W. B.; W, O. L. *J Am Chem Soc* **1974**, *96*.

(2) Liao, M. S.; Scheiner, S. *J Chem Phys* **2002**, *116*, 3635.

(3) Sun, L. C.; Hammarstrom, L.; Akermark, B.; Styring, S. *Chem Soc Rev* **2001**, *30*, 36.

(4) Oregan, B.; Gratzel, M. *Nature* **1991**, *353*, 737.

(5) Baldo, M. A.; O'Brien, D. F.; You, Y.; Shoustikov, A.; Sibley, S.; Thompson, M. E.; Forrest, S. R. *Nature* **1998**, *395*, 151.

(6) ; https://en.wikipedia.org/wiki/Carbon_monoxide_poisoning: accessed 22 October 2015.

(7) Newville, M. *J Sync Rad* **2001**, *8(2)*, 322.

(8) Ravel, B. *Journal of Alloys and Compounds* **2005**, *401(1-2)*, 118

(9) G. Golub, W. K. *J Soc Ind Appl Math: Series B , Numerical Analysis 2* **1965**, *205*.

(10) I. H. M. van Stokkum, D. S. L., and R. van Grondelle, , *Biochim Biophys Acta* **2004**, *82*.

(11) Ding, X. D.; Weichsel, A.; Andersen, J. F.; Shokhireva, T. K.; Balfour, C.; Pierik, A. J.; Averill, B. A.; Montfort, W. R.; Walker, F. A. *Journal of the American Chemical Society* **1999**, *121*, 128.

(12) Bourassa, J. L.; Ives, E. P.; Marqueling, A. L.; Shimanovich, R.; Groves, J. T. *Journal of the American Chemical Society* **2001**, *123*, 5142.

(13) Loan, G. H. G. a. C. F. V. *JHU Press* **1996**.

(14) Sun, Y. J.; Jin, K. L.; Mao, X. O.; Zhu, Y. H.; Greenberg, D. A. *P Natl Acad Sci USA* **2001**, *98*, 15306.

(15) Coyle, C. M.; Vogel, K. M.; Rush, T. S.; Kozlowski, P. M.; Williams, R.; Spiro, T. G.; Dou, Y.; Ikeda-Saito, M.; Olson, J. S.; Zgierski, M. Z. *Biochemistry-Us* **2003**, *42*, 10342.

(16) Zemojtel, T.; Rini, M.; Heyne, K.; Dandekar, T.; Nibbering, E. T. J.; Kozlowski, P. M. *J Am Chem Soc* **2004**, *126*, 1930.

(17) Cornelius, P. A.; Hochstrasser, R. M.; Steele, A. W. *J Mol Biol* **1983**, *163*, 119.

(18) Petrich, J. W.; Lambry, J. C.; Kuczera, K.; Karplus, M.; Poyart, C.; Martin, J. L. *Biochemistry-Us* **1991**, *30*, 3975.

(19) Petrich, J. W.; Lambry, J. C.; Balasubramanian, S.; Lambright, D. G.; Boxer, S. G.; Martin, J. L. *J Mol Biol* **1994**, *238*, 437.

(20) Shreve, A. P.; Franzen, S.; Simpson, M. C.; Dyer, R. B. *J Phys Chem B* **1999**, *103*, 7969.

(21) Cao, W. X.; Christian, J. F.; Champion, P. M.; Rosca, F.; Sage, J. T. *Biochemistry-Us* **2001**, *40*, 5728.

(22) Ye, X.; Demidov, A.; Champion, P. M. *J Am Chem Soc* **2002**, *124*, 5914.

(23) Ionascu, D.; Gruia, F.; Ye, X.; Yu, A. C.; Rosca, F.; Beck, C.; Demidov, A.; Olson, J. S.; Champion, P. M. *J Am Chem Soc* **2005**, *127*, 16921.

(24) Kholodenko, Y.; Gooding, E. A.; Dou, Y.; Ikeda-Saito, M.; Hochstrasser, R. M. *Biochemistry-Us* **1999**, *38*, 5918.

(25) Negrerie, M.; Kruglik, S. G.; Lambry, J. C.; Vos, M. H.; Martin, J. L.; Franzen, S. *J Biol Chem* **2006**, *281*, 10389.

(26) Kruglik, S. G.; Yoo, B. K.; Franzen, S.; Vos, M. H.; Martin, J. L.; Negrerie, M. *P Natl Acad Sci USA* **2010**, *107*, 13678.

(27) Yoo, B. K.; Kruglik, S. G.; Lamarre, I.; Martin, J. L.; Negrerie, M. *J Phys Chem B* **2012**, *116*, 4106.

(28) Kim, J.; Park, J.; Lee, T.; Lim, M. *J Phys Chem B* **2012**, *116*, 13663.

(29) Kim, S.; Lim, M. *J Phys Chem B* **2012**, *116*, 5819.

(30) Kim, S.; Jin, G.; Lim, M. *J Phys Chem B* **2004**, *108*, 20366.

(31) Stavrov, S. S. *Biophysical Journal* **1993**, *65*, 1942.

(32) Zhu, L. Y.; Wang, W.; Sage, J. T.; Champion, P. M. *J Raman Spectrosc* **1995**, *26*, 527.

(33) Stavrov, S. S. *Biopolymers* **2004**, *74*, 37.

(34) Kitagawa, T.; Haruta, N.; Mizutani, Y. *Biopolymers* **2002**, *67*, 207.

(35) Sato, A.; Gao, Y.; Kitagawa, T.; Mizutani, Y. *P Natl Acad Sci USA* **2007**, *104*, 9627.

(36) Schotte, F.; Lim, M. H.; Jackson, T. A.; Smirnov, A. V.; Soman, J.; Olson, J. S.; Phillips, G. N.; Wulff, M.; Anfinrud, P. A. *Science* **2003**, *300*, 1944.

(37) Schotte, F.; Soman, J.; Olson, J. S.; Wulff, M.; Anfinrud, P. A. *J Struct Biol* **2004**, *147*, 235.

(38) Bourgeois, D.; Vallone, B.; Schotte, F.; Arcovito, A.; Miele, A. E.; Sciara, G.; Wulff, M.; Anfinrud, P.; Brunori, M. *P Natl Acad Sci USA* **2003**, *100*, 8704.

(39) Cho, H. S.; Dashdorj, N.; Schotte, F.; Graber, T.; Henning, R.; Anfinrud, P. *P Natl Acad Sci USA* **2010**, *107*, 7281.
(40) Ihee, H.; Kim, K. H.; Oang, K. Y.; Kim, J.; Lee, J. H.; Kim, Y. *Chem Commun* **2011**, *47*, 289.
(41) Oang, K. Y.; Kim, J. G.; Yang, C.; Kim, T. W.; Kim, Y.; Kim, K. H.; Kim, J. H.; Ihee, H. *J Phys Chem Lett* **2014**, *5*, 804−808.
(42) Aziz, E. F.; Ottosson, N.; Bonhommeau, S.; Bergmann, N.; Eberhardt, W.; Chergui, M. *Physical Review Letters* **2009**, *102*.
(43) Lima, F. A.; Penfold, T. J.; van der Veen, R. M.; Reinhard, M.; Abela, R.; Tavernelli, I.; Rothlisberger, U.; Benfatto, M.; Milne, C. J.; Chergui, M. *Phys Chem Chem Phys* **2014**, *16*, 1617.
(44) Sono, M.; Roach, M. P.; Coulter, E. D.; Dawson, J. H. *Chem Rev* **1996**, *96*, 2841.
(45) Wilson, S. A.; Kroll, T.; Decreau, R. A.; Hocking, R. K.; Lundberg, M.; Hedman, B.; Hodgson, K. O.; Solomon, E. I. *J Am Chem Soc* **2013**, *135*, 1124.
(46) Milne, C. J.; Penfold, T. J.; Chergui, M. *Coordin Chem Rev* **2014**, *277*, 44.
(47) Lima, F. A.; Milne, C. J.; Amarasinghe, D. C. V.; Rittmann-Frank, M. H.; van der Veen, R. M.; Reinhard, M.; Pham, V. T.; Karlsson, S.; Johnson, S. L.; Grolimund, D.; Borca, C.; Huthwelker, T.; Janousch, M.; van Mourik, F.; Abela, R.; Chergui, M. *Review of Scientific Instruments* **2011**, *82*, 063111.
(48) Reinhard, M.; Penfold, T. J.; Lima, F. A.; Rittmann, J.; Rittmann-Frank, M. H.; Abela, R.; Tavernelli, I.; Rothlisberger, U.; Milne, C. J.; Chergui, M. *Structural Dynamics* **2014**, *1*, 024901.
(49) Chergui, M. *Acta Crystallogr A* **2010**, *66*, 229.
(50) Yersin, H.; Rausch, A. F.; Czerwieniec, R.; Hofbeck, T.; Fischer, T. *Coordin Chem Rev* **2011**, *255*, 2622.
(51) Sajoto, T.; Djurovich, P. I.; Tamayo, A.; Yousufuddin, M.; Bau, R.; Thompson, M. E.; Holmes, R. J.; Forrest, S. R. *Inorg Chem* **2005**, *44*, 7992.
(52) You, Y.; Seo, J.; Kim, S. H.; Kim, K. S.; Ahn, T. K.; Kim, D.; Park, S. Y. *Inorg Chem* **2008**, *47*, 1476.
(53) Ladouceur, S.; Fortin, D.; Zysman-Colman, E. *Inorg Chem* **2010**, *49*, 5625.
(54) King, K. A.; Watts, R. J. *J Am Chem Soc* **1987**, *109*, 1589.
(55) Wilde, A. P.; King, K. A.; Watts, R. J. *J Phys Chem-Us* **1991**, *95*, 629.
(56) Karatsu, T.; Ito, E.; Yagai, S.; Kitamura, A. *Chem Phys Lett* **2006**, *424*, 353.
(57) Fei, T.; Gu, X.; Zhang, M.; Wang, C. L.; Hanif, M.; Zhang, H. Y.; Ma, Y. G. *Synthetic Met* **2009**, *159*, 113.
(58) Adamovich, V. I.; Cordero, S. R.; Djurovich, P. I.; Tamayo, A.; Thompson, M. E.; D'Andrade, B. W.; Forrest, S. R. *Org Electron* **2003**, *4*, 77.
(59) Sajoto, T.; Djurovich, P. I.; Tamayo, A. B.; Oxgaard, J.; Goddard, W. A.; Thompson, M. E. *J Am Chem Soc* **2009**, *131*, 9813.
(60) Treboux, G.; Mizukami, J.; Yabe, M.; Nakamura, S. *Chem Lett* **2007**, *36*, 1344.
(61) Jung, S. G.; Kang, Y. J.; Kim, H. S.; Kim, Y. H.; Lee, C. L.; Kim, J. J.; Lee, S. K.; Kwon, S. K. *Eur J Inorg Chem* **2004**, 3415.
(62) Kasha, M. *Discuss Faraday Soc* **1950**, 14.
(63) Felker, P. M.; Zewail, A. H. *J Chem Phys* **1985**, *82*, 2975.
(64) Felker, P. M.; Zewail, A. H. *Adv Chem Phys* **1988**, *70*, 265.
(65) Chergui, M. *Accounts Chem Res* **2015**, *48*, 801.
(66) Cannizzo, A.; van Mourik, F.; Gawelda, W.; Zgrablic, G.; Bressler, C.; Chergui, M. *Angew Chem Int Edit* **2006**, *45*, 3174.
(67) Gawelda, W.; Cannizzo, A.; Pham, V. T.; van Mourik, F.; Bressler, C.; Chergui, M. *J Am Chem Soc* **2007**, *129*, 8199.
(68) Clancy, J. P.; Chen, N.; Kim, C. Y.; Chen, W. F.; Plumb, K. W.; Jeon, B. C.; Noh, T. W.; Kim, Y. J. *Phys Rev B* **2012**, *86*.
(69) Vagnini, M. T.; Mara, M. W.; Harpham, M. R.; Huang, J.; Shelby, M. L.; Chen, L. X.; Wasielewski, M. R. *Chem Sci* **2013**, *4*, 3863.
(70) Van der Veen, R. M., EPFL, 2010.
(71) Rittmann-Frank, M. H., EPFL, 2014.
(72) Consani, C., EPFL, 2012.
(73) http://www.esrf.eu/computing/scientific/

xop2.3 Windows: accessed 22 October 2015.
(74) Dejus, M. S. d. R. a. R. **2003**.
(75) Rehr, J. J.; Albers, R. C. *Rev Mod Phys* **2000**, *72*, 621.
(76) Krause, M. O. *J Phys Chem Ref Data* **1979**, *8*, 307.

(77) Antonini, E.; Brunori, M. *Hemoglobin and Myoglobin in their Reactions with Ligands*; Norht-Holland Publishing Company, 1971.
(78) Alves Lima, F., EPFL, 2011.
(79) Denisov, S. A.; Cudre, Y.; Verwilst, P.; Jonusauskas, G.; Marin-Suarez, M.; Fernandez-Sanchez, J. F.; Baranoff, E.; McClenaghan, N. D. *Inorg Chem* **2014**, *53*, 2677.
(80) Baranoff, E.; Curchod, B. F. E.; Monti, F.; Steimer, F.; Accorsi, G.; Tavernelli, I.; Rothlisberger, U.; Scopelliti, R.; Gratzel, M.; Nazeeruddin, M. K. *Inorg Chem* **2012**, *51*, 799.
(81) Tordera, D.; Delgado, M.; Orti, E.; Bolink, H. J.; Frey, J.; Nazeeruddin, M. K.; Baranoff, E. *Chem Mater* **2012**, *24*, 1896.
(82) Teller, E. *Israel J Chem* **1969**, *7*, 227.
(83) Turro, N. J.; Ramamurthy, V.; Scaiano, J. C. *Principles of molecular photochemistry : an introduction*; University Science Books: Sausalito, Calif., 2009.
(84) Hedley, G. J.; Ruseckas, A.; Liu, Z. H.; Lo, S. C.; Burn, P. L.; Samuel, I. D. W. *J Am Chem Soc* **2008**, *130*, 11842.
(85) Elsaesser, T.; Kaiser, W. *Annu Rev Phys Chem* **1991**, *42*, 83.
(86) Nesbitt, D. J.; Field, R. W. *J Phys Chem-Us* **1996**, *100*, 12735.
(87) Lehmann, K. K.; Scoles, G.; Pate, B. H. *Annu Rev Phys Chem* **1994**, *45*, 241.
(88) Gruebele, M.; Wolynes, P. G. *Accounts Chem Res* **2004**, *37*, 261.
(89) Boyall, D.; Reid, K. L. *Chem Soc Rev* **1997**, *26*, 223.
(90) Seyfang, D. G.; http://n.ethz.ch/~seyfangg/WhatIVR.html: Labor für Physikalische Chemie, Accessed October 22, 2015.

(91) Bräm, O. C., EPFL, 2011.
(92) Gschwend, G. e. *Time-correlated single photon counting measurement of the fluorescence of anataseTiO2 nano-particles*, EPFL, 2013.
(93) S., G. J. *The Theory of Transition Metal Ions*; Cambridge Universtity Press, 1961.
(94) Hauser, A.; Amstutz, N.; Delahaye, S.; Sadki, A.; Schenker, S.; Sieber, R.; Zerara, M. *Struct Bond* **2004**, *106*, 81.
(95) Vlcek, A. *Coordin Chem Rev* **2000**, *200*, 933.
(96) Gerloch, M.; Harding, J.; Woolley, R. *The context and application of ligand field theory*, 1981.
(97) Woolley, R. *Ligand-field analysis of transition-metal complexes*, 1987; Vol. 6(2).
(98) A., C. F. *Journol of Chemical Education* **1964**, *41*, 12.
(99) http://chemwiki.ucdavis.edu/Inorganic_Chemistry/Crystal_Field_Theory/Crystal_Field_Theory: accessed 22 October 2015.
(100) Stefan, F. In *Physical Chemistry I*; North Carolina State University Department of Chemistry: 2008.
(101) Cotton, F. A.; Wilkinson, G. *Anorganische Chemie* Verlag Chemie , Weinheim, 1980.
(102) Shriver, D. F.; P. W. Atkins ; Langford, C. H. *Inorganic Chemistry*; Oxford University Press , Oxford, 1991.
(103) Martin Klessinger; Michl, J. *Excited States and Photochemistry of Organic Molecules*; VCH Publishers, Inc.: United States of America, 1995.
(104) U., K.; Wilson, S. *Theoretical Chemistry and Physics of Heavy and Superheavy Elements* Dordrecht, Netherlands: Kluwer Academic Publishers: Netherlands, 2003.
(105) P., A.; R., F. *Molecular Quantum Mechanics*; Fifth ed.; Oxford University Press: UK, 2011.
(106) Azumi, T.; Miki, H. *Top Curr Chem* **1997**, *191*, 1.
(107) Obara, S.; Itabashi, M.; Okuda, F.; Tamaki, S.; Tanabe, Y.; Ishii, Y.; Nozaki, K.; Haga, M. *Inorg Chem* **2006**, *45*, 8907.
(108) Nozaki, K. *J Chin Chem Soc-Taip* **2006**, *53*, 101.
(109) Abedin-Siddique, Z.; Ohno, T.; Nozaki, K. *Inorg Chem* **2004**, *43*, 663.
(110) Yutaka, T.; Obara, S.; Ogawa, S.; Nozaki, K.; Ikeda, N.; Ohno, T.; Ishii, Y.; Sakai, K.; Haga, M. *Inorg Chem* **2005**, *44*, 4737.
(111) Miki, H.; Shimada, M.; Azumi, T.; Brozik, J. A.; Crosby, G. A. *J Phys Chem-Us* **1993**, *97*, 11175.
(112) Hartmann, H.; Parak, F.; Steigemann, W.; Petsko, G. A.; Ponzi, D. R.; Frauenfelder, H. *P Natl Acad Sci-Biol* **1982**, *79*, 4967.
(113) Berg, J. M.; Tymoczko, J. L.; S. L., B. *Biochemistry*, 2002.
(114) kagen, L. J. *Myoglobin: Biochemical, Physiological, and Clinical Aspects.*

; Columbia University Press., 1973.

(115) Brunori, M.; Bourgeois, D.; Vallone, B. *J Struct Biol* **2004**, *147*, 223.
(116) Wittenberg, J. B.; Wittenberg, B. A. *J Exp Biol* **2003**, *206*, 2011.
(117) Brunori, M. *Trends in Biochemical Sciences* **2001**, *26*, 209.
(118) Brunori, M. *Protein Sci* **2010**, *19*, 195.
(119) Brunori, M. *Trends in Biochemical Sciences* **2001**, *26*, 21.
(120) Gibson, Q. H. *J Biol Chem* **1989**, *264*, 20155.
(121) Gibson, Q. H.; Ainsworth, S. *Nature* **1957**, *180*, 1416.
(122) Frauenfelder, H.; McMahon, B. H.; Austin, R. H.; Chu, K.; Groves, J. T. *P Natl Acad Sci USA* **2001**, *98*, 2370.
(123) Moller, J. K. S.; Skibsted, L. H. *Chem Rev* **2002**, *102*, 1167.
(124) Vojtchovsky, J.; Chu, K.; Berendzen, J.; Sweet, R. *Schlichting, Biophys. J.* **1999**, *77*, 2153.
(125) Evans, S. V.; Brayer, G. D. *J Mol Biol* **1990**, *213*, 885.
(126) Balzani, V. *Electron transfer in chemistry*; Wiley-VCH: Weinheim ; New York, 2001.
(127) Stryer, L. *Annu Rev Biochem* **1978**, *47*, 819.
(128) Dosremedios, C. G.; Moens, P. D. J. *J Struct Biol* **1995**, *115*, 175.
(129) Zhang, L. Y.; Kao, Y. T.; Qiu, W. H.; Wang, L. J.; Zhong, D. P. *J Phys Chem B* **2006**, *110*, 18097.
(130) Stevens, J. A.; Link, J. J.; Zang, C.; Wang, L. J.; Zhong, D. P. *J Phys Chem A* **2012**, *116*, 2610.
(131) Weber, G.; Teale, F. J. W. *Discuss Faraday Soc* **1959**, 134.
(132) Willis, K. J.; Szabo, A. G.; Zuker, M.; Ridgeway, J. M.; Alpert, B. *Biochemistry-Us* **1990**, *29*, 5270.
(133) Arcovito, A.; D'Angelo, P.; Della Longa, S. *14th International Conference on X-Ray Absorption Fine Structure (Xafs14), Proceedings* **2009**, *190*.
(134) D'Angelo, P.; Lapi, A.; Migliorati, V.; Arcovito, A.; Benfatto, M.; Roscioni, O. M.; Meyer-Klaucke, W.; Della-Longa, S. *Inorg Chem* **2008**, *47*, 9905.
(135) Arcovito, A.; Ardiccioni, C.; Cianci, M.; D'Angelo, P.; Vallone, B.; Della Longa, S. *J Phys Chem B* **2010**, *114*, 13223.
(136) Westre, T. E.; Kennepohl, P.; DeWitt, J. G.; Hedman, B.; Hodgson, K. O.; Solomon, E. I. *J Am Chem Soc* **1997**, *119*, 6297.
(137) W. S. Caughey , G. I. E. *Inorganic Biochemistry*; American Elsevier: New York, N.Y, 1973.
(138) J. W. Buchler, K. M. S. *Porphyrins and Metalloporphyrin*; Elsevier. Amsterdam, 1975.
(139) Perutz, M. F. *Nature* **1970**, *228*, 726.
(140) Jameson, G. B.; Molinaro, F. S.; Ibers, J. A.; Collman, J. P.; Brauman, J. I.; Rose, E.; Suslick, K. S. *J Am Chem Soc* **1978**, *100*, 6769.
(141) Goff, H.; Lamar, G. N. *J Am Chem Soc* **1977**, *99*, 6599.
(142) Lange, K. M.; Golnak, R.; Bonhommeau, S.; Aziz, E. F. *Chem Commun* **2013**, *49*, 4163.
(143) Rich, A. M.; Armstrong, R. S.; Ellis, P. J.; Lay, P. A. *J Am Chem Soc* **1998**, *120*, 10827.
(144) P., G. J.; Genevive, B. *Journal of the Arkansas Academy of Science* **2001**, *Vol. 55*.
(145) Tilton, R. F.; Kuntz, I. D.; Petsko, G. A. *Biochemistry-Us* **1984**, *23*, 2849.
(146) Du, H.; Fuh, R. C. A.; Li, J. Z.; Corkan, L. A.; Lindsey, J. S. *Photochem Photobiol* **1998**, *68*, 141.
(147) Chantranupong L., L. G. H., Waleh A.; ACS Symposium Series; American Chemical Society: Washington, DC, 1986.: Molecular Theory Laboratory, The Rockefeller University, Palo Alto, CA 94304, 1986, p 2.
(148) Lim, M. H.; Jackson, T. A.; Anfinrud, P. A. *P Natl Acad Sci USA* **1993**, *90*, 5801.
(149) Baldo, M. A.; O'Brien, D. F.; Thompson, M. E.; Forrest, S. R. *Phys Rev B* **1999**, *60*, 14422.
(150) Adachi, C.; Baldo, M. A.; Thompson, M. E.; Forrest, S. R. *J Appl Phys* **2001**, *90*, 5048.
(151) Ikai, M.; Tokito, S.; Sakamoto, Y.; Suzuki, T.; Taga, Y. *Appl Phys Lett* **2001**, *79*, 156.
(152) Lo, S. C.; Male, N. A. H.; Markham, J. P. J.; Magennis, S. W.; Burn, P. L.; Salata, O. V.; Samuel, I. D. W. *Adv Mater* **2002**, *14*, 975.
(153) Grushin, V. V.; Herron, N.; LeCloux, D. D.; Marshall, W. J.; Petrov, V. A.; Wang, Y. *Chem Commun* **2001**, 1494.
(154) Lee, H. S.; Ha, Y. *Mol Cryst Liq Cryst* **2009**, *504*, 67.
(155) Baldo, M. A.; Lamansky, S.; Burrows, P. E.; Thompson, M. E.; Forrest, S. R. *Appl Phys Lett* **1999**, *75*, 4.
(156) Tamayo, A. B.; Alleyne, B. D.; Djurovich, P. I.; Lamansky, S.; Tsyba, I.; Ho, N. N.; Bau, R.; Thompson, M. E. *J Am Chem Soc* **2003**, *125*, 7377.
(157) Hay, P. J. *J Phys Chem A* **2002**, *106*, 1634.
(158) Schmittel, M.; Lin, H. W. *Inorg Chem* **2007**, *46*, 9139.
(159) Finkenzeller, W. J.; Yersin, H. *Chem Phys Lett* **2003**, *377*, 299.
(160) Hofbeck, T.; Yersin, H. *Inorg Chem* **2010**, *49*, 9290.

(161) Meng, S.; Jung, I.; Feng, J.; Scopelliti, R.; Di Censo, D.; Gratzel, M.; Nazeeruddin, M. K.; Baranoff, E. *Eur J Inorg Chem* **2012**, 3209.

(162) Wu, S. H.; Ling, J. W.; Lai, S. H.; Huang, M. J.; Cheng, C. H.; Chen, I. C. *J Phys Chem A* **2010**, *114*, 10339.

(163) Costa, R. D.; Orti, E.; Bolink, H. J.; Graber, S.; Schaffner, S.; Neuburger, M.; Housecroft, C. E.; Constable, E. C. *Adv Funct Mater* **2009**, *19*, 3456.

(164) Minaev, B.; Minaeva, V.; Agren, H. *J Phys Chem A* **2009**, *113*, 726.

(165) Choi, G. C.; Lee, J. E.; Park, N. G.; Kim, Y. S. *Mol Cryst Liq Cryst* **2004**, *424*, 173.

(166) Lai, S. H.; Ling, J. W.; Huang, Y. M.; Huang, M. J.; Cheng, C. H.; Chen, I. C. *J Raman Spectrosc* **2011**, *42*, 332.

(167) Nozaki, K.; Takamori, K.; Nakatsugawa, Y.; Ohno, T. *Inorg Chem* **2006**, *45*, 6161.

(168) Xu, M. L.; Zhou, R.; Wang, G. Y.; Xiao, Q.; Du, W. S.; Che, G. B. *Inorg Chim Acta* **2008**, *361*, 2407.

(169) Park, N. G.; Choi, G. C.; Lee, J. E.; Kim, Y. S. *Curr Appl Phys* **2005**, *5*, 79.

(170) Ichimura, K.; Kobayashi, T.; King, K. A.; Watts, R. J. *J Phys Chem-Us* **1987**, *91*, 6104.

(171) Gupta, D.; Katiyar, M.; Deepak; Hazra, T.; Verma, A.; Marloharan, S. S.; Biswas, A. *Opt Mater* **2006**, *28*, 1355.

(172) Tsai, H. R.; Lu, K. Y.; Lai, S. H.; Fan, C. H.; Cheng, C. H.; Chen, I. C. *J Phys Chem C* **2011**, *115*, 17163.

(173) Consani, C.; Aubock, G.; van Mourik, F.; Chergui, M. *Science* **2013**.

(174) Findsen, E. W.; Friedman, J. M.; Ondrias, M. R.; Simon, S. R. *Biophysical Journal* **1985**, *47*, A83.

(175) Franzen, S. *P Natl Acad Sci USA* **2002**, *99*, 16754.

(176) Strickland, N.; Harvey, J. N. *J Phys Chem B* **2007**, *111*, 841.

(177) Radon, M.; Broclawik, E.; Pierloot, K. *J Phys Chem B* **2010**, *114*, 1518.

(178) Petrich, J. W.; Poyart, C.; Martin, J. L. *Biochemistry-Us* **1988**, *27*, 4049.

(179) Cammarata, M.; Levantino, M.; Schotte, F.; Anfinrud, P. A.; Ewald, F.; Choi, J.; Cupane, A.; Wulff, M.; Ihee, H. *Nature Methods* **2008**, *5*, 881.

(180) Ahn, S.; Kim, K. H.; Kim, Y.; Kim, J.; Ihee, H. *J Phys Chem B* **2009**, *113*, 13131.

(181) Aziz, E. F.; Ottosson, N.; Bonhommeau, S.; Bergmann, N.; Eberhardt, W.; Chergui, M. *Phys Rev Lett* **2009**, *102*.

(182) Stickrath, A. B.; Mara, M. W.; Lockard, J. V.; Harpham, M. R.; Huang, J.; Zhang, X. Y.; Attenkofer, K.; Chen, L. X. *J Phys Chem B* **2013**, *117*, 4705.

(183) Mills, D. M.; Lewis, A.; Harootunian, A.; Huang, J.; Smith, B. *Science* **1984**, *223*, 811.

(184) Martin, J. L.; Vos, M. H. *Annual Review of Biophysics and Biomolecular Structure* **1992**, *21*, 199.

(185) Briois, V.; Moulin, C. C. D.; Sainctavit, P.; Brouder, C.; Flank, A. M. *Journal of the American Chemical Society* **1995**, *117*, 1019.

(186) Gawelda, W.; Pham, V. T.; Benfatto, M.; Zaushitsyn, Y.; Kaiser, M.; Grolimund, D.; Johnson, S. L.; Abela, R.; Hauser, A.; Bressler, C.; Chergui, M. *Phys Rev Lett* **2007**, *98*.

(187) Boucher, L. J. In *Coordination Chemistry of Macrocyclic Compounds*; Melson, G. A., Ed.; Plenum Press New York, 1979.

(188) Verma, S.; Kar, P.; Das, A.; Palit, D. K.; Ghosh, H. N. *J Phys Chem C* **2008**, *112*, 2918.

(189) Lima, F. A.; Milne, C. J.; Amarasinghe, D. C. V.; Rittmann-Frank, M. H.; van der Veen, R. M.; Reinhard, M.; Pham, V. T.; Karlsson, S.; Johnson, S. L.; Grolimund, D.; Borca, C.; Huthwelker, T.; Janousch, M.; van Mourik, F.; Abela, R.; Chergui, M. *Rev Sci Instrum* **2011**, *82*.

(190) Beaud, P.; Johnson, S. L.; Streun, A.; Abela, R.; Abramsohn, D.; Grolimund, D.; Krasniqi, F.; Schmidt, T.; Schlott, V.; Ingold, G. *Phys Rev Lett* **2007**, *99*.

(191) Yilmaz, R. *Radiat Phys Chem* **2014**, *96*, 1.

(192) Joly, Y. *Phys Rev B* **2001**, *63*.

(193) Bunau, O.; Joly, Y. *J Phys-Condens Mat* **2012**, *24*.

(194) Becke, A. D. *J Chem Phys* **1993**, *98*, 5648.

(195) Lee, C. T.; Yang, W. T.; Parr, R. G. *Phys Rev B* **1988**, *37*, 785.

(196) Vosko, S. H.; Wilk, L.; Nusair, M. *Can J Phys* **1980**, *58*, 1200.

(197) Stephens, P. J.; Devlin, F. J.; Chabalowski, C. F.; Frisch, M. J. *J Phys Chem-Us* **1994**, *98*, 11623.

(198) F, N. *WIREs Comput Mol Sci* **2012**.

(199) Schafer, A.; Horn, H.; Ahlrichs, R. *J Chem Phys* **1992**, *97*, 2571.

(200) Weigend, F.; Ahlrichs, R. *Phys Chem Chem Phys* **2005**, *7*, 3297.

(201) Grimme, S.; Ehrlich, S.; Goerigk, L. *J Comput Chem* **2011**, *32*, 1456.

(202) Grimme, S.; Antony, J.; Ehrlich, S.; Krieg, H. *J Chem Phys* **2010**, *132*.

(203) Hochstrasser, R. M.; Negus, D. K. *P Natl Acad Sci-Biol* **1984**, *81*, 4399.

(204) Gray, H. B.; Winkler, J. R. *Q Rev Biophys* **2003**, *36*, 341.

(205) Helbing, J.; Bonacina, L.; Pietri, R.; Bredenbeck, J.; Hamm, P.; van Mourik, F.; Chaussard, F.; Gonzalez-Gonzalez, A.; Chergui, M.; Ramos-Alvarez, C.; Ruiz, C.; Lopez-Garriga, J. *Biophys J* **2004**, *87*, 1881.

(206) Petrich, J. W.; Lambry, J. C.; Poyart, C.; Martin, J. L. *Biophys J* **1988**, *53*, A281.

(207) Gruia, F.; Kubo, M.; Ye, X.; Champion, P. M. *Biophys J* **2008**, *94*, 2252.

(208) Serianni, A. S.

(209) Hedley, G. J.; Ruseckas, A.; Samuel, I. D. W. *J Phys Chem A* **2009**, *113*, 2.

(210) Hedley, G. J.; Ruseckas, A.; Samuel, I. D. W. *Chem Phys Lett* **2008**, *450*, 292.

(211) Bram, O.; Messina, F.; Baranoff, E.; Cannizzo, A.; Nazeeruddin, M. K.; Chergui, M. *J Phys Chem C* **2013**, *117*, 15958.

(212) Tang, K. C.; Liu, K. L.; Chen, I. C. *Chem Phys Lett* **2004**, *386*, 437.

(213) Hedley, G. J.; Ruseckas, A.; Samuel, I. D. W. *J Phys Chem A* **2010**, *114*, 8961.

(214) Cannizzo, A.; Bram, O.; Zgrablic, G.; Tortschanoff, A.; Oskouei, A. A.; van Mourik, F.; Cherguil, M. *Opt Let* **2007**, *32*, 3555.

(215) Cannizzo, A.; Blanco-Rodriguez, A. M.; El Nahhas, A.; Sebera, J.; Zalis, S.; Vlcek, A.; Chergui, M. *J Am Chem Soc* **2008**, *130*, 8967.

(216) Lo, K. K. W.; Zhang, K. Y.; Leung, S. K.; Tang, M. C. *Angew Chem Int Edit* **2008**, *47*, 2213.

(217) Yeh, Y. S.; Cheng, Y. M.; Chou, P. T.; Lee, G. H.; Yang, C. H.; Chi, Y.; Shu, C. F.; Wang, C. H. *Chemphyschem* **2006**, *7*, 2294.

(218) Kozhevnikov, D. N.; Kozhevnikov, V. N.; Shafikov, M. Z.; Prokhorov, A. M.; Bruce, D. W.; Williams, J. A. G. *Inorg Chem* **2011**, *50*, 3804.

(219) Ladouceur, S.; Donato, L.; Romain, M.; Mudraboyina, B. P.; Johansen, M. B.; Wisner, J. A.; Zysman-Colman, E. *Dalton T* **2013**, *42*, 16974.

(220) Kleinschmidt, M.; van Wullen, C.; Marian, C. M. *J Chem Phys* **2015**, *142*.

(221) Domcke, W.; Yarkony, D.; Köppel, H. *Conical intersections : electronic structure, dynamics & spectroscopy*; World Scientific: River Edge, NJ, 2004.

(222) Messina, F.; Bram, O.; Cannizzo, A.; Chergui, M. *Nature Communications* **2013**, *4*.

(223) Sarkar, A.; Chakravorti, S. *J Lumin* **1995**, *65*, 163.

(224) Nozaki, K. *Journal of the Chinese Chemical Society* **2006**, *53*, 101.

(225) Bram, O.; Messina, F.; El-Zohry, A. M.; Cannizzo, A.; Chergui, M. *Chem Phys* **2012**, *393*, 51.

(226) Braem, O.; Penfold, T. J.; Cannizzo, A.; Chergui, M. *Phys Chem Chem Phys* **2012**, *14*, 3513.

(227) Polli, D.; Altoe, P.; Weingart, O.; Spillane, K. M.; Manzoni, C.; Brida, D.; Tomasello, G.; Orlandi, G.; Kukura, P.; Mathies, R. A.; Garavelli, M.; Cerullo, G. *Nature* **2010**, *467*, 440.

(228) Balzer, B.; Hahn, S.; Stock, G. *Chem Phys Lett* **2003**, *379*, 351.

(229) Penfold, T. J.; Karlsson, S.; Capano, G.; Lima, F. A.; Rittmann, J.; Reinhard, M.; Rittmann-Frank, M. H.; Braem, O.; Baranoff, E.; Abela, R.; Tavernelli, I.; Rothlisberger, U.; Milne, C. J.; Chergui, M. *J Phys Chem A* **2013**, *117*, 4591.

(230) Holzer, W.; Penzkofer, A.; Tsuboi, T. *Chem Phys* **2005**, *308*, 93.

(231) Ohsawa, Y.; Sprouse, S.; King, K. A.; Dearmond, M. K.; Hanck, K. W.; Watts, R. J. *J Phys Chem-Us* **1987**, *91*, 1047.

(232) Glusac K. D., J. S. a. S. K. S. *Chem. Commun.* **2002**, 2504.

(233) Andreiadis E. S., I. D., P ecaut J., Calborean A., Ciofini I., Adamo C., Demadrille R., and Mazzanti M. *Inorg. Chem.* **2011**, *50*, 8197.

(234) Ravel, B.; Newville, M. *J Synchrotron Radiat* **2005**, *12*, 537.

(235) Zhang, X. Y.; Canton, S. E.; Smolentsev, G.; Wallentin, C. J.; Liu, Y. Z.; Kong, Q. Y.; Attenkofer, K.; Stickrath, A. B.; Mara, M. W.; Chen, L. X.; Warnmark, K.; Sundstrom, V. *J Am Chem Soc* **2014**, *136*, 8804.

(236) El Nahhas, A.; van der Veen, R. M.; Penfold, T. J.; Pham, V. T.; Lima, F. A.; Abela, R.; Blanco-Rodriguez, A. M.; Zalis, S.; Vlcek, A.; Tavernelli, I.; Rothlisberger, U.; Milne, C. J.; Chergui, M. *J Phys Chem A* **2013**, *117*, 361.

(237) Gawelda, W.; Johnson, M.; de Groot, F. M. F.; Abela, R.; Bressler, C.; Chergui, M. *J Am Chem Soc* **2006**, *128*, 5001.

(238) McDonald, A. R.; Lutz, M.; von Chrzanowski, L. S.; van Klink, G. P. M.; Spek, A. L.; van Koten, G. *Inorg Chem* **2008**, *47*, 6681.

(239) Krappe, H. J.; Rossner, H. H. *Phys Scripta* **2009**, *79*.

(240) Rehr, J. J.; Kas, J. J.; Vila, F. D.; Prange, M. P.; Jorissen, K. *Phys Chem Chem Phys* **2010**, *12*, 5503.

(241) Colombo, M. G.; Brunold, T. C.; Riedener, T.; Gudel, H. U.; Fortsch, M.; Burgi, H. B. *Inorg Chem* **1994**, *33*, 545.

(242) Waern, J. B.; Desmarets, C.; Chamoreau, L. M.; Amouri, H.; Barbieri, A.; Sabatini, C.; Ventura, B.; Barigelletti, F. *Inorg Chem* **2008**, *47*, 3340.

(243) George, S. D.; Petrenko, T.; Neese, F. *Inorg Chim Acta* **2008**, *361*, 965.

(244) Perdew, J. P. *Phys Rev B* **1986**, *33*, 8822.

(245) George, S. D.; Neese, F. *Inorg Chem* **2010**, *49*, 1849.

(246) D. M. P. Mingos, P. D., J. -P. Dahl *Structure and Bonding*; Springer Heidelberg Dordrecht London New York: Springer-Verlag Berlin Heidelberg 2012, 2012; Vol. 142.

(247) Codola, Z.; Cardoso, J. M. S.; Royo, B.; Costas, M.; Lloret-Fillol, J. *Chem-Eur J* **2013**, *19*, 7203.

Mahsa Silatani

Personal details

✉ mahsa.silatani@gmail.com
☎ +41 78 891 8137
Personal address: Chemin de Riant-Mont 3, 1030 Bussigny, Switzerland
Professional address: EPFL SB ISIC LSU; CH H1 565; Station 6; CH-1015 Lausanne; Switzerland
https://www.researchgate.net/profile/Mahsa_Silatani
https://ir.linkedin.com/pub/mahsa-silatani/40/255/763

Date of birth: 05.06.1981
Nationality: Iranian

Education

04.2012-09.2015 **Ph.D. in Physics**,
Department of Chemistry, École Polytechnique Fédérale de Lausanne (EPFL), Lausanne, Switzerland.
Swiss light Source, Paul Scherrer Institut (PSI), Villigen, Switzerland.
Title *Time-resolved X-ray and Optical Studies of Metalloproteins and Iridium Complexes*
Supervisor Professor Majed Chergui

01.2005- 06.2007 **MSc. in Physics,** Department of Physics, Sharif University of Technology,Tehran, Iran
Title *Study of Sonoluminescence of an Argon Bubble in Water and Different Concentrations of Sulfuric Acid Solutions*
Supervisor Professor Rasoul Sadigh-Bonabi

09.1999- 06.2004 **BSc. in Physics**, Department of Basi Sciences, K. N. T University of Technology , Tehran, Iran
Title *Experimental project of taking 3D Holographic photography with a He-Ne Laser*
Supervisor Dr. Darioush Fathi

Work Experiences

2012 - 2015 Doctoral Assistant EPFL/ PSI
2009 - 2012 Researcher of R&D office of Monenco Iran Consultant Engineering Co., Tehran, Iran.
2007-2010 Research Assistant of Laser Research Lab, Dep. of Physics, Sharif University, Tehran, Iran.

Teaching Experience

Teacher Assistant for Molecular Physics for Master grade at EPFL
Instructing two master students of my thesis advisor in the field of Sonoluminescence
Teacher Assistant for Laser Lab, K .N. Toosi University of Technology, winter 2004.

Publications

[1] **M. Silatani**, F. –A. Lima, T. –J. Penfold, J. Rittmann, M. Reinhard, H. –M. Rittmann-Frank, C. Borca, D. Grolimund, C. –J. Milne, M. Chergui, "NO binding kinetics in myoglobin investigated by picosecond Fe K-edge absorption spectroscopy", PNAS, vol. 112, no. 42, 12922–12927, doi: 10.1073/pnas.1424446112, 2015.

[2] F. Messina, E. Pomarico, **M. Silatani**, E. Baranoff, M. Chergui, "Ligand-Centred Fluorescence and Electronic Relaxation Cascade at Vibrational Time Scales in Transition Metal Complexes", *J. Phys. Chem. Lett.*, 2015, 6, pp 4475–4480.
[3] F. G. Santomauro, A. Lübcke, J. Rittmann, E. Baldini, A. Ferrer, **M. Silatani**, P. Zimmermann, S. Grübel, J. A. Johnson, S. O. Mariager, P. Beaud, D. Grolimund, C. Borca, G. Ingold, S.L. Johnson & M. Chergui, "Femtosecond X-ray absorption study of electron localization in photoexcited anatase TiO2",Scientific Reports | 5:14834 | DOI: 10.1038/srep14834,2015.
[4] Kh. Imani**,** F. Bemani, **M. Silatani,** R. Sadighi-Bonabi, "Ambient temperature effect on single-bubble sonoluminescence in different concentrations of sulfuric acid solutions*",*Phys. Rev. E 85**,** 016329 (2012).
[5] R. Sadighi-Bonabi, E. Irani, B. Safaie, Kh. Imani, **M. Silatani**, S. Zare" *Possibility of Ultra-intense Laser Transmutation of* ^{93}Zr*, (γ, n)* ^{92}Zr *a Long-lived Nuclear Waste into a Stable Isotope*", Energy Conversion and Management, 51 (2010) 636–639.
[6] Moshaii A., Kh. Imani, **M. Silatani**, "*Sonoluminescence radiation from different concentrations of sulfuric acid*", Phys. Rev. E, 80, 046325 (2009).
[7] Moshaii A., R. Rezaei-Nasirabad, Kh. Imani**, M. Silatani,** R. Sadighi-Bonabi, *"Role of Thermal conduction in Single-Bubble Cavitation",* Physics Letter A, Volume 372, Issue 8, p. 1283-1287(2007).

Presentations and Posters

Talks

CSX 3rd Workshop on the Simultaneous Combination of Spectroscopies with X-ray Absorption, Scattering and diffraction Techniques, July 4-6, 2012, ETH Zurich, Switzerland.

Posters

Swiss Chemical Society Fall meeting 2013, September 6, 2013, EPFL/Lausanne, Switzerland.
Joint Users' Meetings at PSI: JUM@P series, September 18-20, 2013, PS I Villigen, Switzerland.
SPG Annual Meeting MUST/ ETH-FAST, September 22, 2013, ETH Hönggerberg, Switzerland.
XFEL 2012 summer school, June 4-8, 2012, Annecy, France.
Review panel meeting of the NCCR MUST program, June 6, 2012, University of Bern, Switzerland.
MUST Annual Meeting, June 21-22, 2012, ETH Zurich, Switzerland.

Awards

My doctoral studies have been sponsored by EPFL, PSI, and Swiss National Science Foundation.
Second best Master student in the honor roll of the faculty with a dissertation score of 20/20.
Membership of two National Technical Committees for Standardization of Solar Energy Vocab &Testing.
Membership of TC180 International committee of Solar Cell Standards in Iran.

Skills

Computer skills

General purpose	MacOS, Windows, Linux, Microsoft Office, LateX, Photoshop
Scientific	Visual Basic, Fortran 90, FEFF9, FEFFIT, basics of Matlab and Mathematica, Igor Pro, Origine, GNUplot,Tec plot 10

Language

Persian	Native
Azeri	second mother tongue
English	Fluent
French	Basic (A1/A2- Common European Framework of Reference for Language)
German	Basic (A1- Common European Framework of Reference for Language)

Acknowledgements

Starting my Ph.D., I became a seeker who left behind her home and family (comfort zone) hoping to find my true position in this world; to see if I can become a scientist in the field of Physics that I loved so much. Over the course of the last three years and a half, I was aware that I do not only do science but I also transform into a better version of myself and flourish. In the first place, I would like to express my deepest gratitude to my thesis supervisor Professor Majed Chergui for having offered me this life-changing opportunity to join his amazing group here at EPFL. All these years he was a constant source of scientific knowledge, and inspiration. Moreover, his ability to fluently talk several languages and also his talent in the music always motivated me to learn more languages and value more the artistic part of my soul along with the scientific face. He always insisted on me becoming independent in doing my research. Moreover, he manages an extremely successful team of researchers and guides us towards the frontiers of ultrafast science.

In the first two years of my Ph.D. I had the privilege to work with great scientist at the Swiss Light Source, Paul Scherrer Institute at Villigen. In the first six months of my Ph.D. I was lucky enough to have Dr. Chris Milne as the head of our group at PSI for teaching me how to plan and do time-resolved XAS experiments. He was always available. Even after he had left our group he was always available for scientific discussions and generously welcoming my questions. Since then Dr. Jochen Rittmann was my direct supervisor for two years and I cannot find the appropriate words to acknowledge him for guiding me step by step through these

years. I am grateful for his patience and kindness that made it much easier for me to ask him all my stupid questions and for several hours of discussions, for all the rehearsal presentations. He and his wife, Dr. Hannelore Rittmann-Frank, are the kindest couple I could possibly have as colleagues and friends; they always made my life easier and happier with their support while adopting to the culture of my new home country. Hannelore showed me how to become a strong and confident female scientist, overcoming all the challenges of working in a men's field of research. Moreover, I would like to thank Dr. Andrea Lübcke for an unforgettable cooperation and for the inspiration and best example of being a successful female scientist.

A very big "Thank you" for supporting this work goes to Professor Thomas J. Penfold, who provided all the TDDFT and XANES simulations of all the static and time-resolved X-ray absorption spectra, and also for all the fruitful discussions we have had. I would like to acknowledge Dr. Frederico Alves Lima for his commitment and for helping me taking over the project he had started.

Also I would like to acknowledge every single person that helped me making my experiments and consequently my Ph.D. possible — I would not have succeeded without all the people involved. I am very grateful to the expertise of the MicroXAS beam line: Dr. Camelia Borca, Dr. Daniel Grolimond, Beat Meyer and Mario Birri. It has been a great deal of joy collaborating with the enthusiastic FEMTO group of Prof. Steven Johnson at PSI including Dr. Gerhard Ingold, Dr. Jeremy Johnson, Dr. Sebastian Grübel, Dr. Paul Baud, Alex Oggenfuss, Dr. Andrin Caviezel, and Dr. Andres Ferrer. Also, I appreciate a lot the expertise of the Phoenix and SuperXAS beam line teams, Dr. Thomas Huthwelker, Dr. Jakub Szlachetco, Dr. Maarten Nachtegaal, and Dr. Grigory Smolentsev. Also, I am thankful to Dr. Etienne Baranoff for his collaboration and our fruitful discussions.

When I moved to Lausanne for the last year of my Ph.D., Dr. Enrico Pomarico, and Dr. Jakob Grilj were the people whom I referred to the most for each and every question that I had. I would like to express my deep gratitude to Dr. Enrico Pomarico for several long discussions we had while writing scientific papers. Dear Jakob, please accept my sincere gratitude for being such a wonderful colleague to me. You have been always kind, patient, and supportive. You were always motivating me towards my success and you were always there to help me finding the right answers to my questions and also for correcting my manuscript

until the last minute. I learned from you how much one could be humble and caring about the people around him. Thank you for being such a wonderful person that does not give up in helping people.

In fact, one of the most creative and free minds I have ever seen in my life belongs to my best friend and colleague, Fabio Santomauro. I learned from him how to have different perspectives on one subject and how to search for simple answers to very difficult questions; to be independent and sufficient to follow one's instincts; to live science and enjoy understanding it the most; as well as helping others to do so; how to keep oneself unbiased about science and standing by the truth no matter who presents it. I would like to thank you, dear Fabio, for being such an amazing friend through all these years at PSI and here at EPFL. Thank you for being generous to me with your time and knowledge.

Thank you all for being my dear great friends and memorable colleagues: Dr. André Al-Haddad, Dr. Christopher Arrell, Dr. Gerald Auböck, Edoardo Baldini, Gloria Capano, Dr. Adrien Chauvet, Janina Löffler, Lars Mewes, Dr. Fabrizio Messina, Dr. Roberto Monni, Dr. Frank Van Mourik, Dr. Ahmad Odeh, Jose Ojeda, Dr. Malte Oppermann, Tania Palmieri, Dr. Marco Reinhard, Thomas Rossi, Prof. Jacinto Sa, Patric Zimmerman and all my cheerful friends in the LUMES groupAbove all, my very special thanks go to Ms. Monique Bassin whose kindness and patience made everything easy for me when proceeding with administrative works. Her discipline and talent in speaking many different languages were inspiring me. I would also like to express my gratitude to Ms. Anh Eymann, to my mentor at EPFL and to Professor Vincenzo Savona for being my supportive connections with Physics Doctoral School who always cheerfully helped me to go through all the academic process during these years. I would like to express my deep gratitude to all of the people who contributed to this work through their technical support, the experts of the Electric Workshop at EPFL: Supardi Sujito, Harald Holze, and Grégoire Pasche; also the experts of the Mechanical Workshop at EPFL: Cédric Mora, and André Fattet.

My dear friends whom I am grateful for having them in my life and for encouraging me throughout my Ph.D. and stood by my side in happy and sad days: Ghazal Kashani and Mostafa Bagheri, Elham Ghadiri, Haiying Gou-Güntay and Doruk Güntay, Gwen Pascua Damon, and Sinan Teske. My dear Dr. Sarah Shephard, I would like to thank you for coaching me through

the "Fixing the leaky pipeline" program of EPFL during the last year of my Ph.D. and for teaching me how to manage my professional life and do networking for my future career plans.

Last but not least, my beloved family without whose support and encouragement I would not have been able to overcome all those difficult moments of hard work while missing them so much. I would like to take the advantage of this moment to express my gratitude to them separately in my mother tongue.

You have all touched my heart and influenced me, so thank you for being in my life and I wish you all health, success, and happiness in every step of your life.

Lausanne,
Switzerland

28 October 2015.

پدر و مادر عزیزم و برادر های نازنینم ،

از اینکه هر روز زندگی من رو با حضورتون سبز و روشن کردید سپاسگزارم . بدون تشویقها و حمایتهای شما هرگز به اینجا نمی رسیدم . براتون آرزوی سلامتی و شادکامی و موفقیت دارم و امیدوارم همیشه در کنار هم شاد و خوشبخت باشیم .

مهسا سیلاطانی

لوزان هشتم آبانماه ۱۳۹۴